The clustering properties of the reddest galaxies with UKIDSS-DXS

AIDAN SEDGEWICK

The clustering properties of the reddest galaxies with UKIDSS-DXS

Aidan Sedgewick

A Thesis presented for the degree of
Doctor of Philosophy

Centre for Extragalactic Astronomy
Department of Physics
Durham University
United Kingdom

November 2022

The clustering properties of the reddest galaxies with UKIDSS-DXS

Aidan Sedgewick

Abstract: Deep, photometric near-infrared surveys are the most effective ways to select massive galaxies at redshift $z > 1$, where their characteristic spectral features are observed at wavelengths longer than optical surveys are designed to measure. In this Thesis, we present and study the clustering properties of such galaxies using the UKIDSS-DXS near-infrared survey.

Firstly we produce deep, uniform mosaics for the $28\,\mathrm{deg}^2$ of J and K band imaging, which reach depths of $K_{\mathrm{AB}} \sim 22.7$ (5σ for point sources), and produce galaxy catalogues which we match with deep optical surveys. We demonstrate that these catalogues have reliable photometry (by way of comparison with 2MASS), we are able to efficiently remove foreground galactic stars, and that we produce the expected number counts galaxies. These catalogues will be made available at some point in the near future.

From these catalogues we select Extremely Red Objects (EROs), Distant Red Galaxies (DRGs) and BzKs, all of which aim to exploit the strong 4000Å break which is present in the oldest stellar populations. The combination of area and depth provided by DXS allows us to probe the large scale structure of the universe to tens of megaparsecs at $z > 1$. We demonstrate using the small area of H-band DXS coverage that selection of EROs is still effective with similar criteria in $i - H$ and $r - H$, although do not suggest any new criteria different to those already existing in literature.

We measure the angular two point correlation of the EROs and passive BzK selection of galaxies. We show that these selections of galaxies exhibit significantly stronger clustering on the smallest scales than what is often assumed by the clustering studies of main sequence galaxies, indicating that these galaxies are residing in the most massive dark matter haloes. Further, we demonstrate that there is a strong break in the correlation function in these selections of galaxies.

The correlation length r_0 we measure when considering the small scale (intra-halo) clustering alone is roughly constant for across the range of magnitudes DXS detects EROs, $K \sim 18$

to $K \sim 22$. Given that the halo mass of will be determined by the largest mass galaxy, we interpret this (in a qualitative sense) to mean that the dark matter host halo mass of the most massive EROs is roughly constant over the redshift range DXS measures EROs ($1 < z < 1.5$). A comparison of the angular correlation function for passive and star-forming BzK galaxies (for three magnitude cuts where we have sufficient number counts) indicates that the passive galaxies are indeed much more strongly clustered than the star-forming: evidence of environmental quenching.

We present K-band luminosity functions of our galaxy catalogues, and the ERO selection for $1 < z < 1.5$. We observe that the faint end slope of the ERO luminosity function is much steeper than those of the full galaxy catalogues, confirming that the ERO criteria selects galaxies that are amongst the most luminous in this redshift range. Finally, we measure the galaxy stellar mass function of the full sample of galaxies, and of restframe $U - B$ selected passive galaxies over the range $0.5 < z < 1.5$. We compute the integrated stellar mass density of the full galaxy sample, and our values match well with those in the literature. By computing the galaxy stellar mass density of the passive galaxy sample, and the contribution of the very massive end, we observe that the stellar mass density in the most massive passive galaxies is increasing faster than the stellar mass density of the passive galaxies as a whole, an observation which agrees with previous studies. Given that the galaxy stellar mass function of passive galaxies is well-described by a single Schechter function, which implies a single mechanism of galaxy quenching, we rule out a significant amount of dry mergers at the massive end, and instead postulate that this tentatively suggests that the mass quenching efficiency of the most massive galaxies is lower at later times.

UKIDSS-DXS represents only a fraction of the vast datasets that the upcoming generation of instruments and surveys such as *Rubin*-LSST, *Euclid* and *Roman* will produce, and this work is a precursor to investigations which use these surveys.

Contents

List of Figures

List of Tables

Declaration

The work in this Thesis is based on research carried out in the Centre for Extragalactic Astronomy, Department of Physics, Durham University, United Kingdom. No part of this Thesis has been submitted elsewhere for any other degree or qualification and it is all my own work unless referenced to the contrary in the text.

Content in Chapters 2 and 3 is being prepared for publication in:

Sedgewick, A., Edge, A. C., et al. *in prep* (2022)

The author of the Thesis was primarily responsible for all aspects of this publication.

Acknowledgements

First and foremost, enormous thanks go to my supervisor, Alastair Edge. It is impossible to sum up in just a few sentences how much I appreciate the all the advice and time you have given me. A PhD is a daunting endeavour, and I am exceptionally lucky to have had someone as knowledgeable and enthusiastic as you to guide me through it. But most of all, you are a wonderful, kind person, and I feel privileged to have worked with you for the past four years.

I am also grateful to Profs. Carlton Baugh, Peder Norberg, and Frank Krauss, not only for giving me the opportunity to study for a PhD with the Data Science CDT, but for the many exciting opportunities (and sandwiches) that the CDT has afforded me.

I would like to thank Dr. Ryan Cooke, for his kind advice and mentorship, both before and throughout my PhD. Thanks also to Prof. Ray Sharples for his guidance during my master's project which allowed me to continue on to study for a PhD.

This PhD would have been much more lonely if not for the fantastic friends I have made during my time here in Durham. Of course, it would be impossible to name everyone (and I'm sorry to those I've missed), but in particular, I'd like to thank Aoife, Arnau, Carol, Giorgio, Ed, Ellen, Jack, Josh, Louise, Miguel, Myles, Tom, Ugnė and Vicky. Further - Dan, Owen, Rebekha, Sam, and Steph for their friendship long before I started this.

Finally, I am endlessly grateful to my family: Mam, Dad, Ieuan, and my grandparents. You have always encouraged me to pursue my interests, and have always supported me to "stay in school" for as long as I have! It is *only* because of your love and support that I am where I am today - I love you all.

Chapter 1

Introduction

1.1 Cosmology from observations

The advent of the telescope in the 17^{th} century was the juncture which allowed astronomers to truly begin to understand the universe in which we live. The first great consequence of this was the proof that Earth was not in fact the centre of the universe. A heliocentric model of the universe (or, what was known of it at the time) was first proposed by astronomers and philosophers of antiquity, such as Aristarchus of Samos (c.310-c.230 BCE), but it was not until Galileo Galilei's observations of the moons of Jupiter and the phases of Venus in 1610 (some 1800 years) later that incontrovertible proof was provided.

Arguably, modern cosmology began in 1917 with Einstein's theory of general relativity, but in the early 1920s, debate still existed about whether all observed objects existed with the Milky Way, or that contemporarily-named "spiral nebulae" (now spiral galaxies) were distinct systems. It was proven decisively that the universe extended significantly further than the Milky Way with Edwin Hubble's observations of Cepheid Variables in M31 (Andromeda) placing it at a distance much further than the edge of the Milky Way (Hubble, 1925).

The Freidmann-Lemaître-Robertson-Walker metric (FLRW, developed independently in the 1920s-1930s, by the four scientists who it is named for) is a solution to Einstein's field equation which allows for an expanding universe. Two pieces of observational evidence demonstrated that the universe was indeed expanding. Firstly, Vesto Slipher discovered the redshift of galaxies and interpreted this as a recession velocity of the "spiral neubulae", much greater than that of stars within the Milky Way (Slipher, 1917) ($570\,\mathrm{km\,s^{-1}}$ vs. $20\,\mathrm{km\,s^{-1}}$). Secondly, the demonstration by Hubble (1929) that the recession velocities of (local) galaxies v are

proportional to their distance d, $v = H_0 d$, (Hubble's law, with H_0 as the proportionality constant), even though Hubble's measurement of $H_0 = 500\,\mathrm{km\,s^{-1}\,Mpc^{-1}}$ is quite different from today's accepted value which is closer to $H_0 = 70\,\mathrm{km\,s^{-1}\,Mpc^{-1}}$.

From the FLRW metric emerged the current cosmological paradigm, ΛCDM, which requires two so-called "dark components" in addition to baryonic matter. Firstly, cold dark matter (the CDM component of ΛCDM), which behaves gravitationally identically to baryonic matter but does not interact with photons or itself in the same way that baryonic matter does. The second component, dark energy (Λ), which is understood to be the energy which provides a negative pressure and is actually accelerating the expansion of the universe. The fundamental nature of these two dark components is not understood at all, although crucially their effects can be seen observationally.

Some of the earliest observational evidence for dark matter arises from applying the Virial theorem to the velocities of galaxies in the Coma cluster. Zwicky (1933)[1] notes in his work that the mass of the cluster ought to be approximately 400 times larger than that of luminous material. Zwicky's inference was correct, although recent estimates which use better models for the luminous mass put the dark matter-to-baryon ratio at smaller values of 11:1 (White et al., 1993).

There is also evidence of dark matter to be found on scales of individual galaxies. The spectacular structure of grand design spirals invites investigation into their rotation speeds. A study by Rubin & Ford (1970) of emission regions of across M31 demonstrated strikingly that the circular rotation velocities of the spiral disc appears constant out to large distances from the galactic centre. Given that the surface brightness of these types of galaxy decreases exponentially with radius, a constant mass-to-light ratio (for which starlight alone traces mass) would imply that the circular velocity should decrease as $v_c \propto r^{-1/2}$. Similarly to the conclusions drawn by Zwicky, one explanation with major implications is that a significant amount of mass is not accounted for in the outer regions of galaxies when considering that only contained within baryons. These early observations were corroborated by both optical and 21 cm investigations of more spiral galaxies (Rubin et al., 1980, 1985; van Albada et al., 1985), and found very similar results. Moreover, it was shown that the form of the gravitational potential (and hence the density distribution of the unobserved matter) inferred from the constant rotation curve does *not* depend on the optical morphology of the galaxy, specifically, $\rho_{\mathrm{DM}}(r) \propto r^{-2}$.

[1] English translation from `https://arxiv.org/pdf/1711.01693.pdf`

Another distinct piece of observational evidence for dark matter is gravitational lensing. Einstein's theory of gravity predicts that the light from distant objects will be distorted (or lensed) by massive foreground objects which act as the lens, if aligned properly. The first gravitationally lensed object to be observed was the "Twin Quasar" (Walsh et al., 1979) at redshift 1.413, which is doubly imaged, with the lensing caused by a galaxy at redshift 0.355. Importantly, the strength of the distortion is related to the mass of the lens object, and observations of galaxy clusters with many galaxies such as Abell 1689 (Abell et al., 1989) show the distinct arcs of lensed distant galaxies to be much stronger than could be explained if the lensing cluster were only composed of baryonic matter. Further, reconstruction of the distribution of dark matter within the lensing object (often extremely massive clusters with thousands of galaxies) can be attempted if there are sufficiently many lensed galaxies, (eg. the cluster merger MACSJ0416-0213; Jauzac et al., 2015; Natarajan et al., 2017).

The second of the dark components, dark energy, has similarly extensive evidence to support its existence. Type Ia Supernovae can be calibrated to act as "standard candles" (Phillips, 1993; Riess et al., 1996; Perlmutter et al., 1997); objects with an intrinsic luminosity whose distance can then be accurately inferred using only their apparent magnitudes, which crucially is a measurement independent of their redshift. In some cases they can appear as bright as the host galaxy, before fading over a period of weeks to months. Comparing these distances as a function of redshift to those predicted by models of cosmology with varying matter and dark energy content allows for precise determination of these parameters. This acts as an extension of the work done by Hubble, whose empirical linear relation does not hold at high redshifts. Indeed, measurements such as Hubble's and those provided by SNeIa are referred to as "rungs on the cosmic distance ladder".

Entering the era of precision cosmology, the Cosmic Microwave Background anisotropy measurements of the Cosmic Background Explorer (COBE), Wilkinson Microwave Anisotropy Probe (WMAP) and *Planck* (Planck Collaboration, 2020) simultaneously measure the dark and baryonic matter and dark energy content of the universe to incredible precision.

The final major piece of cosmology to consider in the FLRW metric is the curvature of the universe. For the universe to be "flat", the total energy density of the universe must equal the critical density,

$$\rho_{\rm crit} = \frac{3H^2}{8\pi G}, \tag{1.1.1}$$

where H is the Hubble parameter and G is the gravitational constant. A density parameter $\Omega = \rho/\rho_{\rm crit}$ can then be defined, meaning that a flat universe would have $\Omega = 1$. The

proportions that dark energy Ω_Λ and baryonic matter $\Omega_\mathrm{M} = \Omega_b + \Omega_\mathrm{DM}$ contribute to the overall energy density of the universe is crucial to this. The Planck Collaboration (2020) report a universe which is 13.801(24) Gyr old with dark energy density $\Omega_\Lambda = 0.6889 \pm 0.0056$ and matter density $\Omega_\mathrm{M} = 0.3111 \pm 0.0056$, of which 84% is dark matter, and the remaining 16% baryonic. They also derive $\Omega_\mathrm{K} = 0.001 \pm 0.002$, the fraction which the curvature contributes to the energy density. These measurements are consistent with the universe being flat.

1.2 Galaxy evolution

Galaxies are not static objects - rather, they evolve through cosmic time due to a wide range of processes. Based on their rates of star formation, galaxies can be roughly divided into those with steady, on-going star formation, and those who are mostly passively evolving (also often referred to as quiescent galaxies). The bimodality between these two galaxy populations is much more stark when studied as the star formation rate–stellar mass relation (SFR-SM relation; eg. Elbaz et al., 2007; Wuyts et al., 2007), which demonstrates that star-forming galaxies have predictable rates of star formation (for a given stellar mass), a relation named the main sequence. Elliptical galaxies, which in general are more massive than spirals, are said on the whole to be quiescent or passively-evolving, meaning that there is no steady rate of star formation. Given these galaxies are no longer forming stars, they are made primarily of the oldest stellar populations, and are able to grow only through mergers. As they typically live in the most dense environments, it is unlikely that they merge with other gas-rich galaxies, meaning the resultant is unlikely to be a starburst.

The main sequence relation demonstrates that (for actively star-forming galaxies) stellar mass $\log M_\star$ is proportional to star formation rate, $\log \mathrm{SFR}$ (measured in units of $\mathrm{M}_\odot\ \mathrm{yr}^{-1}$, solar masses formed per year). For instance, the Milky Way, a $6 \times 10^{10}\ \mathrm{M}_\odot$ spiral galaxy has been estimated to have a SFR of $\sim 2\ \mathrm{M}_\odot \mathrm{yr}^{-1}$ Licquia & Newman (2015). It has been shown that this relation holds until at least $z \sim 6$ (Salmon et al., 2015, eg). Star formation is possible only when there is a reserve of cold gas in the galaxy, which can be consumed and converted into new stars.

The rate of star formation on average, measured as the star formation rate density, SFRD (in $\mathrm{M}_\odot\ \mathrm{yr}^{-1}\ \mathrm{Mpc}^{-3}$), has *not* been constant throughout cosmic history, and in fact peaks at around $z \sim 2$ (Madau & Dickinson, 2014). Madau & Dickinson's review and compilation of the SFRD throughout cosmic history estimates that around 25% of the observed stellar mass

in galaxies today was formed before this peak, and 75% before $z = 0.7$, when the universe was half of its current age.

Of course, this process of star formation in galaxies does not continue indefinitely. Quenching is the process by which star formation is "switched off" - when the gas in the galaxy is heated so that it can no longer condense and form stars, or when there is sufficient heating to prevent new gas from accreting onto the halo. For the most massive spirals, it is theorised that the energy to provide this heating is produced by gas accreting onto the central black hole in "AGN feedback" (eg. Alexander & Hickox, 2012; Fabian, 2012). This accretion is extremely efficient, and can release $\sim$ 10% of the rest mass energy of the accreted matter, which is easily sufficient to heat the gas so that is can no longer collapse.

Conversely, at the low mass end of the galaxy population, the dominant mechanism for gas heating is supernovae feedback. Simulations such as Smith et al. (2018) demonstrate that supernovae feedback is able to suppress star-formation in line with observations. Further, they also demonstrate that these mechanisms can eject sufficient fractions of gas to account for the observations of metal-enriched gas which is observed in the circum-galactic medium.

Returning to the SFR-SM relation, a small population of galaxies exists at SFRs significantly larger (by factors of 10) than the star-forming main sequence for the same stellar mass, termed 'starbursts' (eg. Giavalisco, 2002). These extreme objects are expected to be driven primarily by mergers (or close encounters), in which a large fraction of the gas available for star formation is used in a very short timescale. Even though these violent events have such extreme rates of star formation, Rodighiero et al. (2011) estimate that even at the peak of cosmic star formation ($z \sim 2$), starbursts comprise only 2% of their mass-selected sample of star-forming galaxies, with a contribution of around $\sim$ 10% towards the overall cosmic SFR density. Rodighero do conclude, however, that "[starbursts] represent a critical phase toward the quenching of star formation and morphological transformation in galaxies".

Observational studies have revealed a "galaxy downsizing" scenario (Cowie et al., 1996; Mortlock et al., 2011), in which the most massive galaxies form their stellar populations (which are now observed to be old stellar populations) at early times, with progressively less massive galaxies going through a phase of star formation, and then quenching to become part of the quiescent population.

Galaxy downsizing is also predicted by models of galaxy formation: by considering the redshift at which current number density of stars formed in galaxies is greater than the average over the previous cosmic time, the models in Bower et al. (2006) predict that the most massive

galaxies ($M > 10^{10}\mathrm{M}_{\odot}$) have already formed the majority of their stellar mass by $z \sim 1$. Less massive galaxies have only recently crossed this threshold. They also quote similar to values Madau & Dickinson (2014)'s estimates: 20% of the total stellar mass in galaxies in the models has formed by $z = 3$, and 50% by $z = 1.6$. These predictions in Bower arise because of AGN feedback.

Two very useful tools used in studying galaxies in the context of galaxy evolution are the galaxy luminosity function[2] (LF; eg. Schmidt, 1968; Mortlock et al., 2017), and galaxy stellar mass function (GSMF; eg. Ilbert et al., 2013; Davidzon et al., 2017), which describe the number density of galaxies in terms of these two properties. Many of the properties of galaxy evolution are displayed by these two statistics. For instance, the GSMF is often modelled as a Schechter function, which is a power law modulated by an exponential cutoff (mode rigorously defined in Chapter 5). Not only does this often provide a very good fit to the measured GSMF, but can also be physically motivated: Peng et al. (2010) interpret the exponential cutoff of the Schechter function as the increasing probability (as a function of mass) that a star-forming galaxy will be quenched and join the passive galaxy population. This is the so-called "mass-quenching mechanism", for which the AGN feedback described above is a strong candidate. Further, a consistent value of the cutoff (characteristic) mass in the LF/GSMF is indicative of the downsizing picture: although the overall normalisation of the GSMF might increase, on the whole, the masses to which galaxies are able to grow before they are quenched is not changing with cosmic time.

These mechanisms explain why the observed galaxy stellar mass function is suppressed at low and high masses when compared to the halo mass function (eg. Davidzon et al., 2017): galaxies more massive than a characteristic mass are no longer able to increase their stellar mass.

The current paradigm of cosmic structure formation requires that galaxies form in the centre of, and co-evolve with, dark matter haloes (White & Rees, 1978; White & Frenk, 1991). From this, it can be expected that these luminous galaxies are tracers of the underlying dark matter structure, although they are said to be biased tracers, as it is expected that not all dark matter haloes host galaxies (Kaiser, 1984).

[2] the galaxy luminosity function is often described in terms of absolute magnitude

1.3 Galaxy clustering

Galaxy evolution is intrinsically tied to the evolution of structure in the universe on much larger scales than the galaxies themselves.

A further prediction of the cosmological models is that structure should form hierarchically (Lacey & Cole, 1993; Navarro et al., 1997); that is, the largest objects should assemble last, and that there should also be substructure within the haloes which host galaxies and clusters. For the former, evidence of this picture can be found locally. The alternative "top-down" scenario is that galaxies should form in large groups, and "escape" to less dense environments. Under this picture, Peebles (1993) argues that galaxies within the local group would show strong peculiar (excess) velocities away the likely site of their formation, the Virgo cluster, the nearest massive galaxy cluster. Instead, the local group in fact shows the opposite, and is on the whole moving in the direction of the Virgo cluster (Huchra, 1988), supporting this "bottom-up" hierarchical picture.

Note that this hierarchical picture is not antithetical to the downsizing scenario described in Section 1.2. In their work, Neistein et al. (2006) use N-body simulations to demonstrate that the downsizing trend of increasing stellar mass emerges with the hierarchical structure . However, Fontanot et al. (2009) raise some tension in that while their hierarchical galaxy formation models produce the general trend of star formation moving to less massive galaxies at later times, they do not recover the same differential trend in stellar mass as observations. Rather, their models predict too many low mass galaxies at high redshifts.

One statistical tool to quantify this large scale structure is galaxy clustering, or more specifically, two-point correlation functions, which measure the likelihood of finding pairs of galaxies at a given separation (physical or angular) as compared to a random distribution (eg. Peebles, 1993).

Peebles (1974) demonstrate that galaxy clustering follows (to first approximation) a power law over galaxies from 1 to 20 deg, using the galaxy catalogues produced by Zwicky. Further, they show the striking result that there is no anti-correlation around clusters: "there are no holes around galaxy clusters".

The strength of clustering is also correlated strongly with the properties of the sample of galaxies which is being studied. In general, the reddest, most luminous and massive elliptical galaxies are observed to be much more strongly clustered than those which are selected with the opposite properties (Norberg et al., 2001; Blanc et al., 2008; Hartley et al., 2008, 2010;

McCracken et al., 2010; Kim et al., 2011; Wake et al., 2011; Kim et al., 2014; Sato et al., 2014).

These clustering properties are not unexpected, though. Observations show that bluest galaxies are more likely to be star-forming spirals, which form hot, blue, short-lived stars at predictable rates, and the live in (relative) isolation. However, when they undergo disruptive merging events (ie, in more galaxy-rich environments), they can use large fractions of their gas reservoirs in bursts which (after settling) increase their stellar mass, redden their colours, and can destroy the fragile disc structures turning them into passively-evolving ellipticals (see Section 1.4). In the extreme scenario, galaxy clusters represent gravitationally-bound collections of up to thousands of galaxies whose members are typically dominated by the red ellipticals which are expected to be the most strongly clustered (Abell et al., 1989; Kim, 2011). The morphology-density relation (eg. Dressler, 1980; Goto et al., 2003) demonstrates these properties succinctly: plotting the fraction of morphological classification as a function of surface number density shows that elliptical galaxies do contribute the greatest numbers of galaxies to the most dense environments, and vice-versa. This infall of less massive galaxies into more massive dark matter haloes is another postulated galaxy quenching mechanism, "environmental quenching", explaining its lack of dependence on mass: star-forming galaxies of any mass which fall into a halo orders of magnitude more massive (eg. a cluster halo) are all very likely to be quenched.

Higher-order n-point correlation functions (Peebles & Groth, 1975; Groth & Peebles, 1977) which consider the separations between n galaxies simultaneously can also be computed, but these statistics are not considered further in this Thesis.

One of the recent standout achievements of results using galaxy clustering analysis is the measurement of the baryon acoustic oscillation (BAO, Eisenstein et al., 2005; Percival et al., 2007; Dawson et al., 2013; Alam et al., 2021). Assuming gravitational attraction alone is responsible for the patterns in large scale structure in the early universe, it could be expected that the strength of clustering of galaxies which trace this would decrease monotonically with increasing (co-moving) separation in the low redshift universe. However, the BAO is a prediction made by ΛCDM (Peebles & Yu, 1970; Sunyaev & Zeldovich, 1970) about the remnants of sound waves in the primordial mixture of photons and baryons in the very early universe, which were imprinted on the large scale structure of the universe as fluctuations in the large scale distribution of matter (and so galaxies) when the universe first became neutral. Spectroscopic galaxy surveys find that there is indeed a preferred separation of galaxies, at

approximately $100\,\mathrm{Mpc}\,h^{-1}$, which is well-matched by the ΛCDM predictions and the matter contribution to the overall energy density of the universe measured in the CMB experiments.

1.4 Selecting galaxies at $z > 1$

In addition to the redshifting of the stellar light to redder (observed frame) wavelengths, galaxies intrinsically show variation in colour.

Quiescent or passive galaxies (those who have been evolving without recent periods of star formation) have stellar populations which consist mainly of older, cooler stars which are inherently redder than the more massive hot stars.

This "colour" (or more correctly "colour index") is quantified simply as the difference between magnitudes in two different (observed) wavelength bands. For instance,

$$B - V = -2.5\log_{10}\left(f_B/f_{B,0}\right) - \left(-2.5\log_{10}\left(f_V/f_{V,0}\right)\right) = 2.5\log_{10}\left(f_V/f_B\right),$$

which is effectively the log of a flux ratio. Typically bands in such colours are presented such that the longer wavelength band is on the right (V in the example above), so that a very positive colour represents a very red flux ratio. In the AB magnitude system (Oke & Gunn, 1983), objects are measured relative to a constant flux density of 3631 Jy (so $f_{B,0} = f_{V,0} = f_0$), whereas Vega magnitudes would have a constant offset.

1.4.1 Spectral features

The optical and near-infrared (NIR) light in a galaxy comes primarily from populations of stars, although strong identifying features of galaxy spectra are also imprinted during this light's journey between emission and observation.

The strong Lyman break in galaxy spectra appears because the light bluewards of 912 Å (the Lyman limit) is absorbed by neutral gas between emission and the observer, or by star-forming regions around the galaxy. (This is the ionization energy required for neutral Hydrogen atoms energy level $n = 1$.)

Similarly, the Balmer break (sometimes called the Balmer jump) at rest frame 3645 Å, can produce a discontinuity in galaxy spectra. (This is the ionization energy required for Hydrogen energy level $n = 2$.)

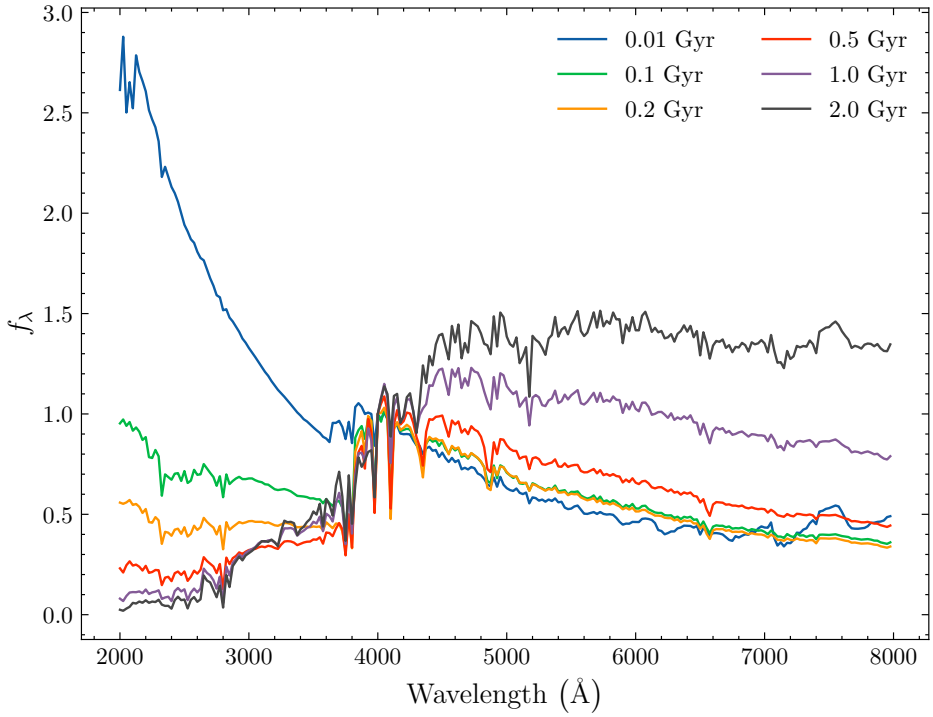

Figure 1.1: Rest-frame spectral energy distributions (SEDs) of simple stellar populations (with solar metallicity) of various ages, plotted using `Prospector` (Johnson et al., 2021). SEDs are normalised to the flux at 4000 Å. Examples of how observed frame colours of these objects vary with redshift are shown in Figure 1.2.

At marginally longer wavelengths, the λ4000 Å break ("the four-thousand Angstrom break"), often referred to as D_{4000}, is caused by a number of strong metal absorption lines (particularly the Calcium H and K lines at 3936 Å and 3934 Å) which occur around this wavelength (Bruzual A., 1983). The strength of D_{4000} increases with spectral type, metallicity and stellar population age, and is in general stronger for elliptical galaxies (Poggianti & Barbaro, 1997).

Figure 1.1 shows some example spectral energy distributions (SEDs) of simple stellar populations (with solar metallicity), for various ages, and demonstrates how the strength of D_{4000} changes with stellar population age.

This type of simple stellar population can be thought to model a galaxy produced by a single instantaneous starburst. Shortly after the galaxy is formed (the SED for the 0.01 Gyr in Figure 1.1), there is still a large fraction of extremely massive, hot, luminous stars in the population. These stars have extremely short lifetimes, and contribute to the SED for only a very short time (in a cosmological sense). The SED of the next youngest stellar population at 0.1 Gyr has already lost a significant amount of the blue stars which provide the large flux at short wavelengths. The oldest stellar populations contain only the cool, red, metal-rich stars, which contribute to the strong D_{4000} break.

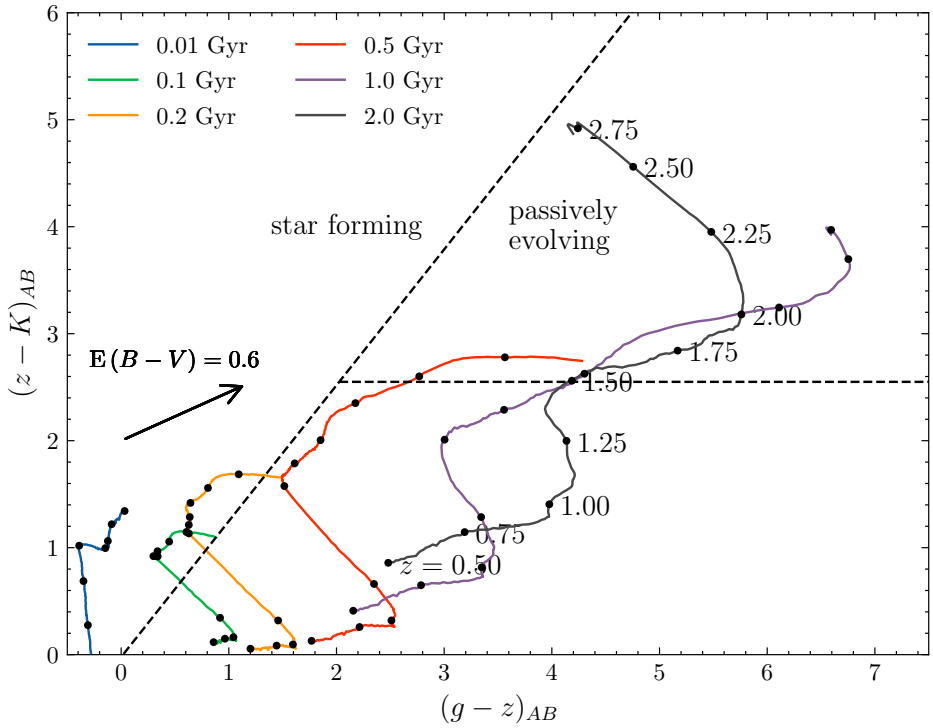

Figure 1.2: Movement of simple stellar populations with varying ages through $g - z$ vs. $z - K$ colour-colour space (using HSC and WFCAM filters). The tracks are shown for $0.5 < z < 3.0$, with black markers at redshift intervals of 0.25 (shown explicitly for the oldest stellarp population). No galactic extinction is applied, although we do indicate the direction of reddening with $\mathrm{E}\,(B - V) = 0.6$, taking the suggested R_v extinction coefficients from the HSC and WFCAM literature. Also shown are the criteria for selecting populations of star-forming and passively-evolving galaxies (SF-gzKs and PE-gzKs; see Sections 1.4.3 and 3.5 for more detail on these specific selections). Rest-frame spectra for these stellar populations are shown in Figure 1.1.

Figure 1.2 shows how the observed colours of these stellar populations change with redshift, and demonstrates criteria which are discussed in more detail in later sections.

At increasingly long near- and mid-infrared wavelengths, dusty star-forming galaxies exhibit a power law, as the (rest-frame) UV emission from the young, hot stars is absorbed and re-emitted by this dust, at the longer wavelengths.

1.4.2 Imaging surveys

Untargeted surveys of the sky have been a cornerstone of astronomy throughout its history, allowing for the exploration of a diverse range of astronomical objects. The first such surveys were completed with photographic plates, but the introduction of CCDs whose response properties are significantly less complex allowed for much more uniform samples of objects to be selected.

Broadband imaging surveys reach impressive depths and areas, so are able to select large samples of galaxies to understand cosmology. Both of these properties are necessary to explore large cosmological volumes, and are often traded off against each other for a survey with an allocated time.

Large photometric surveys are crucial for testing models of cosmology and galaxy formation. For instance, the clustering studies presented of Peebles used the photographic plate surveys from Zwicky.

As well as this, photometric surveys are also necessary for input catalogues for spectroscopic surveys.

An extremely successful example of this are the imaging surveys of Sloan Digital Sky Survey (SDSS, York et al., 2000), which between 2000 and 2009 covered over $7600\,\mathrm{deg}^2$ in the optical *ugriz* bands. These imaging data sets were then used for SDSS's later spectroscopic surveys, such as the Baryon Oscillation Spectroscopic Survey (BOSS, Dawson et al., 2013), and extended-BOSS (eBOSS, Blanton et al., 2017), of which one of the primary goals was to extend the measurement of the BAO to increasingly high precision, and at higher redshifts.

A more recent example is the Deep Extragalactic Visible Legacy Survey (DEVILS, Davies et al., 2021), which leverages existing imaging datasets at 22 wavelengths from ultraviolet (UV) to far-infrared (FIR) to produce excellent photometric estimates of the physical properties of galaxies, which are then used as spectroscopic input catalogues.

As Figure 1.2 demonstrates, all ages of stellar population become increasingly red with increasing redshift, meaning a significant fraction of the starlight is shifted into infrared wavelengths, and galaxies with similar properties become extremely faint at high redshifts. To exploit this, NIR surveys perform similar work to the large optical surveys. One of the first large NIR surveys was the Deep Near-infrared Survey of the Southern Sky (DENIS, Harmon & Mamon, 1993; Epchtein et al., 1994), which aimed to provide "the first complete census of astronomical sources in the near-infrared spectral range", reaching Vega magnitudes of 14.5 in the 2.15 micron (K) band, with complementary I_{Vega} data reaching 18.0.

Subsequent and future surveys have often repeated this strategy, building object catalogues covering large wavelength ranges to capture a majority of the available starlight, covering increasingly large areas to extreme depths. There will be more discussion on various existing and future NIR surveys in Section 2.2.

1.4.3 Colour selection

The broad spectral discontinuities discussed in Section 1.4.1 can be used to select populations of galaxies based on expected properties. As they are not narrow emission or absorption lines, broadband photometry is easily sufficient to exploit them. For instance, for increasing redshift z, the Balmer break will appear at $3645\,(1+z)$ Å, so finding a pair of bands with a strong red colour will indicate that the break is somewhere in between these two bands. Generally, this method is called the "dropout" method (especially in the case where the object is *not* detected in bands bluer than a given band).

Bracketing the Balmer/D_{4000} breaks with the NIR bands J & K at 1.2 and 2.2 μm selects a sample of galaxies which are $z > 2$, named Distant Red Galaxies (DRGs, Franx et al., 2003). Samples of DRGs whose photometric redshifts are $2 < z < 3$ have been spectroscopically confirmed to be massive passive galaxies, although lower redshift dusty star-forming interlopers ($z < 2$) are also selected with this criteria (eg, van Dokkum et al., 2003; Grazian et al., 2006, 2007). Saracco et al. (2004) argue that it is very unlikely that (a majority of) these objects are AGN; although $z < 0.3$ QSOs have been detected with very red colours, they are at $K < 16$, and QSOs with $K > 20$ (at which the surface density of DRGs becomes significant) would be three orders of magnitude less luminous (too faint to be AGN), or have extinction coefficients in excess of $A_V > 3$ at $z > 2$. For the latter, Banerji et al. (2012) find tens of such objects in $\sim 1000\,\mathrm{deg}^2$ at $K_{\mathrm{AB}} < 18.4$.

Elston et al. (1988) first measured objects with colours $R-K > 5$ (Vega), and suggested that one population of these galaxies could be passively-evolving galaxies at $z > 1$, and galaxies selected with this method are often referred to as extremely red objects (EROs). Later works successfully used other optical r, i and I bands (as R replacement) to select EROs (Kim et al., 2011, 2014; Nieves-Seoane et al., 2017). Given that the i-band is around[3] 7600 Å and the K-band is 22 000 Å, a strong red colour criteria is likely to select the Balmer/D_{4000} feature of old, red, massive galaxies at $z > 1.0$. It has been shown (McCracken et al., 2000; McCarthy, 2004) show that there is evolution of the $I-K$ red colour, even thought the D_{4000} is within the $I-K$ bands for a very large redshift range. McCarthy argue that D_{4000} is not entire contribution the red colour, but also the steep slope of the rest-frame UV falling in the optical band, and the flatter, rest-frame optical portion now in the near-infrared.

The ALHAMBRA survey (Moles et al., 2008) is a medium-band photometric survey using 20

[3]Effective wavelengths of i-band are 7534 Å and 7727 Å in PS1 and HSC respectively

medium optical bands plus NIR JHK_s, designed to produce a large sample of galaxies with excellent photometric redshift accuracy ($\sigma_{\rm NMAD} \sim 0.01$). Nieves-Seoane et al. (2017) use the ALHAMBRA-K_s survey to select EROs using a range of $I-K$ criteria, and demonstrate that the distribution of ERO redshifts is indeed majority $0.9 \lesssim z \lesssim 1.4$ for $I-K>2$, with increasing median redshift for redder $I-K$ cuts (although skewed towards the lower end of this redshift range), as one would expect from the results on redshift dependency on $I-K$.

However, it is not only passively-evolving galaxies which are selected using this ERO selection; a degeneracy between dusty star-forming galaxies and the $z>1$ passive galaxies exists. Spectroscopic observations of EROs (Cimatti et al., 2002) indeed show that this is the case. Studies (Pozzetti & Mannucci, 2000; Fang et al., 2009; Kim et al., 2011) attempt to break this degeneracy by using an additional criteria in $I-K$ vs $J-K$, which aims to highlight the difference between the strong discontinuity for passive galaxies, and the smooth power law from dust emission in star-forming galaxies. Star-forming galaxies are expected to contribute between $30-50\%$, depending on exact selection criteria. This selection avoids expensive spectroscopic observations to measure the narrow emission lines, targeted far-infrared observations to measure the hot dust, or very-high resolution optical/near-infrared imaging to study morphology, all of which are currently impractical for very large samples of galaxies. This, however, is likely to change in the near future, with the advent of very large, multiplexed spectroscopic instruments. For instance, VLT MOONS will obtain S/N ~ 5 spectra for 500 $H_{\rm AB} \sim 22$ objects, with a (rebinned) spectral resolution $R \sim 1000$ in an hour of observing (Cirasuolo et al., 2020).

The BzK selection of galaxies introduced by Daddi et al. (2004) jointly selects star-forming and passively-evolving galaxies at $1.4 < z < 2.5$ ("sBzKs" and "pBzKs" respectively), using only a two-colour criteria in $B-z$ vs $z-K$. Given the (relatively) high exposure times required to obtain spectra for objects at these redshifts, the reliable photometric classification and low cost (in terms of required data) from the BzK selection is a significant advantage; its continued popularity (the introductory paper has 500+ citations) attests to this (eg., Hartley et al., 2008; McCracken et al., 2010; Bielby et al., 2012; Arcila-Osejo & Sawicki, 2013; Ishikawa et al., 2015; Seo et al., 2021).

For a given K-band magnitude, this selection requires much deeper B band data to select pBzKs than sBzKs, as the former requires a very red $z-K$ colour *and* a red $B-z$ colour, whereas an object can be selected as star-forming with only moderately red colours. Arcila-Osejo & Sawicki (2013) remedy this by introducing an additional colour criterion in $z-H$ vs

$H-K$ (introducing only one additional band). This works in a similar manner to the $J-K$ cut which distinguishes the dusty star-forming and $z>1$ passively evolving EROs. They too make a similar argument that the star-forming galaxies will follow a smoother power law from the presence of dust emission, whereas passive galaxies will have a much stronger distinction between the two colours.

As with EROs and DRGs, the strong Balmer/D_{4000} breaks are the primary features being selected with the red $z-K$ colour, and the colour in the bluer $B-z$ to break the degeneracy between old, massive ellipticals and dusty star-forming galaxies.

Although the above mostly discusses selecting Balmer/D_{4000} break galaxies using the K band (with i for EROs, J for DRGs, and B or g and z for BzK), other pairs of band which bound these strong spectral features can be employed to select galaxies in different redshift ranges; clearly, the longer the wavelength of the "blue" band (ie. i for EROs, J for DRGs), the higher (median) redshift of the sample. The degeneracy between those galaxies with old stellar populations, and those with younger stellar populations but are highly dust-reddened will still exist in whichever pair of bands is chosen. This is particularly true for increasingly long wavelength blue bands.

Xu et al. (2020) demonstrate that effective selection at similar intermediate redshifts ($1<z<1.5$) is also possible with shorter wavelength broadband imaging. They select a sample of quiescent, massive galaxies with $z\sim1.2$ using $i-Y>1.3$. They show that the contribution of these iY galaxies to the total number counts of galaxies should peak at around $Y\sim22.5$. As the effective wavelength of HSC-Y is 9760 Å, this red $i-Y$ colour corresponds to the Balmer/D_{4000} breaks being shifted to the expected redshift range. *Rubin* LSST is expected to reach $y\sim24.9$ (with much deeper i) across the whole $18,000$ deg^2 Deep-Fast-Wide component, so could use this simple criteria to produce vast (and uniform) samples of massive $z\sim1$ galaxies, even without exploiting the NIR synergy with *Euclid* or *Roman*. Xu estimate that 78% of the galaxies they select in this way are passively evolving.

At higher redshift, studies (Girelli et al., 2019; Alcalde Pampliega et al., 2019) use $H-[3.6]$ or $K-[3.6]$ to select these massive quiescent galaxies which are more specifically refer to as Balmer break galaxies (BBGs). They find that the majority of their candidates are actually at $z>4$, providing more evidence for evolved stellar populations at high redshifts (Fontana et al., 2009; Schreiber et al., 2018; Santini et al., 2021). Alcalde Pampliega et al. (2019) propose that the strong colour of these candidates is predominantly the Balmer break rather than D_{4000} because the age of the universe at $z\sim4$ is only 1.5 Gyr, and stellar populations

older than 1 Gyr at this time are unlikely. It is worth noting that the samples of galaxies at these redshifts are significantly smaller - tens to hundreds of galaxies rather than the thousands in shorter wavelength studies, due to the extreme depth required because of their faintness (their sample has average $H = 27.1$ and $[3.6] = 24.0$), and the fact that these galaxies are intrinsically rare. An additional complication at these wavelengths is the much greater risk of Active Galactic Nuclei (AGN) contamination, as most galaxy templates at these high redshifts fall within the so-called "AGN wedge" in $[3.6] - [4.5]$ vs. $[5.8] - [8.0]$ colour space (or other combination of these IRAC colours). Alcalde Pampliega et al. (2019) state that 25% of their sample are detected at 24 µm, which could be explained either by star formation, or AGN activity. Daddi et al. (2004) also mention this in their discussion of a higher redshift BzK analogue, $RJL_{3.6}$ galaxies[4]. They note that in addition to the usual dusty/old degeneracy, an additional problem could be faced by the inclusion of dust from low-redshift galaxies with a significant AGN contribution. Further, increasingly long wavelength MIR and FIR data are required to obtain reliable photometric redshifts, which is often impractical for very large samples. Even more extreme, there is very tentative evidence for evolved stellar populations at $z > 5$ (Mawatari et al., 2016, 2020), selected with criteria in K, [3.6] and [4.5].

A more data-intensive way to select galaxies at high redshift is to use SED template or model fitting. Properties of the best fitting template model can be then extracted directly for further analysis. For instance, populations of galaxies can be selected from the appropriate region of a rest-frame $U-V$ vs. $V-J$ colour-colour diagram (calculated from the template flux), which has been shown to be a powerful tool to select star-forming or passive galaxies from at least $0.5 < z < 3.5$ (Wuyts et al., 2007; Williams et al., 2009). These methods require significantly more data points than the two- or three-colour selections discussed previously. Clearly, the more photometric data points provided, the more accurate SED fitting or modelling can be. For very high precision in the model parameter estimates of the most promising candidates, very resource-intensive targeted observations in the far-infrared or sub-mm wavelengths can be used to extend the model fitting and properly account for the reprocessed dust emission (eg. Battisti et al., 2019; Dudzevičiūtė et al., 2020; Johnson et al., 2021). These longer wavelength observations, however, are beyond the scope of this Thesis.

[4] $L_{3.6}$ is a no-longer-common 3.6 µm band

1.5 This work

This work uses UKIDSS-DXS data to study the reddest populations of galaxies at intermediate redshifts ($1 < z < 1.5$). DXS' strategy aims to provide a compromise between the extremely wide area of the Large Area Survey, and the depth of the Ultra Deep Survey. At an area of ~ 28 square degrees, to a depth of $K_{\rm AB} \sim 22.7$, we are able to measure the angular clustering properties of these galaxies over three orders of magnitude in angular scale, which is very competitive with other surveys which employ a similar strategy. Further, we are able to investigate the K-band galaxy luminosity function at these redshifts, and again, the depth provided by DXS allows us to measure this statistic to at least one magnitude fainter than the knee of the galaxy luminosity function. It is effectively a precursor to the enormous improvement in statistics that will be enabled by the vast samples of these galaxies (in area and depth) selected by *Rubin*-LSST, *Euclid*, *Roman*, and JWST.

The scientific aim of this Thesis is to investigate the growth of the most massive, passive galaxies at the redshifts DXS is able to probe. Key to selecting and studying these objects are large cosmological volumes, given their rarity. This is expressed as the exponential tail of the galaxy stellar mass and luminosity functions, which we will use in our investigation. As DXS was designed to observe large cosmological volumes at intermediate redshifts (compared to contemporary surveys), it is ideally positioned to measure this end of the mass function. However, producing and verifying usable imaging and catalogues for the entire DXS survey is one of the significant aims of this Thesis in itself.

The rest of this Thesis is as follows.

Chapter 2 outlines the survey definition of UKIDSS, and more specifically the UKIDSS-DXS. We then describe how DXS compares to other existing NIR surveys, and the expected performance of next-generation surveys and instruments. Next, we detail the procedure for constructing the deep mosaics and catalogues from the DXS data, before summarising available complementary datasets available, and finally some brief discussion on photometric redshifts.

Chapter 3 lays out the types of objects that we select using catalogues constructed in Chapter 2 (DRGs, EROs and BzKs), and reports number counts and photometric redshift distributions for each. We then discuss the overlap between these selections of objects. There is then a short discussion of selections of red galaxies using the DXS' available H-band data, with a view to selecting similar selections of galaxies using *Euclid*.

Chapter 4 shows angular correlation functions for the selections of objects detailed in Chapter 3, with discussion particularly on how the strength of clustering changes with varying limiting apparent magnitude.

Chapter 5 first presents investigations of luminosity functions of galaxies, and the EROs selected in Chapter 2. Then, by computing the galaxy stellar mass functions of passive galaxies and considering the integrated stellar mass density of the passive selections, we present evidence that suggests that the quenching of the most massive galaxies is less efficient at lower redshifts relative to the highest redshifts we measure.

Finally, Chapter 6 has some concluding remarks.

Chapter 2

UKIDSS-DXS

This chapter will outline the UKIDSS-DXS survey: the survey definition, a brief discussion of the observing strategy, and a comparison of the survey with a number of other near-infrared surveys. We will then discuss our procedure for creating mosaics and catalogues and future improvements that we would make, and summarise the coverage of these data products. We describe some complimentary datasets that we use in our analysis, and finally, there is a brief discussion on photometric redshift estimates.

2.1 UKIDSS, WFCAM, and UKIDSS-DXS definition

The UKIRT Infrared Deep Sky Survey (UKIDSS, Lawrence et al., 2007) is a near-infrared (NIR) survey carried out using the infrared wide-field camera (WFCAM, Casali et al., 2007) mounted on UK Infrared Telescope (UKIRT). UKIRT is a 3.8 m telescope at an altitude of 4200 m on Mauna Kea, Hawaii. WFCAM comprises four 2048×2048 Rockwell Hawaii-II PACE arrays, spaced by 94% of a detector side (see Figure 2.1, left). The spacing of the detectors means that four interlocking pointings are required to image a contiguous area (see Figure 2.1, right). These four pointings result in a 'tile' of area $\sim 0.78\,\mathrm{deg}^2$ (0.883 deg per side, or 3.88 detector widths) - approximately four times the area of the full moon. The pixel scale of WFCAM is $0.4''$/pixel which, given typical seeing of $\sim 0.8''$ in K can undersample the point-spread function (PSF) of point sources. To counteract this, a microstepping procedure is employed whereby the telescope is offset by a non-integer number of pixels, and the resulting data interlaced. UKIDSS-DXS uses a 2×2 microstepping strategy, meaning the offset is by $\frac{1}{2}$ pixels, resulting in a pixel scale of $0.2''$/pixel and 4096×4096 pixels images from each of the four detectors.

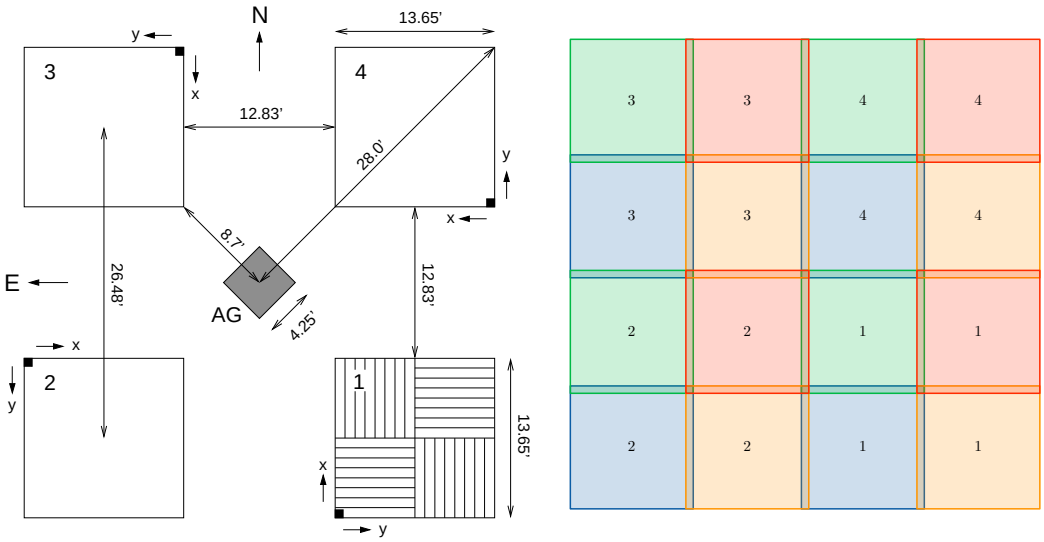

Figure 2.1: *Left*: The WFCAM focal plane, from Dye et al. (2006). The four detectors are shown, spaced by 94% of the length a detector side. The small black square indicates the (0,0) pixel of each detector. Detector 1 additionally shows the readout directions of each quadrant. *Right*: The interlocking pattern to cover a contiguous area of $\sim 0.7\,\mathrm{deg}^2$.

For a given total observing time, wide and shallow surveys produce larger samples. However, the universe is not a uniform distribution of sources locally, nor will wide and shallow surveys effectively select distant galaxies. The "wedding cake" strategy of UKIDSS with an ultra-deep, fairly deep and wide-but-shallow component serves to maximise the science output by addressing a variety of object samples, not only seeking to maximise the total number of objects detected.

UKIDSS-DXS (Deep eXtragalactic Survey, DXS hereafter) is one of the five components of UKIDSS, covering $\sim 28\,\mathrm{deg}^2$ in four fields in the J and K bands. The four fields, ElaisN1, SA22, Lockman Hole (Lockman) and XMM-LSS (see Table 2.1), were chosen as some the most well-studied extragalactic fields (Lawrence et al., 2007; Swinbank, 2013) with existing (or planned) deep observations in optical and longer-wavelength infrared (see Section 2.5), while also being reasonably well spaced in right ascension. Figure 2.4 shows the layout of the WFCAM tiles in each field. The target depth of $K \sim 22.7$ set out by Lawrence et al. (2007), means that the galaxies selected with DXS will be at intermediate redshifts, $1 < z < 1.5$.

UKIDSS-UDS (Ultra Deep Survey, UDS hereafter, Lawrence et al., 2007; Almaini et al., in prep.), by far the deepest ($K \sim 25.5$) and narrowest UKIDSS component, is a single WFCAM tile (area $\sim 0.8\,\mathrm{deg}^2$) located in XMM-LSS. The main aim of UDS, at survey design, was to select elliptical galaxies at high redshift ($z \sim 3$).

The final component of UKIDSS with an extragalactic focus is the widest and shallow-

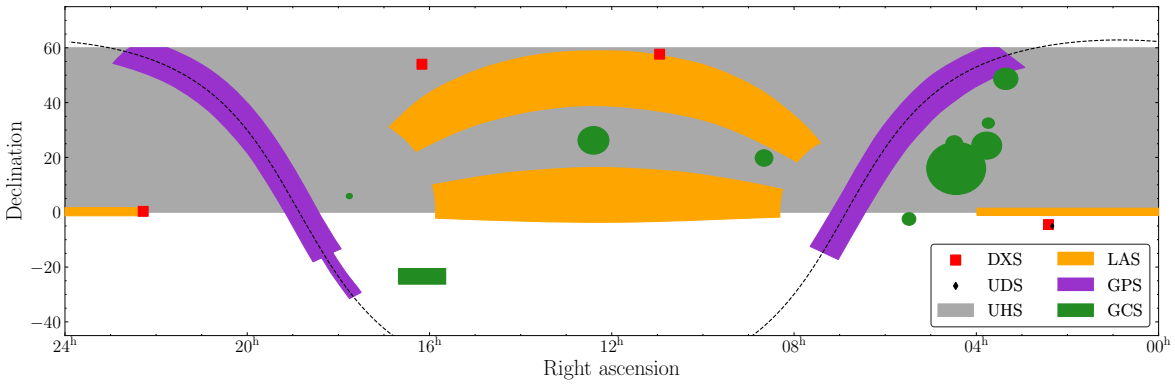

Figure 2.2: The layout of the survey components of UKIDSS. The extent and locations of three wide-shallow components (LAS, GPS and GCS) and the UHS are shown. The red and black markers show only the locations of the four DXS and UDS fields respectively (ie, do not indicate the shape or extent of these fields, see Figures 2.4 and 2.6). The black dashed line indicates the galactic plane. Adapted from Lawrence et al. (2007).

Table 2.1: Representative coordinates of the four fields which comprise UKIDSS-DXS. Also included are the number of contiguous 'tiles' in each field - note that only four of the eight DXS tiles in XMM-LSS have both J and K.

Field	R.A	Dec	Tiles
ElaisN1	16 10 00	+54 00 00	12
SA22	22 17 00	+00 20 00	12
Lockman	10 57 00	+57 40 00	11
XMM-LSS	02 25 00	−04 30 00	8+UDS

est, UKIDSS-LAS (Large Area Survey DR8, Lawrence et al., 2007, 2012), aiming to map 4000 deg^2, mapping hundreds of thousands of galaxies, and producing similar numbers of photometric redshifts when combined with SDSS optical photometry.

Extending the tiered strategy to address the broadest possible range of science cases are UKIDSS-GCS and -GPS (Galactic Cluster Survey & Galactic Plane Survey, Lawrence et al., 2007, 2012). GPS surveys $\sim 1850\,\mathrm{deg}^2$ in the galactic plane (latitude $|b| < 5°$) to $K_{\mathrm{Vega}} \sim 18.8$ to investigate the low-mass end of the initial mass function in star-forming regions close to the Sun ("the solar neighbourhood"), and post-AGB stars throughout the Milky Way. Finally, GCS surveys $\sim 1000\,\mathrm{deg}^2$ to $K_{\mathrm{Vega}} \sim 18.6$ targeting 10 nearby open star clusters, including the well-known Pleiades, or Subaru.

More recently, the UKIRT Hemisphere Survey (UHS) survey is observing all regions below declination $\delta < 60\,\mathrm{deg}$ in the northern hemisphere which are not already covered by the shallowest three UKIDSS surveys (LAS, GCS, and GPS) to a similar depth, of $K_{\mathrm{Vega}} \sim 18.4$.

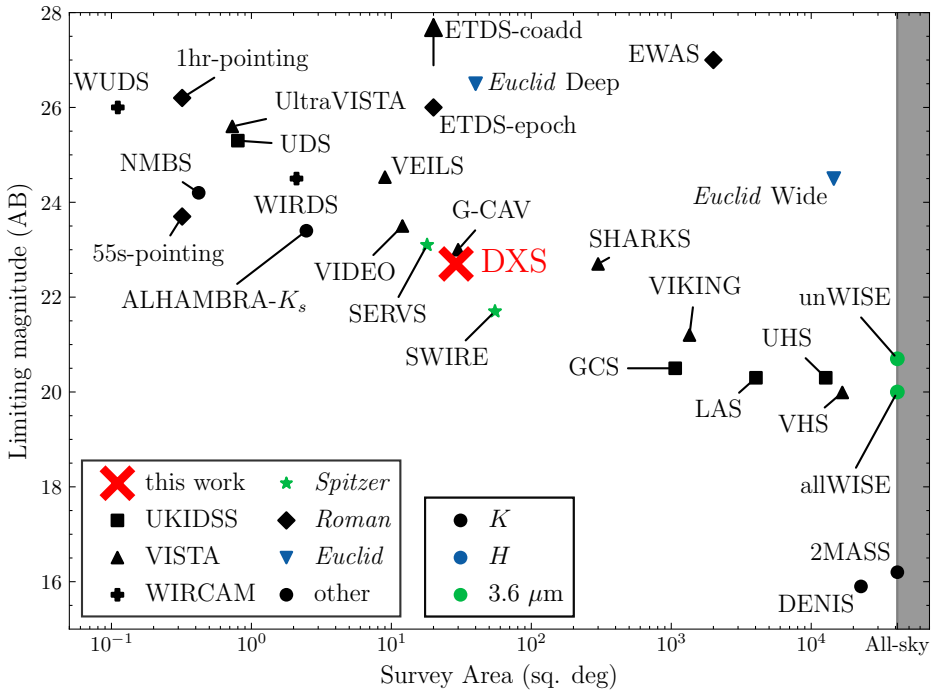

Figure 2.3: DXS' place amongst other NIR surveys, with depth and area values taken from the quoted K band components (or Roman $F213$ band). Note that the depths quoted with blue points (ie, the *Euclid* surveys) are for H band, and green are for $3.6\mu m$ (or equivalent) depths. Values shown in this figure are reported (with references) in appendix Table B.2.

2.2 DXS' place amongst other NIR surveys

Figure 2.3 shows DXS' place amongst other NIR surveys, and demonstrates the broad range of scientific goals that NIR surveys can address.

The other extragalactic UKIDSS components (UDS, LAS) are square markers. GPS (Galactic Plane Survey) is not included in this comparison, as it is not an extragalactic survey (and has variable depth). Although it is not strictly a UKIDSS survey, UHS is included as an extension of the shallowest UKIDSS components (LAS, GPS and GCS).

The VISTA public surveys (using the VIRCAM instrument on the VISTA telescope Dalton et al., 2006) form a similar tiered observing strategy, and span a similar range of survey areas and depths. They are plotted as triangle markers in Figure 2.3. UltraVISTA, the deepest extragalactic component (McCracken et al., 2012; Moneti et al., 2019, DR4) was designed to provide extremely deep NIR coverage of the COSMOS field, reaching $K \sim 25.6$, with a similar aim to UDS of selecting the high redshift galaxies which are too old or dusty to be observed with the previous optical coverage of this field.

The VISTA Hemisphere Survey (VHS) is another very wide-shallow survey to $K \sim 18.8$. The combination of VHS and UHS hemisphere surveys will produce a (nearly) all-sky NIR map,

approximately 4 magnitudes deeper than 2MASS.

VIDEO (VISTA Infrared Deep Extragalactic Observations, Jarvis et al., 2013a,b) and VEILS (VISTA Extragalactic Legacy Survey, Hönig et al., 2017) perform a similar role to DXS in relation to their other components: bridging the the gap between the wide but shallow VIKING (and VHS), and the extreme depth in a small area from UltraVISTA. VIDEO surveys $12\,\mathrm{deg}^2$ in 3 fields (including XMM-LSS) to $K \sim 23.5$. VEILS will image a further $9\,\mathrm{deg}^2$ in J and K in the same fields, although Hönig et al. (2017) emphasise one of the strengths of VEILS is the time-domain focus, rather than final combined depth; visiting each field 45 times, approximately once a fortnight, for three years. Combined with the optical *griz* data from Dark Energy Survey (DES) which has a similar cadence of 7 days, VEILS will result in a very powerful dataset.

Also shown in the plot is the Galaxy Clusters at VIRCAM (G-CAV) survey which looks like it is competitive with DXS, reaching similar depths $K_s \sim 22.7$ in $30\,\mathrm{deg}^2$. However, G-CAV targets 20 individual galaxy clusters, in approximately $1.75\,\mathrm{deg}^2$ areas each, meaning that it is not well-suited to the study of large scale structure at high redshift like DXS. Further, DXS has a wealth of complimentary optical and MIR imaging available, which is not consistently available for all of the G-CAV clusters.

The final VISTA public survey that we have included in Figure 2.3 is SHARKS, a K_s-only survey of $\sim 300\,\mathrm{deg}^2$, much of which is a single contiguous region in the *Euclid* field. It will also reach $K_s \sim 22.7$. SHARKS will be one of the prime catalogues for selecting large samples of relatively faint K-selected galaxies, given the very large (and homogeneous) area, and the much greater depths *Euclid* will reach at shorter wavelengths, in combination with the *Rubin* Legacy Survey of Space and Time (LSST).

At slightly longer wavelengths, the space-based instrument WISE (Wide-field Infrared Survey Explorer) conducted an all-sky survey beginning in 2010, observing in bands centred at at $3.6\mu m$ and $4.5\mu m$ ($W1$ and $W2$ band). We have included the two coadditions allWISE (Wright et al., 2010; Mainzer et al., 2011) and unWISE (Lang, 2014; Meisner et al., 2017, see Section 2.5.5).

We also include in Figure 2.3 estimates of surveys from future (primarily space-based) instruments. *Euclid*, an ESA mission (Laureijs et al., 2011), has the primary objective of measuring galaxy weak lensing and BAO as probes of the accelerating expansion of the universe. However, the legacy of the *Euclid* Wide survey will be (at least) 15,000 deg^2 of imaging at $H_{\mathrm{AB}} \sim 24$, significantly deeper and wider than any existing NIR survey. The Deep survey

will be at least $H_{\rm AB} \sim 26$ (a further 2 magnitudes deeper than the wide survey) and $40\,{\rm deg}^2$. This area is comparable with the DXS (in fact 40% larger than the final DXS survey), but measuring galaxies 4 magnitudes fainter. *Euclid* will also have a PSF better than $0.35''$ (Laureijs et al., 2011).

Finally, the *Roman* space telescope will have a wide-field NIR camera with a $0.32\,{\rm deg}^2$ field-of-view, capable of reaching depths equivalent[1] to $K \sim 23.4$ in a single 55 s exposure, and $K \sim 26.2$ in 1 hr of exposure time. We also include nominal survey strategies (Benford & McEnry, 2021) - a proposed Extragalactic Wide Area Survey (EWAS), which would cover $2000\,{\rm deg}^2$ to $K \sim 27$, and the narrower Extragalactic Time Domain Survey (ETDS), which would image a $20\,{\rm deg}^2$ area at $K \sim 26$ for a single epoch, reaching $K \sim 28$ once all epochs are coadded.

2.3 DXS Mosaics & Catalogues

From the WFCAM archive[2] we collect 5485 science stacks taken between April 2005 and December 2013, totalling 300 GB (compressed). Inital processing of these images has already been done by CASU[3], with accurate WCS and zero-point information included, frames from the microstepping procedure interlaced, and various other detector effects taken care of.

We use SWarp (Bertin et al., 2002) to produce mosaics of the contiguous 'tiles' in Figure 2.4. We chose not to create mosaics for an entire field to a) avoid unnecessarily large files (`fits` files of individual tiles are already ∼1GB and ∼16000 × 16000 pixels), and b) to minimise variation in zero point magnitudes and seeing. However, we include frames from adjacent tiles (where these exist), to minimise artefacts at the ragged edges of mosaics. We use SWarp parameters such that the WCS for a mosaic is the same for all bands in a tile. This makes forced photometry easier.

We do not homogenise the PSF in each input stack, justifying this by noting that spread of the seeing FWHM of input stacks is typically less than the pixel scale (per tile). The main panel of Figure 2.5 shows, for all of the input stacks that are included in a single tile, the histogram of the absolute deviation of the seeing FWHM from the median seeing FWHM of those stacks. Each histogram is for a separate tile. To estimate the seeing FWHM, we use

[1] proposed band $F213$, $1.95 - 2.30\,\mu$m, `https://roman.gsfc.nasa.gov/science/WFI_technical.html`
[2] `http://wsa.roe.ac.uk/`
[3] `http://casu.ast.cam.ac.uk/surveys-projects/wfcam/technical`

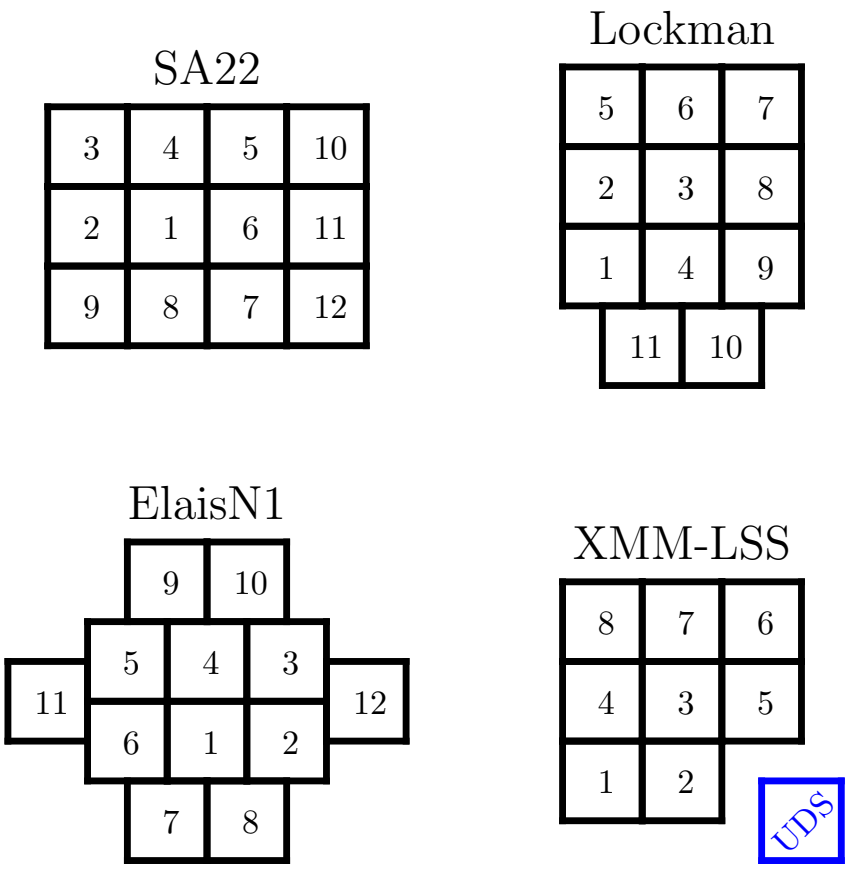

Figure 2.4: Layout of (oriented 'north up, east left'), including location of UKIDSS-UDS survey within XMM-LSS. SA22 tiles 2-7 (inclusive) are observed in H. XMM-LSS tiles 4, 6, 7 and 8 are not observed in J.

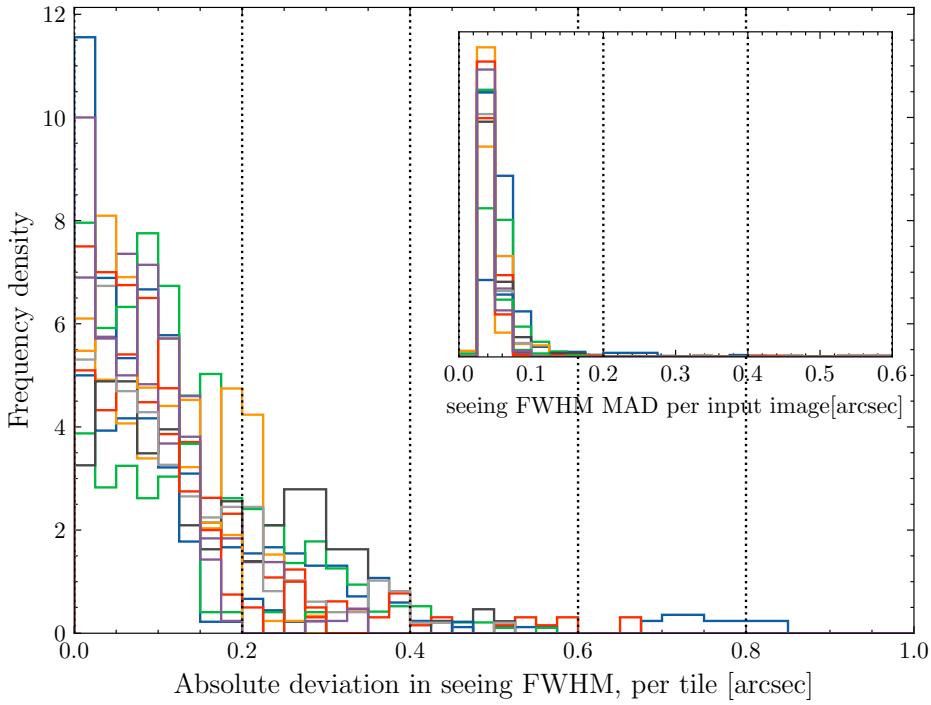

Figure 2.5: Absolute deviation from median tile seeing FWHM (estimated with SExtractor's 50% `FLUX_RADIUS`). Dotted lines indicate multiples of pixel scale, 0.2″. The inset panel show the PSF variation (as the MAD) across each individual input stack, which is significantly less than one pixel.

(double) the SExtractor parameter `FLUX_RADIUS` for the radius which contains 50% of the flux, taking the median value of all objects with $15 < K < 17$. In this magnitude range, stars are not yet saturated, and there are very few galaxies per square degree (see eg. Figure 3.5 in Chapter 3), which will have larger half-flux radii. The median estimator is robust to outliers, and the few galaxies which are included will not affect the median. This "half-flux radius" (more accurately half-flux diameter) is equivalent to the seeing FWHM for point sources with a Gaussian PSF (ie, stars). The majority of these deviation measurements are less than one pixel in the interlaced images (0.2″). The inset panel further justifies the use of the median half-flux diameter as a useful measurement: the histograms show the median absolute deviation of the half-flux diameter *across each input stack*, grouped by tile. These values are extremely small (and certainly smaller than the pixel scale); for the purpose of demonstrating that not homogenising the image PSF does not significantly affect the catalogues, the median half-flux diameter is good enough to estimate the seeing FWHM.

Figure 2.6 summarises the coverage of the J and K mosaics.

We then produce J, K, and H catalogues from these mosaics using SExtractor (SourceExtractor, Bertin & Arnouts, 1996), and perform forced photometry for each pair of bands

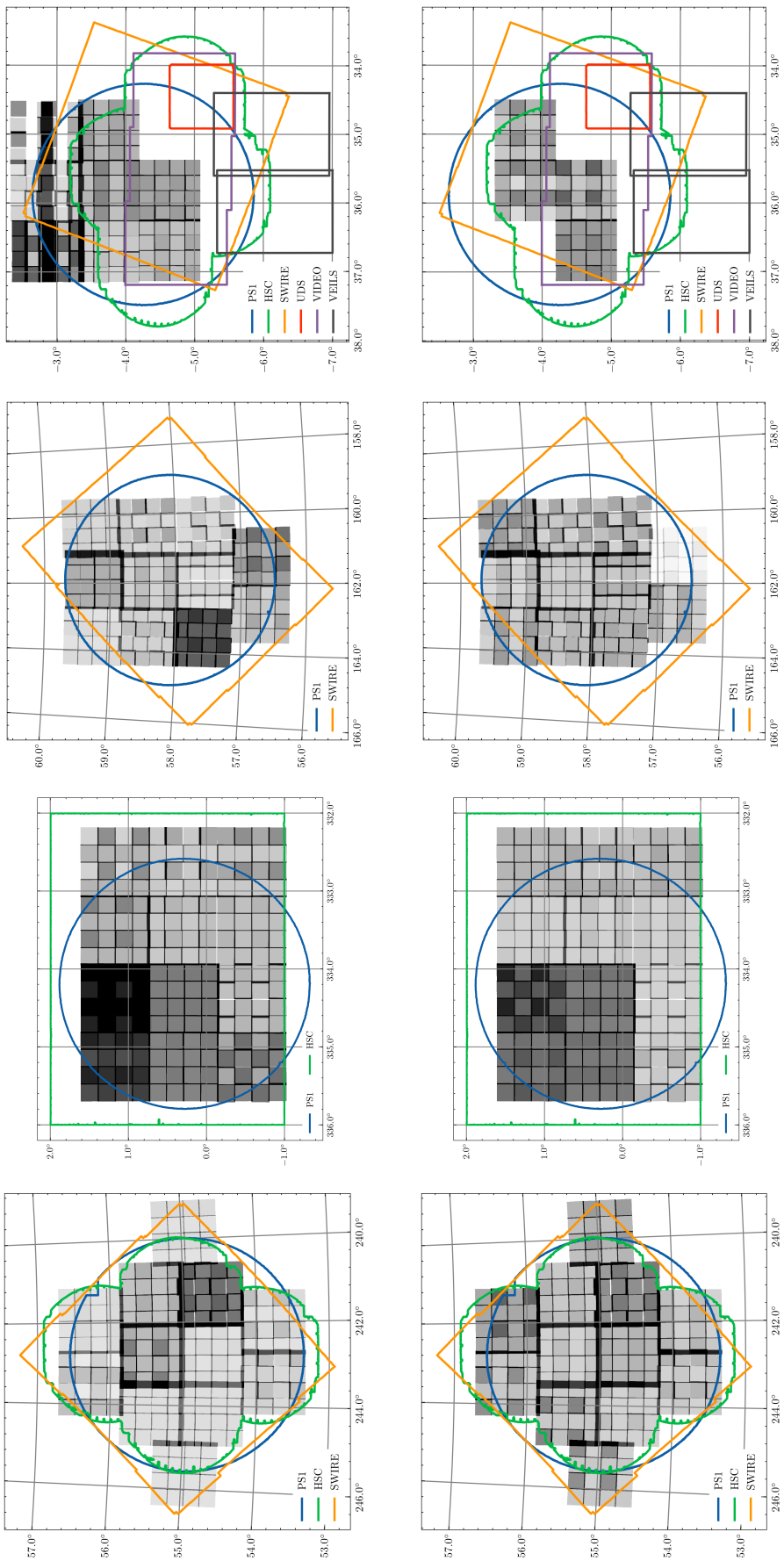

Figure 2.6: Exposure time maps for the four fields ElaisN1, SA22, Lockman and XMM-LSS (left to right), and K and J band (top and bottom). Darker regions indicate greater total exposure time. Coloured polygons represent the boundaries of some complementary datasets, and in XMM-LSS, some other deep NIR surveys. The maps are presented in the usual "North up, East left" orientation.

Table 2.2: Total area in square degrees in each field covered by the J and K bands plus various combinations of data. *2MASS*, *unWISE*, and *Gaia* are all-sky, so the area of these surveys is the same as for the JK combination. Areas quoted for IRAC are estimated using 3.6 µm data, although these are very similar for all other bands from the same instrument.

Field	SA22	ElaisN1	Lockman	XMM-LSS	**Total**
JK	8.89	8.42	7.81	3.06	**28.18**
JKH	4.45	-	-	-	**4.45**
JK+PS1-i	7.01	6.94	6.76	3.06	**23.76**
JK+PS1-gz	6.93	6.94	6.76	2.18	**22.81**
JK+HSC-i	7.90	6.60	-	2.54	**17.04**
JK+HSC-gz	7.82	6.59	-	2.55	**16.96**
JK+PS1-i+IRAC	-	6.88	6.52	2.94	**16.34**
JK+HSC-i+IRAC	-	6.41	-	2.43	**8.84**

using SExtractor's dual-image mode.

We then merge the per-tile catalogues, matching with a 0.8″ radius, a representative value of the seeing full-width half maximum (FWHM), and keep the object with the highest signal-to-noise ratio. For the most part, we use the catalogue with J-band forced photometry from the K-band apertures.

We use stilts (Taylor, 2006) for any catalogue matching processes, using the `tskymatch2` algorithm, with the `match` type set to `best`, and either the `1or2` (full outer join) for merging the individual band catalogues or `all1` (left outer join) for matching external catalogues to the DXS catalogues.

Figure 2.7 shows a summary of the steps we take to produce the mosaics and catalogues used throughout this Thesis.

2.3.1 Background subtraction

We use a two-step process to remove the background in the frames for coaddition. First we use the default settings in SWarp to estimate (and subtract) the background in each input frame and produce initial median coadd mosaics. We then pass these mosaics to SExtractor to produce segmentation maps. For the second step, we use these segmentation maps to mask bright objects in input frames, using reproject (Robitaille, 2018) to reproject from the mosaic WCS to the frame WCS and photutils' (Bradley et al., 2021) implementation of the SExtractor background algorithm to estimate the background (as this implementation allows for easy masking). An example input frame before and after (masked) subtraction and the segmentation mask used for masking are show in Figure 2.8, for tile 1 of the ElaisN1

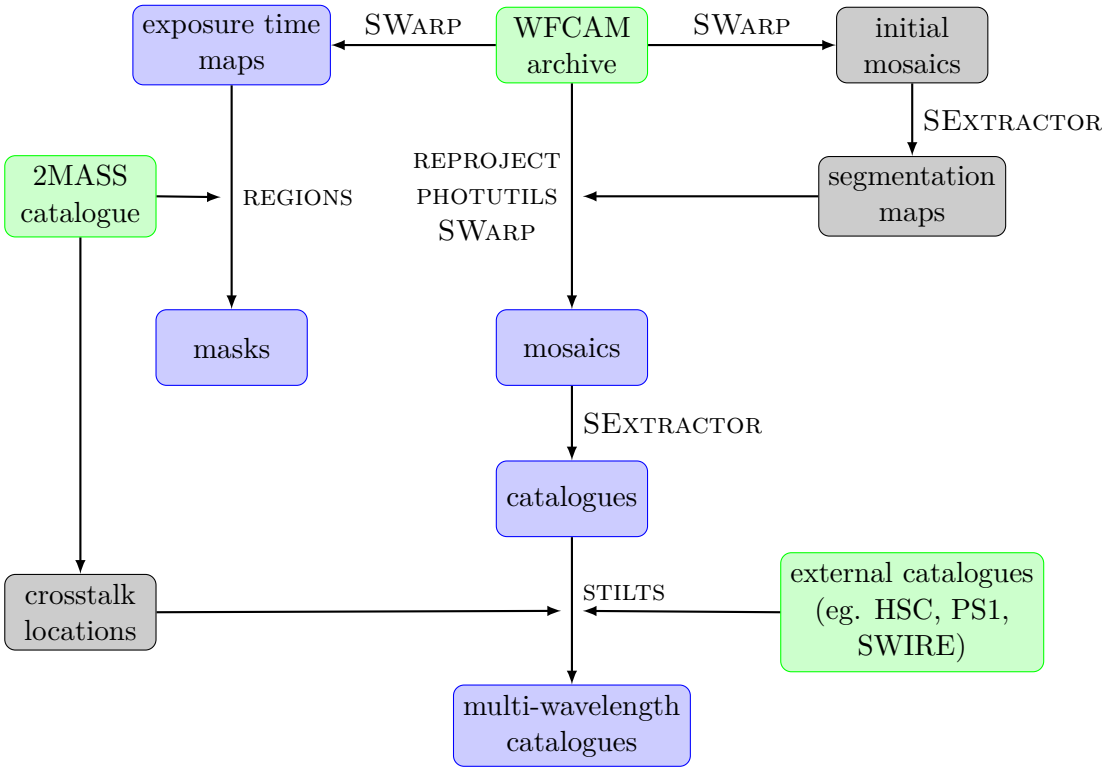

Figure 2.7: A summary of the workflow for producing mosaics, catalogues, and maps. The labels on arrows (if present) indicate software used in that step in addition to PYTHON (and commonly used packages NUMPY and ASTROPY). Input data are in green, and useful products are in blue.

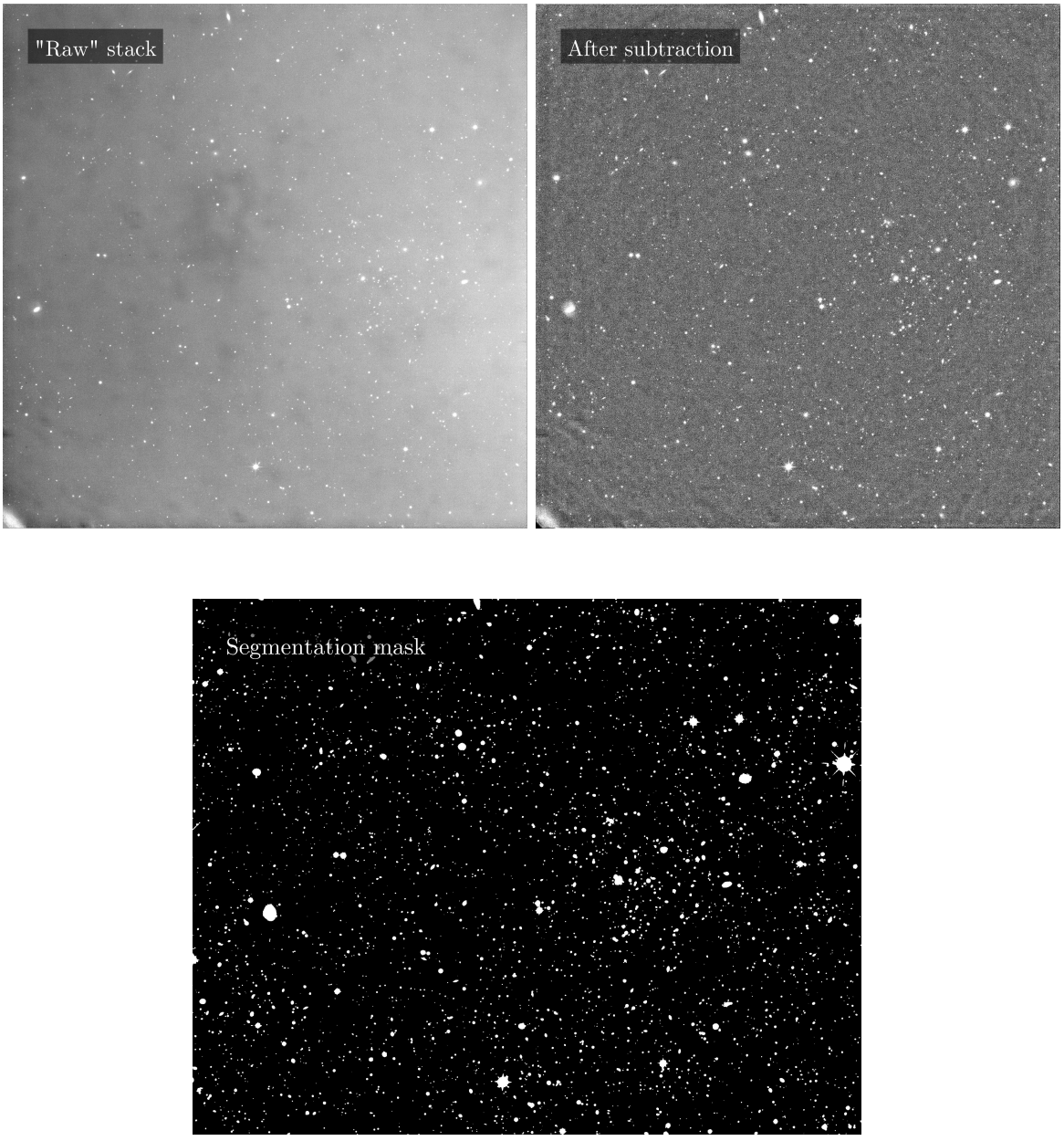

Figure 2.8: CCD 2 from the "1" pointing in Figure 2.1, in ElaisN1 tile 1, K-band. *Left*: The stack as downloaded from CASU. *Right*: The background-subtracted stack, which is then used in the median coadd. A clear gradient has been removed from the stack. *Lower*: the cutout of the segmentation image used as a mask. The segmentation image is slightly more extended than the CCD images.

field. This allows us to use a smaller grid to estimate the (local) background, as there is now reduced risk of including the many bright pixels from large objects in the estimate. The segmentation maps used as source masks are produced with a fairly conservative per-pixel detection threshold (parameter `DETECT_THRESH`) of 1.4σ, so not to select apparently low surface brightness artefacts. This produces better mosaics than using only the single-step background subtraction, as shown in see Figure 2.9. We point out that the majority of the dark imprints caused by bright stars have been removed (although they may appear more egregious in the default Figure than in reality due to JPEG artefacts), and the 'grouting' (regions between overlapping CCDs) appears smoothed. Input frames are then combined with a median average at each pixel in the coadd reprojection.

To ensure the difference in photometry will not cause catastrophic systematic errors in later analysis, Figure 2.10 illustrates the difference in the photometry of (all) objects from the two-step to one-step background removal, $K_{\rm masked} - K_{\rm default}$. We use SExtractor to extract the sources in the two-step mosaic, and perform forced photometry on the one-step mosaic using the same apertures (with SExtractor's dual-image mode). The solid line is the median value of the difference in magnitude, as a function of $K_{\rm masked}$, the magnitude from the two-step photometry. The shaded error region is the median magnitude error for objects in these 0.25 mag bins, plotted relative to the median value. The dashed lines are the 16% and 84% percentiles, in the same 0.25 mag bins.

We also show the variation in sky background for each input stack that goes into a tile (with a histogram for each tile) in counts per second in Figure 2.11. The median is around 1.1 counts per second, with a median absolute deviation of ~ 0.3 for each tile. This, along with the completeness plots in Section 2.3.3 indicate that the depth of the survey is uniform across the area.

2.3.2 Spurious detections

To avoid spurious objects appearing at the ragged edges of mosaics as much as possible, we include frames from adjacent tiles (where these exist). However, where there are no adjacent tiles (at the edges of the fields), or in central portions of mosaics where detectors have left gaps (due to jitter strategy, or to avoid bright stars), we reject objects in pixels which do not have the same number of visits as the rest of the tile.

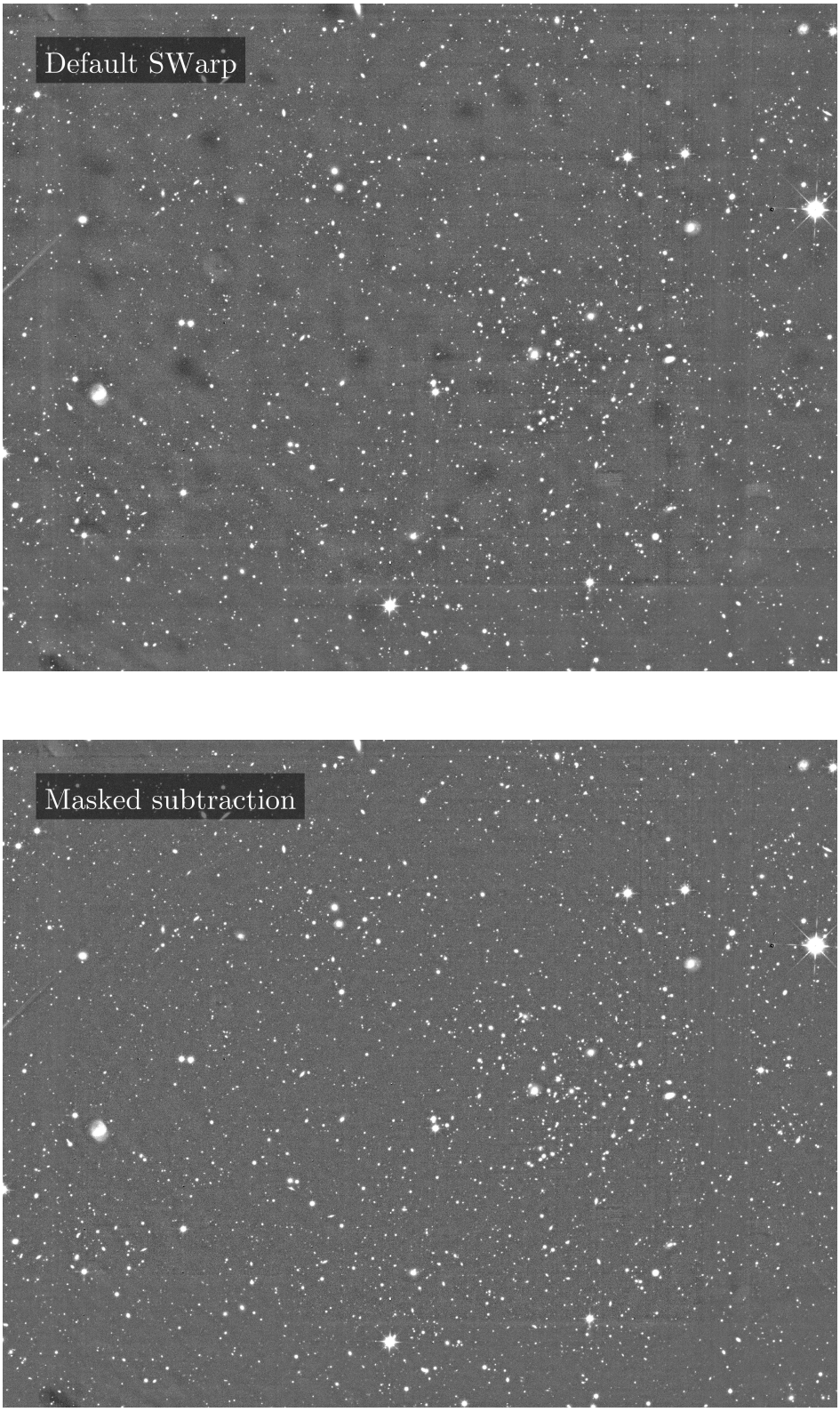

Figure 2.9: Comparison of one-step (default SWarp) and two-step (masked) background removal. Masking sources in the input stacks before background subtraction allows a smaller background estimation mesh, which produces visibly better mosaics. The two cutouts are from K band images in ElaisN1 tile 1, at $\alpha = 242.96, \delta = 54.285$.

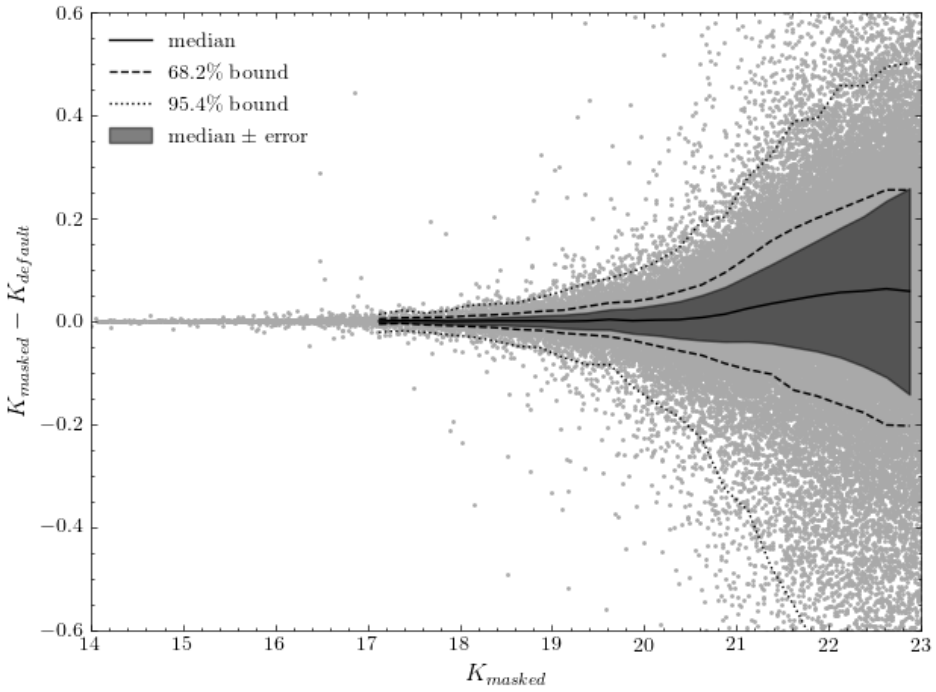

Figure 2.10: Difference in K-band magnitude from one-step (default) background subtraction, and two-step (masked source) background subtraction. Photometry from the one-step mosaic is forced from the two-step mosaics.

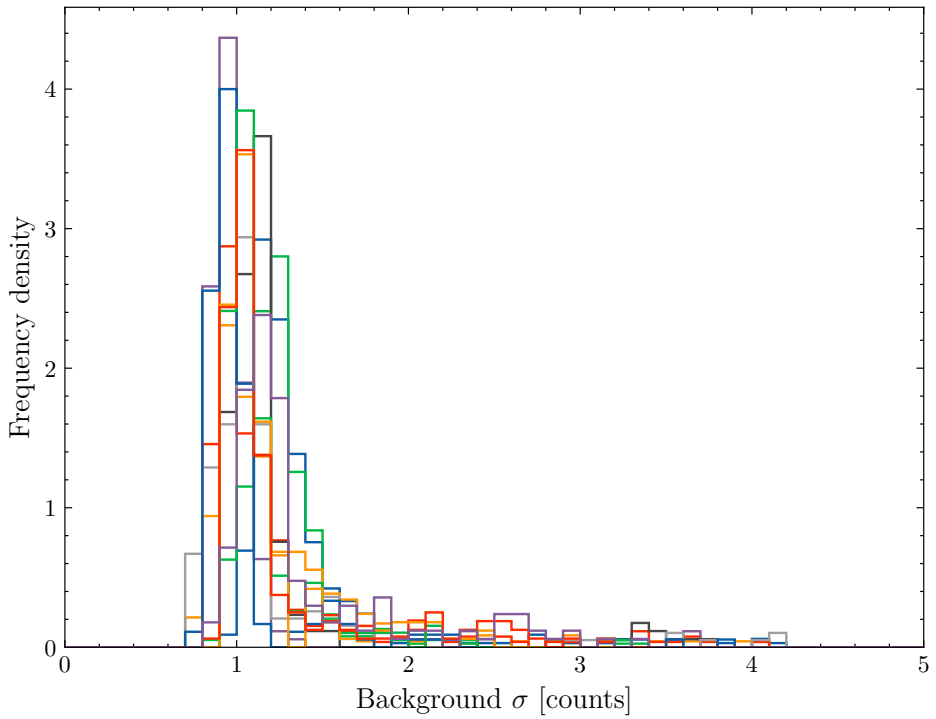

Figure 2.11: The variation in background (in counts per second) for each input stack, for each tile in Elais-N1 (there are 12 in tiles, so twelve histograms). The median is around 1.1 counts per second, with a median absolute deviation of ~ 0.3 for each tile. Histograms are normalised to one (as there are differing numbers of input stacks per tile).

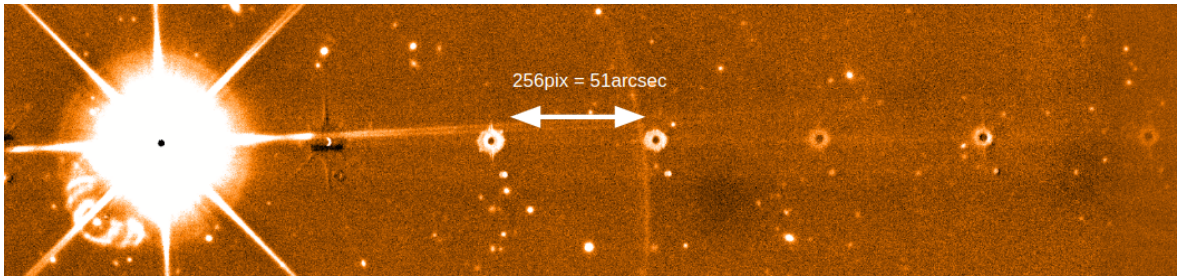

Figure 2.12: An example of cross-talk artefacts, from a bright (and saturated) star. Cross-talks scatter perpendicular to the direction of readout in detector coordinates, and are spaced 256 pixels apart.

2.3.2.1 Cross-talk images

Cross-talk images are spurious, non-astronomical objects (Dye et al., 2006) caused by bright stars. Figure 2.12 shows an example of cross-talk images in relation to a saturated star. They are caused by the readout electronics of the WFCAM CCDs.

They scatter away from bright (saturated) stars perpendicular to the direction of readout of each detector quadrant (see Figure 2.1, left). Fortunately, their locations are predictable, as they are spaced by $m \times 128$ pixels, where m is the microstepping strategy ($m = 2$ for DXS). We flag all objects in the catalogue within $3''$ of positions 256 pixels in detector coordinates from very bright stars ($K < 15$ or $J < 15$).

Bright star positions are selected from 2MASS catalogues (Skrutskie et al., 2006, see Section 2.5.3), due to our own DXS catalogues saturating at $K \sim 14$.

The careful photometry of objects in different brightness regimes gives the 2MASS point source catalogue high photometric and astrometric accuracy over a very large dynamic range, with astrometry better than $0.2''$ for objects from as bright as $K_s \sim 5$, to the faint limit. Determining the locations of the cross-talks which DXS imaging suffers from relies on reasonably good astrometry for the parent star. By their nature, the cross-talks which DXS suffers from are caused by saturated point sources, meaning that we will *not* have reliable astrometry for the brightest sources. For this reason, we choose to use (relevant portions of) the 2MASS point source catalogue as input for determining the detector locations of cross-talk images.

2.3.2.2 Diffraction spikes

We determine locations where objects are likely contaminated with flux from diffraction spikes and haloes of bright stars. We flag these in the catalogues, with mask sizes depending on magnitude of the bright star, measured by median-stacking all bright stars in SA22, shown

in Figure 2.13, and estimating the extent of diffraction spikes and halos by visual inspection. Masks are a combination of one circular (for the bright halo) and four long, thin rectangular regions (for the diffraction spikes), constructed with REGIONS (Bradley et al., 2022). Bright star positions are selected from 2MASS catalogues (Skrutskie et al., 2006, see Section 2.5.3), due to our own DXS catalogues saturating at $K < 14$. We also add in "by hand" the extremely bright variable star Mira[4] at $\alpha_{2000}, \delta_{2000} = 02\ 19\ 20,\ -02\ 58\ 39.5$.

2.3.3 Completeness and depth

The target depths of DXS set out by Lawrence et al. (2007) are $J_{\rm AB} = 23.2$ and $K_{\rm AB} = 22.7$, with a secondary goal of reaching $H_{\rm AB} = 23.2$ in a smaller area (SA22 was chosen as it was the first field to be complete). To ensure that we have met these goals, we have performed an injected point-source test. We inject a large number of fake sources (10,000 sources per square degree) at random positions, with random magnitudes into each mosaic, discarding those which overlap with real sources (using the segmentation map created by SEXTRACTOR when creating catalogues).

We run SEXTRACTOR on these modified mosaics (and exclude real sources), and measure the fraction recovered as a function of input magnitude. The results for each tile are shown in Figures 2.14, 2.15, and 2.16.

Figure 2.14 shows that we have above 90% recovery rate in K for point sources in each tile at the target depth. XMM-LSS tiles 7 and 8 are incomplete and not shown, but less important, however, as the J imaging is missing from these tiles. The unusual shape of the XMM-LSS tile 6 curve is due to the alignment of the pointings, overlapping in a different configuration to the usual interlocking four (to avoid the bright star Mira); see the top right corner of the top right panel of Figure 2.6, as compared with the interlocking pattern in Figure 2.1.

Similarly, the recovery rate is approximately 90% for a majority of tiles in J at the target depth. Noticeably, Lockman tile 10 and ElaisN1 tile 1 drop below 90% a few tenths of a mag below the target. These can be explained when considering the exposure time maps presented in Figure 2.6: these tiles have shorter exposure times than all others in the J coverage.

Finally, the H band data does not meet the target depth in any of the tiles. For tiles 2 through 6, completeness is around 60% at the $H = 23.2$ target. SA22 tile 7 falls significantly below the target, but this tile was observed with far shorter exposure time than any of the

[4] http://simbad.u-strasbg.fr/simbad/sim-basic?Ident=mira&submit=SIMBAD+search

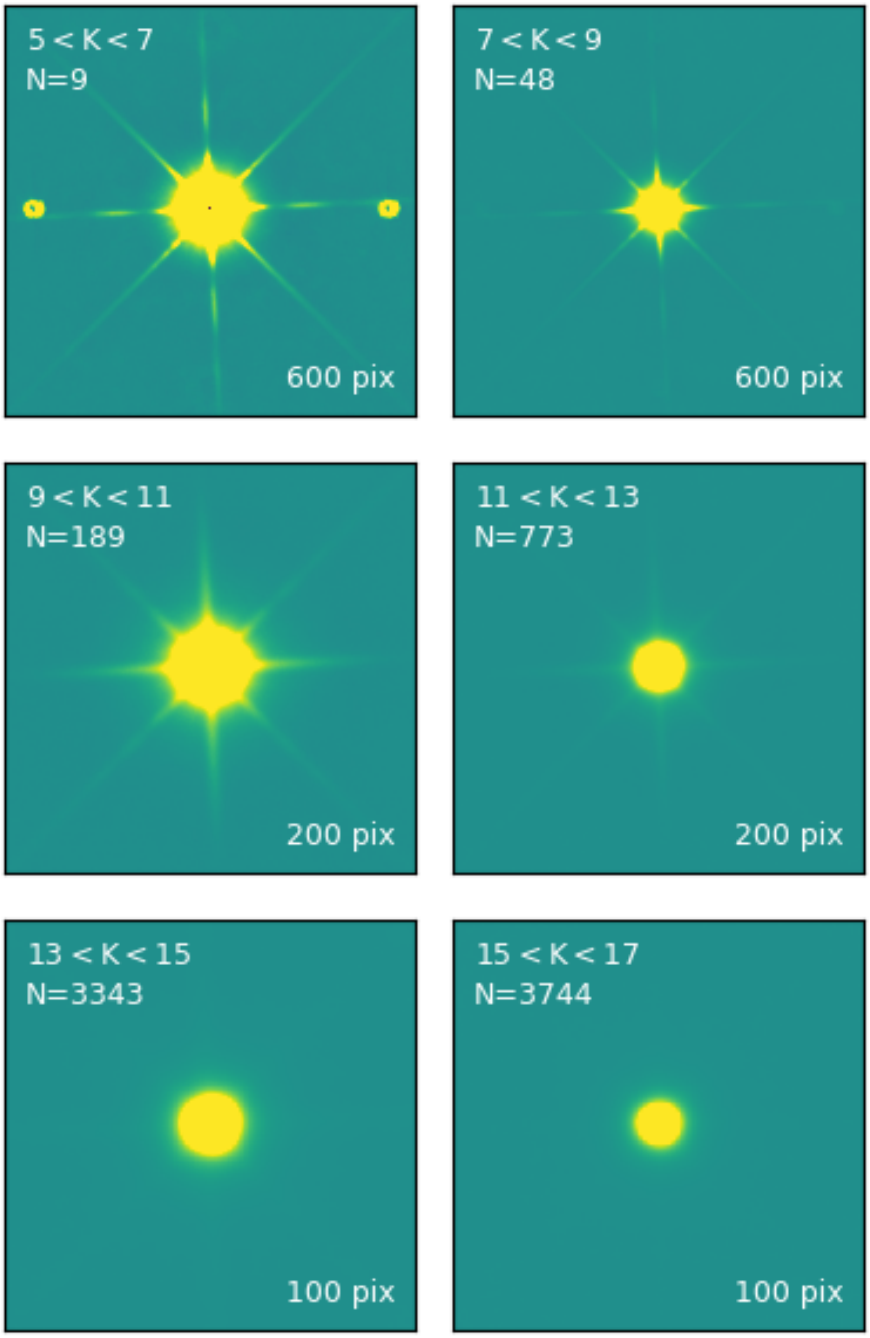

Figure 2.13: Median-stacked cutouts of all stars in the SA22 tiles, with positions taken from 2MASS. Magnitude ranges and number of objects stacked in each panel are displayed in the top left, and cutout size in pixels in the bottom right. Note that the vertical and horizontal diffraction spikes are rotated anti clockwise (in detector coordinates) by $\sim 2.5°$. Diffraction spikes are barely visible for stars $K > 13$.

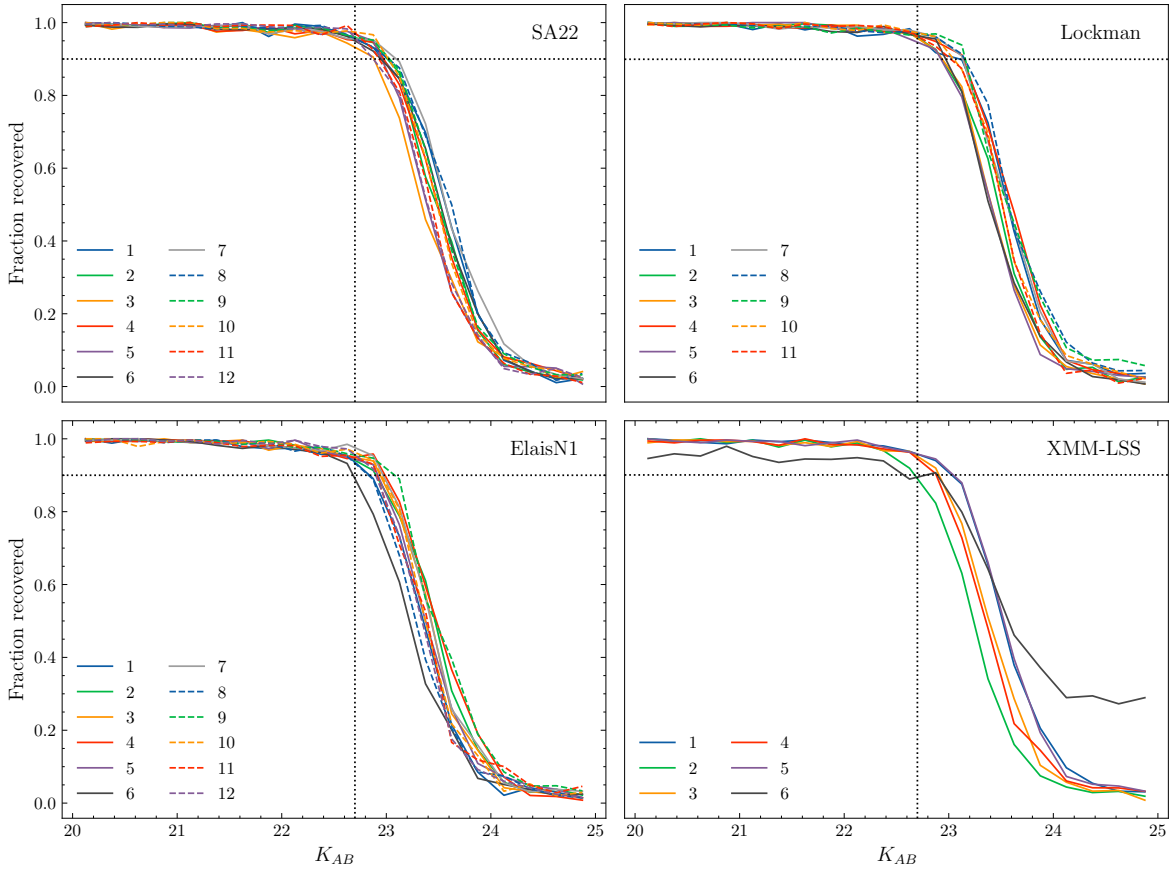

Figure 2.14: Fraction of injected (fake) point sources recovered as a function of magnitude for the K mosaics, for each $0.8\,\mathrm{deg}^2$ tile. The vertical dotted line is the target depth of $K_{\mathrm{AB}} = 22.7$, the horizontal dotted line is 90% recovery.

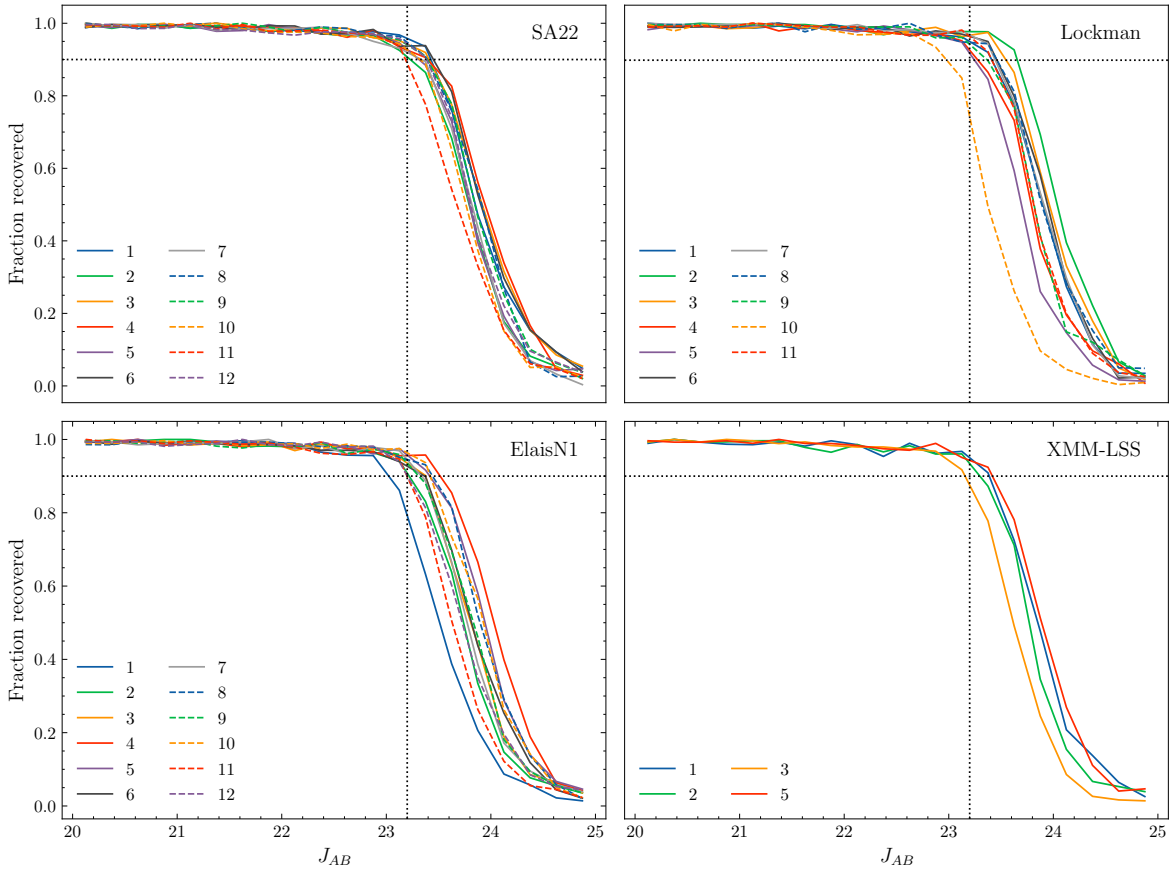

Figure 2.15: Fraction of injected (fake) point sources recovered as a function of magnitude for the J mosaics, for each 0.8 deg^2 tile. The vertical dotted line is the target depth of $J_{\rm AB} = 23.2$, the horizontal dotted line is 90% recovery.

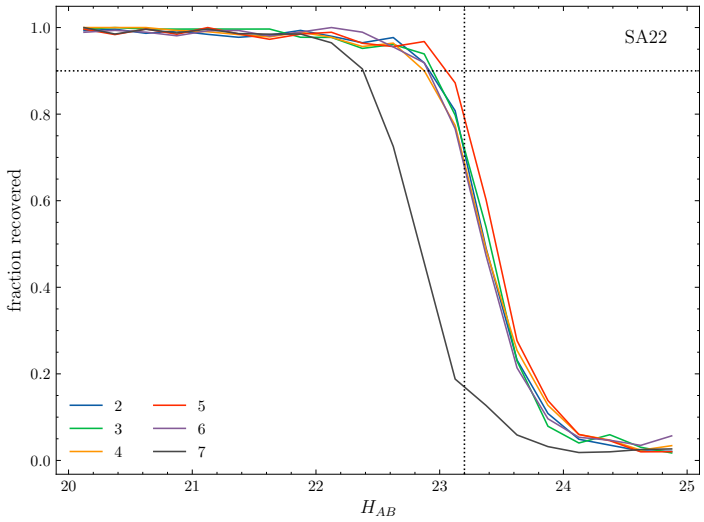

Figure 2.16: Fraction of injected (fake) point sources recovered as a function of magnitude for the H mosaics, for each 0.8 deg^2 tile. The vertical dotted line is the target depth of $H_{\rm AB} = 23.2$, the horizontal dotted line is 90% recovery. H data is only available in a subset of SA22 tiles.

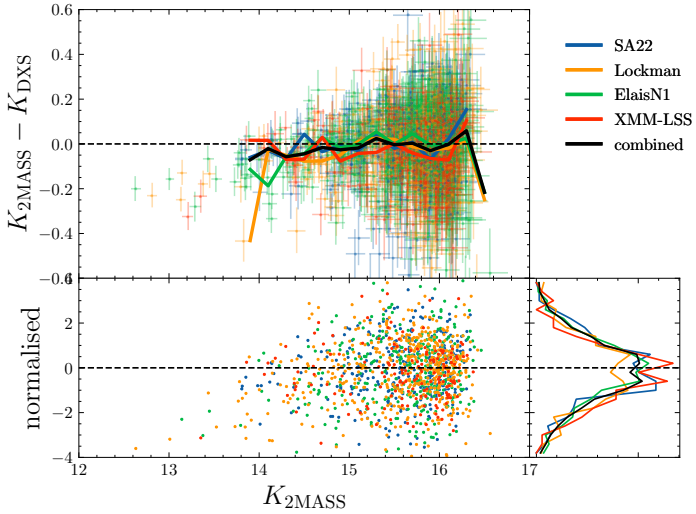

Figure 2.17: Difference between 2MASS and DXS photometry as a function of 2MASS K band magnitude, in AB. K_{2MASS} has been transformed from K_s to K with the transformations detailed in Hodgkin et al. (2009). Uncertainties for $K_{2MASS} - K_{DXS}$ are computed as the separate components summed in quadrature. Solid lines are the median values in bins of 0.2 magnitude. The lower panel shows this photometry difference normalised to these error bars.

other five tiles. Nevertheless, the other five tiles are roughly consistent, within 0.5 mag of the target, and H-band observations were the lowest priority for DXS, so we do not consider our analysis to be a failure, or incomplete. We estimate from Figure 2.16 that the five 'good' H tiles are 90% complete at $H \sim 22.9$.

2.3.4 Validation against 2MASS

For each of the four fields, we match our DXS catalogues to the extended source catalogues (XSC) from 2MASS[5] (see 2.5.3 for 2MASS description), which are complete to $K_{s,\mathrm{AB}} \sim 16.1$.

Figure 2.17 shows the difference in DXS photometry and 2MASS photometry. The transformations detailed Hodgkin et al. (2009) to transform 2MASS magnitudes into the WFCAM system have been applied, although these are extremely small. We also present this photometry difference normalised to the uncertainties, and the histogram of these residuals. They are relatively well-behaved: 71% of these normalised residuals are within one standard deviation (compared with the expected 68%).

At $K > 14$, the median is roughly zero for all four fields.

At $K_{\mathrm{AB}} < 14$, there are very few data points: there are very few galaxies this bright in areas the size of DXS, and further: Figure 3.5 in a later section demonstrates that we expect fewer

[5] https://irsa.ipac.caltech.edu/Missions/2mass.html

than one galaxies per square degree brighter than this magnitude. The few data points that there are consistently show $K_{\rm 2MASS} < K_{\rm DXS}$, which is expected for saturated sources (ie, DXS flux is underestimated).

2.4 Future improvements

2.4.1 PSF homogenisation and PSFex

Earlier, we noted that we do not homogenise the PSFs betweeen input stacks. However, this process would allow use of SExtractor's more sophisticated `SPREAD_MODEL` parameter as additional tool for separating point-sources from extended. It relies on a well-defined and modelled PSF, which can be computed using the PSFex software. Further homogenisation of the PSF between bands would also allow for better probability images (see Section 2.4.2).

2.4.2 Probability images

One further step that could be taken would be to produce so-called probability images or χ^2-images from the individual band mosaics. Szalay et al. (1999) have shown that this combination method is the optimum way to extract sources from panchromatic data, given that each mosaic is background-limited, with uncorrelated noise between frames, and with a homogenised PSF. They show that the quantity

$$y = \sum_{i=1}^{k} g_i^2 = \sum_{i=1}^{k} \frac{(f_i - \mu_i)^2}{\sigma_i^2}, \tag{2.4.1}$$

where f_i is the pixel value, μ_i is the mean background value, and σ_i is the standard deviation of the sky background, for i in $1..k$ single-band mosaics will, for background (sky) pixels, follow the χ^2 distribution

$$dP\left(y;k\right) = \frac{1}{2^{k/2}\Gamma\left(k/2\right)} \mathrm{e}^{-y/2} y^{k/2-1} dy, \tag{2.4.2}$$

where k are the number of degrees of freedom - here the number of single-band mosaics included in the probability image. This probability image can be then used as the detection image in SExtractor's dual mode, for instance.

As an example, we plot the distribution of g_i in the SA04 tile, for each of JHK in Figure 2.18. We make the estimation of σ slightly easier by excluding pixels which are identified as sources

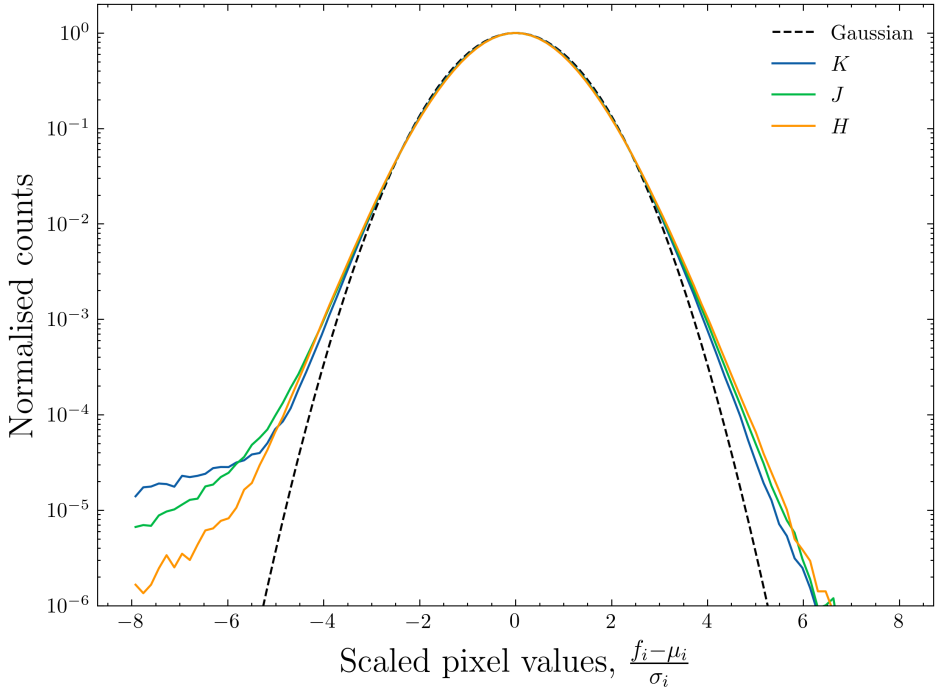

Figure 2.18: Distribution of scaled pixel values.

in SExtractor segmentation maps. The positive non-Gaussian tails represent the source pixels which have not been extracted. The negative non-Gaussian tails are likely bad rows, or other negative flux artefacts. During the quadrature addition these pixels will become very positive, which seems like a catastrophic failure of the probability image selecting these sources. However, it can be resolved by requiring some fraction of the flux in each of the measurement images be non-negative.

We also plot the distributions of pixels for constructed probability images from K, $K\&J$ and $K, J\&H$ in Figure 2.19.

2.5 Complementary datasets

2.5.1 Pan-STARRS1 MDS (PS1)

The Pan-STARRS Surveys (Panoramic Survey Telescope and Rapid Response System, Chambers et al., 2016) are a set of large optical imaging surveys using a 1.8 m telescope (PS1) and 1.4 Gigapixel camera, with a 3.2 deg diameter field of view, in five broadband filters, *grizy*. The Pan-STARRS Surveys have a broad set of astronomical goals, from solar system science to extragalactic and cosmological studies. PS1's large field of view means that it is able to image the whole visible sky (declination $\delta > -30°$) in a matter of weeks; indeed, the main

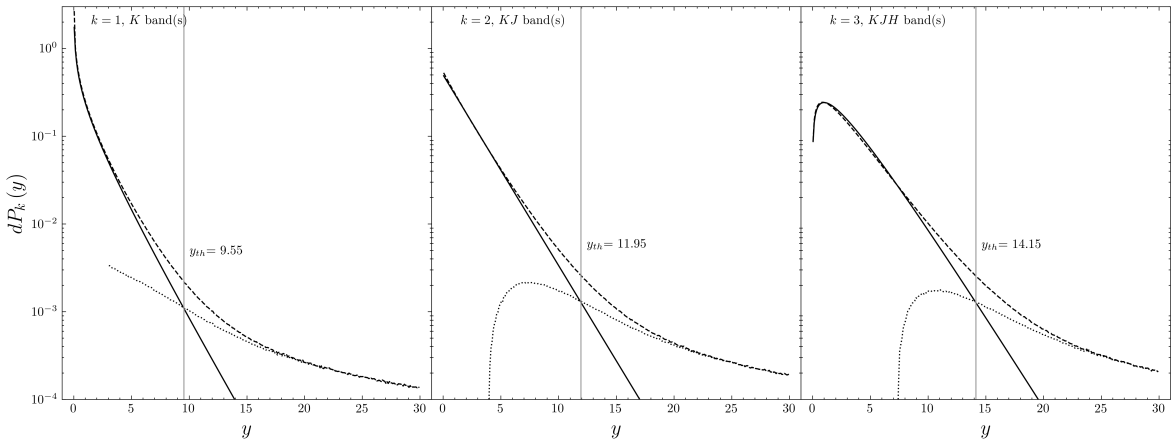

Figure 2.19: Distribution of y values for $k = 1, 2, 3$ (left to right). The solid back lines are the distribution expected from Equation 2.4.1. The dashed lines are the distribution of pixels in the constructed probability image, scaled such that the values at $y = 1$ are equal. The dotted line is the difference between the expected and measured distributions, meaning that it should be the distribution of object pixels. Finally, the grey vertical line is the threshold at which the inferred distribution of object pixels becomes greater than the distribution of sky pixels.

3π Steradian survey's aim was to scan this footprint 60 times in 3.5 years.

The second largest component of the Pan-STARRS Surveys is the Medium Deep Survey (MDS), which provides *grizy* imaging in twelve fields of a single field of view ($\sim 7\,\mathrm{deg}^2$) each, four of which overlap significantly with the DXS fields[6].

We use the band-merged catalogues from MDS (priv. comm., Metcalfe & Draper, 2021), and choose the best match for each DXS source within $1''$.

We correct for galactic extinction using the dust maps from Schlegel et al. (1998), using the python DUSTMAP implementation from Green (2018), and extinction coefficients for PS1 from Tonry et al. (2012).

2.5.2 Subaru HSC-SSP

HyperSuprimeCam (HSC) is a large optical camera, mounted on the 8.2 m Subaru Telescope on Mauna Kea, Hawaii. As part of the HSC-SSP (HyperSuprime-Cam Subaru Stratigic Program, Aihara et al., 2019); further optical *grizy* catalogues are available in three of the four fields: UltraDeep ($i \sim 28$) in UDS, Deep in Elais-N1 and XMM-LSS ($i \sim 27$), and Wide in SA22 ($i \sim 26$, which is W04 in HSC nomenclature). As with Pan-STARRS, we correct for

[6]MDS fields MD01, MD05, MD08, and MD09 correspond to XMM-LSS, Lockman, ElaisN1 and SA22 respectively.

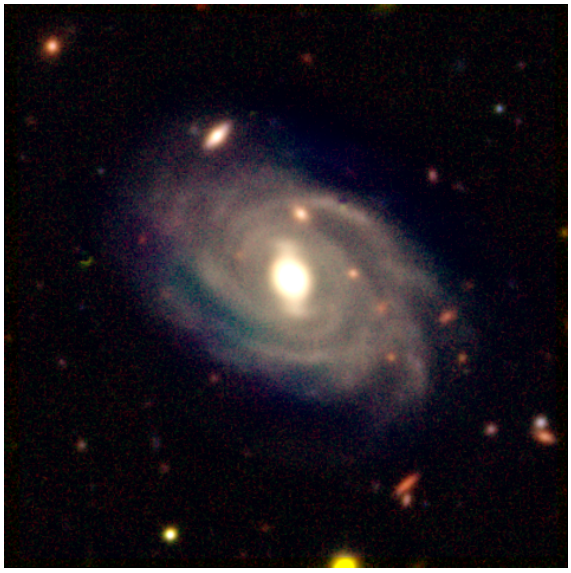

(a) $\alpha = 241.406, \delta = +55.6148$ (EN03) (MCG +09-26-052, Vorontsov-Vel'Yaminov & Arkhipova, 1962)

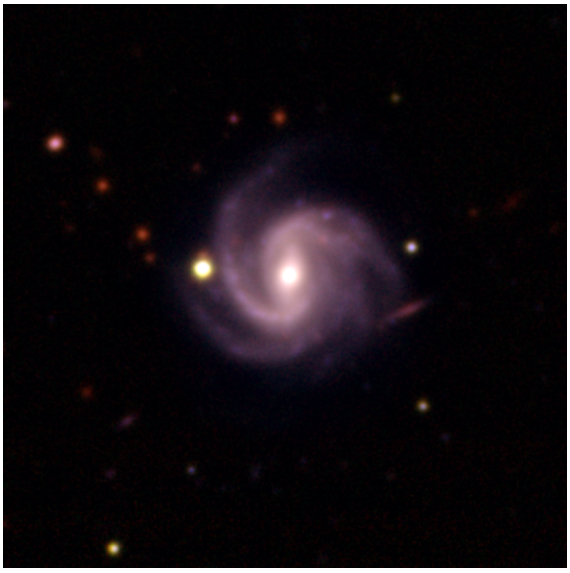

(b) $\alpha = 242.524, \delta = +54.17435$ (EN01) (2MASS J16100577+5410290, Willett et al., 2013)

(c) $\alpha = 241.540, \delta = +55.4248$ (EN03) (UGC10214 "the Tadpole Galaxy", Nilson, 1973)

Figure 2.20: A gallery of RGB images (using WFCAM-K, WFCAM-J, HSC-i as RGB channels, respectively). Coordinates are the centre of the image, not object coordinates.

galactic extinction using the dust maps from Schlegel et al. (1998). We also use the larger, more conservative saturated star masks available for the HSC-SSP (Coupon et al., 2018). Given the excellent quality of the HSC imaging (cutouts of which are publicly available as of DR2[7]), we have constructed a RGB images using HSC-i to complement WFCAM-JK to showcase the WFCAM mosaics, shown in Figure 2.20.

[7] `https://hsc-release.mtk.nao.ac.jp/doc/index.php/tools-2/`

2.5.3 2MASS

2MASS (Skrutskie et al., 2006) is an all-sky survey NIR survey carried out between June 1997 and February 2001, which provides JHK data for extended and point sources, to a 10σ depth of at least $K_s = 14.3$ mag (Vega). As mentioned in Section 2.3.2.1, the photometry and astrometry of bright sources $K_{\rm Vega} < 14$ in 2MASS is excellent, and continues to be used in many studies. As our mosaics are built with the goal of detecting faint, extragalactic objects, the astrometry and photometry of the brightest (and saturated) point sources is poor, so we choose to use 2MASS as the basis for any analysis/artefact detections that rely on this.

2.5.4 *Spitzer* SWIRE

Deep mid-infrared (MIR) data is available from the *Spitzer* Wide-Area Infrared Extragalactic survey (Lonsdale et al., 2003), and also significantly overlaps with three of four fields; XMM-LSS, Elais-N1 and Lockman. Imaging and catalogue data in broadbands at 3.6 μm and 4.8 μm (written as [3.6] and [4.8] bands) are also available.

2.5.5 unWISE

unWISE (Lang, 2014; Meisner et al., 2017) are deep, un-blurred coadds of five years of *WISE* data for the MIR $W1$ and $W2$ bands ($\lambda_{\rm eff} = 3.55\,\mu$m and $4.60\,\mu$m respectively). As *WISE* was an all-sky mission, all four DXS fields are fully covered by unWISE data, but they are much shallower than the SWIRE MIR data, and have significantly broader PSFs.

2.5.6 UDS

As described in Section 2.1, UDS is the deepest component of UKIDSS, located at the edge of the DXS XMM-LSS field. JHK catalogues (DR11) are available for the $0.87\,{\rm deg}^2$ field[8]. There are very deep optical data from HSC which overlap with UDS (in the same HSC field as XMM-LSS), along with the *Spitzer* Public Legacy-UDS programme, SPUDS[9].

[8] `https://www.nottingham.ac.uk/astronomy/UDS/data/dr11.html`
[9] `https://irsa.ipac.caltech.edu/data/SPITZER/SpUDS/`

2.6 Photometric redshifts

Photometric redshifts ("photo-zs") are an inexpensive way to obtain redshift estaimtes for large samples of galaxies. At at its simplest, this process involves fitting templates of galaxy spectral energy distributions of to the broadband fluxes measured through photometric imaging surveys. The wider the the wavelength range, and the more photometric points are provided, the better the photo-z estimate will be. Clearly though, they will not be as precise or accurate as redshifts obtained though spectroscopy, determined by eg. identifying strong emission lines.

We use the photometric redshift template fitting code EAZY-PY, a PYTHON implementation of the EAZY code (Brammer et al., 2008), using the default parameter set, the default `tweak_FSPS` templates, and the `K_extend` prior.

Photometric redshifts are estimated only in regions where there are J and K WFCAM data, *Spitzer* SWIRE data, and either Pan-STARRS PS1 or *Subaru* HSC data. This means that we have photometric redshifts for three of four fields using PS1, and two using HSC (see Table 2.2). Additionally, if there is photometry available from the UV satellite GALEX (Martin et al., 2005)[10], we include these points, although these data are typically available only for the brightest K sources.

Conveniently, the HSC optical data includes a very large selection of spectroscopic redshift data points which we use to test our photometric redshifts.

We estimate photometric redshifts with fluxes from both Kron and fixed $3''$ apertures. The fractional errors $(z_{\mathrm{EAZY}} - z_{\mathrm{spec}}) \,/\, (1 + z_{\mathrm{spec}})$ are for each of these are shown for both of these sets of estimates for the XMM-LSS field, in Figure 2.21. We choose to present these for the XMM-LSS field as opposed to ElaisN1 because there are more spectroscopic redshift points at $z > 1$.

These fractional errors show that the overall quality of the photometric redshift we obtain is poor, most likely due to our choice of parameters tuning and/or templates in EAZY.

The strong curved lines are where the photometric redshift fitting chooses a particular redshift (often $z \sim 0.3$ and 0.4). These points would appear as a constant (horizontal) line in a z_{spec} vs. z_{EAZY} plot.

Although the median fractional error (solid black line) is closer to zero for a larger redshift range for photo-zs estimated with fixed-aperture fluxes, the 68% confidence interval is

[10] `https://galex.stsci.edu/GR6/`

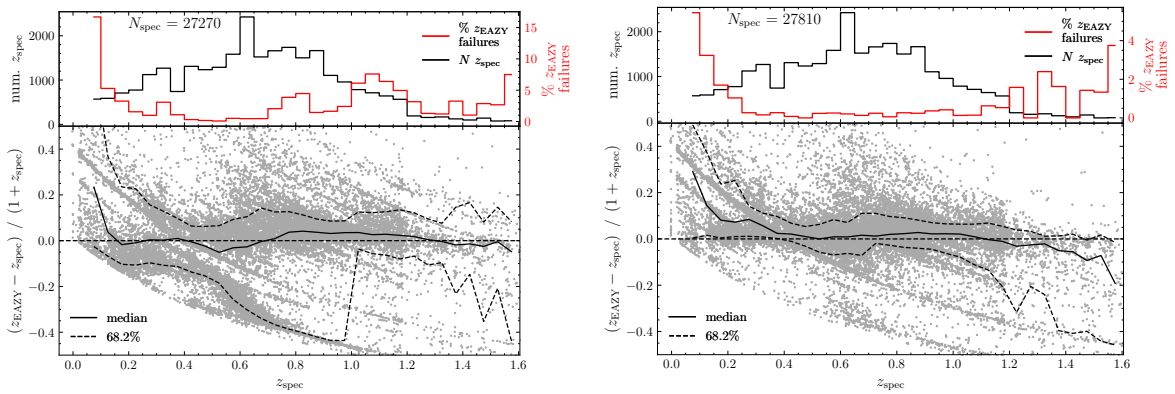

(a) Using fixed 3″ aperture flux measurements. (b) Using Kron aperture flux measurements.

Figure 2.21: The fractional errors $(z_{\rm EAZY} - z_{\rm spec}) / (1 + z_{\rm spec})$ as a function of spectroscopic redshift $z_{\rm spec}$, for the DXS-HSC-SWIRE(-GALEX) catalogue for XMM-LSS. The solid black line shows the median fractional error in bins of $\Delta z = 0.05$, and the dashed black line is the 68% confidence interval. The black histogram in the upper panel shows the total number of spectroscopic data points in the same redshift bins, and the red histogram is the fraction of these objects for which the photometric estimation with EAZY fails (ie, where there is no estimate at all).

significantly wider, and less "well-behaved": there is a strong jump in the lower bound at $z \sim 1$. Even without the confidence interval, the number of catastrophic failures for the fixed aperture measurements is clearly higher, especially for negative errors (overestimated redshifts).

Taking the Kron aperture photo-zs as the better estimates, their poor quality is particularly evident at $z < 0.4$, where even the lower bound of the 68% interval is above zero, implying that greater than 84% of the galaxies here have overestimated redshifts. The physical interpretation of the poor accuracy is a lack of short-wavelength data: at $z < 0.4$, the D_{4000} break appears at observed wavelengths $\lambda < 5600$Å, and the PS1 g-band (the shortest band we reliably have for a large area) has an effective wavelength $\lambda_{\rm eff} = 4810$Å, meaning that we cannot use this strong, characteristic feature to separate the star-forming and passive galaxies for a large fraction of these galaxies.

Further, the fraction of objects whose photo-z estimate fails completely is much higher for the fixed aperture flux estimates.

For the $z > 0.5$ range of redshift that we trust, and where there are a reasonable number of spectroscopic data points ($z \lesssim 1.2$), the 68% limit of the fractional error is around 10%. The median is within 5% (although are systematically overestimated by ~ 0.01).

To demonstrate that it is our deficient application of EAZY, and not our photometry which is causing these errors, we show the same fractional error plots for the UDS-HSC-SPUDS

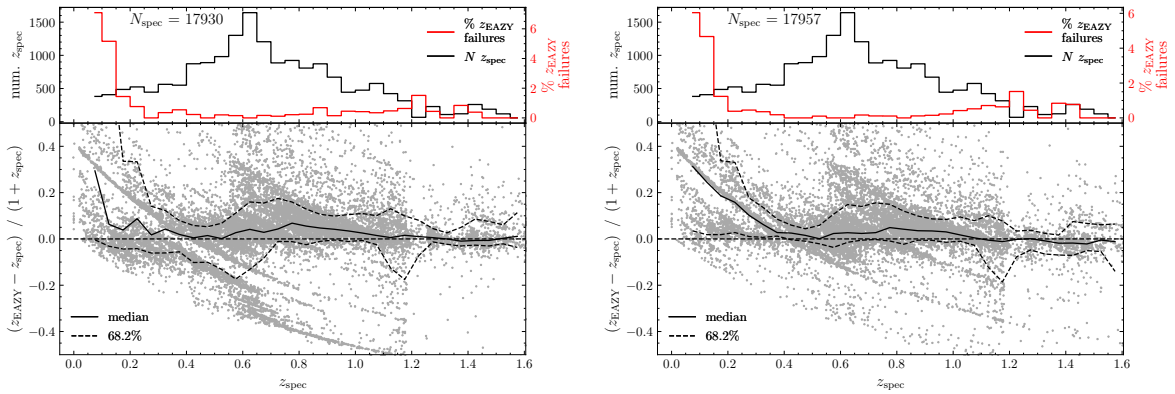

(a) Using fixed 3″ aperture flux measurements. (b) Using Kron aperture flux measurements.

Figure 2.22: Fractional photometric redshift errors, for the UDS-HSC-SPUDS(-GALEX) catalogue.

catalogue.

Given that the UDS photometry is extremely reliable, the fact that that photo-zs using Kron and fixed aperture flux estimates show the same behaviour as those for our DXS catalogues is indication that this is a plausible explanation.

We stress that obtaining excellent photometric redshifts was *not* a primary goal of this work, and so we consider our photometric redshifts (at least for $z \gtrsim 0.4$) to be sufficient for studying properties of galaxies in (relatively wide) redshift intervals.

Chapter 3 shows photometric redshift distributions of various selections of objects.

2.7 Summary

UKIDSS-DXS is a large NIR survey in J and K covering $\sim 28\,\mathrm{deg}^2$ in four fields, reaching $K \sim 22.7$, using the WFCAM instrument on UKIRT. We describe the survey by comparing it to the other UKIDSS components, and further, describe its place amongst other NIR surveys which probe different areas and depths.

We have produced deep mosaics using SWarp, and outline the two-step sky background subtraction method we employ to improve the uniformity of the mosaics' background. By comparing the photometry from the improved mosaics to those which use the default SWarp procedure, we show that this procedure does not have a significant impact on the photometry.

We also describe our process of eliminating cross-talk images, spurious sources which appear in locations in detector coordinates at predictable locations around saturated stars. We choose to use 2MASS catalogues for this, as finding their locations requires accurately knowing the

positions of the stars which cause them, and the 2MASS astrometry is excellent over its whole $5 < K_{s,\mathrm{Vega}} < 14$ magnitude range. The brightest stars in DXS imaging also show diffraction spikes. To counteract these, we produce masks, which consist of one circular and four rectangular regions, also using positions from 2MASS.

Catalogues from these mosaics are produced using SExtractor, and we primarily use forced photometry from the K-band apertures on the J-band imaging. Using an injected point source test, we demonstrate that the depth of the imaging in the majority of the tiles reaches the target depths of $K_{\mathrm{AB}} \sim 22.7$ and $J_{\mathrm{AB}} \sim 23.2$ with a 90% recovery rate.

Given that we intend to exploit the strong 4000Å to select galaxies at $z > 1$, we describe the available optical data, namely, HyperSuprimeCam, and PanSTARRS Medium Deep Survey data. We also describe the MIR data which are available.

Finally, we produce photometric redshift estimates using eazy.

Although these are poor, we argue (by comparison with reliable UDS data), that it is our application of the photometric redshift code that is the issue, with insufficient data at short (blue) wavelengths to produce reliable photo-zs for the lowest redshift galaxies, and not the photometry of our NIR catalogues.

Chapter 3

Object selection

This chapter will detail the objects selections we will make (primarily galaxies at $z > 1$) for analysis in later Chapters.

Throughout, we use SExtractor's `MAG_AUTO` Kron-aperture magnitudes as total magnitudes, and fixed-aperture magnitudes to calculate colours.

As the principal goal of this Thesis is to investigate the most massive, passive galaxies in the redshift range probed by DXS, we require galaxy selections which exploit the strong features exhibited in the spectra of passive galaxies: the strong breaks.

Although the dropout technique based on the Lyman break is a powerful method of selecting samples of high-redshift galaxies (Giavalisco, 2002; Tilvi et al., 2013), we will focus in this work on Balmer/D_{4000}-selected galaxies. The reason is that at intermediate redshifts ($1 < z < 1.5$), the Lyman break will still fall between the U, V and I bands, meaning that (deep) optical and UV data are sufficient to bracket this break. However, for the Lyman break to cross (for example) the HSC-i band, and be an i-dropout, and make the NIR data useful, the object would have to be at $z > 7$, for which our survey is much too shallow.

3.1 Removing galactic stars

One simple technique to remove galactic stars is to select only objects with $(J-K)_{\rm Vega} > 1.0$, corresponding to $(J-K)_{\rm AB} > 0.04$, when using the appropriate Vega-AB transformations for the WFCAM filters. However, given the large number of photometric bands we have which cover (large portions of) each field, we can do better by using colour-colour selections.

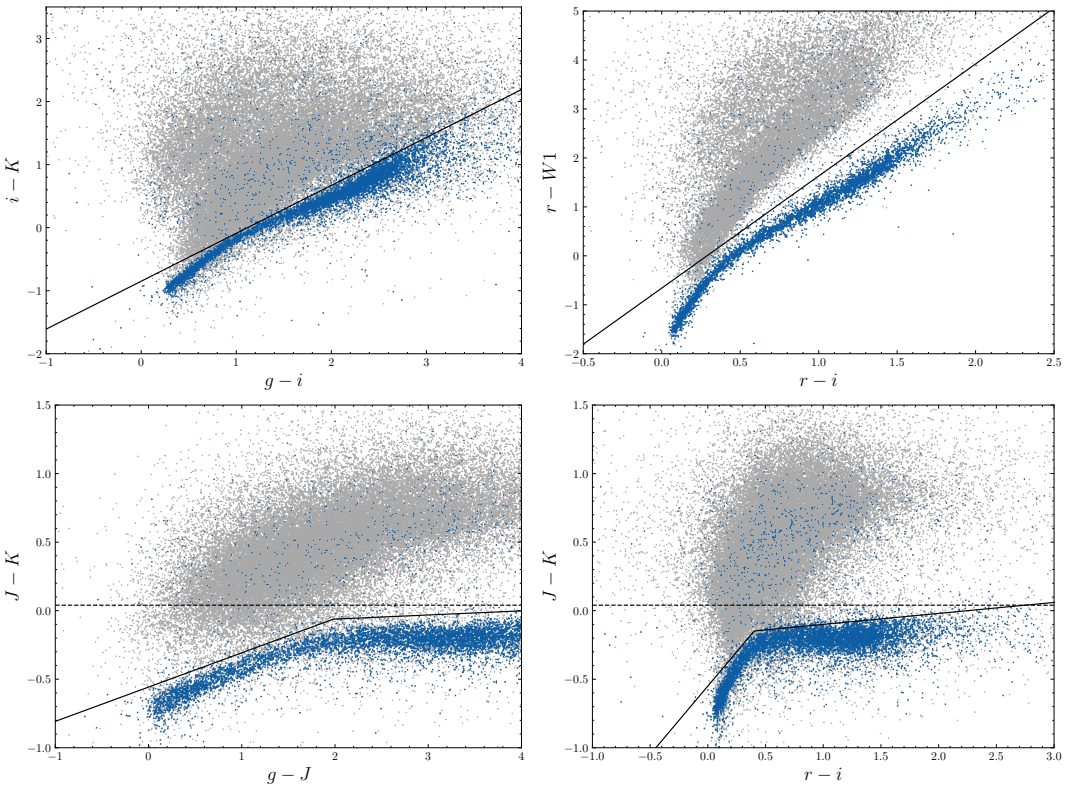

Figure 3.1: Stellar sequences in (left to right, top to bottom): $i - K$ vs. $g - i$, ri vs $r - W1$, $g - J$ vs. $J - K$ and $r - i$ vs. $J - K$, identified from the ElaisN1 catalog. 20% of all objects brighter than $K < 22.7$ (with the appropriate matching bands) are show in each panel. Additionally, objects who have SExtractor parameter `CLASS_STAR` > 0.95 are highlighted in blue. In the plots which involve $J - K$, the commonly used $J - K < 0.04$ criteria is shown as a dashed black line. Note that the $W1$ data is shallowest data, meaning that the top right panel only contains the brightest objects, so the separation of stars and galaxies looks artificially good. Similarly, the g data is the shallowest of the g, r and i bands, so it looks the better of the two bottom panels. We choose to use the $r - i$ vs $J - K$ colour criteria.

Another simple method to reject galactic stars would be to use SExtractor's helpful parameter `CLASS_STAR`, a single value (between zero and one), which indicates the likelihood of an object being a point source, using knowledge only of the seeing FWHM of the input image, and iso-flux contours measured during the photometry. However, this value tends towards 0.5 (ie, unclassified) for the faintest detected objects in a mosaic, and we also risk rejecting quasars (which appear as point sources). It will still be valuable information to have as a self-consistency check, though.

A variety of colour-colour selections are available to remove galactic stars from an optical-NIR catalogue, a number of which are shown in Figure 3.1 Kim et al. (2014) use a combination of criteria in $g - i, i - K$ and $r - i, r -$ [3.6] colour-colour spaces. However, we have IRAC [3.6] data in only three of our four fields. For a comparison, we choose to use the shallower but all-sky *unWISE* $W1$ as a replacement for the [3.6] band. We show both of these criteria

in the top two panels of Figure 3.1. We highlight in each panel of this figure the objects that have `CLASS_STAR` > 0.95; that is, objects that are *very* likely to be point sources. As mentioned earlier, there are still some high-likelihood point source objects which appear in the redder $i - K$ galaxy 'cloud'.

The separation of the stellar sequence in the $r - i$ vs $r - W1$ in Figure 3.1 (upper right) looks very good, however, the fraction of objects with a WISE counterpart drops below 80% at $K \sim 20$, meaning that only relatively bright objects are included on this plot.

Maddox et al. (2008) use a broken-line criteria (in Vega magnitudes) $g - J = 4\,(J - K) - 0.6$ for $J - K \leq 0.9$ and $g - J = 33.33\,(J - K) - 27$ for $J - K > 0.9$ (the break corresponds to $g - J = 3$). We transform this into AB magnitudes, and rearrange to make the blue colour $g - J$ the subject,

$$J - K < \begin{cases} 0.03\,(g - J) - 0.1214, & \text{for } (g - J) \leq 2.0, \\ 0.25\,(g - J) - 0.5575, & \text{for } (g - J) > 2.0. \end{cases}$$

We plot this criteria in the lower left panel of Figure 3.1.

Finally, we look at an optical vs. NIR colour-colour diagram: $r - i$ vs $J - K$ (lower right). Nieves-Seoane et al. (2017) show that this type of colour-colour diagram can provide an accurate discrimination between stars and galaxies, although they use the slightly 'wider' $F489M - F814W$ optical colour. We draw a broken line, similar to theirs (and that of Maddox et al., 2008),

$$J - K < \begin{cases} (r - i) - 0.55, & \text{for } (r - i) \leq 0.4, \\ 0.08\,(r - i) - 0.18, & \text{for } (r - i) > 0.4. \end{cases}$$

Kim et al. (2011) use the same $r - i$ vs $J - K$ colours to demonstrate the stellar sequence, although they do not use it as their star/galaxy separation criteria.

To compare the effectiveness of the criteria discussed above, in Figure 3.2 we plot the distribution of `CLASS_STAR` for each of the rejection criteria, along with all objects brighter than $K < 22.7$, $K < 22$, and $K < 21$. A 'good' criteria in this figure (from the point of view of obtaining a 'pure' galaxy sample) will reject the majority of objects with `CLASS_STAR` close to one, while rejecting as few galaxy candidates (ie, non-point sources) with `CLASS_STAR` ~ 0 as possible. This histogram is constructed using the ElaisN1 catalogue, which has the second highest density of galactic stars per square degree of the four fields. As we expected, the selections using $W1$ reject very few galaxy candidates, but do not reject as many point

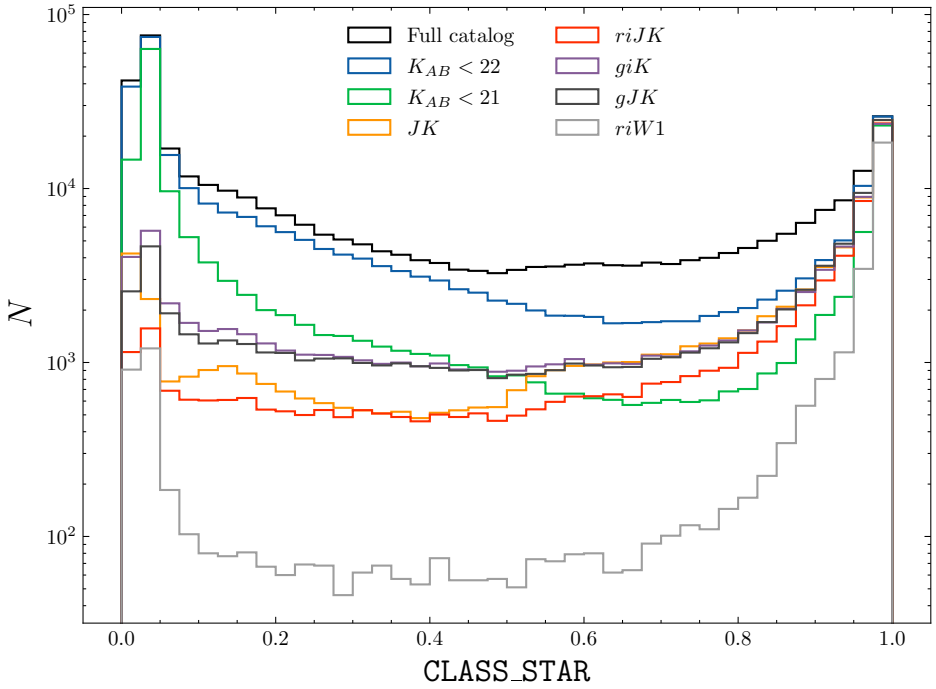

Figure 3.2: Distrubution of SExtractor parameter `CLASS_STAR` (measured from the K band mosaic) of objects rejected with various criteria. The distribution of the whole catalogue at three K band cuts (the full catalogue at $K < 22.7$, and $K < 22$ and $K < 21$) is shown for comparison. The counts are shown on a log scale. We ultimately choose the $riJK$ criteria.

source candidates as criteria with optical bands (due to the depth of the optical bands). The simple $J - K$ criterion rejects many point sources, but also rejects more galaxy candidates than the $riJK$ criteria. This can also be seen in the lower panels of Figure 3.1; the dashed horizontal line (indicating the $J - K < 0.04$ cut) cuts into the galaxy 'cloud' significantly. For this reason, and that the fraction with a match in ri is higher than g, we ultimately prefer to use the $riJK$ criteria to reject galactic stars. However, in regions where r or i data are absent, or the optical data are saturated, the $J - K$ criteria is a useful replacement, especially if the galaxy selections are red. The latter will certainly be the case for HSC data; Aihara et al. (2019) measure the saturation magnitude of the HSC-i and -r bands to be 17.4 and 18.0 in the shallowest fields. The top left panel of Figure 3.1 shows that we can expect $-1 \lesssim i - K \lesssim 1$ for the stellar sequence, meaning that HSC counterparts of stars will begin to saturate at $K \lesssim 19$.

Figure 3.3 shows the fraction of objects which have a counterpart in the complementary PS1-i, g and r and unWISE-$W1$ datasets. This figure shows that on the whole, there are a higher fraction of objects with an r or i match than a g match. As mentioned above, this is part of the justification for choosing the $riJK$ criteria over the gJK. Approximately 15% of the Lockman field does not have PS1 r-band data, so we resort to the $J - K$ selection in these

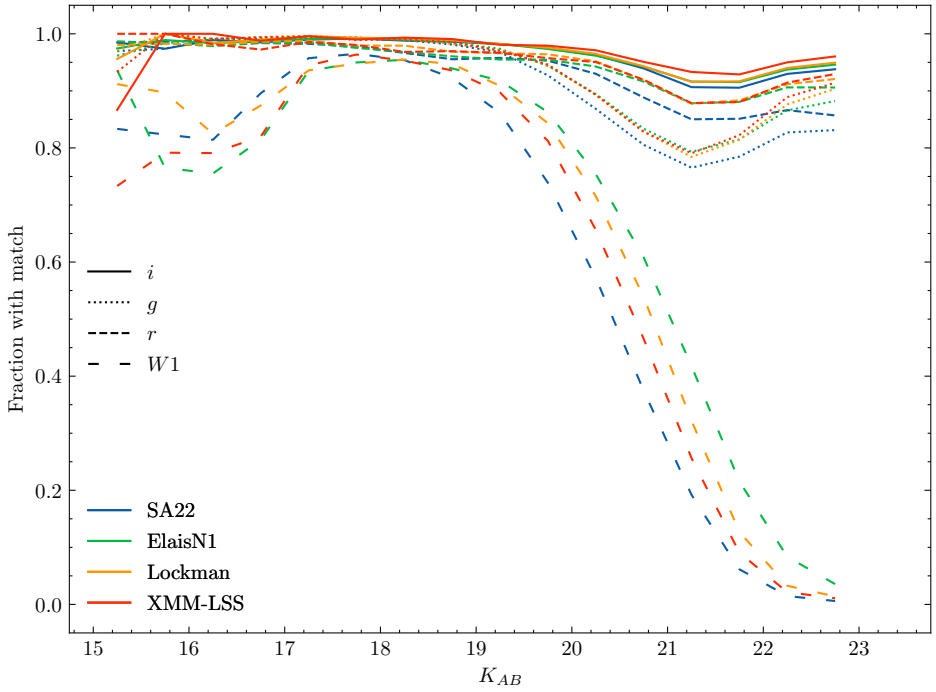

Figure 3.3: The fraction of objects which have a match in the four additional bands considered for star-galaxy separation. Solid lines, dotted lines, dashed lines and loosely dashed lines represent the fractions for i, g, r and $W1$ respectively, with the colours indicating the field. Note that $\sim 15\%$ of the Lockman field is missing r-band data.

areas.

To check that we are removing roughly the correct numbers of galactic stars, we compare number counts of rejected stars with *Gaia*. We use the colour transform equations from the *Gaia* DR2 documentation[1] (Gaia Collaboration et al., 2016) to calculate $G - K_s$ colours (and hence G magnitudes),

$$G - K = 0.23587 + 4.0548\,(J-K) - 2.5608\,(J-K)^2 + 2.2228\,(J-K)^3 - 0.54944\,(J-K)^4\,.$$

Number counts of galactic stars from DXS in this transformed *Gaia* G magnitude are shown in Figure 3.4. They are consistent with those from *Gaia* for $G > 18$ for each field (until the *Gaia* number counts fall off due to the limiting magnitude of $G \sim 21$). *Gaia* stars are selected from the *Gaia* DR2 database within a simple latitude & longitude box, approximately the R.A. and Dec limits of each DXS field. There is no consistency in number counts between fields due to the differing galactic latitude/longitude of each field.

[1] available from `https://gea.esac.esa.int/archive/documentation/GDR2/Data_processing/chap_cu5pho/sec_cu5pho_calibr/ssec_cu5pho_PhotTransf.html`, their Table 5.8.

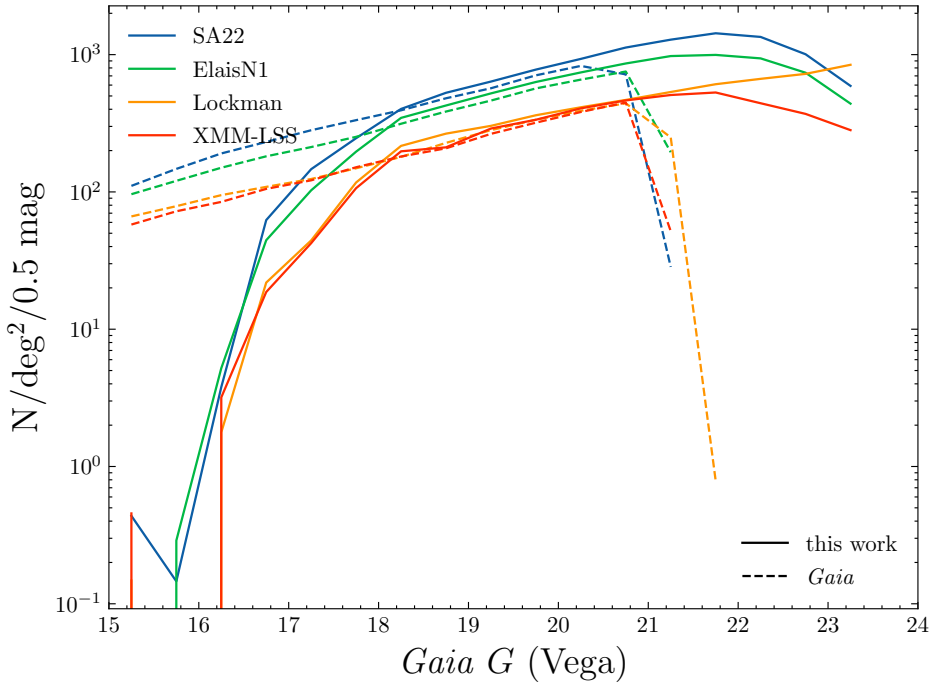

Figure 3.4: Comparing number of galactic stars with *Gaia* for each field, using the transformed *Gaia G*, described in the text. The limiting magnitude for *Gaia* is $G \sim 21$.

3.2 *K*-band galaxy number counts

Figure 3.5 shows the number counts of galaxies in half-magnitude bins (per square degree) after the rejection of galactic stars. We plot the number counts for each field in turn, and then the combination of the four fields. The lower panel shows the ratio of the number counts of galaxies from each of the individual fields to the combination of the four fields.

The uncertainties on these number counts are calculated as the quadrature sum of Poisson and jackknife estimates. Including the jackknife uncertainty estimates will help to account for spatial variation in galaxy selections: jackknife estimates are approximately a factor of two larger than the Poisson estimates at the bright end.

We further plot a number of literature results for comparison. Kim et al. (2014), who use a subset of the ElaisN1 data, show number counts which are very similar to our own. Further, we include the number counts from Davies et al. (2021), who discuss the input catalogue for the spectroscopic DEVILS survey (using VISTA-VIDEO; see Section 2.2), McCracken et al. (2010) who use VISTA data from the COSMOS field, and the joint UDS-HSC catalogue, all of which are deeper than our own DXS. At the bright end, we include number counts from Frith et al. (2003) who use the 2MASS North Galactic Cap ($K_s \lesssim 15.5$), and counts from DENIS (Mamon, 1998). Our number counts are concordant with those of Frith until $K \lesssim 14.0$.

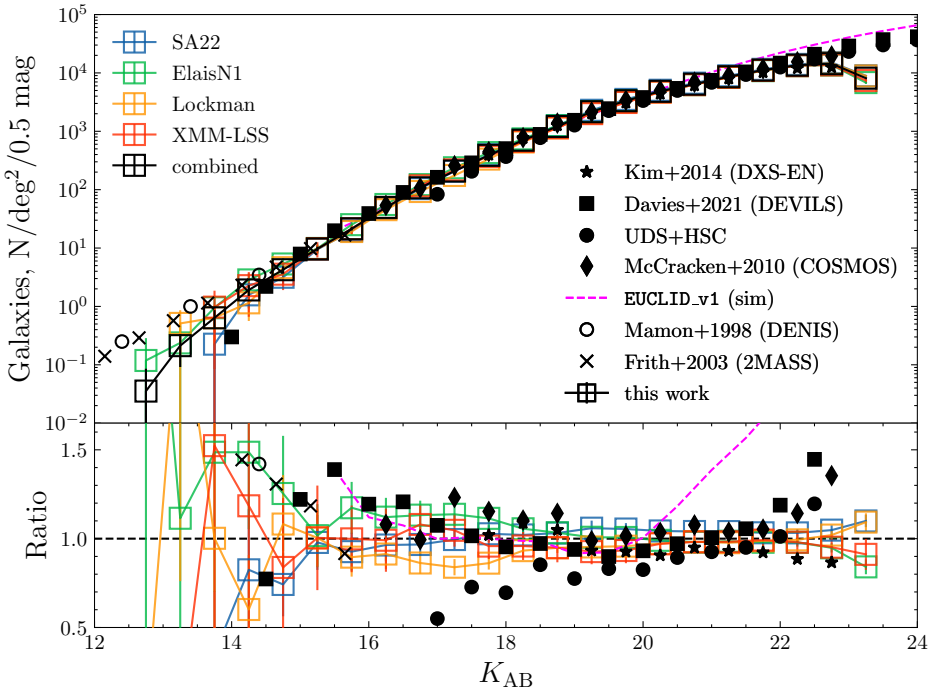

Figure 3.5: Galaxy number counts after removal of galactic stars using the $riJK$ criteria. The top panel shows the number counts in each field, and the combined result. Various values from the literature are also plotted. The lower panel shows the ratio with the combined four DXS fields for each of the (other) datasets in the top panel. This shows that the galaxy counts begin to deviate (significantly) from the much deeper datasets at $K \sim 21.7$.

At this magnitude, we measure around one galaxy per square degree. This corresponds to around 30 galaxies at this magnitude and brighter, so there is insufficient area with DXS to measure the counts of galaxies brighter than this. Coincidentally, this is the point the DXS imaging begins to saturate for stars. Only one of the points from the DENIS data is fainter than this bright limit (meaning that it is the only one of these DENIS points which is comparable fairly).

Finally, we include number counts estimates from a *Euclid* DEEP-type simulation, `EUCLID_v1`, produced using the semi-analytic model GALFORM (Merson et al., 2013; Gonzalez-Perez et al., 2014) produced for a *Euclid*-DEEP type survey[2] (~ 20 sq deg). The galaxy counts are shown as the dashed magenta line in both panels, although are effectively hidden until $K > 20$ where the the GALFORM counts exceed that of our own. We note that below $K_{\rm AB} < 20$, GALFORM agrees excellently with our number counts, and literature.

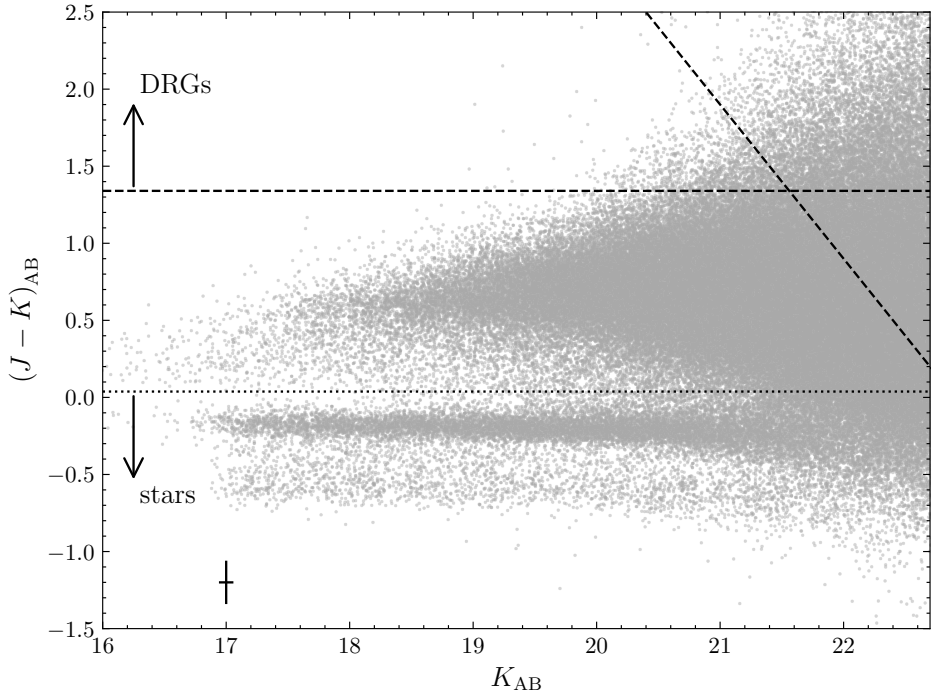

Figure 3.6: $J-K$ vs K for all objects $K < 22.7$. The diagonal dashed line is the J band limit $J_{\rm AB} < 23$. The cuts for DRGs, and galactic stars are also shown. The figure shows 5% of the total objects. The average error on $K_{\rm AB}$ and $J-K$ measurements in the interval $20.5 < K_{\rm AB} < 21.5$ (ie, the faintest DRGs in DXS) is indicated at coordinate (17, -1.2).

3.3 Distant red galaxies (DRGs)

We select DRGs using $(J-K)_{\rm AB} > 1.34$ criteria, corresponding to the well-used $(J-K)_{\rm Vega} > 2.3$, as shown in Figure 3.6. The completeness tests in Figure 2.15 show that we should use $J < 22.9$ (at which all of the tiles are far above 90% complete), meaning that we should not select DRGs fainter than $K = 21.5$ which is well inside the K band completeness limit. This is also the J limit that Kim et al. (2011) use. Figure 3.6 also demonstrates the effectiveness of simple $J-K$ star-galaxy separation technique at bright K magnitudes; the stellar sequence is quite well-separated to at least $K \sim 20$. The DRG selection does not rely on any of the matched optical data. As mentioned in Section 3.1, as not all of the JK area is covered by (any) optical data, meaning that we must rely on the simple $J-K$ criteria to reject stars. However, we are not overly concerned about this, as the blue galaxies that may be rejected are by definition not DRGs.

Figure 3.7 presents our number counts for DRGs, with uncertainties computed as the quadrature sum of the Poisson and jackknife estimates. The four individual fields are consistent with

[2]Provided by (Baugh, 2021, priv. comm.)

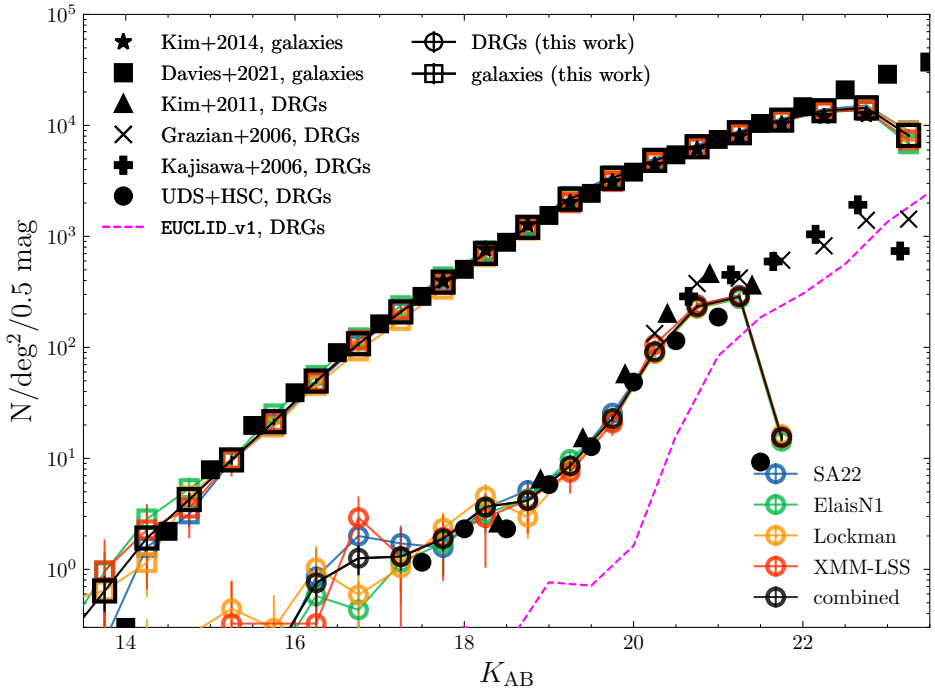

Figure 3.7: Differential number counts of DRGs ($(J-K)_{AB} > 1.34$ selected), with $J_{AB} < 23$. Number counts of literature of objects are also plotted Kajisawa et al. (2006), Grazian et al. (2006), and Kim et al. (2011), with N=91, N=179, and N=3414 detections respectively, compared to our 20130 DRGs in all four fields. Number counts of all galaxies (and a subset of counts from other studies) are plotted for reference. Error bars are calculated as $\sqrt{N}$/area. Coloured lines are number counts from each field, black lines are number counts of the combined 28 deg^2. The dashed magenta line shows DRG counts as estimated by GALFORM.

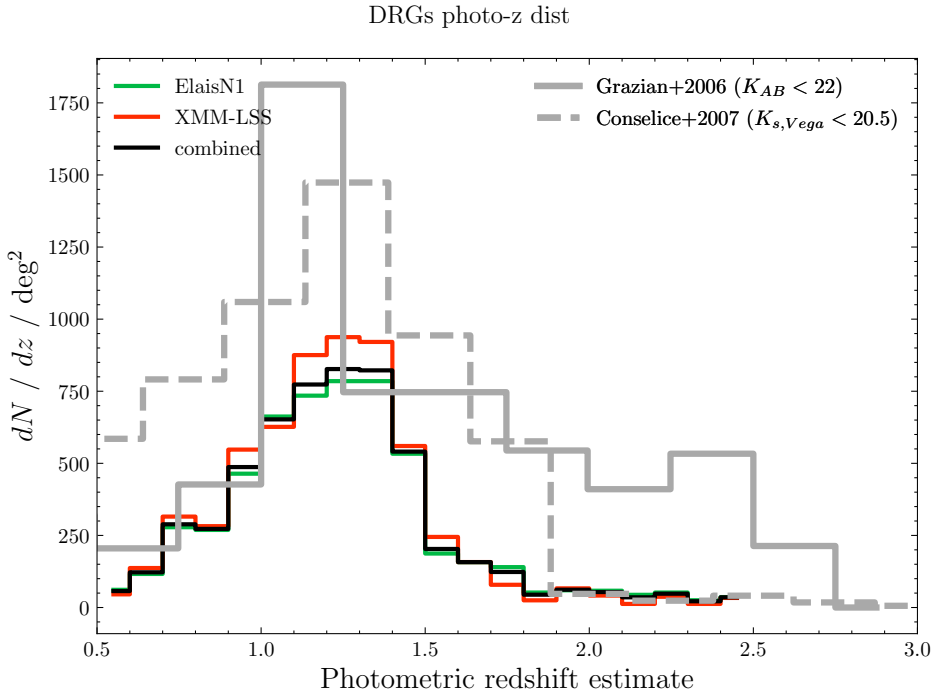

Figure 3.8: Distribution of photometric redshifts of DRGs ($J - K > 1.34$ selected galaxies) with $K_{\mathrm{AB}} < 21.9$ from `EAZY`, using the DXS-HSC-SWIRE catalogue (meaning only two of the four fields are present). Also shown are the distributions from Grazian et al. (2006, 2007), and Conselice et al. (2007).

each other at all magnitudes. At $18 < K < 21$, our DRG number counts are consistent with previous studies. We show Kim et al. (2011), who use a subset of the SA22 DXS data (tiles 1-4), and Kajisawa et al. (2006), which presents much deeper, but narrow (24 arcmin^2) observations, and Grazian et al. (2006) from the GOODS-MUSIC sample, covering 135 arcmin^2. Although the number counts of Kajisawa et al. (2006) and Grazian et al. (2006) extend to much deeper magnitudes, the area over which we select DRGs is significantly larger; they select $N = 91$ and $N = 179$ DRGs respectively, compared to Kim et al. (2011)'s $N = 3414$ DRGs, and the $N = 20130$ we detect. As expected, the our number counts of DRGs drop off at $K \sim 21.5$, due to the J limit. We also present the number counts of DRGs from the UDS field, using the UDS DR11 catalogue. The DRG counts from GALFORM are significantly lower than literature counts, until $K \sim 23$. In their discussion on EROs, a similar D_{4000}-break selection population (see Section 3.4), Gonzalez-Perez et al. (2014) expect that the discrepancy could arise due to gas depletion timescales: the relatively slow gas depletion timescale implemented in this model allows for residual star formation to later times, resulting in less red galaxies. Number counts of all galaxies are shown, for comparison with other selections.

We also plot the distribution of photometric redshifts in Figure 3.8, along with distributions from literature. The fact that the vast majority of DRG galaxies appear at redshifts below

$z = 1.8$ is at first alarming, given that this selection is designed to select galaxies at $z > 2$. However, Grazian et al. (2006) and Conselice et al. (2007) both show that the redshift distribution for DRGs extends down to intermediate redshifts at brighter magnitudes (they present distributions for $K_{s,\mathrm{AB}} < 22$ and $K_{s,\mathrm{AB}} = 22.4$ respectively), and that the high redshift samples of DRGs are only selected with the faintest magnitudes. The redshift distribution for Grazian et al. (2006) appears to reach higher magnitudes than our sample, even though the data presented is for a shallower K selection. This can be explained when considering the J-band data: their J-band cut from the GOODS-MUSIC sample is $J_{\mathrm{AB}} < 26.8$ for a signal-to-noise ratio of 1, compared to our much shallower $J_{\mathrm{AB}} < 22.9$.

3.4 Extremely red objects (EROs)

To select EROs, we will primarily use a colour cut of $(i - K)_{\mathrm{AB}} > 2.45$, equivalent to the widely-used $(I - K)_{\mathrm{Vega}} > 4$, although there will be some discussion in later chapters of using redder selection criteria. Kim et al. (2014) calculate that there is a 0.1 mag difference between PS1 and HSC i-band magnitudes for EROs, so we will also use this offset, meaning that for HSC-selected EROs, the equivalent colour cut is $i - K < 2.55$ - although, for clarity, we will refer to this as the $i - K > 2.45$ sample.

Figures 3.9 and 3.10 shows $i - K$ vs. K colour magnitude diagrams for the DXS-PS1 and DXS-HSC catalogues. Because we have two optical data sets, DXS-PS1 and DXS-HSC, we present colour-magnitude diagrams for both, showing the ERO selection criteria, and the i magnitude limits. Figure 3.9 shows that shallow i-band data (or an overly-restrictive magnitude cut) can also restrict the sample in K, too; note that the diagonal i restriction crosses the $i - K$ ERO criteria at $K \sim 22.5$ The limiting K band magnitude has here been reduced to 22.6, which is only a very minor change. However, for surveys such as SHARKS (which will also reach $K \sim 22.7$), using DES as the complimentary optical dataset will have an i limit of 23.5 mag (Abbott et al., 2018), meaning that EROs can effectively only be selected to $K \sim 21.1$. However, one of the advantages of SHARKS is the 10 times increase in area over DXS, meaning that SHARKS will have significantly improved statistics at the brightest magnitudes, which DXS is able to constrain as well - similar to DXS' relationship to the GOODS-MUSIC sample of DRGs.

Figures 3.11 and 3.12 show number counts of the selected EROs for the DXS-PS1 and DXS-HSC catalogues, and all galaxies, as a function of K-band total (Kron) magnitude. From

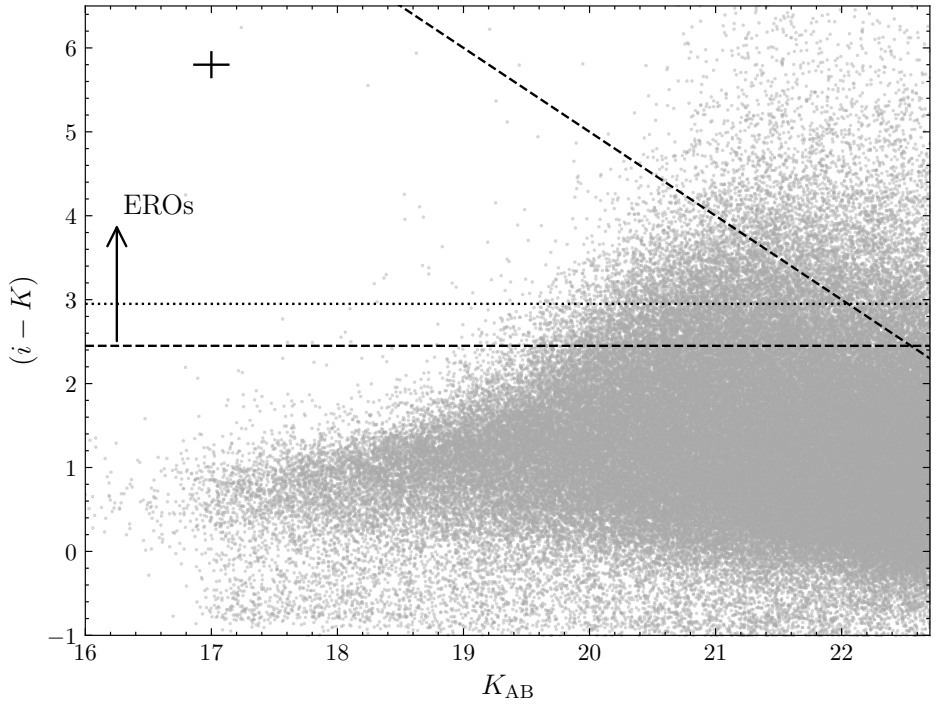

Figure 3.9: The horizontal dashed and dotted lines show colour cuts of $i - K > 2.45$ and a further suggested cut of $i - K > 2.95$ respectively. The diagonal line represents the i band depth, $i < 25$ for PS1. The right edge of the panel is $K = 22.7$, the limit of our survey. The average error on $K_{\rm AB}$ and $i - K$ measurements in the interval $22 < K_{\rm AB} < 22.7$ (ie, the faintest EROs in DXS) is indicated at coordinate (17, 5.8).

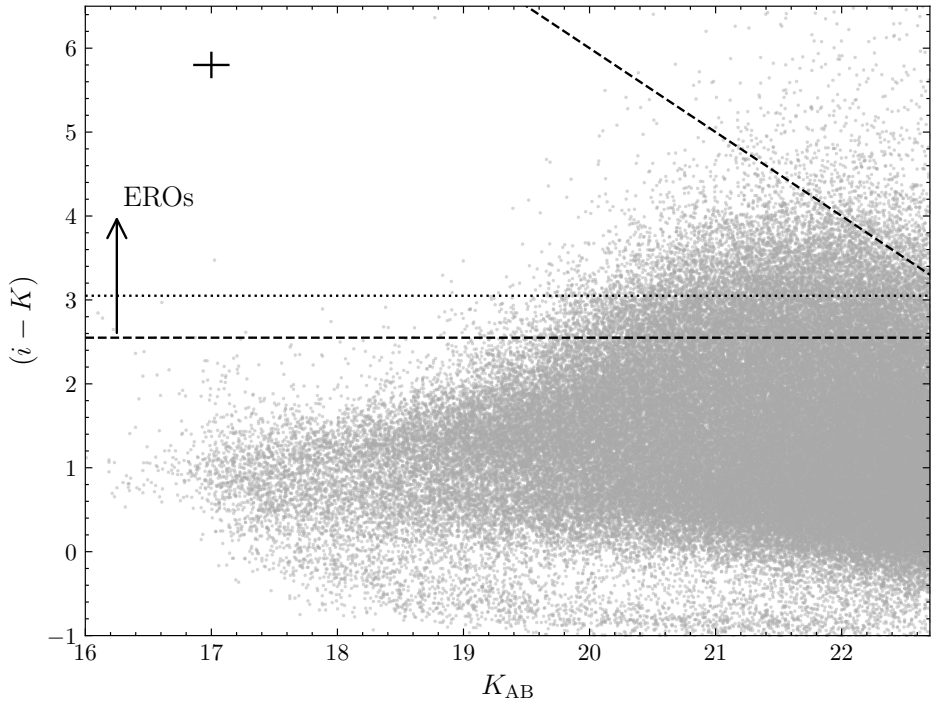

Figure 3.10: EROs with HSC-i. Horizontal lines show the ERO criteria of $i - K > 2.55$, and a further suggested cut of $i - K > 3.05$. The diagonal line represents the i band depth, $i < 26$. The average error on $K_{\rm AB}$ and $i - K$ measurements in the interval $22 < K_{\rm AB} < 22.7$ (ie, the faintest EROs in DXS) is indicated at coordinate (17, 5.8).

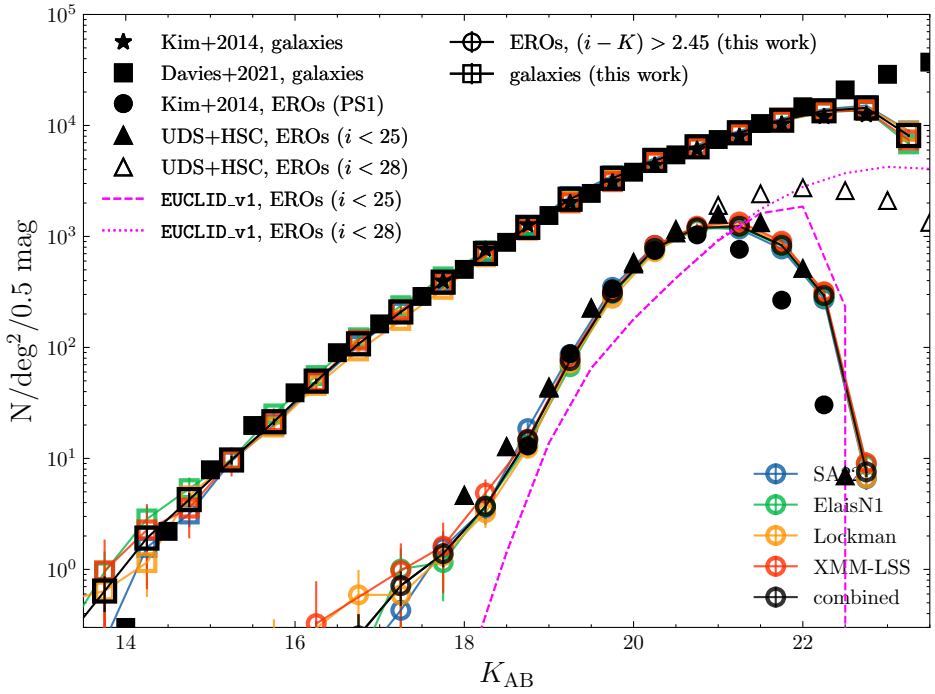

Figure 3.11: The number counts for PS1-selected EROs with $i - K > 2.45$ are the solid lines, and all galaxies are dashed lines. Coloured lines show individual fields, and black lines are combined counts (for both EROs and galaxies). Poisson error bars are shown ($\sqrt{N}$/area). Number counts from the UDS-HSC catalogue are also shown in each panel, using the same $i < 25$ cut as the DXS-PS1 selection.

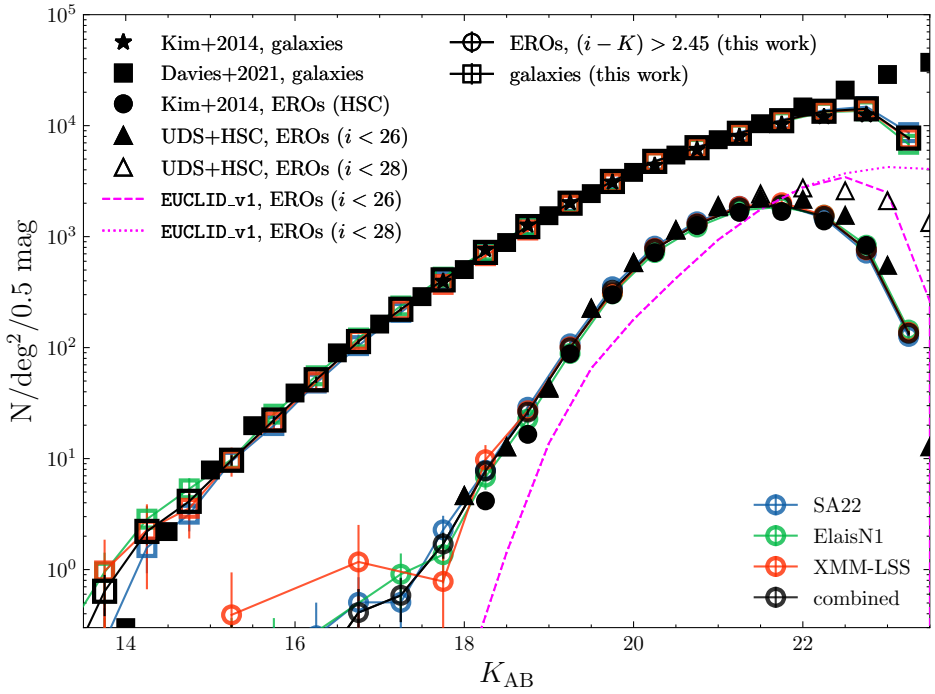

Figure 3.12: The number counts for HSC-selected EROs with $i - K > 2.45$ are the solid lines, and all galaxies are dashed lines. Coloured lines show individual fields, and black lines are combined counts (for both EROs and galaxies).Poisson error bars are shown ($\sqrt{N}$/area). Number counts from the UDS-HSC catalogue are also shown in each panel, using the same $i < 26$ cut as the DXS-HSC selection, and the full depth of $i < 28$.

the regions of the four fields which have PS1 data, we select 111058 DXS-PS1 EROs with total magnitude $K_{\rm AB} < 22.7$. From the three DXS-HSC fields, we select a total of 119695 EROs $K_{\rm AB} < 22.7$, a slightly larger number than the DXS-PS1 EROs from all four fields. Number counts of EROs are consistent between fields (within error bars), and are consistent with previous works at $K_{\rm AB} < 21$. As demonstrated by the colour-magnitude diagrams in Figure 3.10 and the number counts, the increase in the depth of the optical by only 1 mag has a significant impact on the number of objects which can be selected. However, moving to the extreme optical depth available in the UDS field ($i < 28$ - a two magnitude increase in depth), we observe that the increased number counts measurable at the depths our survey is complete to does not increase as dramatically. This indicates that there are diminishing returns for increasing the depth of a complimentary optical survey for a fixed depth NIR survey.

Further, the galaxies we select with our $i < 26$ sample means our galaxy sample is very close to complete at the point at which the UDS counts begin to turn over: this turnover is no longer simply a systematic effect of the depth of the optical counterpart, but represents knee of the ERO luminosity function (in the redshift interval that EROs are selected). Reading this peak at $K \sim 22.25$, and using a median redshift of $z \sim 1.3$ (from Figure 3.13b) to estimate the distance modulus gives a very crude estimate that the turnover in the ERO luminosity function should occur somewhere around $M^*_K \sim -22.8$ for the whole sample. We are unable to compute this value for the DRG selection, and later gzK selections, as these samples are not complete in terms of their redshift: they are designed to select galaxies primarily at redshifts greater than DXS observes.

We also (for both the DXS-PS1 and DXS-HSC samples) plot the number counts from the UDS-HSC data, using the appropriate i band cut. The DXS-PS1 and UDS-HSC samples which both use $i < 25.0$ are consistent, but show more EROs than Kim et al. (2014)'s PS1 sample selected with this same i cut. Similarly, the UDS-HSC and DXS-HSC samples which both use $i < 26$ are consistent. Kim et al. (2014) show that the slight differences between the HSC and PS1 i band filters mean that a DXS-PS1 colour of $i - K > 2.45$ is equivalent to $i - K > 2.55$ with DXS-HSC data. Finally, we plot the ERO counts for GALFORM. As with the DRG passive selection, GALFORM under predicts the number of EROs at bright magnitudes. In their work, Gonzalez-Perez et al. (2014) explicitly compute the number counts of EROs, and also point out that their number counts are mismatched especially for the least extreme $R - K$ cuts they consider, equivalent to those we present. They postulate that "uncertainties in the treatment of dust attenuation might also be partially responsible" for

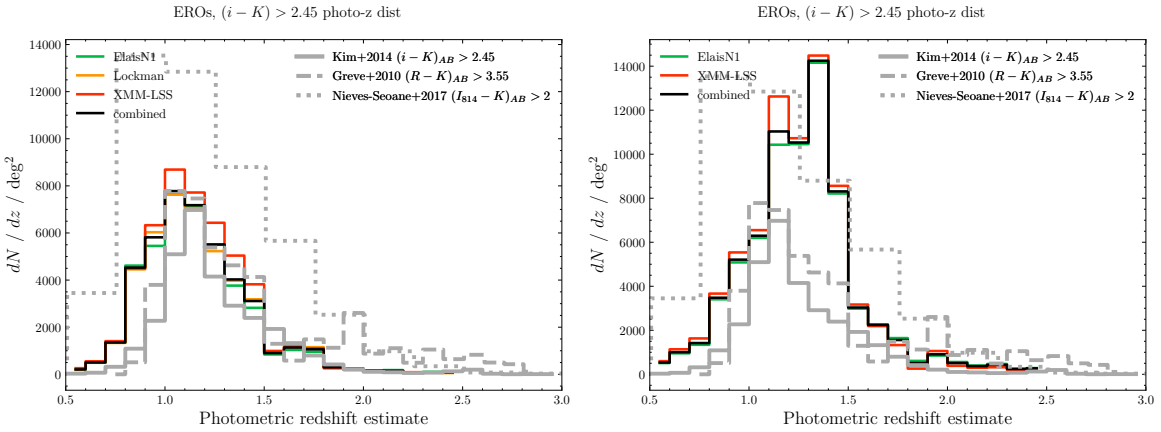

(a) EROs with PS1-i (b) EROs with HSC-i

Figure 3.13: Distribution of photometric redshifts from EROs ($i - K > 2.45$) using `EAZY`. Distributions are shown for both the DXS-PS1-SWIRE (left panel) and DXS-HSC-SWIRE (right panel) catalogues. Distributions from Kim et al. (2014)'s DXS-PS1-SWIRE catalogue and Nieves-Seoane et al. (2017)'s ALHAMBRA-K_s catalogues are also shown.

the discrepancy, although we expect that this is the less likely explanation given the strong agreement in number counts between fields.

Redshift distributions for our ERO selections are presented in Figure 3.13. For the DXS-PS1-SWIRE sample, the redshift distribution peaks at $z \sim 1.1$. As expected, there are more galaxies at high redshifts for the DXS-HSC-SWIRE sample, due to the increased number counts which include galaxies with fainter i-component. The ERO redshift distribution from Kim et al. (2014)'s DXS-PS1-SWIRE sample is lower than ours, but this again can be explained by comparing their number counts of EROs to ours (see Figure 3.11) - theirs are lower than ours at the faintest magnitudes. Finally, the distribution from Nieves-Seoane et al. (2017) peaks at a lower redshift than ours, because of the slightly bluer selection criteria ($I_{814} - K > 2$ compared to our $i - K > 2.45$). There is a similar normalisation at the highest redshifts DXS measures.

3.4.1 ERO populations

To further classify EROs, we can use the criteria introduced by Pozzetti & Mannucci (2000), and modified and demonstrated by Fang et al. (2009) and Kim et al. (2011) to separate EROs into DG-EROs (dusty star-forming galaxies) and OG-EROs (old, passively evolving galaxies),

$$(J - K) = 0.2(i - K) + 0.42$$

(after converting from Vega to AB).

In a similar manner to BzK, this selection attempts to break this degeneracy by selecting a strong red colour combined with a second and relatively blue in a Balmer or D_{4000} break galaxy, compared with two moderately red colours in a dusty star-forming galaxy. This means that, perhaps counter-intuitively, the dusty star-forming galaxies appear as the reddest in both colours in this selection.

To compensate for the slightly different bands, we use a small modification to the criteria presented in Fang et al. (2009).

$$(J - K) = 0.2\,(i - K) + 0.48. \tag{3.4.1}$$

Figure 3.14 shows this criteria separating EROs into the two populations, selected using the HSC i-band data. The main panel of this figure shows the colour-colour diagram. We present this with $J - K$ on the horizontal axis and $i - K$ on the vertical axis for comparison with the Figures shown in Pozzetti & Mannucci (2000), Fang et al. (2009, their Figure 5) and Kim et al. (2011, their Figure 12).

The dotted vertical line in the main panel is the DRG criteria. This suggests that the low redshift DRGs that we select are predominantly dusty star-forming galaxies, rather than the galaxies with significantly evolved populations which are expected at $2 < z < 3$ when the D_{4000} break appears between the J and K bands.

The auxiliary panels show the distributions of both of the $i - K$ and $J - K$ colours for each of the two populations. The dashed black line in the lower panel is the $J - K$ distribution of all galaxies, and the solid black line for EROs. We do not plot the $i - K$ distribution of EROs in the right panel; by definition, all galaxies with this colour are EROs. Similarly, the these distributions show that the $J - K$ colour for the two populations is significantly different compared to the $i - K$ distributions which appear to change only in normalisation. This argument is circular in that the distributions of colour are determined entirely by geometry of the criteria in colour-colour space. However, the criteria is physically motivated, so these distributions do still give some insight into the colours of the populations.

At $K \sim 21$, the limits of $i \sim 26$ and $J \sim 22.9$ imply that the reddest we are able to (reliably) select these populations is $i - K < 4.5$ and $J - K < 1.9$, which, at which the distributions of these colours in Figure 3.14 are not significant. Because they require the redder $J - K$ colour for selection, the DG-ERO population will suffer from the $J - K$ incompleteness more than the OG-EROs.

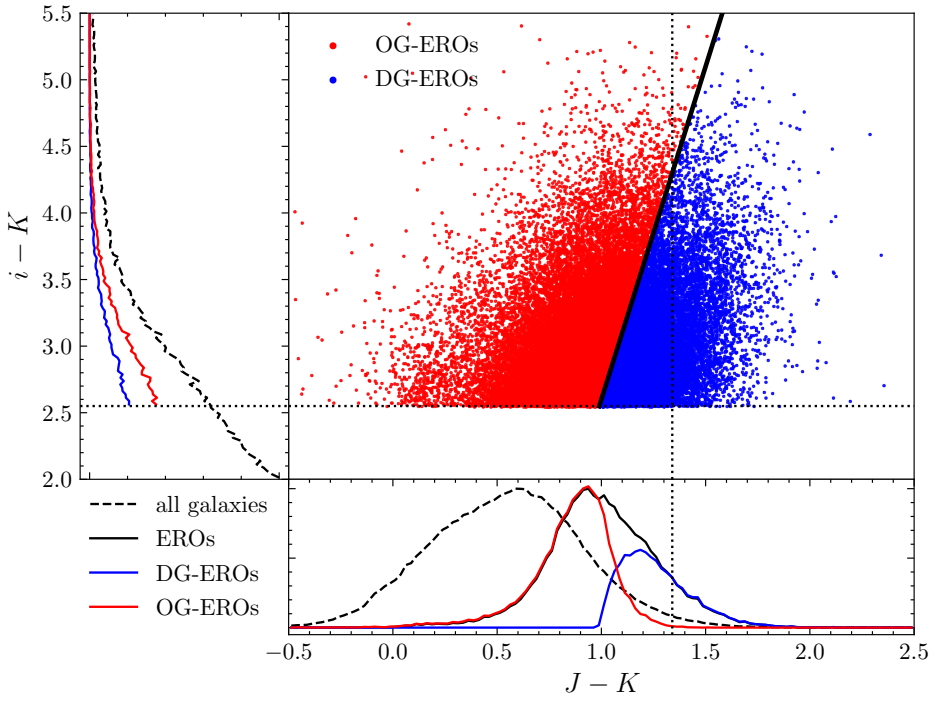

Figure 3.14: Discriminating between old, passively evolving (OG-EROs, red) and dusty, star-forming (DG-EROs, blue) populations of EROs using additional $J - K$ information. The lower and left narrow panels show the distributions of colours for each of these populations. The distribution of $J - K$ for all galaxies is also shown, normalised so that it is the same height as the ERO distribution. The horizontal and vertical dotted lines are the definitions of EROs and DRGs, respectively. All EROs with $K < 22.7$ which also meet the i and J cuts are shown, although the samples will *not* be complete to this limit. The solid black line is the ERO population criteria, Equation 3.4.1.

Using the data from all three fields with HSC data, we detect 35923 OG-EROs and 28209 DG-EROs with $K < 21.5$, meaning that 44% of EROs selected at this magnitude are DG-EROs. For EROs $K < 20.7$, 40% of our sample are DG-EROs, compared with the 43% reported by Kim et al. (2011) with similar $i - K$ colours.

We also note that the separation of these two populations is quite delicate: McCarthy (2004) point out that the redshift evolution of the two tracks representing evolved and dusty galaxies in Pozzetti & Mannucci (2000) appear very closely to the dividing line, meaning that the error in photometry becomes quite important. Figure 2.10 shows that the average error in K-band magnitude reaches around 0.1 at $K \sim 21.5$. This line of argument is further justification for truncating the study of these populations at this magnitude. It is also apparent from the ERO $J - K$ distribution that there is no obvious or visible separation between the two populations as there is in eg. the (restframe) $B - V$ vs. B or UVJ diagrams.

In Figure 3.15 we present similar data to that shown in Figure 3.14, but now showing only objects whose i or J (or both) detections are beyond the quoted depths at which the catalogues have acceptable completeness. The objects with only one "untrustworthy" detection (eg. the magenta or cyan points) scatter in the expected directions - poor i band detections are for the reddest $i - K$ objects and poor J detections are the reddest $J - K$ galaxies. We note also that the untrustworthy i detections reach bluer $J - K$ colours; the stellar sequence is separated again visible in this data. There are fewer of these objects than the other two, as the i-band data in this figure are all bonafide detections from the HSC pipeline which are then cross-matched to the K band catalogues, whereas the J detections are estimated using forced photometry from the K-band catalogues. The sharp cutoff in these points (more clear in the left and right lower panels of Figure 3.15) corresponds to replacing the i and J in these two colours with a fixed depth value, giving the straight line $i - K = J - K + 3.3$.

The grey points (objects which have reliable detections in either i or J) are most likely the faintest objects in K. If we were to present only upper limits, all of the grey points would lie on the line $i - K = J - K + 3.3$.

3.5 *BzK* galaxies

The BzK criteria in Daddi et al. (2004) are $(z - K)_{\rm AB} - (B - z) \geq 0.2$ for star-forming galaxies, and $(z - K)_{\rm AB} - (B - z) < 0.2 \cap (z - K)_{\rm AB} > 2.5$ for passively-evolving galaxies.

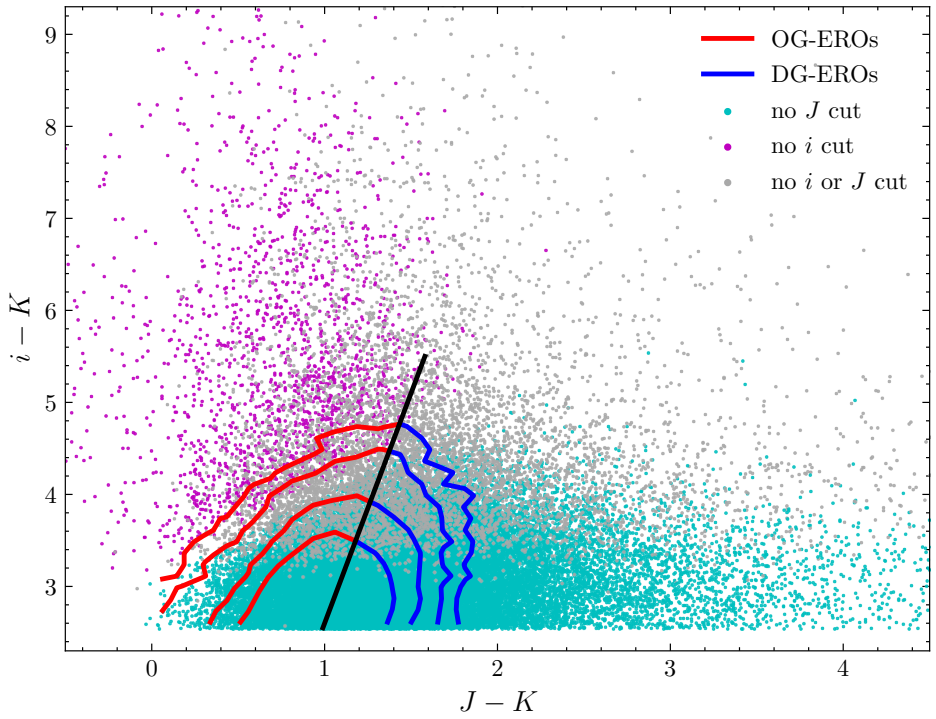

(a) Selection of ERO populations with untrustworthy detections in J (magenta), i (in cyan) and both i and J (in grey).

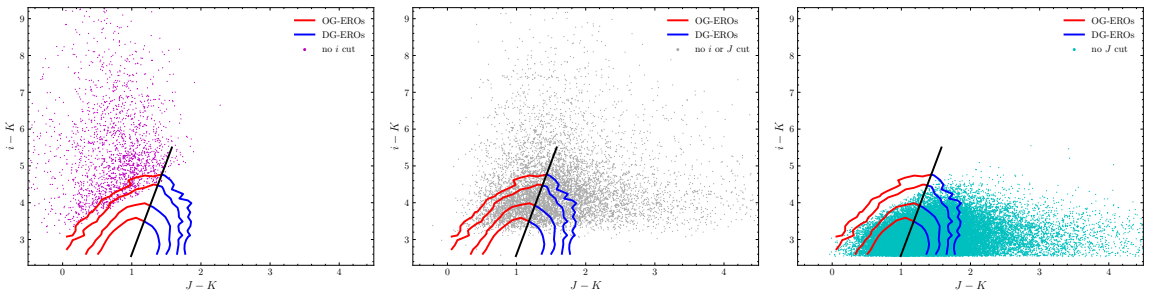

(b) Untrustworthy i (c) Untrustworthy i and J (d) Untrustworthy J

Figure 3.15: Selection of ERO populations with untrustworthy detections in i, J and both i and J data (magenta, cyan and grey). Note that all i data are bonafide detections from the HSC-selection which are then crossmatched to the K positions, whereas J data are forced photometry from K apertures. Contours show the extent of the populations OG- and DG-ERO populations as shown in Figure 3.14. The separating criteria is again shown as the black line.

.

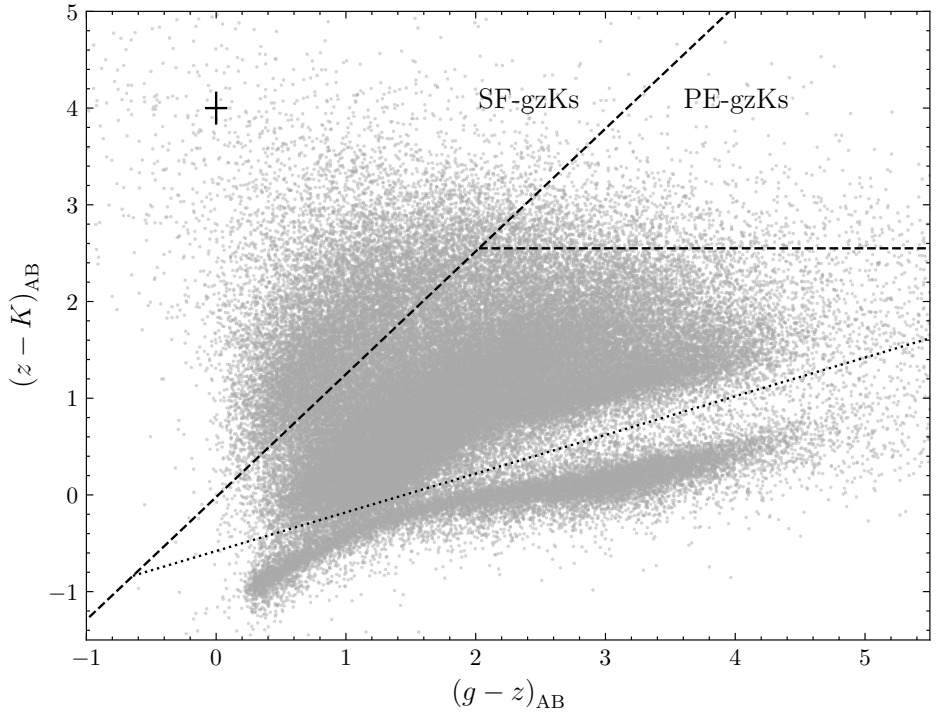

Figure 3.16: $g-z$ vs. $z-K$ colour-colour diagram using DXS-HSC catalogues. PE-gzK and SF-gzK selection criteria are shown as dashed lines. A further star-galaxy separation criteria is also shown as the dotted line. The average error on $g-z$ and $z-K$ measurements in the interval $22 < K_{\rm AB} < 22.7$ (ie, the faintest gzKs in DXS) is indicated at coordinate (0, 4).

We select gzK galaxies using the gzK criteria in Arcila-Osejo & Sawicki (2013) and Arcila-Osejo et al. (2019), which aim to select the same populations of star-forming and passively evolving galaxies as Daddi et al. (2004)'s selection of BzK galaxies, but with slight transformations to their equations to account for the difference between Johnson-Cousins B and z bands and SDSS/PS1 g and z bands. Their modified criteria are

$$(z-K)_{\rm AB} - 1.27\,(g-z) \geq -0.022 \tag{3.5.1}$$

for star-forming galaxies ("SF-gzKs"), and

$$(z-K)_{\rm AB} - 1.27\,(g-z) < -0.022 \quad \cap \quad (z-K)_{\rm AB} > 2.55 \tag{3.5.2}$$

for passively-evolving galaxies ("PE-gzKs"). These criteria are both shown in Figure 3.16.

Number counts of star-forming gzKs are shown in Figure 3.17, and passively-evolving gzKs in Figure 3.18. In each panel we also present number counts from the (much deeper) UDS-HSC catalogue. We use the HSC limits of $g < 26.6$ and $z < 26.3$ for the SF-gzK selection. For the PE-gzKs, we use the same $z < 26.3$ limit, but require only a g-band detection. We feel that this is a reasonable approach to maximising the number of PE-gzKs that we select from our

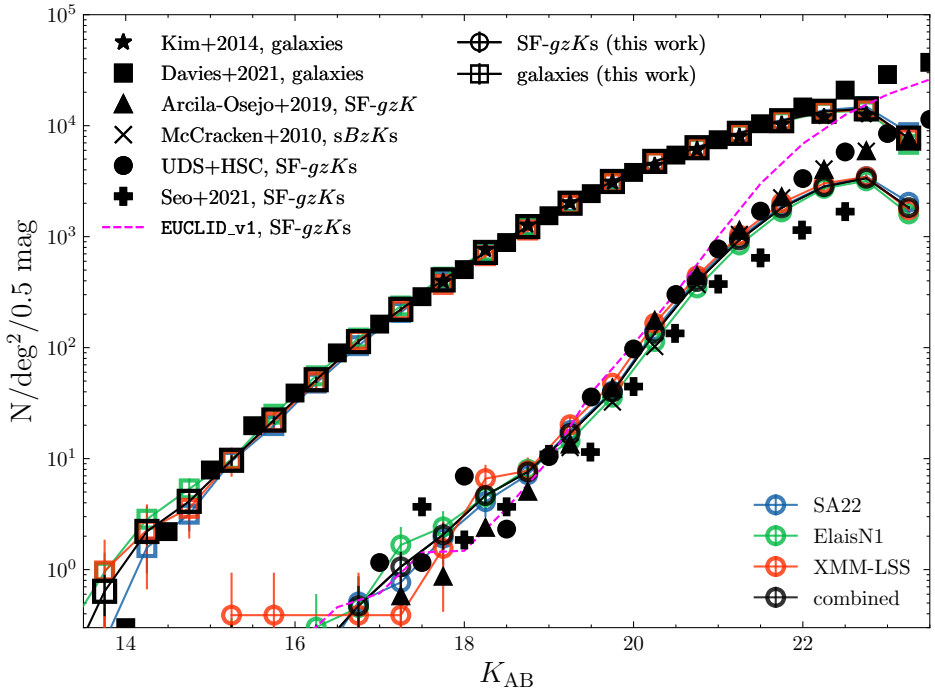

Figure 3.17: Differential number counts of all galaxies and star-forming gzKs in each field from the DXS-HSC catalogues. Number counts from the UDS-HSC catalogue are also shown.

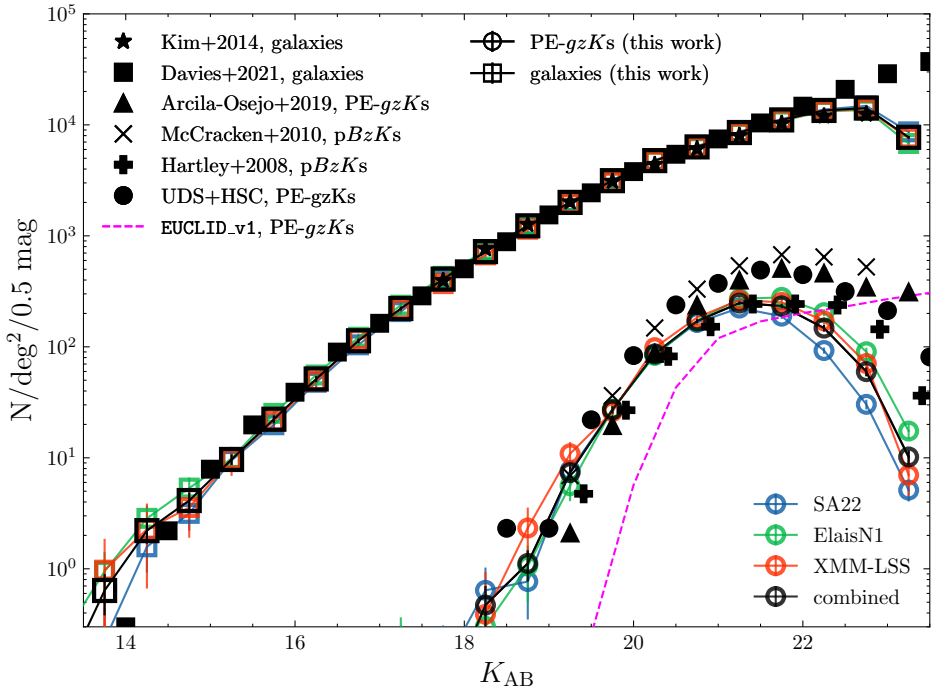

Figure 3.18: Differential number counts of all galaxies and passively evolving gzKs from the DXS-HSC catalogues. Number counts from the UDS-HSC catalogue are also shown.

catalogues, as the selection of these galaxies requires only that the $g-z$ limit is more red than the criteria; the actual value is less important. Firstly, this is still a requirement of a detection in the z-band within the detection limit, and also the HSC photometry is performed such that aperture fluxes are measured from a detection with a higher signal-to-noise ratio ($irzyg$, in order of preference). We select 127948 SF-gzKs from the three DXS-HSC fields with $K < 22.7$. Unlike with our UDS-HSC ERO selection, we have not included any additional cuts for direct comparison with the DXS-HSC catalogues, but include all the data to the quoted UDS $K_{\rm AB} < 25$ depth for comparison with previous deeper works (McCracken et al., 2010; Arcila-Osejo et al., 2019). This demonstrates that Equations 3.5.1 and 3.5.2 are effective at selecting the same objects despite the small differences in WFCAM-K and WIRCAM-K_s filters, and HSC-gz and Megacam-$g'z'$ filters. The number counts of GALFORM are again shown as the magenta dashed line. As with the sBzK counts presented from GALFORM in Merson et al. (2013), they agree well with other literature measurements and our own, although begin to over-predict at the faintest magnitudes, which Merson comment could simply be incompleteness in the observed sBzKs.

As in previous studies, the selection of the passively-evolving galaxies is limited by the depth of the optical g-band data (see Section 1.4.3). For this reason, we will not present number counts of gzKs for the DXS-PS1 catalogues, only the DXS-HSC catalogues. We do not have H data sufficient to attempt the separation of SF-gzKs and PE-gzKs in the manner that Arcila-Osejo & Sawicki (2013) demonstrate. However, the number counts presented in Figures 3.17 and 3.18 show that our selections of galaxies are still very comparable with the un-modified gzK selection and the original BzK selection for the star-forming sample. They are incomplete for the passive sample at $K > 21.5$ compared with literature studies, however. Figure 3.18 further shows that the number counts of the passive sample are lower for the SA22 field than for ElaisN1 and XMM-LSS. This can be explained by the slightly shallower depth of the HSC optical data (SA22 is in the HSC wide component). Knowing from Equations 3.5.2 and 3.5.1 that the bluest a galaxy can be and classified as a PE-gzK is $z-K = 2.55$ and $g-z \sim 1.95$, a galaxy at $K \sim 22$ would have to be $g \sim 26.5$, which is approaching the 5σ point source depth for the Wide fields. In total, we select 16252 PE-gzKs from the three DXS-HSC fields, although this figure is not as representative of the density as the previously quoted values for DRGs and EROs given the difference in differential number counts between fields. From the two fields with the more consistent number counts (XMM-LSS and ElaisN1), we select 9921. McCracken et al. (2010) also use a sophisticated postage-stamp stacking approach to estimating $B-z$ flux upper limits for missing B detections, which we do not attempt. The

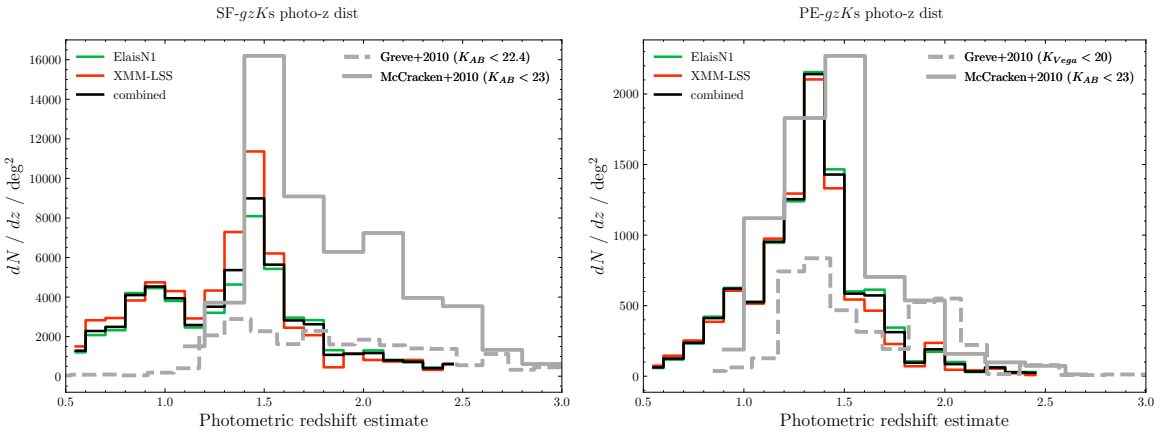

(a) SF-gzKs (b) PE-gzKs

Figure 3.19: Photometric redshift distributions for EROs, using the DXS-PS1-SWIRE (left panel) and DXS-HSC-SWIRE (right panel) catalogues. Distributions from Greve et al. (2010) and McCracken et al. (2010) are also shown.

number counts from GALFORM for PE-gzKs behave similarly to the earlier passive selections: under-predicting at the brightest magnitudes. Here, we plot the gzK selection, rather than the pBzK in Merson. Although they continue to increase, at the faintest magnitudes we show, the counts do agree more with the counts which exhibit a less extreme turnover (eg. McCracken et al., 2010; Arcila-Osejo & Sawicki, 2013).

Finally, we present the redshift distributions from `EAZY` for both of the gzK selections using the DXS-HSC-SWIRE catalogues in Figure 3.19. For each, we also plot the redshift distribution from Greve et al. (2010)'s sample which is limited to $K_{\rm Vega} < 20$, which is equvalent to $K_{\rm AB} < 21.9$. The BzK selection is designed to select galaxies primarily with $1.4 < z < 2.5$, and our redshift distributions show a significant peak at $z \sim 1.4$ and drop off towards the expected maximum redshift with DXS ($z \sim 1.5$).

3.6 Selection comparison

Figures 3.20 and 3.21 summarise the galaxy selections made in this chapter: EROs, DRGs, and $gzKs$.

Note that the here we present $i - K$ on the horizontal axis and $J - K$ on the vertical axis (the reverse of Figure 3.14) for comparison with Greve et al. (2010, their Figure 1), and so that the stellar sequence appears similarly to Figure 3.16.

All objects $K_{\rm AB} < 21.5$ (the DRG limiting magnitude) are included in these figures, from the HSC-DXS catalogues in the ElaisN1 and XMM-LSS fields. We do not include SA22 in

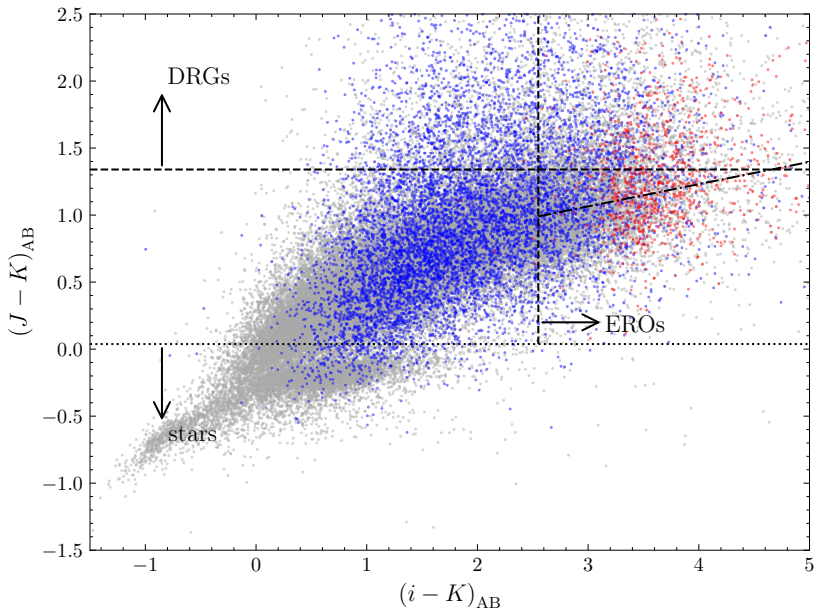

Figure 3.20: $i-K$ vs. $J-K$ from the DXS-HSC data. The dot-dashed diagonal line shows the OG/DG ERO separation. PE-gzKs are also plotted in red, and SF-gzKs in blue. Dashed horizontal and vertical lines show DRG and ERO selection respectively. The dot-dash diagonal line shows the OG- and DG-ERO separation, with DGs appearing above this line, and OGs below it.

Figure 3.21: Overlap of objects which are selected as combinations of DRGs, EROs, and BzKs. Diagrams are constructed using the ElaisN1 and XMM-LSS fields, including all sources $K < 21.5$ (the limit of the DRG selection).

these figures, as any comparisons made for PE-gzKs would be incorrect due to the reduced number counts in this field. EROs and DRGs are represented by their respective colour cuts made in this plane, with SF-gzKs and PE-gzKs highlighted in blue and red respectively.

In the Venn diagrams, we plot only objects who appear in the footprint of the $gizJK$ imaging, so that no objects are not selected due to their missing imaging.

There is significant overlap between EROs and DRGs; we find that 4417 of our 5781 DRGs are also selected as EROs (76%). Lane et al. (2007) show a similar 75% (249 of 330) in a similar comparison in their Figure 4, with a limiting $K_{\rm AB} < 21.2$, with ERO criteria $(R-K)_{\rm Vega} > 5.3$. At $K_{\rm AB} < 21.9$, however, Greve et al. (2010) report a value of 50.2%.

As they have strong red colours by definition, gzKs mostly appear at the reddest end of the galaxy sequence in both $i-K$ and $J-K$ (although SF-gzKs do scatter down towards the bluer end).

In absolute terms, more SF-gzKs are selected as EROs than PE-gzKs, but corresponds to fractions 48% of SF-gzKs and 97% of PE-gzKs. Lane et al. (2007) quote 32% and 95%, and Greve et al. (2010) 30.4% and 98.0%. This difference is most likely due to the difference in ERO selection.

Further, these Figures also show that (at $K < 21.5$) as well as the fact that a majority of PE-gzKs are also classified as EROs, a very large fraction (84%) of such jointly selected PE-gzK-EROs are *not* also selected as DRGs (3930 out of 4856). Lane et al. (2007) show a similar result for their PE-gzK counts: none of their non-ERO selections are both PE-gzKs and DRGs (although they have much smaller samples of 214 and 330 respectively). This makes sense, as the strong DRG colour may imply that the D_{4000} break appears in between the J and K bands, putting these galaxies at at least $z \sim 2.0$, and our PE-gzK redshift distribution is shown in Figure 3.19 to have very few objects at this redshift. Very few objects which are not EROs are jointly selected as DRGs and PE-gzKs; there are only 30 objects out of 5164 PE-gzKs and 5781 DRGs (approximately 0.5% of each).

In Figure 3.22, we also show the comparison of objects which have been separated into the two populations of EROs. Note that as this selection requires the J-band, we are limited to these objects which have J less than our limit (as is the selection for DRGs), meaning that the sum of OG- and DG-EROs from this figure does not match the total number of EROs in Figure 3.21. We select 34401 EROs with J counterparts (before separation) compared with 37882 EROs whose J component is not considered.

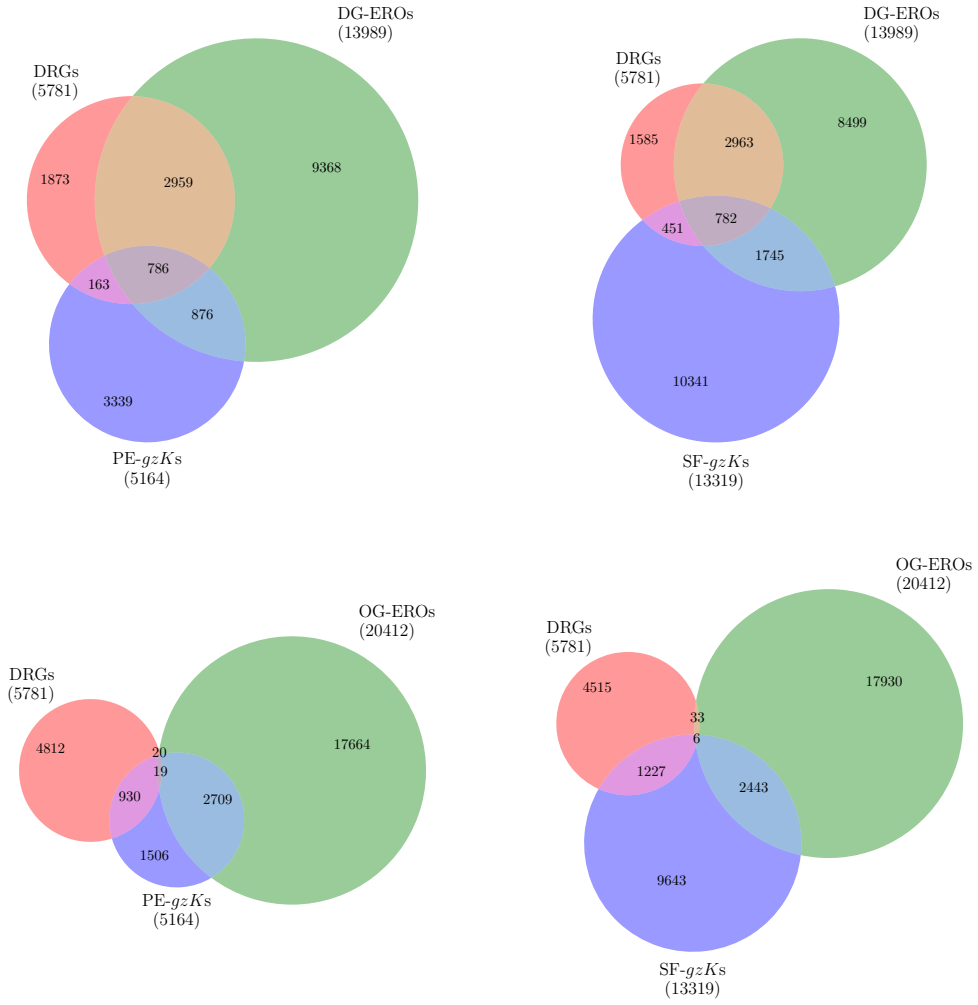

Figure 3.22: Venn diagrams for DRGs, OG- and DG-EROs, and PE- and SF-gzKs. By definition, an object cannot be both an OG- and DG-ERO, nor a PE- and SF-gzK, so these combinations are ignored.

As expected from Figures 3.14 and 3.20, almost all of the joint DRG-ERO selections are from the DG-ERO population. There are 3633 DG-EROs out of 13989 (27%) jointly selected as DRGs, compared with the 29 OG-EROs out of 20412 (which is consistent with zero).

Finally, we look at the overlap of the passive and star-forming selections of EROs and gzKs. The fraction of passive gzKs which are also dusty EROs is 32%, compared with 19% of the star-forming gzKs. Conversely, 53% of passive $gzKs$ are old EROs, compared with 18% of the star-forming $gzKs$.

As a comment on the usefulness of each of these selections, it is most likely that the gzK criteria are the most useful, given their ability to separate populations of galaxies into the star-forming and passively evolving subsets, and is useful over a larger redshift range. However, in this Thesis we will use these along with the ERO criteria, both due to the absolute number of galaxies we are able to select, and the existing literature which performs similar analyses with this selection. The large overlap between the gzK populations and EROs (in the redshift range EROs are able to cover) indicates that these are indeed the same selection of passive galaxies. The least useful selection (discussing in the context of this Thesis) is the DRG selection, as it is the selection with the least faint limit (in K), and hence, the smallest number of galaxies. We have, however, still computed the number counts of this selection as it may be useful for comparisons with other, future data, and also as a test of the J band data: recovering appropriate (when compared with literature) numbers of DRGs is further proof that our J catalogues are reliable.

3.7 *K*-band counts summary

Differential number counts (per square degree, per half magnitude) of selections of galaxies from the DXS-PS1 and DXS-HSC catalogues are summarised in Tables 3.1 and 3.2 respectively. Selection criteria are described in detail earlier in this Chapter. Uncertainties reported are the combined Poisson and jackknife estimate. We remove galactic stars using an optical-NIR ($r - i$ vs. $J - K$) criteria.

We note that the differing counts for galaxies and DRGs between the DXS-HSC and DXS-PS1 catalogues may be due to both different areas used, but any small difference is more likely due to the superior HSC optical data which is used to separate stars from galaxies. The counts are not dissimilar, though, and are still within uncertainties. ERO counts will appear different predominantly due to fainter i-band limit in HSC. We do not report SF-gzK

Table 3.1: Number counts of various galaxy selections using PanSTARRS MDS optical data. DRGs are included, even though this selection does not rely on optical data.

K	galaxies	DRGs	EROs	DG-EROs	OG-EROs
11.25	-	-	-	-	-
11.75	-	-	-	-	-
12.25	-	-	-	-	-
12.75	0.04 ± 0.05	-	-	-	-
13.25	0.2 ± 0.1	-	-	-	-
13.75	0.6 ± 0.2	0.04 ± 0.06	-	-	-
14.25	1.9 ± 0.4	0.04 ± 0.06	-	-	-
14.75	4.3 ± 0.6	-	-	-	-
15.25	9.7 ± 0.9	0.2 ± 0.1	-	-	-
15.75	21.4 ± 1.5	0.2 ± 0.1	0.04 ± 0.06	-	0.04 ± 0.06
16.25	50 ± 3	0.8 ± 0.3	0.08 ± 0.08	-	0.08 ± 0.08
16.75	108 ± 4	1.3 ± 0.4	0.3 ± 0.1	0.04 ± 0.06	0.2 ± 0.1
17.25	209 ± 7	1.3 ± 0.3	0.7 ± 0.2	-	0.7 ± 0.2
17.75	387 ± 12	1.9 ± 0.4	1.4 ± 0.3	0.08 ± 0.08	1.2 ± 0.3
18.25	703 ± 17	3.7 ± 0.7	3.7 ± 0.5	0.5 ± 0.2	2.8 ± 0.5
18.75	1210 ± 20	4.2 ± 0.6	14.7 ± 1.3	3.2 ± 0.5	11 ± 1
19.25	2160 ± 40	8.6 ± 0.9	76 ± 3	21.4 ± 1.5	54 ± 3
19.75	3340 ± 60	22.8 ± 1.6	310 ± 9	96 ± 4	213 ± 7
20.25	4840 ± 80	91 ± 4	779 ± 18	270 ± 9	507 ± 14
20.75	6420 ± 90	232 ± 7	1190 ± 20	440 ± 11	742 ± 17
21.25	8590 ± 120	286 ± 8	1240 ± 20	409 ± 11	735 ± 16
21.75	11150 ± 160	15.5 ± 1.2	832 ± 16	90 ± 3	446 ± 10
22.25	13560 ± 190	-	293 ± 8	0.04 ± 0.06	81 ± 3
22.75	14400 ± 200	-	7.6 ± 0.8	-	0.9 ± 0.3
23.25	8100 ± 200	-	-	-	-

Table 3.2: Number counts of various galaxy selections using HyperSuprimeCam HSC-SPP optical data. DRGs are included, even though these selection does not rely on optical data.

K	galaxies	DRGs	EROs	EROs	SF-gzKs	PE-gzKs	OG-EROs	DG-EROs
11.25	-	-	-	-	-	-	-	-
11.75	-	-	-	-	-	-	-	-
12.25	-	-	-	-	-	-	-	-
12.75	0.05 ± 0.07	-	0.06 ± 0.08	0.06 ± 0.08	0.06 ± 0.08	-	0.06 ± 0.08	-
13.25	0.10 ± 0.10	-	-	-	-	-	-	-
13.75	0.6 ± 0.3	-	0.06 ± 0.08	-	-	-	0.06 ± 0.08	-
14.25	2.2 ± 0.5	-	-	-	-	-	-	-
14.75	4.1 ± 0.8	-	-	-	-	-	-	-
15.25	9.7 ± 1.1	0.06 ± 0.08	0.2 ± 0.1	0.06 ± 0.08	0.2 ± 0.1	-	0.2 ± 0.1	-
15.75	22.3 ± 1.7	0.1 ± 0.1	0.1 ± 0.1	0.06 ± 0.08	0.1 ± 0.1	-	0.1 ± 0.1	-
16.25	51 ± 3	0.5 ± 0.3	0.1 ± 0.1	0.06 ± 0.08	0.2 ± 0.1	-	0.1 ± 0.1	-
16.75	113 ± 6	1.2 ± 0.4	0.4 ± 0.3	0.2 ± 0.2	0.5 ± 0.2	-	0.2 ± 0.2	0.06 ± 0.08
17.25	222 ± 9	1.4 ± 0.4	0.6 ± 0.3	0.4 ± 0.2	1.1 ± 0.4	0.1 ± 0.1	0.5 ± 0.2	-
17.75	408 ± 14	1.5 ± 0.5	1.7 ± 0.5	0.5 ± 0.2	2.1 ± 0.5	0.06 ± 0.08	1.2 ± 0.4	0.4 ± 0.2
18.25	720 ± 20	3.0 ± 0.6	7 ± 1	2.5 ± 0.6	4.7 ± 0.7	0.5 ± 0.2	5.6 ± 0.9	1.2 ± 0.4
18.75	1230 ± 30	4.6 ± 0.8	26.3 ± 1.9	5.7 ± 0.8	7 ± 1	1.1 ± 0.4	19.5 ± 1.7	6.0 ± 0.8
19.25	2000 ± 40	8.1 ± 1.1	100 ± 4	24.4 ± 1.9	16.9 ± 1.6	7 ± 1	69 ± 3	28 ± 2
19.75	3140 ± 60	21.9 ± 1.9	328 ± 13	100 ± 4	40 ± 2	27.1 ± 1.8	225 ± 8	100 ± 5
20.25	4770 ± 90	91 ± 5	780 ± 20	285 ± 9	135 ± 6	86 ± 4	485 ± 13	286 ± 11
20.75	6330 ± 110	236 ± 8	1300 ± 40	559 ± 16	395 ± 12	171 ± 7	706 ± 18	558 ± 16
21.25	8530 ± 140	287 ± 10	1820 ± 50	880 ± 20	930 ± 20	248 ± 9	850 ± 20	625 ± 16
21.75	11080 ± 170	15.8 ± 1.3	1920 ± 50	930 ± 20	1820 ± 40	234 ± 11	642 ± 15	125 ± 5
22.25	13490 ± 200	-	1520 ± 40	606 ± 19	2820 ± 60	148 ± 9	140 ± 5	-
22.75	14200 ± 200	-	770 ± 20	160 ± 7	3360 ± 70	60 ± 5	14.7 ± 1.4	-
23.25	7700 ± 200	-	135 ± 6	2.7 ± 0.6	1830 ± 60	10.2 ± 1.4	0.5 ± 0.3	-

or PE-gzK counts for the DXS-PS1 catalogue. Further, the OG- and DG-ERO counts do not sum to the ERO counts, due to the limiting J-band data.

We report the counts of all objects to magnitudes which are often fainter than the appropriate magnitude cut.

3.8 DXS H-band data

For the majority of this Thesis, we focus on the detection and clustering properties of galaxies using the K-band as the primary selection. However, not all future instruments will observe in the K-band. In particular, the *Euclid* instrument, which will cover a large fraction of the *Rubin* Deep-Wide-Fast footprint and the Deep Drilling Fields, will use H (1.6 µm) as the longest observing wavelength. Our discussion earlier demonstrates that deep, high-quality optical data are required to leverage the NIR to select large samples of intermediate reshift galaxies. *Rubin* will provide the premier optical dataset of the next several decades when it begins full-scale operation in 2023/24. At longer wavelengths than H and K, *Spitzer* has imaged the Deep Drilling fields (in regions which are not already covered by SERVS) in the [3.6] and [4.5] bands to magnitude of 23.1 with the *Spitzer* DeepDrill survey (Lacy et al., 2021).

Approximately $5\,\mathrm{deg}^2$ of the SA22 field (tiles 2 through 7; see Figure 2.4) have H band imaging. We present a summary of this in Figure 3.23, which shows that all tiles except tile 7 have similar exposure time. Figure 2.16 also demonstrates tile 7's significantly shallower H depth. Therefore, we use only tiles 2 through 6 in our analysis, limiting us to $\sim 4\,\mathrm{deg}^2$.

Unfortunately *Spitzer* does not provide MIR imaging in the SA22 field. However, in addition to this DXS H-band imaging, we are also able to use the UDS JHK imaging does which does have the benefit of the very deep [3.6] and [4.5] data from the *Spitzer* UDS (SpUDS Dunlop et al., 2007) programme.

3.8.1 NIR stellar sequence

To demonstrate SA22 H-band data, Figure 3.24 shows a $J-H$ vs. $H-K$ colour-colour diagram, with points coloured by $i-K$.

The stellar JHK stellar sequence is clearly visible in the bluest parts of both colours; the $i-K$ colour reddens with redder $J-H$ and $H-K$, and "resets" at the bluest extent of the cloud of points representing extragalactic objects.

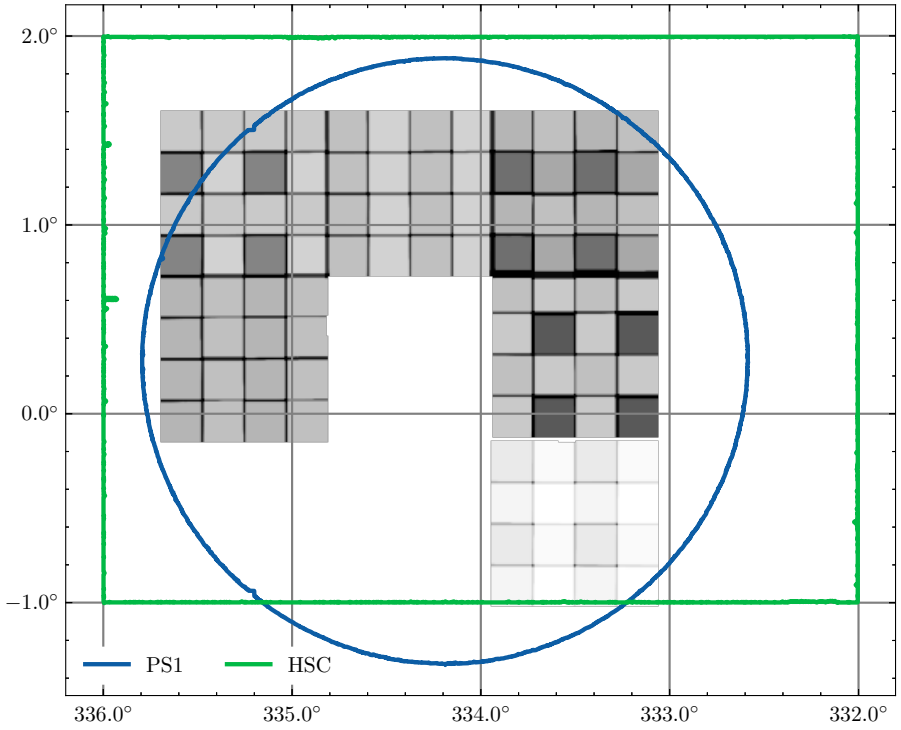

Figure 3.23: Exposure time map for H-band coverage in SA22 (tiles 2-7, moving clockwise from left). Darker regions indicate longer exposure times. Tile 7 clearly has shorter exposure time than the other five tiles.

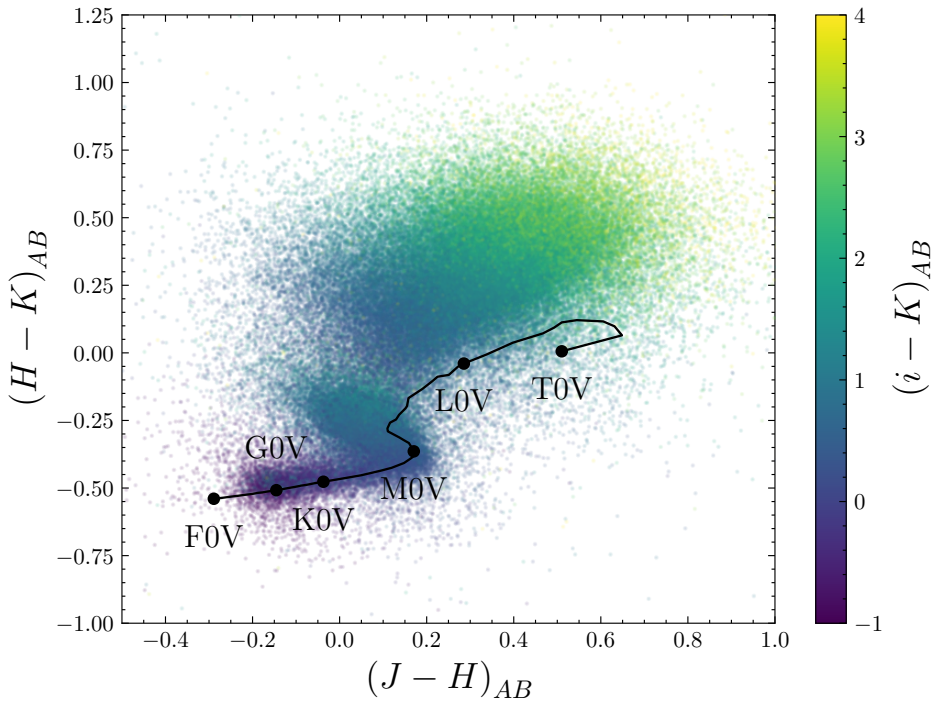

Figure 3.24: DXS $J-H$ vs. $J-K$ colour diagram for the H data available in SA22. Points are coloured by $i-K$ (using HSC i data). Spectral type tracks taken from Pecaut & Mamajek (2013).

We also show the track of the evolution of main sequence stars with spectral type (from F0V to T0V), as computed by Pecaut & Mamajek (2013)[3], who report these colours in 2MASS filters. We transform these to WFCAM colours by combining Equations (6), (7) and (8) in Hodgkin et al. (2009), who detail the WFCAM/2MASS photometric calibration, to give

$$(J-H)_{\mathrm{WFCAM}} = 0.865\,(J-H)_{\mathrm{2MASS}} + 0.03, \tag{3.8.1}$$

and

$$(H-K)_{\mathrm{WFCAM}} = 0.990\,(H-K)_{\mathrm{2MASS}} + 0.060\,(J-H)_{\mathrm{2MASS}} - 0.03, \tag{3.8.2}$$

and then applying the AB to Vega offsets of 0.938, 1.379 and 1.900 for J, H and K. This track shows that the bluest branch in our NIR stellar sequence is selecting G- to M-type stars. As we plot these colours in AB magnitude, F-type stars (ie, Vega-like stars) do not appear at (0,0) as they would do in a Vega magnitude plot.

3.8.2 *H*-band ERO selection

We attempt selections by directly replacing the K in the ERO selection with H, $i-H$, and a similar $r-H$. To choose a new "cut", we look at the recovery rates for $i-H>X$ for a variety of values of X.

Figure 3.25 shows the recovery rate of $i-K>2.55$ selected EROs from the DXS-HSC catalogues, plotted as False Positive Rate (FPR) against True Positive Rate (TPR). FPR is calculated as the number of objects which are not EROs but are incorrectly selected as such, as a fraction of the total number of non-EROs in the catalogue. Conversely, TPR is the number of objects which *are* correctly selected as EROs as a fraction of the total number of EROs in the catalogue. The traces move from top right to bottom left with increasingly red criteria (ie, moving from $i-H>0$ to $i-H>5$).

We do this analysis for all objects which have $r<22.5$, $i<25.5$, $H<22.7$ and $K<22.7$, so that we are not counting objects which are impossible to be selected by their non-detection .

These plots are often referred to as Receiver-Operator Characteristic curves for classification problems which use machine learning (or otherwise). In these problems, the "perfect" classifier has a trace which is a step-function at FPR = 0. That is, the best classifier has a point at which it correctly selects all of the "positives" (here $i-K$ selected EROs), while rejecting

[3]Data available at `https://www.pas.rochester.edu/~emamajek/EEM_dwarf_UBVIJHK_colors_Teff.txt`

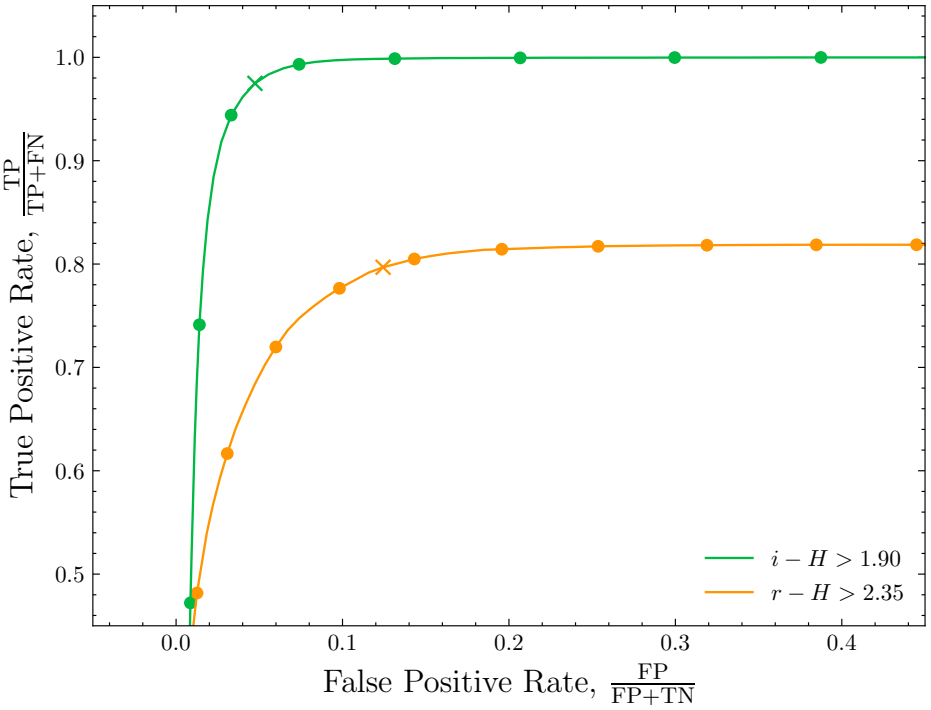

Figure 3.25: Recovery rates of $i - K$ EROs for increasing $i - H$ and $r - H$ cuts, shown as False Positive Rate against True Positive Rate. Solid lines are those for the DXS-HSC SA22 H-band catalogue. The traces are move from the top right for "blue" cuts (ie, $i - H > 0$) to the bottom left for "red" cuts ($i - H > 5.0$). The round markers are spaced 0.25 mags apart, and the cross shows the selected "best" cut, which is also indicated in the legend.

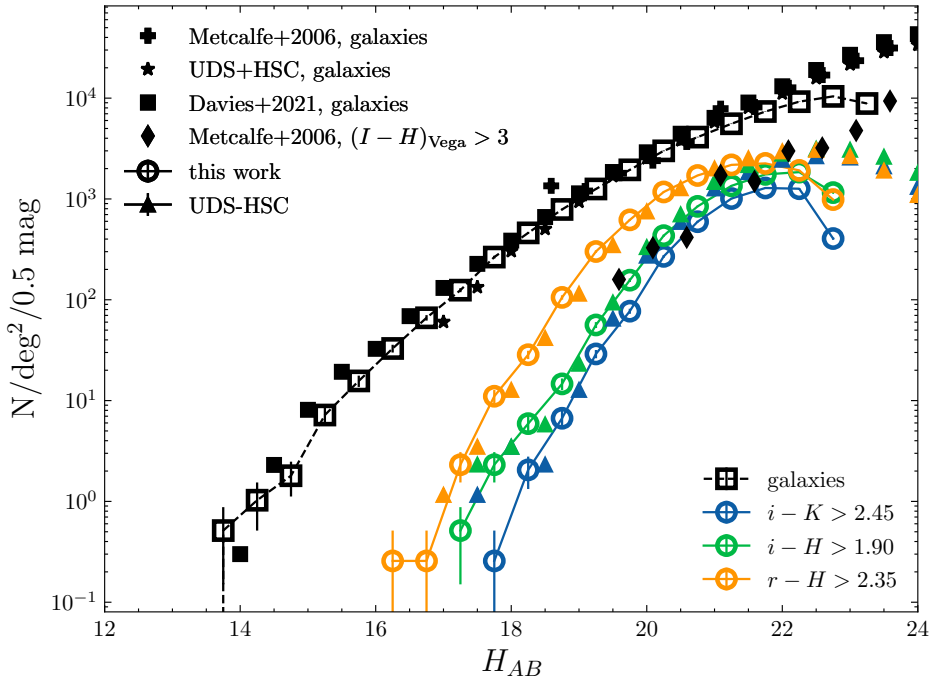

Figure 3.26: Number counts of H-selected EROs with $i - H > 1.90$, $r - H > 2.35$ and $i - K > 2.55$ (plotted as a function of total H-band magnitude). Triangle markers are the number counts of the same cuts from the UDS-HSC catalogue, in the same colours as the DXS counts. $(I - H)_{Vega}$ counts are also shown from Metcalfe et al. (2006) as diamond markers, for $H_{\rm AB} > 19.5$. Number counts of all galaxies are also shown, from our work, the UDS-HSC catalogue, Metcalfe et al. (2006) and Davies et al. (2021).

all of the "negatives" (non-EROs). The best value of the tunable parameter in the model (here, the value of the cut) is the point on the curve which is closest to $(\mathrm{FPR}, \mathrm{TPR}) = (0, 1)$, under the hypothesis that false positives are as equally undesirable as false negatives. We can calculate this geometrically as

$$\text{argmin} \sqrt{\left(1 - \mathrm{TPR}^2\right) + \mathrm{FPR}^2}.$$

It would be disingenuous to call our problem a true classification problem in the sense that we are not separating objects into distinct classes (compared with eg. stars vs. galaxy classification, stars vs. AGN). Rather, we are attempting to recover a subset of objects which are chosen with a cut (in a continuous variable) which is itself somewhat arbitrary. However, this ROC curve approach is still useful for justifying our $i - H$ and $r - H$ selection criteria.

It is logical that the $i - H$ selection has the better ROC curve than $r - H$; the former is only one band different from the original $i - K$ selection. We find that $(i - H)_{\rm AB} > 1.90$ and $(r - H)_{\rm AB} > 2.35$ are the best criteria from the DXS-HSC catalogue using the geometric argument.

H	galaxies	$(i-K)$ EROs	$(i-H)$ EROs	$(r-H)$ EROs
13.75	0.5 ± 0.5	-	-	-
14.25	1.0 ± 0.8	-	-	-
14.75	1 ± 1	-	-	-
15.25	7.2 ± 1.9	-	-	-
15.75	16 ± 3	-	-	-
16.25	33 ± 5	-	-	0.3 ± 0.4
16.75	66 ± 7	-	-	0.3 ± 0.4
17.25	125 ± 12	-	0.5 ± 0.5	2.3 ± 0.9
17.75	270 ± 20	0.3 ± 0.4	2 ± 1	11 ± 2
18.25	460 ± 30	2 ± 1	6 ± 2	29 ± 5
18.75	790 ± 40	6.7 ± 1.8	15 ± 3	106 ± 10
19.25	1260 ± 70	29 ± 4	56 ± 6	300 ± 20
19.75	1940 ± 110	77 ± 8	156 ± 11	620 ± 40
20.25	3000 ± 150	269 ± 18	430 ± 30	1170 ± 60
20.75	4110 ± 190	590 ± 40	840 ± 40	1710 ± 70
21.25	5600 ± 200	1010 ± 60	1350 ± 60	2180 ± 80
21.75	7400 ± 300	1280 ± 80	1750 ± 80	2250 ± 90
22.25	9200 ± 400	1260 ± 70	1850 ± 80	1920 ± 80
22.75	10400 ± 400	400 ± 20	1160 ± 50	990 ± 30
23.25	8800 ± 400	-	-	-

Table 3.3: $H_{\rm AB}$-band number counts of galaxies, and several ERO selections

Figure 3.26 presents H-band number counts of EROs and galaxies. Counts are also listed in 3.3. We show the $i-K>2.55$ EROs as a function of their H-band magnitude for direct comparison to the new H selections. As the ROC curves suggest, the $i-H$ selection more closely matches the $i-K$ selection (at least at the bright magnitudes). We also plot the $(I-H)_{\rm Vega}>3$ EROs in Metcalfe et al. (2006), who select these from the 7×7 arcmin^2 William Herschel Deep Field, from the 3.5m Calar Alto telescope. Their Vega colour selection corresponds to a similar criteria to ours in AB, and we convert their H counts to AB from Vega with an offset of 1.34. In the magnitude range that our study overlaps with theirs ($19.5<H_{\rm AB}<22$), our H-band counts of $i-H>1.95$ and $i-K>2.55$ are comparable with theirs, although we note that their absolute number of objects is significantly smaller than ours because of the area available.

We caveat that the exploration of H-selected EROs here uses the WFCAM H-band data. The *Euclid* instrument's H-band will be significantly broader: approximately a top-hat function $1.5\,\mu{\rm m}<\lambda<2.0\,\mu{\rm m}$ compared with WFCAM's $1.5\,\mu{\rm m}<\lambda<1.75\,\mu{\rm m}$, meaning the criteria we show here as 'optimal' will not be so for *Euclid*. However, three of the four DXS fields (ElaisN1, Lockman and XMM-LSS), along with deeper surveys (UDS, UltraVISTA) are in the nominal *Euclid*-wide footprint, so more appropriate criteria could readily be developed

for comparison of *Euclid*'s ERO selections with previous works.

3.9 Summary

We test a number of colour-colour selections, and determine that an optical-NIR pair $r-i$ vs. $J-K$ is the most suitable for excluding galactic stars at faint magnitudes, although the common $J-K$ cut is sufficient at the brighter end of our measurements (where our matched optical datasets saturate). Using our DXS catalogues, we are measure the K-band number counts of galaxies over a large magnitude range, $14 < K22$. We demonstrate that our number counts are consistent between the four DXS fields, and further, with literature measurements over this range.

We make a number of observed-frame NIR-band selections of galaxies, in order to select the most luminous (hence massive) and passive galaxies, namely: Distant Red Galaxies (DRGs), Extremely Red Objects (EROs), and gzK, which makes a joint selection of star-forming (SF-gzKs) and passively evolving (PE-gzKs) At the brighter end of our galaxy selection ($K_{AB} < 21.5$, the limiting magnitude of the DRG selection), we

Arguments could be made for several of the galaxy selections being the most useful for the rest of this Thesis. As the ERO selection is designed for $z > 1$ and DXS' redshift limit of $z \sim 1.6$, EROs are certainly the most numerous passive galaxy selection we are able to make.

For surveys which go much deeper (ie, UDS), the gzK selection would certainly be the most useful: large samples of galaxies which are reasonably well-separated into the star-forming and passive populations. Here, however, the redshift limits of this selection (approximately $1.4 < z < 2.5$) of these galaxies is approaching the extreme of what DXS can measure.

For this reason, we choose not to perform all analysis with all samples, but choose the selection technique which is most appropriate.

Given the large errors that which will be in present at the largest scales, it will be advantageous to use the ERO selection to measure the clustering of passive galaxies at the brightest magnitude, where the number counts of PE-gzKs are very small.

However, for fainter magnitude cuts, the gzK selection will certainly be more useful for comparing the clustering of the star-forming and passive samples,

For the study of the luminosity functions, the passive samples which cover a large redshift range are most useful: EROs, and the restframe-selected red $U-B$ galaxies (of which there

is more discussion in Chapter 5). As we use the redshifts only from the two fields in the DXS-HSC-SWIRE samples

Finally, we use the fraction of the DXS SA22 field with H-band coverage ($\sim$ 5 sq. deg) to investigate the H-band number counts of galaxies, which could be useful for future surveys whose longest waveband is H (eg. *Euclid*). We present H-band number counts of the full galaxy sample for $14 < H < 22$, which could be useful for

Chapter 4

Angular clustering properties

In this chapter, we will present angular two-point correlation functions calculated from the selections of ERO and passive PE-gzK galaxies in Chapter 3.

We choose to measure the correlation functions in magnitude-limited selections (as opposed to mass or redshift limited) mainly for comparison with other observational works which measure the angular correlation functions. However - this also maximises the area we can use (ie, only two of the four fields have reliable photo-zs), which is crucial when measuring the correlation function on large scales.

4.1 Angular correlation function

The angular two-point correlation function (2PCF) $\omega(\theta)$ can be interpreted as the likelihood of finding a pair of objects separated by an on-sky angle θ in the interval $[\theta, \theta + \Delta\theta]$ compared to a random, unclustered distribution. In this way, it is defined as

$$dP = N\left[1 + \omega(\theta)\right] d\Omega, \tag{4.1.1}$$

where dP is the probability of finding a second galaxy at a separation θ (from a randomly selected galaxy in the catalogue) in a solid angle $d\Omega$ (Groth & Peebles, 1977). N is the surface density of objects being analysed. A random uniform distribution of objects would have $\omega(\theta) = 0$. That is, $\frac{dP}{d\Omega} = N$; the probability of finding a pair of objects separated by θ is related only to the surface density of objects. The angular 2PCF is also often denoted as $w(\theta)$.

In practice, $\omega(\theta)$ is estimated by counting the number of pairs of objects with a given separation, and comparing this to a uniform distribution. The naive estimator would calculate

this directly as

$$1 + \omega(\theta) = \frac{DD(\theta)}{RR(\theta)},$$

where θ is the angle between a pair of galaxies (measured in degrees), $DD(\theta)$ is the normalised observed number of data-data pairs in the interval $[\theta, \theta + \Delta\theta]$. It is normalised to $N_{dd} = N_d(N_d - 1)/2$, the total possible number of data-data pairs. Similarly, $RR(\theta)$ is the number of random-random pairs in the interval normalised by $N_{rr} = N_r(N_r - 1)/2$ (total number of random-random pairs), where N_d and N_r are the total numbers of data points, and random points.

We use the Landy-Szalay estimator (Landy & Szalay, 1993), to estimate the (observed) two-point correlation function,

$$\omega_{\rm obs}(\theta) = \frac{DD(\theta) - 2DR(\theta) + RR(\theta)}{RR(\theta)}, \tag{4.1.2}$$

The components $DD(\theta)$ and $RR(\theta)$ are the same as in the naive estimator, and similarly, $DR(\theta)$ is normalised by $N_{dr} = N_d N_r$ (number of data-random pairs).

This is the estimator that has been shown to be the estimate which is the least biased. It is least affected by observational effects (bright star masks, field shape, etc.), due to the DR term.

We use TreeCorr (Jarvis et al., 2004) to calculate the 2PCF, considering minimum and maximum separations of $10^{-3.3}$ deg ($\sim 1.8''$) and $10^{0.3}$ deg (~ 1.99 deg). We choose $\Delta \log(\theta) = 0.1$ bin spacing for all clustering analyses.

Random points are drawn on a sphere within the limits of each of the four fields. We choose a constant 90,000 random points per square degree (25 per square arcminute) for all analyses. This is ~ 10 times the surface density of any of the galaxy selections we make in Chapter 3.

To combine the results from more than one field, we calculate the components in Equation. (4.1.2) as the sums of the un-normalised pair histograms divided by the sum of the total number of pairs in each field. That is $DD_{\rm combined} = \sum_i dd_i(\theta) / \sum_i N_{dd,i}$ for each of the i fields.

The distinction $\omega_{\rm obs}$ in 4.1.2 is because the true angular correlation function $\omega(\theta)$ differs from the observed $\omega_{\rm obs}(\theta)$ by a constant offset $\mathcal{I}$ at all scales,

$$\omega(\theta) = \omega_{\rm obs}(\theta) + \mathcal{I} \tag{4.1.3}$$

where $\mathcal{I}$ is known as the integral constraint. $\mathcal{I}$ arises due to the finite size of the survey area, and is large in comparison to $\omega(\theta)$ at separations θ which are comparable to the angular

size of the survey. The integral constraint is calculated as the double integral of the true correlation function $\omega(\theta)$ over the field area Ω. It can be calculated numerically using the random distribution used to calculate $\omega_{\rm obs}(\theta)$,

$$\mathcal{I} = \frac{1}{\Omega^2} \iint \omega(\theta)\ d\Omega_1\, d\Omega_2 \approx \frac{\sum RR(\theta)\,\omega(\theta)}{\sum RR(\theta)}, \tag{4.1.4}$$

as described in Roche et al. (1999). It is because the random distribution is uniform (ie, $\frac{dP}{d\Omega} = N_r$) that allows it to be used in this way: this sum over RR is effectively an integral, weighted by the (true) angular correlation function $\omega(\theta)$.

However, as $\omega(\theta)$ is a function with parameters to be determined, we use the iterative method used in many previous studies (eg. Kim et al., 2011; Wake et al., 2011) to estimate $\mathcal{I}$. With an appropriate functional form (see Section 4.1.1 below), parameters are fit to $\omega_{\rm obs}(\theta)$ (using for instance SCIPY's least squares fitting routine `curve_fit` or an MCMC sampling technique), and an estimated correction is calculated with Equation 4.1.4. We then add this correction to $\omega_{\rm obs}(\theta)$, re-fit the parameters, recalculate $\mathcal{I}$, and repeat until convergence.

We note that the integral constraint only has a significant effect at large scales. There will be (relatively) more large-scale pairs missing, as one of the sources (of the pair) is more likely to reside outside of the survey area than for small-scale pairs precisely because the separation θ considered is larger.

4.1.1 Functional forms

A simple power law,

$$\omega(\theta) = A_\omega \theta^{-\delta} \tag{4.1.5}$$

has been used successfully in many studies in the past to model the correlation function of various selections of galaxies, often with a slope fixed to a value of $\delta = 0.8$. However, others (Sawangwit et al., 2011; Kim et al., 2011, 2014; Sato et al., 2014) demonstrate that a single power law is not sufficient to fully model the correlation function across a large range of angular scales. Given the range of scales that we are able to probe with the DXS data, we adopt the power law-plus-exponential cutoff ('PLE' model),

$$f(\theta) = A_1 \theta^{-d} + A_2 \exp(-\beta\theta), \tag{4.1.6}$$

considered in Kim et al. (2014). Alternatively, Kim et al. (2011) use the sum of two power laws, $A_1\theta^{-d_1} + A_2\theta^{-d_2}$.

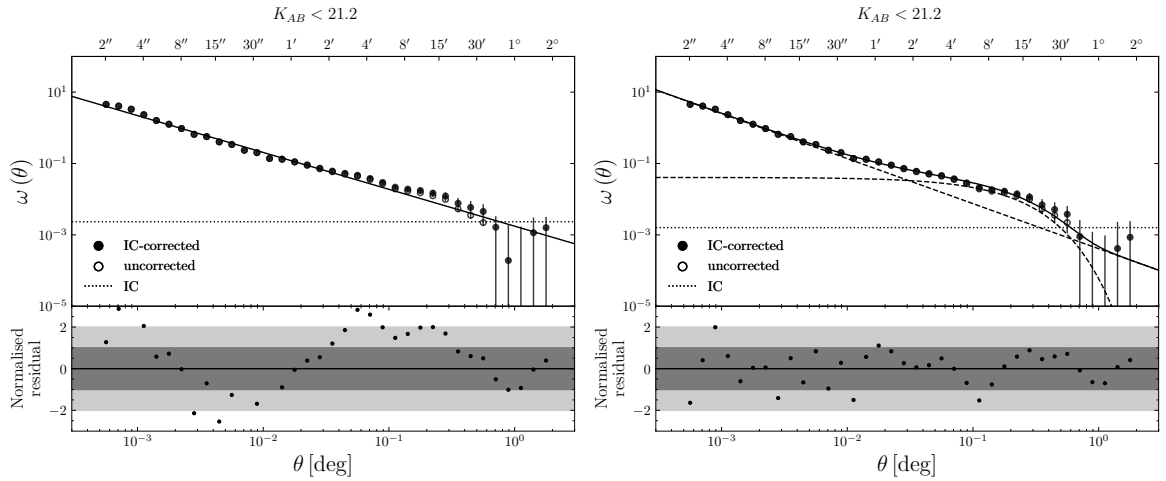

(a) Simple power law fit

(b) Power law plus exponential

Figure 4.1: Corrected and uncorrected angular correlation function for EROs $K < 21.2$, using two functional forms. The uncorrected measurement data points are plotted as open circles, corrected are plotted as filled circles. The residuals (normalised by jackknife-estimated errors) show much less structure for the more complex function than the power law. The value of the integral constraint $\mathcal{I}$ is plotted as a horizontal dotted line, to indicate the scales where the integral constraint is comparable to the correlation function measurement. The value of $\mathcal{I}$ is comparable for both functional forms.

To demonstrate the need for a functional form more complex than a power law, Figure 4.1 presents the correlation function of DRGs with $K < 21.7$ (using the combined data from all four fields), along with the best-fitting power law, and best-fitting PLE model (Equation 4.1.6). Both the uncorrected and integral-constraint corrected are shown in both panels. The residuals from the more complex functional form clearly show far less structure than those of the power law.

Palamara et al. (2013) and Shin et al. (2017) argue that these models are still only empirically motivated, and a robust analysis of galaxy clustering can only be performed using Halo Occupation Distributions and halo modelling (see Section 4.5.1 for a brief discussion on this). They therefore perform their analysis with a power law (with either varying or fixed slope).

One reason, however, we argue that there is still value in the more complex models is the dependence of the estimate of $\mathcal{I}$ (the integral constraint) on the function form. Although for the examples we provide in Figure 4.1 the values of $\mathcal{I}$ do not appear significantly different, this may not be the case for galaxy selections whose large scale clustering is especially shallow compared to small scales. Also, the fact that the fits are significantly improved with this model is motivation in itself to use them over the single power law.

Ideally, we would use a form such as

$$f(\theta) = A_1\theta^{-d}\exp(-\kappa\theta) + A_2\exp(-\beta\theta), \tag{4.1.7}$$

where the power law function which describes the small scales is truncated so it does not contribute to the fit on large scales (effectively a Schechter function). With $\kappa = 0$, this reduces to Equation 4.1.6.

The angular scale at which the power law component (which can be thought to represent the clustering of galaxies within the same halo) would again begin to dominate at large scales is comparable to the largest angular scale which we measure. Although it is unphysical that this component is dominant again at large scales ($\sim 2°$, see the right panel of Figure 4.1), when we attempt to fit the truncated power law in Equation 4.1.7, the truncation parameter κ is poorly constrained, or driven to zero by the fitting procedure because there is no data to do otherwise (or the measurements at large scales have very large uncertainties). However, for studies which probe much larger scales, such as those with current surveys VIKING, SHARKS, or the UHS, or future surveys like *Euclid* and *Roman*, this may be of concern.

It is expected that the behaviour of the correlation function on large scales depends linearly on the dark matter distribution of the universe, whereas the small scale behaviour is driven by the physics of galaxy formation. Therefore, the strongest effects of galaxy formation (ie, the interactions of galaxies) will be observed as the strongest deviations from the large scale behaviour. For the galaxies which are evolving in isolation, in galaxy-underdense regions (which for the most part are star-forming spirals), we expect to see smallest deviations from large scale behaviour.

All of this aside, the single power law can still give meaningful insight into the amplitude of the correlation function. The more complex functions are more difficult to find convergent solutions when considering the integral constraint (and solutions which are consistent for all four fields), especially for galaxy selections which give (relatively) small samples, or whose measurements of $\omega(\theta)$ have very large uncertainties on the largest scales. Given these reasons, and that many previous studies also used single power laws (often using a fixed slope $\delta = 0.8$), for comparison, we also fit single power laws to our measurements of the correlation function.

4.1.2 Uncertainty estimates

We calculate the uncertainty in the measurement of the correlation function using the jack-knife method ("leave one out" resampling), discussed at length in Norberg et al. (2009). We

divide each field into N sub-fields with a (target) size of $0.33\,\mathrm{deg}^2$, using the k-means routine available in TreeCorr. The covariance matrix elements $\boldsymbol{C}_{ij}$ (for the i and j^{th} θ interval) are calculated as

$$\boldsymbol{C}_{ij} = \frac{N-1}{N} \sum_{k=1}^{N} \left(\omega_i^k - \bar{\omega_i}\right) \left(\omega_j^k - \bar{\omega_j}\right), \tag{4.1.8}$$

where N is the number of sub-fields, ω^k is the estimate of ω_{obs} excluding the k^{th} sub-field, $\bar{\omega}$ is the mean estimate of ω_{obs} (ie, using all of the available data), and k goes from 1 to N. The jackknife-estimated uncertainties, $\sigma_{\mathrm{jackknife}}$, are then simply the square root of the diagonal of the covariance matrix,

$$\sigma^2_{\mathrm{jackknife}} = \mathrm{diag}\,\boldsymbol{C} \tag{4.1.9}$$

for each i^{th} bin.

This provides a better estimate than using the Poisson "shot-noise" estimate,

$$\sigma_{\mathrm{shot}}\left(\theta\right) = \frac{1 + \omega_{\mathrm{obs}}\left(\theta\right)}{\sqrt{dd}}, \tag{4.1.10}$$

where dd are the unnormalised pair counts.

The lower panel of Figure 4.2 shows the ratio of $\sigma_{\mathrm{shot}}/\sigma_{\mathrm{jackknife}}$. The estimates are similar on small scales, but σ_{shot} (comparatively) underestimates the uncertainty on large scales, by factors of ~ 10 at the very largest scales. This is similar to the behaviour found by Sawangwit et al. (2011, their Figure 4) and Seo et al. (2019, their Figure 10) at the largest scales in their surveys.

This is most likely due to cosmic variance (our individual fields probe only a very small fraction of the sky), and inevitable non-uniformities in the depth of the survey.

4.2 ERO clustering

As it is the largest galaxy sample when considering depth and the number of fields available, we choose to present the clustering results for EROs first.

4.2.1 HSC-selected EROs

Figure 4.3 shows the measured angular 2PCFs of HSC-selected EROs for the three DXS fields which have HSC data, and the combined measurement of these three fields. We choose to present $\omega\left(\theta\right)$ for the $K_{\mathrm{AB}} < 21.2$ sample as representative, as it is roughly the magnitude at which the ERO number counts turn over for both HSC and PS1 selected samples (see

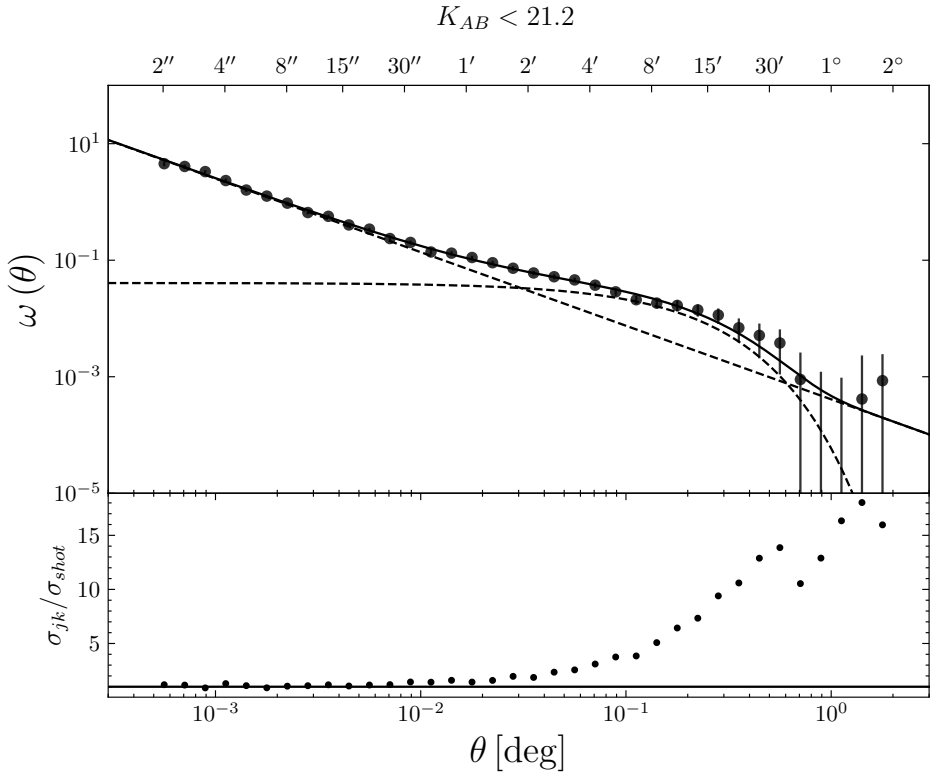

Figure 4.2: Upper panel is the same as in the right panel of Figure 4.1, using the jackknife uncertainty estimates. The lower panel show the ratio of shot noise uncertainty to jackknife uncertainty.

Figures 3.12 and 3.11). At small scales (where the power law component dominates), all three fields and the combined measurement appear consistent, although the best fitting power law slope for XMM-LSS (red) is shallower than the other two fields. XMM-LSS does not match the other two fields as well for large scales and the error bars are much larger. This can be explained simply by the field size; the available HSC-DXS data is $2.54\,\mathrm{deg}^2$, compared with the 6.60 and $7.90\,\mathrm{deg}^2$ for ElaisN1 and SA22 respectively (260% and 310% larger). Nevertheless, we do not exclude this data when computing the combined $\omega(\theta)$.

We report the best fitting values for PLE model in Table 4.1. We note that most of the χ^2_ν are less than unity, which would indicate that the uncertainties on the measurements are overestimated. However, as discussed in Sections 4.1.2, the Poisson noise estimates of uncertainty on $\omega(\theta)$ do not sufficiently account for cosmic variance, especially on the largest scales. Continuing the discussion in Section 4.1.1, the need for the more complex functional form is evident here, with a clear break from a single power law.

As a comparison, we show the same $\omega(\theta)$ again compared with the measurement of the same selection of objects from Kim et al. (2014), who use a subset of the DXS data, in Figure 4.4. Our measurements agree well with theirs although they measure stronger clustering than our

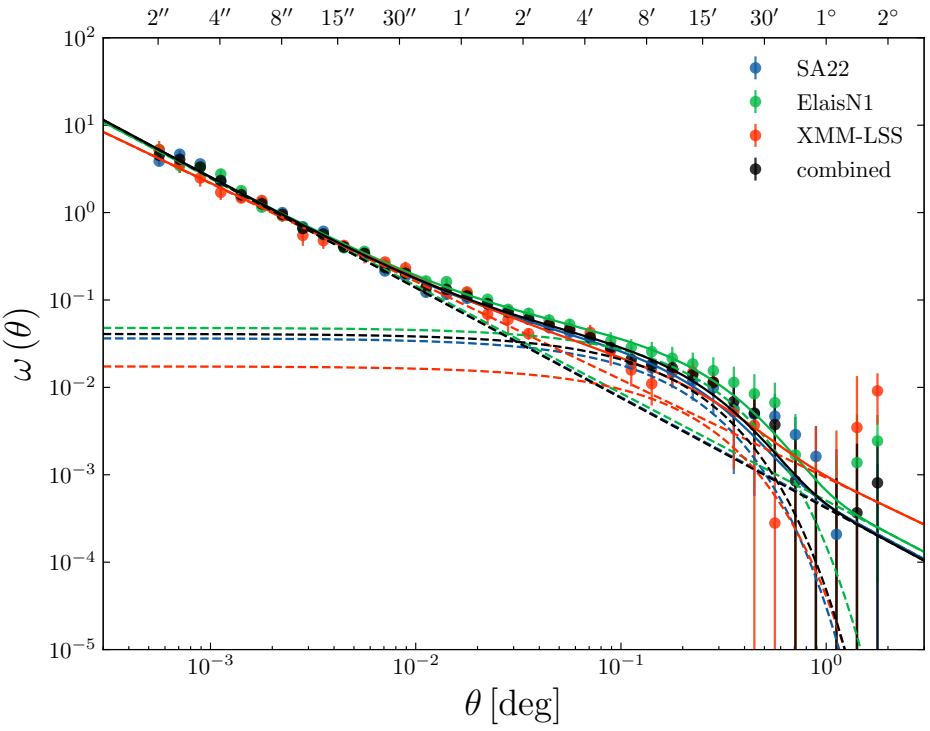

Figure 4.3: Integral constraint-corrected angular two point correlation function, $\omega(\theta)$, for $K_{\rm AB} < 21.2$ HSC-selected EROs. Measurements of $\omega(\theta)$ are shown for the three individual fields with HSC available data, and the combined measurement. The solid line is the fitted function for each dataset, and the dashed lines the two components of the function.

Table 4.1: Best fitting parameters for the PLE model to the angular two point correlation function of HSC-selected EROs, for the three fields and combined. We also provide the reduced χ^2 (χ^2 per degree of freedom) goodness-of-fit statistic for each fit, χ^2_ν. Parameter uncertainties are estimated using the PDFs shown in Figure 4.5.

Parameter	A_1 ($\times 10^3$)	d	A_2 ($\times 10^3$)	β	χ^2_ν
SA22	$0.43\pm^{0.11}_{0.09}$	1.25 ± 0.04	$36\pm^{9}_{8}$	$7.0\pm^{2.1}_{1.8}$	1.291
ElaisN1	$0.5\pm^{0.2}_{0.1}$	1.23 ± 0.05	$48\pm^{11}_{9}$	$5.8\pm^{1.7}_{1.3}$	0.550
XMM-LSS	$0.9\pm^{0.4}_{0.3}$	1.12 ± 0.06	$18\pm^{10}_{9}$	$6.1\pm^{4.7}_{2.2}$	0.886
combined	$0.41\pm^{0.08}_{0.07}$	1.26 ± 0.03	41 ± 6	$6.8\pm^{1.2}_{1.1}$	0.734

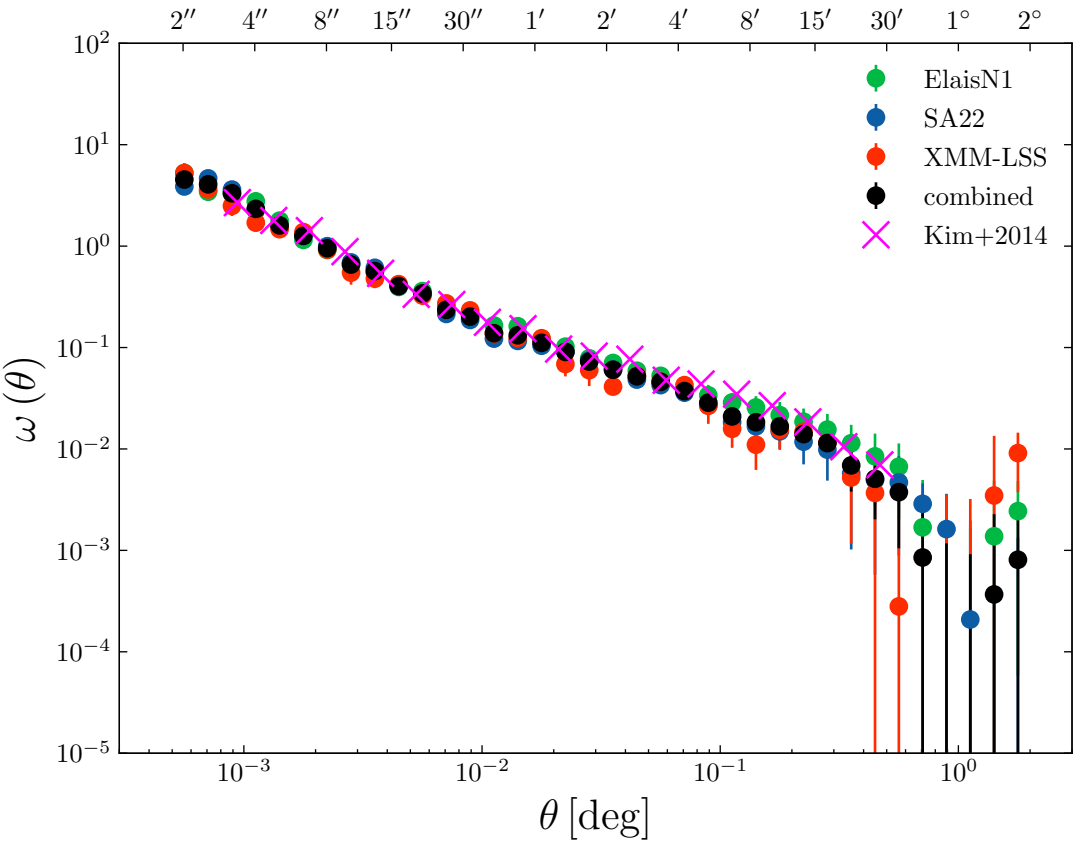

Figure 4.4: The integral constraint-corrected measurement of $\omega(\theta)$ for $K < 21.2$ selected EROs, compared with the measurement from Kim et al. (2014), with their data plotted as the magenta plus symbols.

measurement from the three combined fields on the largest scales. We also note that we measure $\omega(\theta)$ to smaller scales than their work.

Figure 4.5 shows probability distribution function (PDF) for the parameters in the fit. We estimate these PDFs using MCMC sampling with EMCEE (Foreman-Mackey et al., 2013). Similarly to the how we present the 2PCFs (and number counts and redshift distributions in earlier Chapters), we show the PDF for each of the fields, and the combined measurement. The significant overlaps of the 2D PDFs (particularly for SA22 and ElaisN1) are encouraging, and demonstrate that the clustering properties of this selection of galaxies is concordant between fields. These PDFs allow us to estimate the uncertainties on each of the parameters. For parameters whose 1D PDFs (along the 'main' diagonal of Figure 4.5) appear Gaussian, we can reasonably estimate the uncertainty on these parameters as the standard error; the standard deviation of the samples. When estimating the PDF for these parameters, we bound β (the exponential cutoff parameter) to be lower than 20, and allow all other parameters to vary between much larger limits. This has no real impact other than for the XMM-LSS field, but prevents β from becoming extremely large, essentially reducing the functional form to

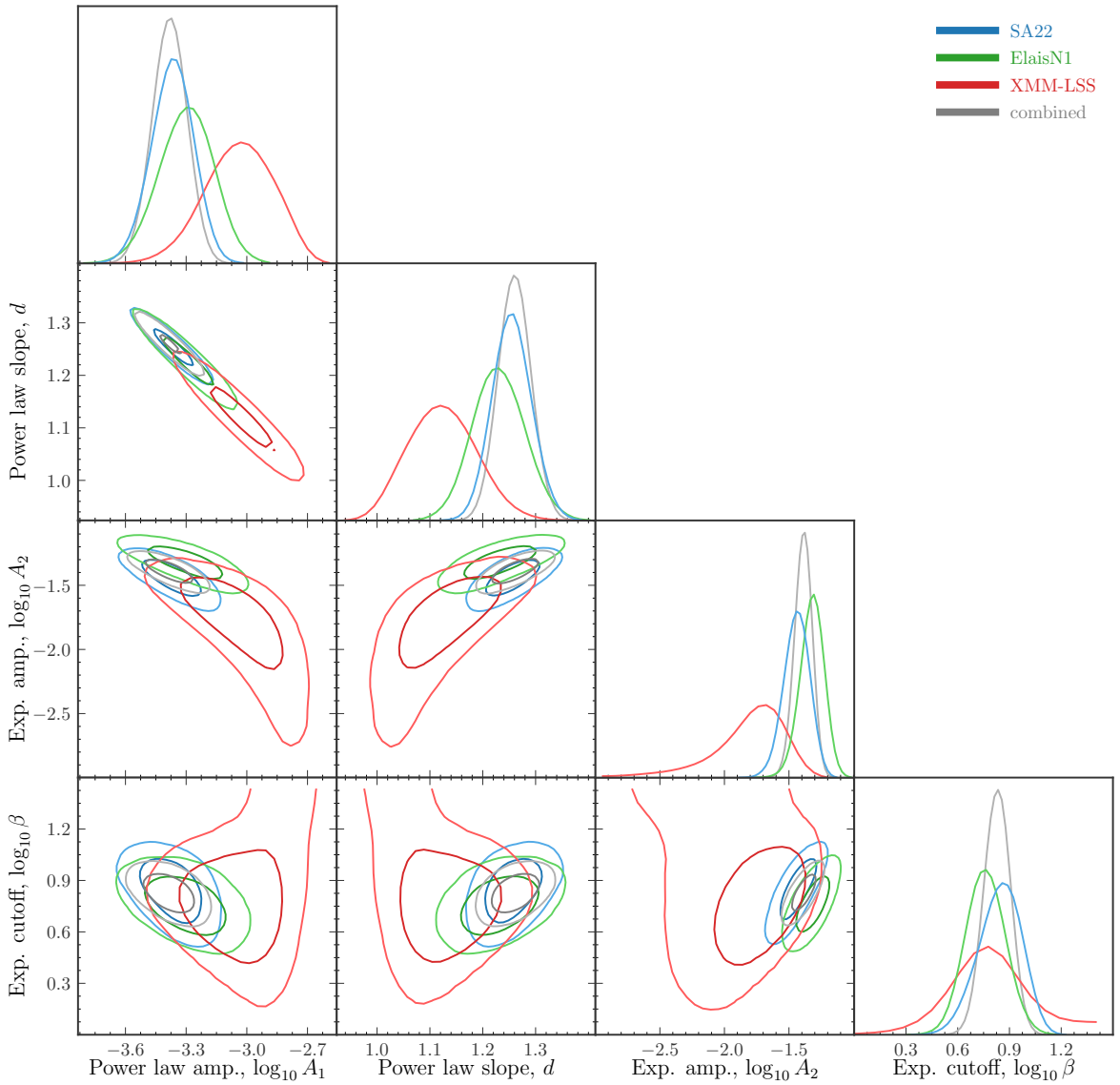

Figure 4.5: Best fit parameter PDFs for fitting Equation 4.1.6 to the $\omega(\theta)$ measurements presented in Figure 4.3 (EROs selected with HSC data). PDFs are presented for each of the three fields with HSC data, and the combined measurement. The 1D PDFs for the amplitude parameters A_1 and A_2 and β cutoff parameter (the first, third and fourth panels along the diagonal) are not Gaussian, but appear more symmetric in log scale, so are presented as such.

a power law. The 1D PDFs show that the combined measurement of $\omega(\theta)$ is dominantly influenced by SA22 and ElaisN1, although this is to be expected, as these are significantly larger fields than XMM-LSS (as mentioned earlier).

The 2D PDFs also provide insight into the correlation of the parameters. The more angled the contours are in parameter space (from the away from the axes), the more correlated two parameters are. The logic is that an elliptical PDF aligned with the axes indicates that one parameter can be adjusted without having any impact on the second; they are in some sense orthogonal (Hughes & Hase, 2010). Unsurprisingly, there is a very strong correlation between A_1 and d, and also between the amplitude of the exponential component A_2, and the cutoff parameter β. There is comparatively little correlation between the power law parameters and β, as this cutoff has very little effect on the small scales, and the power law does not contribute strongly at scales which the scales at which β has a large impact (and the data points have small enough uncertainties to significantly affect the fits). However, there is correlation between the amplitude of the exponential component and the power law parameters. A steep power law and large exponential component (which behaves as a constant term at scales $\theta < 0.1^\circ$ - see the dashed lines in Figure 4.3) can be traded off with a shallower power law and lower amplitude exponential. The latter is in fact the case for the XMM-LSS best fitting model.

We highlight that Figure 4.5 shows the log of the PDF of the amplitude parameters A and the cutoff parameter β on a logarithmic scale. This presentation means that the 1D PDFs of these parameters appear symmetric. We quote the uncertainties on our parameters as the 16% and 84% percentiles.

Previous works estimate the fits of power laws in the two different regimes of $\omega(\theta)$, or measure separately for one of the two regimes either due to the size of their fields, or otherwise. For comparisons, we perform the same analysis. We point out that the two power laws are not joined; neither smoothly nor continuously.

In Figure 4.6, we present the same correlation function data as in Figure 4.3, but with two power laws fit separately to small and large scales, as in Kim et al. (2011, ; K11) and Kim et al. (2014, ; K14). Parameter PDFs are shown in Figures 4.7a and 4.7b for small and large scales respectively. We choose to fit the small scale power law for $\theta < 36''$, and the large scale at $36'' < \theta < 30'$. This break scale of $36'' = 0.01^{\mathrm{deg}}$ is visually where the break appears, and corresponds to $\sim 900\,\mathrm{kpc}$ at $z = 1.1$, and is similar to the break observed by K11 at $0.76' = 0.012^\circ$.

For their separate power law fits with a similar HSC-selected ERO sample, K14 report in their Table 1 $A_{\omega}^{\rm small}(1.42 \pm 0.4) \times 10^{-3}$, and slope$^{\rm small} = 1.08 \pm 0.05$ for the small scale, compared with our $A_{\omega,\rm ss} = (0.61 \pm^{0.09}_{0.08}) \times 10^3$ and $d_{\rm ss} = 1.21 \pm 0.02$ (for the combined measurement). However, we note that their values were obtained by fitting from the data in the interval $0.001^\circ < \theta < 0.02^\circ$, whereas our fitting reaches smaller scales.

For the large scale, K14 report an amplitude of $A_{\omega}^{\rm large}(7.35 \pm 2.3) \times 10^{-3}$, and slope$^{\rm large} = 0.69 \pm 0.10$. This is more comparable to our $A_{\omega,\rm ls} = 4.8 \pm^{0.6}_{0.5}$ and $d_{\rm ls} = 0.78 \pm 0.03$ than the small scale values. The disparity between the two measurements of power law slope on large scales is large although within overlapping uncertainties. Their amplitude implies overall stronger clustering on large scales, however. We note again that we use different scale intervals to fit this large scale power law; our ($0.01^\circ < \theta < 0.5^\circ$) compared with their ($0.02^\circ < \theta < 0.33^\circ$). As K14 state, the most meaningful conclusion to draw from this is that the slope of the clustering on small scales is significantly steeper than the $\delta = 0.8$ that is often assumed, and tentatively that it is shallower on the largest scales.

K11 report slopes of $\delta_{\rm ss} = 0.99 \pm 0.10$ and $\delta_{\rm ls} = 0.4 \pm 0.03$, the latter of which is significantly shallower than both our measurements, and K14's. However, K14 discuss that this is most likely to be due to the smaller area of the K11 study (they use four tiles in SA22), and the use of the Poisson estimates of uncertainty.

At lower redshifts, ($0.6 < z < 0.8$), Ross et al. (2008) measure the angular correlation function of Luminous Red Galaxies (LRGs, which are expected to be the descendents of EROs) with the AAOmega survey and 2SLAQ survey, from which they measure slopes of $\delta_{\rm ss} = 1.16 \pm 0.07$ and $\delta_{\rm ss} = 1.28 \pm 0.04$ (small scale), and $\delta = 0.58 \pm 0.09$ and $\delta = 0.58 \pm 0.09$. Using a larger sample of the AAOmega survey, Sawangwit et al. (2011) measure the angular correlation function of LRGs (with mean redshift $\bar{z} = 0.68$) to scales $\theta \sim 10$, and report $\delta_{\rm ss} = 1.14 \pm 0.01$ and $\delta_{\rm ls} = 0.81 \pm 0.02$. Their lower redshift samples ($\bar{z} = 0.35$ and $\bar{z} = 0.55$) from SDSS and 2SLAQ provide similar values.

As is suggested in K11, this similarity in the strength of the break between LRGs and EROs, in terms of the difference in the power law slope and requirement for the functional form which considers the small and large scales, points to a "continuation in the selection of massive-passive galaxies that can be made from optical and NIR surveys".

We further point out that the slope of the PLE models' power law component is slightly steeper than the slope of the small scale individual component, although for the individual fields, they are consistent within uncertainties. Following on from the discussion on parameter

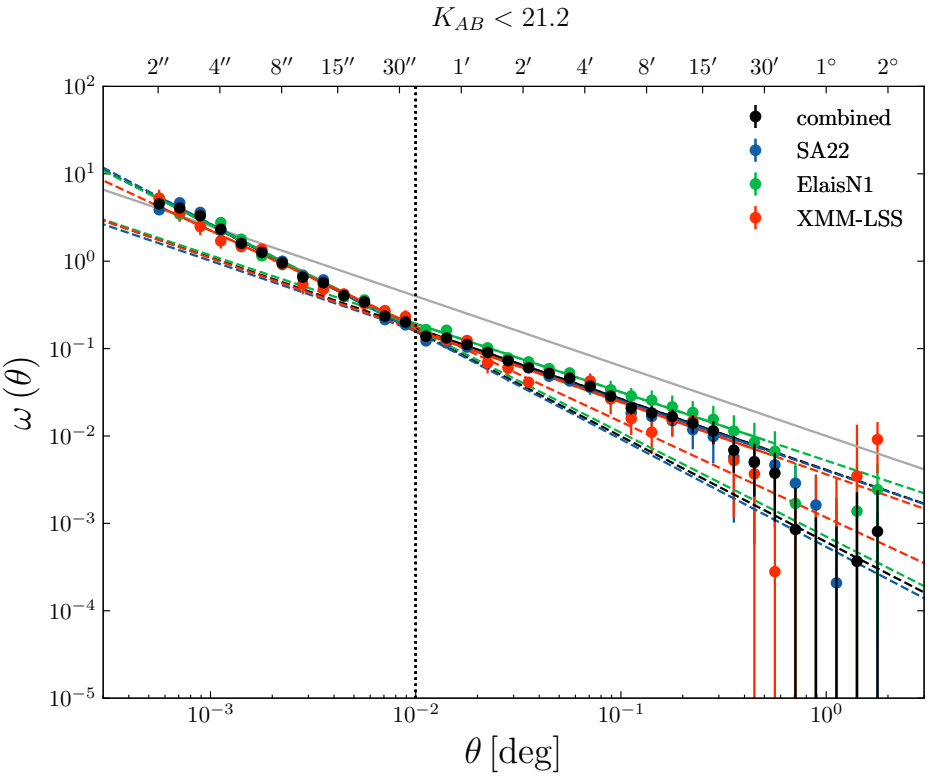

Figure 4.6: Separate power law fits for small and large scales, for EROs $i - K > 2.45$ selected with HSC optical data. The vertical dotted line shows the scale at which we 'break' the power law fits; at $0.01° = 36''$. Solid lines show the data ranges that the function is has been fit over.

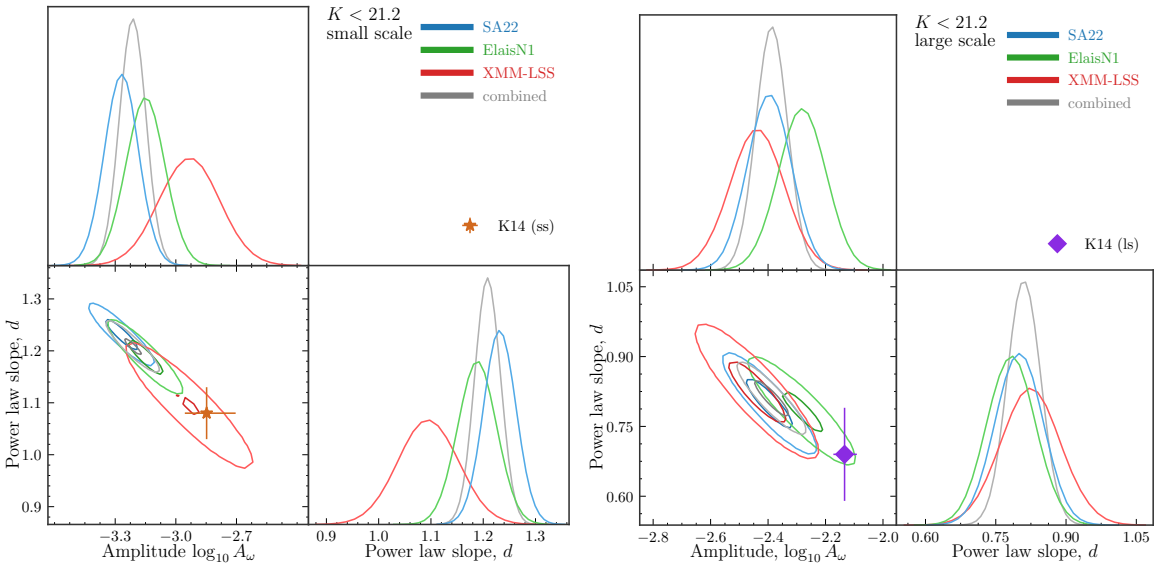

(a) Small-scale power law fit.

(b) Large-scale power law fit.

Figure 4.7: PDFs for parameters for small and large scale power laws, estimated separately. Also shown are the parameters at this magnitude from Kim et al. (2014).

Table 4.2: Best fitting parameters for the power law plus exponential cutoff model to the angular two point correlation function of HSC-selected EROs, for the three fields and combined. We also provide the reduced χ^2 (χ^2 per degree of freedom) goodness-of-fit statistic for each fit. Parameter uncertainties are estimated using the PDFs shown in Figure 4.5.

Field	$A_{\omega,\mathrm{ss}} \times 10^3$	d_{ss}	$A_{\omega,\mathrm{ls}} \times 10^3$	d_{ls}	$\chi^2_{\nu,\mathrm{ss}}$	$\chi^2_{\nu,\mathrm{ls}}$
SA22	$0.54\pm^{0.11}_{0.09}$	1.23 ± 0.03	$4.0\pm^{0.7}_{0.6}$	0.80 ± 0.05	2.483	0.516
ElaisN1	$0.7\pm^{0.2}_{0.1}$	1.19 ± 0.04	$5.2\pm^{1}_{0.9}$	0.78 ± 0.05	0.963	0.176
XMM-LSS	$1.2\pm^{0.5}_{0.3}$	$1.09\pm^{0.06}_{0.05}$	$3.6\pm^{0.8}_{0.7}$	0.82 ± 0.06	0.527	1.174
combined	$0.61\pm^{0.09}_{0.08}$	1.21 ± 0.02	4.1 ± 0.5	0.81 ± 0.03	1.250	0.413

correlations in Figure 4.5, this can be explained by the single power law needing to explain all of the data in the small scale range, whereas the PLE model's power law has the contribution from the exponential component (allowing for a marginally steeper slope). This indicates that careful modelling of the intermediate scales is still important, even if only the smallest scales are of interest. However, the extrema of the uncertainties from the two methods do still overlap, meaning that further investigation is still required, using larger samples which probe smaller scales.

Here, the χ^2 values are closer to one for the small scale power law best fits than they are for large scale (with the exception of XMM-LSS). The ratio of Poisson to Jackknife uncertainties in Figure 4.2 gives insight into this. This ratio is close to unity for the small scales, meaning that the χ^2 statistic behaves as expected with Poisson errors. The large scale $\omega(\theta)$ have larger uncertainties than would be provided by Poisson statistics, meaning these uncertainties are overestimated from a Poisson point of view. The χ^2 values for the power law fits in Kim et al. (2014) also show similar behaviour.

Finally, Figure 4.8 shows the spatial distributions of EROs whose correlation function is measured in Figure 4.3. The unmasked regions (where data could be selected from, and where random data points are place) are shown in grey. Large holes where extremely bright stars which are significantly saturated in HSC data are visible (from using saturated star masks available for the HSC-SSP; Coupon et al., 2018). The spatial distribution appears uniform, so we do not expect there to be unforeseen, significant systematic affects.

If we convert the angular scale of the break in the power laws (Figure 4.6), $\theta = 1 \times 10^{-2}$ deg to a comoving separation at $z = 1.2$ (the peak of the ERO redshift distribution), we obtain a value of $\sim 1.0\,\mathrm{Mpc}\ h^{-1}$. At an angular scale of $\theta \sim 4 \times 10^{-2}$ deg, where the exponential

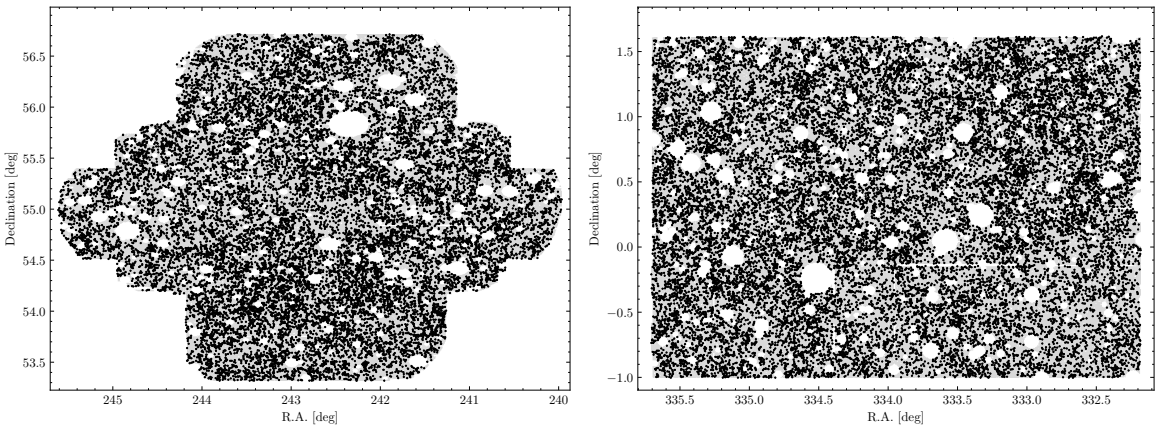

(a) ElaisN1 (b) SA22

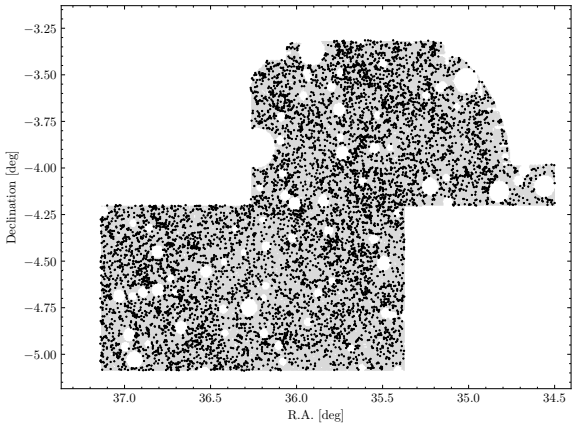

(c) XMM-LSS

Figure 4.8: Spatial distributions of HSC-selected EROs $K < 21.2$, for each of the three fields with HSC data. Grey regions are not masked, and are where random data points are placed. The empty circles within the are masked regions using the HSC masks.

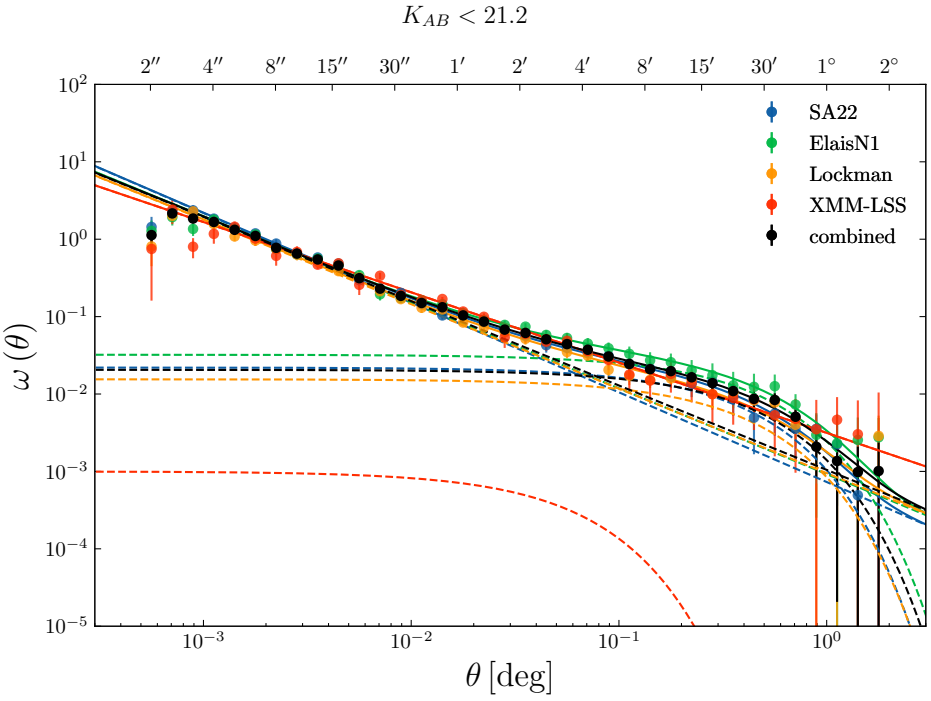

Figure 4.9: Integral constraint-corrected angular two point correlation function, $\omega(\theta)$, for $K_{\rm AB} < 21.2$ PS1-selected EROs. Measurements of $\omega(\theta)$ are shown for all four DXS fields, and the combined measurement. The solid line is the fitted function for each dataset, and the dashed lines the two components of the function. No convergent PLE model solution could be found for XMM-LSS, which is driven to a power law, and the exponential component's parameters shown represent the lower bounds of the parameter.

component begins to dominate in PLE fitting model (Figure 4.3), the corresponding comoving physical separation is $\sim 4.0\,{\rm Mpc}\ h^{-1}$. These can be interpreted as crude estimates of the size of the dark matter host halo of ERO galaxies. We prefer the latter, as it is considers the clustering at all scales simultaneously.

4.2.2 PS1-selected EROs

Figure 4.9 shows the 2PCF of PS1-selected EROs $(i-K)_{\rm AB} > 2.45$ with $K_{\rm AB} < 21.2$.

We choose to fit the model in Figure 4.9 using data points only $\theta > 0.001^\circ = 3.6''$, as the $\omega(\theta)$ data points on scales smaller than this appear to drop off for all fields, whereas those from HSC continue to increase with smaller θ. This effect and subsequent choice can be justified by considering the imaging quality of the PS1 survey as compared to HSC. PS1 quotes an average i-band FWHM seeing value of $1.1''$ compared to HSC's $0.6''$, meaning that the very close pairs of red galaxies (which are, by selection, faint at these optical wavelengths) are more likely to be blended in PS1 imaging.

We do not find any convergent PLE solution for the XMM-LSS measurement of $\omega(\theta)$; the

fit continually reduces to a power law by driving A_2 to zero, and β to large numbers, due to the proportionally larger uncertainties on the XMM-LSS measurements. Because of this, the best fitting power law slope for XMM-LSS is necessarily shallower in an attempt to explain the large scale $\omega(\theta)$ data points.

The values for the best fit are recorded in Table 4.3. We do not report the best fitting A_2 and β parameters for XMM-LSS; they are arbitrarily small and large respectively.

The power law slopes for the PLE model fits for the PS1/DXS selection are shallower than those of the HSC/DXS selection. This can again be explained when considering the PS1/DXS catalogue missing small scale pairs; the smallest scales (where the power law component dominates) are crucial for estimating the slope without the influence of the exponential component.

Figure 4.10 shows the PDF of the PLE model fitting parameters for the four fields, and the combined measurement, for the $K_{\rm AB} < 21.2$ PS1-selected EROs. As with the HSC-selected EROs, we present the log of the amplitude parameters A_1 and A_2, and the cutoff parameter β. The XMM-LSS PDF is clearly not concordant with the other PDFs, nor the combined measurement. The 1D β PDF for XMM-LSS shows that there is no local maximum that the fitting procedure has missed. The amplitude of the exponential component A_2 is effectively irrelevant for very large β values. This PDF is also obviously not symmetric, or finite, further justification for not reporting the values in Table 4.3. On the other hand, the PDFs for the other three fields (SA22, ElaisN1 and Lockman) and the combined measurement show strong agreement. The conclusions we draw about the correlation of the parameters based on the contours for HSC-selected sample (in Figure 4.5) also hold for these three fields; the strongest correlations between parameters are in the component parameters, and secondly the power law parameters and the exponential parameters.

Figure 4.11 shows power laws fit separately to the small and large scales. We use the same break 0.01° as with the HSC sample, and keep the lower limit of 0.001° for the smallest scales.

For the PS1-selected samples, we do not observe a strong disparity between the PLE model compared to the individual power law fit to the small scales measurements alone. This can be explained using the same logic as the HSC sample having the steeper PLE slopes compared to the PS1 PLE slopes; the smallest scales are very most important for this measurement.

The PLE parameters in Table 4.3 for the XMM-LSS field are clearly extremely different to those in the other three fields, as are the power law parameters in Table 4.4. However, the PDFs in Figure 4.12 show that this does not significantly affect the combined measurement, as the three other fields are concordant with it.

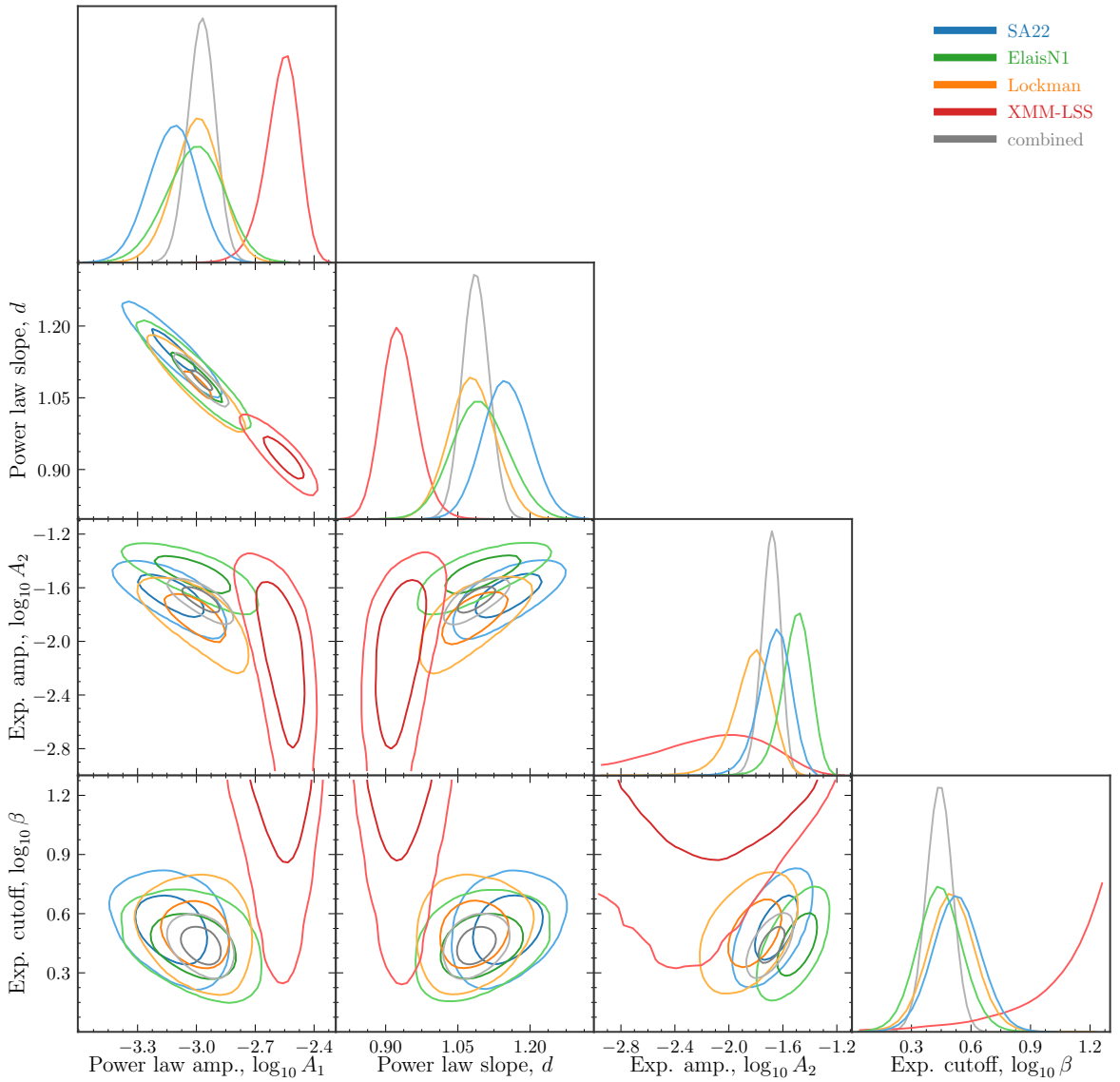

Figure 4.10: PDF corner plot for fitting Equation 4.1.6 to the $\omega(\theta)$ measurements presented in Figure 4.3 (EROs selected with PS1 data). PDFs are presented for each of the four DXS fields, and the combined measurement. The 1D PDFs for the amplitude parameters A_1 and A_2 and β cutoff parameter (the first, third and fourth panels along the diagonal) are not symmetric, but appear so in log scale.

Table 4.3: Best fitting parameters for the power law plus exponential cutoff model to the angular two point correlation function of PS1-selected EROs, for all four DXS fields, and the combined measurement. We also provide the reduced χ^2 (χ^2 per degree of freedom) goodness-of-fit statistic for each fit. Parameter uncertainties are estimated using the PDFs shown in Figure 4.10. [a]We do not report the parameters A_2 or β; Figure 4.10 shows there is no convergent solution.

Parameter	A_1 ($\times 10^4$)	d	A_2 ($\times 10^2$)	β	χ^2_ν
SA22	$7.3\pm^{2.5}_{1.9}$	1.16 ± 0.05	$2.2\pm^{0.7}_{50.5}$	$3.1\pm^{1.1}_{0.8}$	0.511
ElaisN1	$9.2\pm^{4.0}_{2.9}$	$1.11e \pm 0.06$	$3.2\pm^{0.9}_{0.7}$	$2.6\pm^{0.8}_{0.6}$	0.461
Lockman	$9.5\pm^{3.2}_{2.4}$	1.09 ± 0.05	$1.6\pm^{0.6}_{0.4}$	$2.9\pm^{1.0}_{0.7}$	0.778
XMM-LSS	$3.1\pm^{0.6}_{0.4}$	0.91 ± 0.03	-[a]	-[a]	0.753
combined	$10.5\pm^{1.8}_{1.5}$	1.09 ± 0.032	$2.06\pm^{0.34}_{0.29}$	$2.69\pm^{0.43}_{0.37}$	0.605

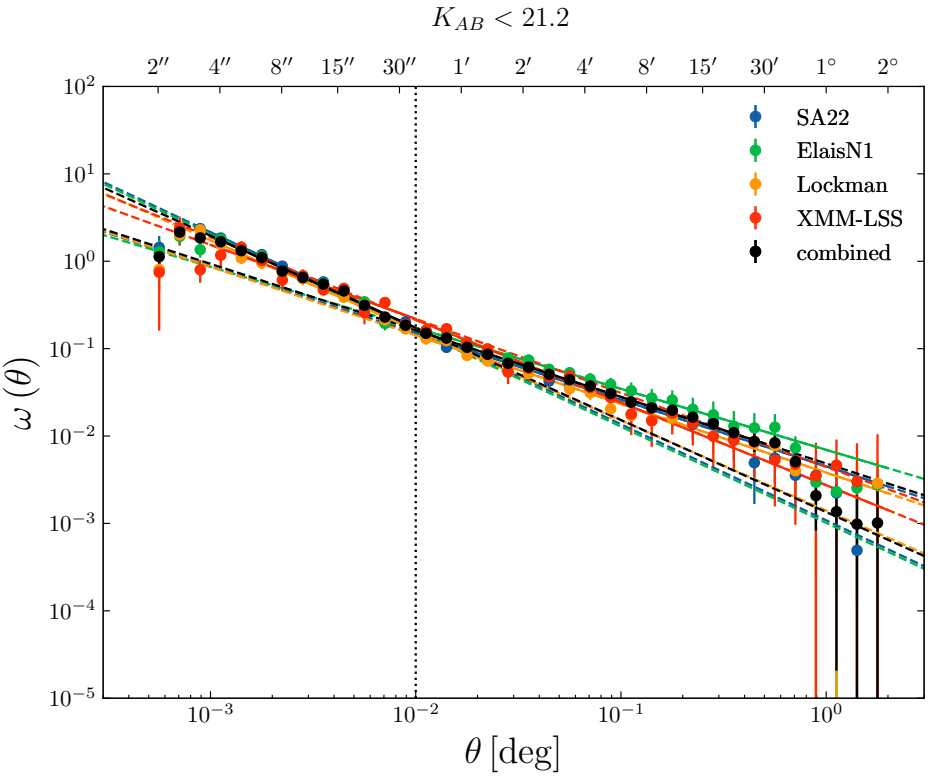

Figure 4.11: Separate power law fits for small and large scales, for EROs $i-K > 2.45$ selected with PS1 optical data. Solid lines are the power laws over which the data were fit; dashed lines extrapolate these fits over the whole range of scales.

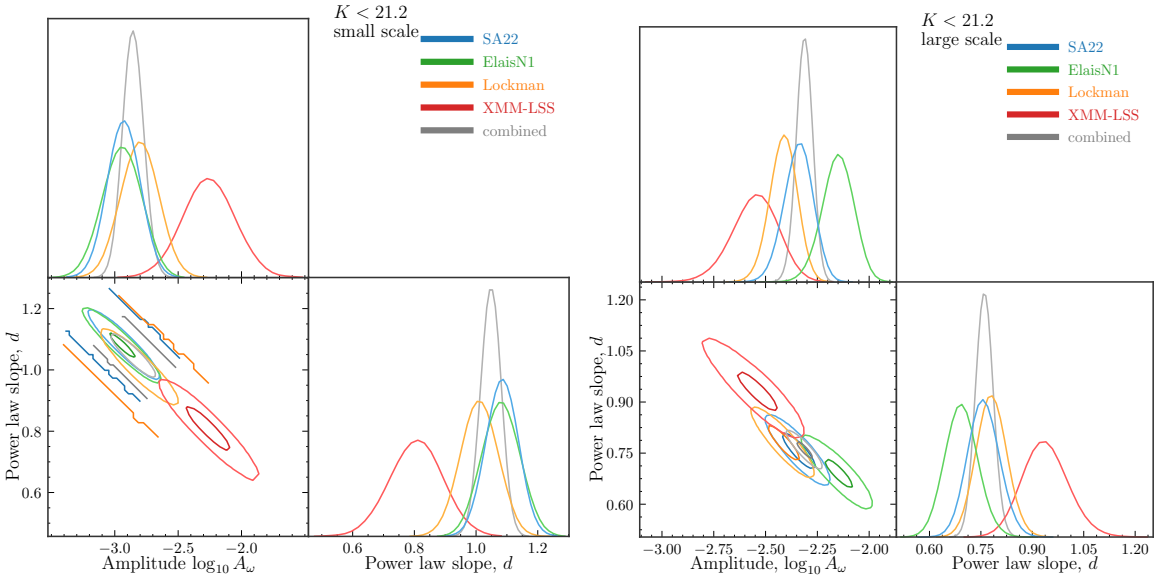

(a) Small-scale power law fit.

(b) Large-scale power law fit.

Figure 4.12: PDFs for parameters for small and large scale power laws, estimated separately, for PS1-selected EROs $K < 21.2$.

Table 4.4: Best fitting parameters for the power law plus exponential cutoff model to the angular two point correlation function of PS1-selected EROs, for the three fields and combined. We also provide the reduced χ^2 (χ^2 per degree of freedom) goodness-of-fit statistic for each fit. Parameter uncertainties are estimated using the PDFs shown in Figure 4.5.

Field	$A_{\omega,ss} \times 10^3$	$d_{\rm ss}$	$A_{\omega,ls} \times 10^3$	$d_{\rm ls}$	$\chi^2_{\nu,\rm ss}$	$\chi^2_{\nu,\rm ls}$
SA22	$10.9\pm^{4.1}_{3.1}$	1.10 ± 0.05	$4.5\pm^{0.8}_{0.7}$	0.76 ± 0.04	0.985	0.275
ElaisN1	$10.2\pm^{4.9}_{3.5}$	1.10 ± 0.06	$7.0\pm^{1.3}_{1.1}$	0.70 ± 0.05	0.847	0.145
Lockman	$14.1\pm^{6.4}_{4.6}$	1.03 ± 0.05	$3.8\pm^{0.6}_{0.5}$	0.79 ± 0.04	0.431	0.504
XMM-LSS	$44\pm^{35}_{22}$	0.84 ± 0.08	$2.7\pm^{0.8}_{0.6}$	0.94 ± 0.06	1.523	0.559
combined	$13.5\pm^{0.3}_{0.2}$	1.05 ± 0.03	$4.9\pm^{0.45}_{0.40}$	0.76 ± 0.02	1.269	0.253

Recalling the values from K14 of amplitude $A_{\omega,\mathrm{small}} = (1.42 \pm 0.4) \times 10^{-3}$ with slope $\mathrm{slope}^{\mathrm{small}} = 1.08 \pm 0.05$ on small scales, and $(7.35 \pm 2.3) \times 10^{-3}$ with $\mathrm{slope}^{\mathrm{large}} = 0.69 \pm 0.10$ on large scales, we see that our values (from the DXS-PS1 selected sample) of $A_{small} = (1.35 \pm^{0.3}_{0.2}) \times 10^{-3}$ with $d_{small} = 1.05 \pm 0.03$, and $4.9 \pm^{0.45}_{0.4}$ with 0.76 ± 0.02 are in much closer agreement. On small scales we attribute this to the similar ranges of fitting as compared with our much steeper HSC-selected sample; as discussed before, we choose to fit the data in the interval $(0.001^\circ < \theta < 0.01^\circ)$, which has the same lower bound as their $(0.001^\circ < \theta < 0.02^\circ)$. This adds weight to the conclusion that the smallest scales (where intra-halo clustering is dominant) are important for estimating the slope of the small scale power law.

4.2.3 Magnitude-limited clustering

We now look at the variation in the slopes and amplitudes of ERO clustering with magnitude limited samples, and will compare how our results compare to those in the literature.

Figure 4.13 shows the measurement of $\omega(\theta)$ of HSC-selected EROs, for various magnitude cuts, ranging from $K < 20.2$ to $K < 22.7$. We show the power laws fit separately to small and large scales in these panels. The data in the middle left panel is the same as in Figure 4.6.

The solid grey line in each of the panels is identical. It is a power law with slope 0.8 and amplitude 1×10^{-2}, and is added to guide the eye when making comparisons between panels. Visually this demonstrates that the brightest selections of EROs are more strongly clustered on all scales, as has been demonstrated in previous studies (Brown et al., 2005, ; K11; K14). It also demonstrates that the break observed in $\omega(\theta)$ is present at all magnitude limits considered.

We note that the integral constraint for the brightest selection of galaxies is significantly larger than for the other samples at 0.014, as compared to the ~ 0.003 for the rest of the magnitude limits.

Figure 4.14 shows the power law parameters plotted against limiting magnitude. This show more explicitly that the brightest selections of EROs do indeed exhibit the strongest clustering. We present also some measurements from previous works for comparison. For the Kim et al. (2014) data points, we agree reasonably well, although their amplitudes slightly larger, with shallower slopes. The amplitudes of Brown et al. (2005) are estimated with a fixed slope of 0.87, and the correlation function measured over a smaller range of scales

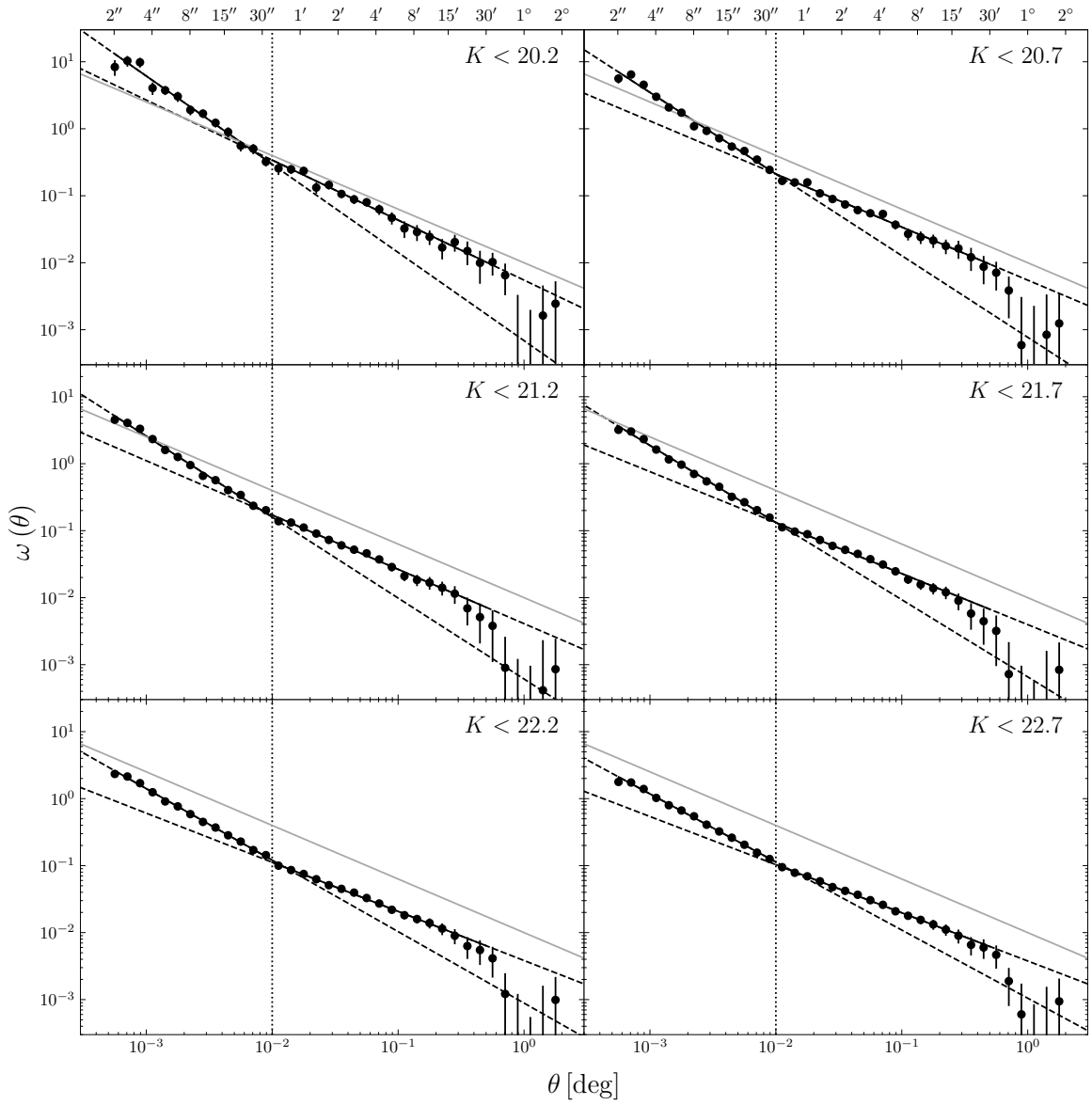

Figure 4.13: Separate power law fits for small and large scales, for several magnitude K-band magnitude cuts, for the combined measurement from the four fields. In each panel, the solid grey line is the same power law, with slope 0.8, and amplitude 1×10^{-2}, to guide in comparisons between panels. We note that the integral constraint for the brightest cut is larger than that for the the other five by some margin (0.014, as compared to the ~ 0.003), although we do not expect this to make a significant difference, especially for the smallest scales.

($0.003 < \theta < 0.7$), and with a much larger $\Delta \log(\theta)$. Our large scale amplitudes are similar to theirs at the brightest magnitudes, but with slopes slightly steeper (although within the error bars). Table 4.5 reports the parameters plotted in this Figure. For the combined measurement, we observe that the amplitudes increase by around 40% for both the small and large scales, but change in the small scale power law slope is much larger than that of the large scales. The small scale slope at the brightest limit is 1.32 ± 0.06, and reaches 1.02 ± 0.02 at the faintest cutoff. As a comment on the χ^2_ν values for these fits: for the small scales, $\chi^2_{\nu,\mathrm{ss}}$ are close to one, where as those for the large scales, $\chi^2_{\nu,\mathrm{ls}}$ are much less than one. Following on from the discussion of the discussion in Section 4.1.2, and on the χ^2_ν values for the PLE model fits, this is not unexpected for the large scales. As the small scale fitting uses $\theta < 1 \times 10^{-2}$ (less than $1'$) where the uncertainties behave as Poission (jackknife uncertainties are comparable with the Poisson estimates up to scales of a few arcminutes), we expect that their χ^2_ν values should be comparable with unity.

For the faintest magnitude cuts ($K < 21.2$ and fainter), the estimation of the integral constraint converges readily for the individual fields. However, this is not the case for the brightest cuts. We can force the integral constraint to converge by applying a very strong prior - using the posterior distribution of the final best fit parameters from the combined fields as a prior on the parameters for the individual fields makes this calculation converge. This use of the posterior is not strictly allowed; it could be argued that we are in effect "using the data twice", although it is a superset of the data we are using twice. We note that the values of $\mathcal{I}$ that obtain with this method are not different to those without applying this constraint at the K cuts where the prior is not needed. Further, after we have determined $\mathcal{I}$ we again use an uninformative prior to estimate final parameters which we quote, eg. for the PDFs presented in Figure 4.5, and the power laws for the small and large scales).

For their small scale slopes, K11 also observe decreasing slopes, from $\delta = 1.15 \pm 0.15$ at $K_{\mathrm{Vega}} < 18.3$ to $\delta = 0.99 \pm 0.05$ at $K_{\mathrm{Vega}} < 20.0$, although their large scale slopes are much shallower than ours for all magnitude cuts.

The strong clustering of red galaxies is a result of the so-called "environmental quenching", mentioned in Section 1.2: the merging of galaxies depletes reservoirs of gas, disfavouring star formation causing galaxies to become passive. As we measure the clustering of EROs with varying apparent magnitude limits for comparison with literature, understanding the exact dependence of the clustering strength on mass and redshift is difficult to determine. However, as the brighter magnitude cuts on the whole select the most massive, and lowest redshift

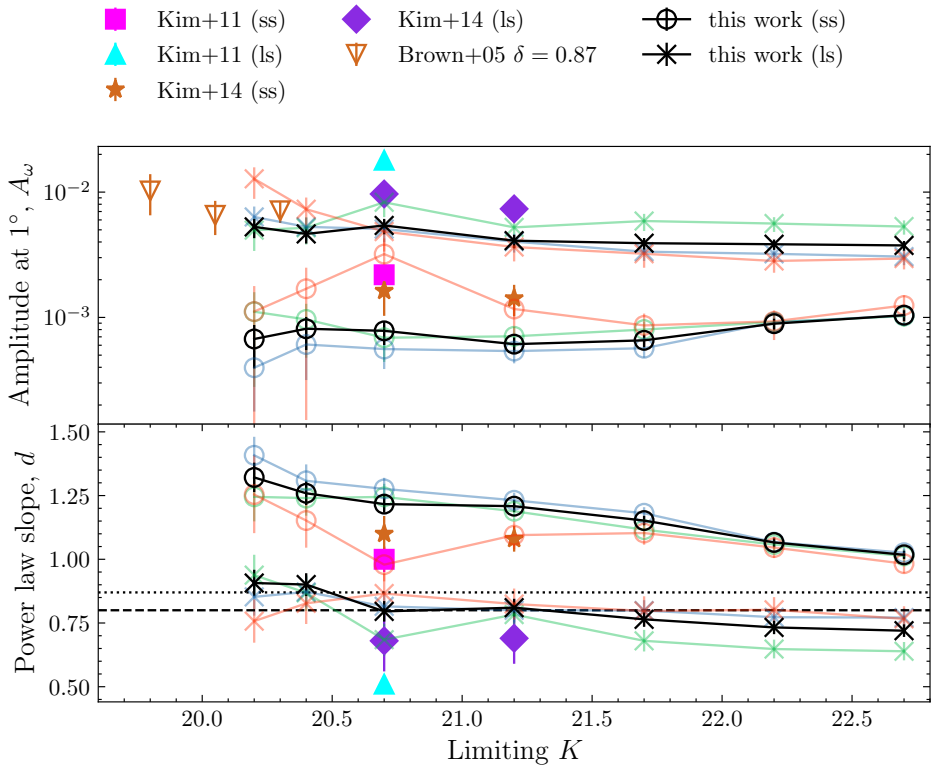

Figure 4.14: The changing power law best fitting parameters with varying K limiting magnitude. The upper panel shows the amplitude at 1°, and the lower panel the power law slope. Black circles and crosses show our parameters for the best small and large scales respectively. Grey data points are literature values. The Kim et al. (2011) are data point is from their least red ERO selection ($(i-K)_{\rm Vega} > 3.96$), Kim et al. (2014) from their HSC sample (their Table 4). The Brown et al. (2005) data points were fitted with a fixed power law slope of 0.87 (which is therefore not shown in the lower panel), and were quoted as being measured at 1′, which we then extrapolate to 1° with their fixed slope. The dashed line in the lower panel shows the fiducial fixed slope of $\delta = 0.8$, and the dotted line $\delta = 0.87$

galaxies, we tentatively say that the trend is for the more massive, and lower redshift galaxies to be the more strongly clustered (both in terms of absolute values of ω, and the steeper slopes). With the simple empirical fits we compute, we are unable to say whether this is environmental quenching becoming more efficient at lower redshifts, or simply a compounding effect where this process builds up over cosmic time. In their study of passive galaxies, Ji et al. (2018) expect that the efficiency of the environmental quenching is in fact increased at lower redshifts due to the fact that structures in the universe (on the whole) grow with cosmic time.

4.2.3.1 Single power law models

Similarly, Figure 4.15 shows how the parameters of a single power law change with magnitude. As previously, we observe that the brightest selections of galaxies show the strongest

Table 4.5: Parameters for power laws fit separate small and large scales, for HSC-selected EROs for varying magnitude cuts, for the combined fields (presented in Figure 4.14) We report the reduced χ^2 goodness-of-fit statistic in the last two columns.

K_{lim}	$A_{\omega,ss} \times 10^3$	$d_{\rm ss}$	$A_{\omega,ls} \times 10^3$	$d_{\rm ls}$	$\chi^2_{\nu,\rm ss}$	$\chi^2_{\nu,\rm ls}$
20.2	$0.7\pm^{0.3}_{0.2}$	1.32 ± 0.06	$5.3\pm^{1}_{0.8}$	0.91 ± 0.05	1.071	0.429
20.4	$0.8\pm^{0.3}_{0.2}$	1.26 ± 0.05	$4.6\pm^{0.8}_{0.6}$	0.90 ± 0.04	1.431	0.555
20.7	$0.8\pm^{0.2}_{0.1}$	1.22 ± 0.03	$5.4\pm^{0.8}_{0.7}$	0.80 ± 0.04	1.270	0.505
21.2	$0.61\pm^{0.09}_{0.08}$	1.21 ± 0.02	4.1 ± 0.5	0.81 ± 0.03	1.250	0.413
21.7	$0.66\pm^{0.08}_{0.07}$	1.15 ± 0.02	3.9 ± 0.4	0.76 ± 0.03	1.390	0.524
22.2	0.89 ± 0.09	1.07 ± 0.02	$3.8\pm^{0.4}_{0.3}$	0.73 ± 0.03	1.001	0.198
22.7	$1.04\pm^{0.11}_{0.10}$	1.02 ± 0.02	$3.8\pm^{0.4}_{0.3}$	0.72 ± 0.02	1.193	0.117

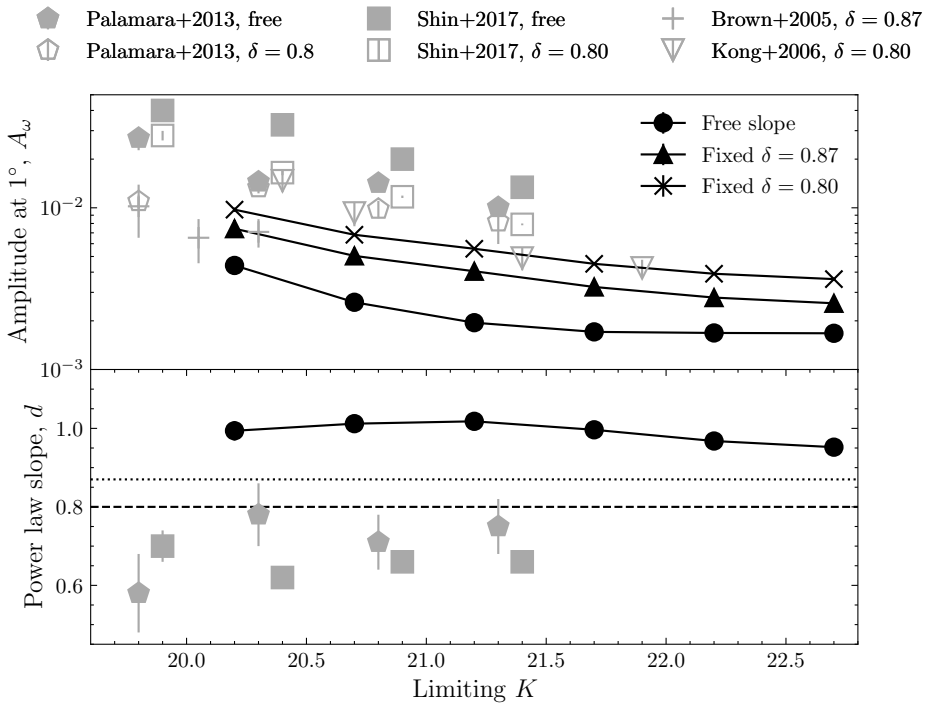

Figure 4.15: Parameters for single power laws fit to HSC-selected EROs, for varying limited magnitudes, with the slope as a fixed parameter, and fixed to $\delta = 0.80$ and 0.87 as seen in the literature. We do not plot the fixed slopes in the lower panel, but the dashed and dotted lines are $\delta = 0.80$ and 0.87 respectively. Literature data are plotted with solid symbols having fixed slopes, and empty symbols having fixed slopes. Measurements reported at $1'$ are extrapolated to $1°$, slopes reported as γ are plotted as $\delta = \gamma - 1$, and Vega magnitudes are converted to AB.

clustering. Predictably, the steeper fixed slope of 0.87 requires smaller amplitudes at 1°. We observe that the slope of the clustering begins to plateau at the faintest magnitude cuts, especially for the free slope estimates. This can be attributed to the turnover in number counts in Figure 3.12; we are adding fewer galaxies to the sample after this point, and they are likely at higher redshifts, so serve only to 'dilute' the strong clustering exhibited by the brightest selections. This Figure also shows estimates of the clustering amplitude of EROs from previous works. The estimates for Brown et al. (2005) are for EROs selected with $R - K_s > 5.0$, and use a fixed slope of $\gamma = 1.87$ (which we write as $\delta = 0.87$; see Equation 4.4.1), and have R band imaging significantly deeper than the K_s (their distribution of $R-K_s$ reaches at least 6). Data from Palamara et al. (2013) also shows the same trends. The most recent estimates presented are from Shin et al. (2017), who measure the clustering of $(R - K)_{\rm Vega} > 5.0$ EROs in the *Subaru* SuprimeCam GTO 2deg^2 field, which is a broader and redder colour than our selection. They use a fixed slope of $\delta = 0.8$, and also allow a freely varying slope. At all magnitude cuts, they observe larger amplitudes at 1°, but with significantly shallower slopes. As we find from our analysis, their steeper slopes require smaller amplitudes, although they report best-fitting slopes that are significantly shallower than our own, including the slope used for their fits. We also point out that all of these studies use significantly larger $\Delta \log(\theta)$ to measure $\omega(\theta)$ than our work.

4.3 Passive BzK clustering

The number counts of PE-gzKs are significantly smaller than that of EROs (see Figures 3.17 and 3.12). The differential number counts are similar approaching the limiting depth of our survey, but at the brighter magnitudes, the counts of EROs are significantly higher. Figure 3.21 shows that at $K < 21.5$ for instance, there are 36424 EROs in the ElaisN1 and XMM-LSS fields, compared to the 14124 SF-gzKs, and 5543 PE-gzKs.

The advantage DXS has is the large area covered at this slightly shallower depth, so we feel that our analysis of this selection of galaxies is still worthwhile.

As with the number counts, we use only the HSC-selected sample of gzKs.

Figure 4.16 shows the spatial distribution of PE-gzKs in the three DXS-HSC fields. They demonstrate that there are no significant spurious structures which would affect the clustering measurements. Given that the surface density of these objects is lower, we choose to show the distribution for a fainter magnitude cut that the EROs. We also show these distributions

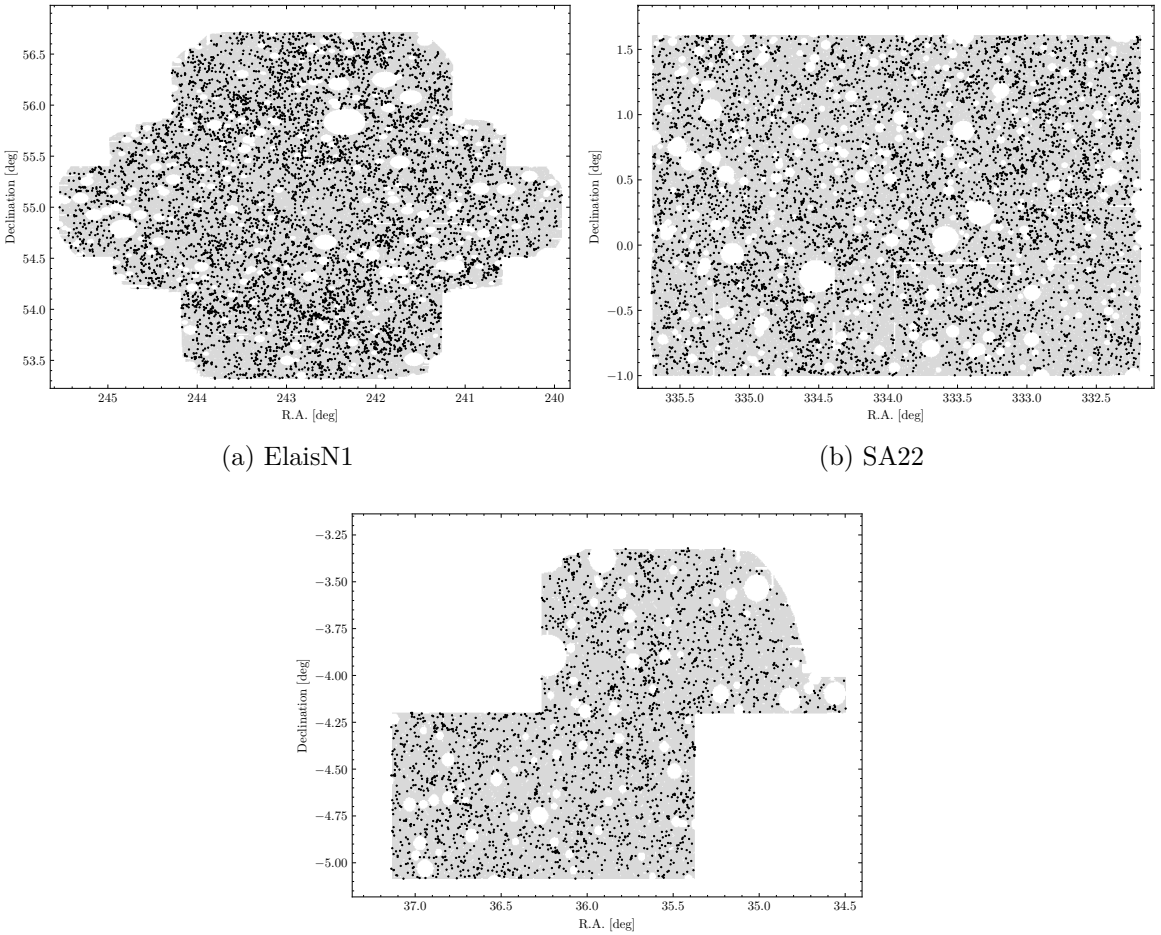

(a) ElaisN1

(b) SA22

(c) XMM-LSS

Figure 4.16: Spatial distributions of HSC-selected PE-gzKs, $K < 22$, for each of the three fields with HSC data. Grey regions are not masked, and are where random data points are placed for the correlation function measurements. The white circles are regions which are masked due to saturated stars, using the masks provided on the HSC webpages.

to check that the incompleteness in the number counts of PE-gzKs is not restricted to one specific region of the any one field, unfairly biasing measurements of $\omega(\theta)$.

However, this lower object surface density means that the clustering measurements for the individual fields are extremely noisy, and for the brightest magnitude cuts, do not have convergent values for the integral constraint. For this reason, we only show the combined measurements, which are presented in Figure 4.17.

As we observe that our number counts of PE-gzKs are especially low for the SA22 field, we do not include the data from this field in measuring the combined $\omega(\theta)$ for $K > 21.5$.

We note further that as our number counts of PE-gzKs are significantly lower than those in the literature by $K \sim 22$ (ie, the sample is not complete), our clustering measurements will not be as robust as other deeper, studies at the faintest magnitudes.

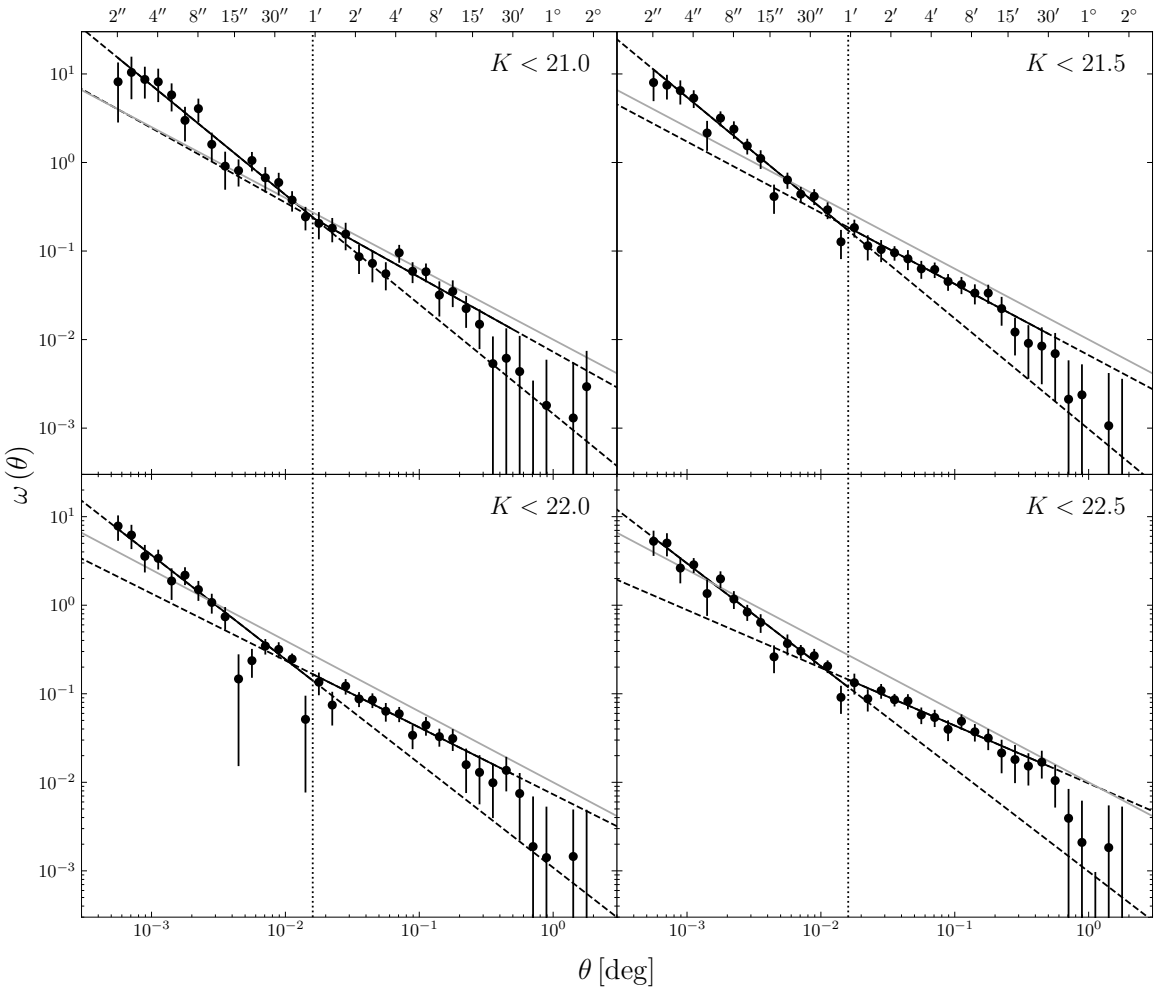

Figure 4.17: Integral constraint-corrected angular correlation function $\omega(\theta)$ of HSC-selected PE-gzKs using the measurement from the three combined fields, for various K-band magnitude cuts. Power laws are fit separately to the small and large scales, but are not joined - neither smoothly, nor continuously. Solid black lines are the range of separation θ where these have been fit, and the dashed black lines extrapolate these to contrast with the other fit. The break scale $1'$ is denoted by the vertical dotted line (the same in all panels). The solid grey line is a constant power law with slope $\delta = 0.8$, to guide the eye in comparison.

Table 4.6: Best fitting power laws for small and large scales, for magnitude-limited samples of PE-gzKs. The last two columns are the reduced χ^2 goodness-of-fit statistic for the small and large scale fits. Amplitudes A_ω are reported as the amplitude at 1°.

K limit	$A_{\omega,\mathrm{ss}} \times 10^3$	d_{ss}	$A_{\omega,\mathrm{ls}} \times 10^3$	d_{ls}	$\chi^2_{\nu,\mathrm{ss}}$	$\chi^2_{\nu,\mathrm{ss}}$
21.0	$1.5\pm^{1}_{0.6}$	1.24 ± 0.10	$7.2\pm^{2.6}_{1.9}$	0.8 ± 0.1	0.738	1.065
21.5	$1.0\pm^{0.5}_{0.3}$	1.25 ± 0.07	$6.7\pm^{1.8}_{1.4}$	0.80 ± 0.08	1.326	0.407
22.0	$1.1\pm^{0.5}_{0.4}$	1.18 ± 0.07	$7.3\pm^{2.1}_{1.6}$	0.76 ± 0.09	2.426	0.651
22.5	$1.0\pm^{0.4}_{0.3}$	1.16 ± 0.06	$9.7\pm^{2.3}_{1.9}$	0.65 ± 0.07	1.170	0.330

Table 4.7: Best fitting parameters estimated for the power law-plus-exponential model

K limit	$A_1 \times 10^3$	d	$A_2 \times 10^3$	β	χ^2_ν
21.0	$1.2\pm^{1}_{0.5}$	1.2 ± 0.1	59 ± 26	$7.5\pm^{3.1}_{1.9}$	0.551
21.5	$0.6\pm^{0.4}_{0.2}$	1.29 ± 0.08	$55\pm^{15}_{14}$	$5.5\pm^{1.4}_{1.1}$	0.644
22.0	$0.3\pm^{0.3}_{0.1}$	1.35 ± 0.10	$68\pm^{16}_{15}$	$5.9\pm^{1.5}_{1.2}$	1.080
22.5	$0.5\pm^{0.3}_{0.2}$	1.24 ± 0.09	$55\pm^{11}_{10}$	$4.0\pm^{0.9}_{0.8}$	0.644

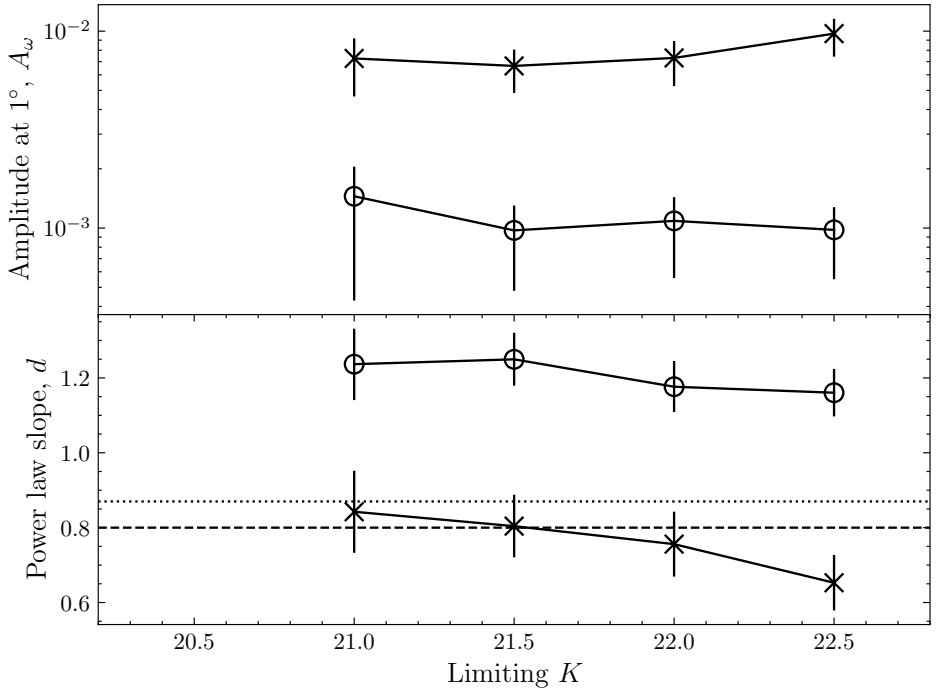

Figure 4.18: Small and large scale power law parameters for HSC-selected PE-gzKs, for the combined measurements. Large open circles are parameters estimated for the small scales, and crosses are those for large scales. Dashed and dotted black lines in the lower panel are commonly used slope values of $\delta = 0.8$ and 0.87.

As with our investigation of the correlation functions of EROs, we use the PLE function in order to find an appropriate value for the integral constraint, and then separately fit power laws to the small and large scales, up to the break scale, $\theta < 1'$, for small scales, and $1' < \theta < 30'$ for large scales. The best fitting values of this are tabulated in Table 4.6, and plotted against limiting magnitude in Figure 4.18.

The values for the integral constraint $\mathcal{I}$ we obtain for this galaxy selection is typically $0.003-0.005$.

We visually determine the break to be at $\sim 1' = 0.017°$, which is larger than the $36''$ ERO break we used in the earlier Sections. This corresponds to 1.22 Mpc comoving at redshift $z = 1.35$, the centre of the modal bin of the photometric redshift distribution (see Figure

3.19b). The break (at least visually) appears to be much stronger than that for EROs, and the larger difference in the power law slopes between scales at all magnitude cuts also indicates this.

For the brightest magnitude cut, $K_{\rm AB} < 20.5$, there are very few pairs at the smallest separations, so there are no $\omega(\theta)$ points for the smallest θ bins.

As with the EROs, clearly the brightest samples of PE-gzKs are the most strongly clustered. We observe that the slopes of large scales decrease for fainter magnitude cuts to shallower than $\delta = 0.8$ However, with the complex relationship between depth, angular separation, and redshift distribution, it is difficult to say if this is due to physical properties of the clustering, or a result of selection effects. The slopes for the brightest cut do not appear follow this trend, although the uncertainty on these values are extremely large, so could still be considered to be consistent with this.

In the discussion of the reduced χ^2_ν statistics for the ERO coefficients, we noted that those for the small power law were concordant with one, whereas the small scales were consistently much smaller. This holds for the faintest three magnitude cuts here, although the brightest one has χ^2 values indicating that the jackknife errors are similar to the Poisson estimates here (that is, the number counts are so small, the Poisson uncertainties approach jackknife estimates).

Table 4.7 further lists the best fitting parameters of the PLE function. As with the EROs, we also see here that the power law slope (which explains the small scale) of the PLE is consistently steeper than the single power law fit to the small scale $\omega(\theta)$ measurements.

Sato et al. (2014) also discuss using a more complex fitting than the single power law, to their sample of PE-$gzHK$ selected galaxies (the selection criteria discussed in Arcila-Osejo & Sawicki, 2013), to $K \sim 23$ in $2.5\,\mathrm{deg}^2$ of imaging. Similar to Kim et al. (2011)'s ERO and DRG study, they use the linear sum of two power laws. In contrast to our work, they observe the departure from the single power law at an angular scale of $\log_{10}(\theta/1^\circ) = -2.7$ ($\theta = 0.002^\circ$). From their Figure 11, we extract a slope of $\delta = 1.80$ for the small scale power law, which is significantly steeper even than the power law component in our PLE models. They also observe clustering on large scales which is slightly shallower than the typical $\delta = 0.8$ slope.

Finally, we plot the parameters of a single power law for increasingly faint magnitude cuts in Figure 4.19. Similarly to the discussion of the EROs, the freely-varying power law consistently gives slopes steeper than the often-assumed $\delta = 0.8$, resulting in smaller amplitudes at 1°.

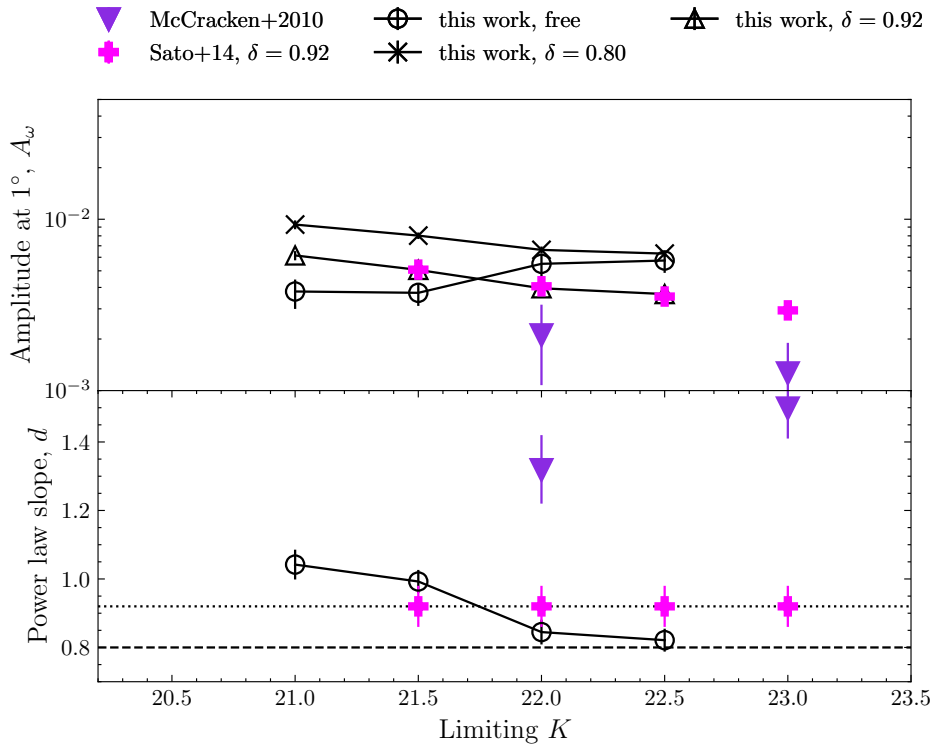

Figure 4.19: Parameters for a single power law, for both a fixed slope of $\delta = 0.8$, and a freely-varying slope. Also plotted are values from similar investigations from Sato et al. (2014) and McCracken et al. (2010). We convert the amplitude values from these works from $1'$ to $1°$ for comparison with our work.

We also plot similar values from Sato's work and that of McCracken et al. (2010), who use deeper COSMOS-WIRCAM data. Sato's work uses a constant slope of $\delta = 0.92$ (reported as $\gamma = 1.92 \pm 0.06$), which they determine from the faintest magnitude cut (ie, the entire sample), and then apply to brighter cuts. Figure 4.19 shows that if we apply a fixed $\delta = 0.92$, the amplitudes we measure are not dissimilar to those measured by Sato at overlapping magnitudes. They measure the correlation function from $0.01^\circ < \theta < 0.32^\circ$ which is a similar range to the range we measure the large scale slope in. We further note that the values of the integral constraint are larger when using the single power law, especially for the brightest magnitude limits, where $\mathcal{I} \sim 0.01$ compared to the $\mathcal{I} \sim 0.003$ we observe for the PLE form. For the case where we allow the slope to vary freely, our slopes (and hence amplitudes) are not in absolute agreement, although for $K < 21.5$ and $K < 22$, we obtain $\delta = 0.99 \pm 0.03$, and $\delta = 0.84 \pm 0.04$, so both still steeper than $\delta = 0.8$. At the brighter end (where the sample is certainly complete), our slopes are certainly steeper.

In contrast, the work of McCracken shows significantly steeper slopes than even the power law in our PLE functional form. Further, they observe the opposite trend in slopes, and show the sample selected with the fainter magnitude cut has the steeper slope. We point out that their work probes scales smaller still than our work and Sato's (their smallest bin is at 4×10^{-4} deg) but do not measure $\omega(\theta)$ for $\theta \gtrsim 0.2^\circ$. In this sense, it may make more sense to compare their values with our small scale power law from Table 4.6, and the PLE power law in Table 4.7. At $K < 22$ they measure a slope of $\delta = 1.32 \pm 0.10$ ($\gamma = 2.32 \pm 0.10$), with an amplitude at $1'$ $A_\omega = (8.41 \pm 4.15) \times 10^{-2}$, which we extrapolate to $A_\omega = (2.12 \pm 1.04) \times 10^3$ at 1° (keeping the same fractional uncertainty). Tenuously, this is similar to that of our PLE slope at this magnitude cut.

Earlier, we discussed Kim et al. (2011)'s conclusion of the continuity between lower redshift LRGs and EROs, based on the strong break. It does not seem unreasonable to extend this conclusion to continuity between EROs and the higher-redshift PE-gzKs: that is, EROs are the same selection of passive galaxies as PE-gzKs, but at a lower redshift. The very large overlap between the selections presented in the Venn diagrams in Chapter 3 makes this argument more compelling. We recall that 97% of the PE-gzKs we select at $K_{\rm AB} < 21.5$ are also selected as EROs, and that when considering the J-band selection to break the old/dusty degeneracy, 53% of the PE-gzKs were also selected as the old EROs (with the added $J_{\rm AB} < 22.9$ constraint).

Finally, we present a comparison between the clustering of the PE-gzKs and the star-forming

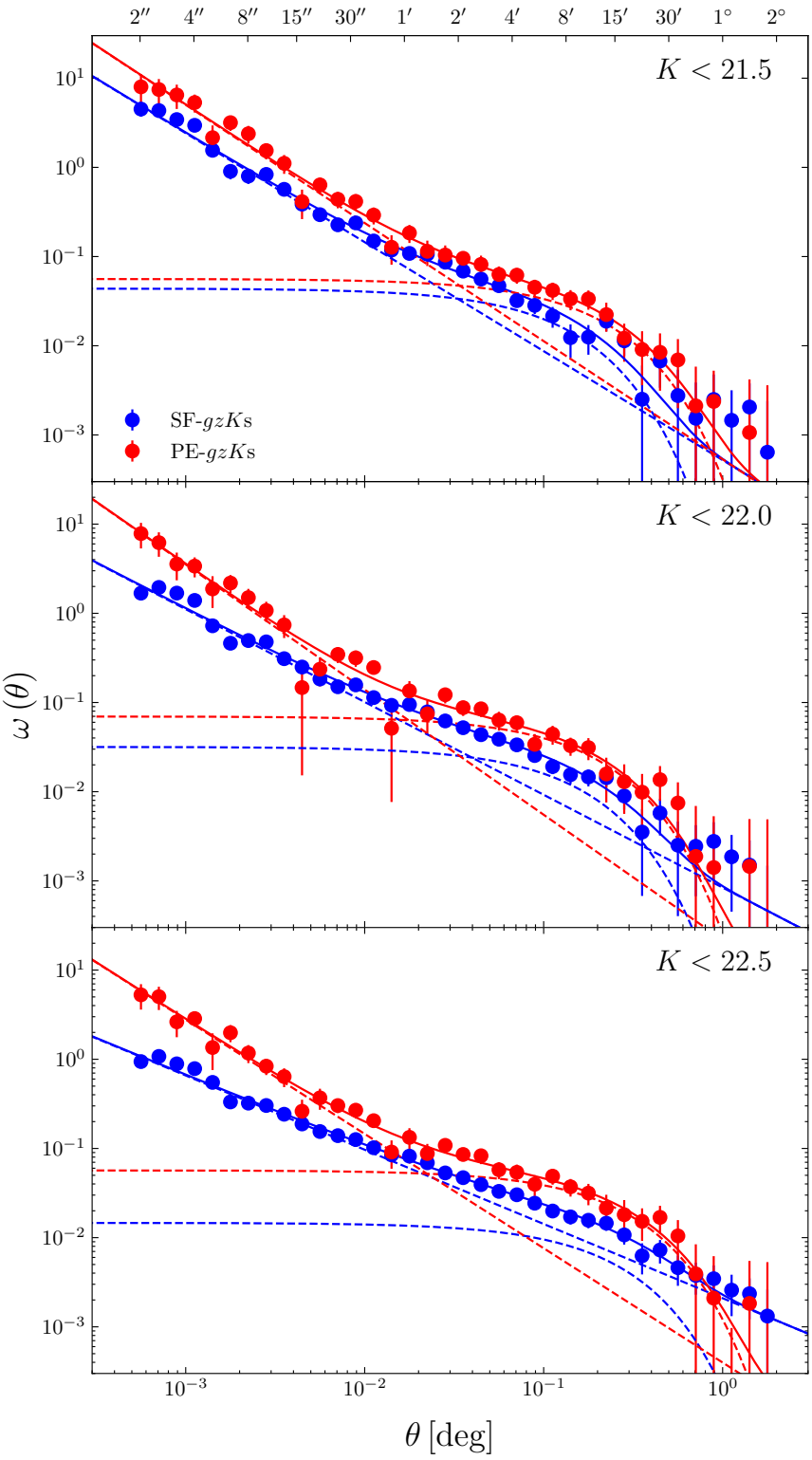

Figure 4.20: Comparison between star-forming and passively-evolving samples of gzK galaxies, at for three limiting magnitudes. SF-gzKs are shown in blue, and PE-gzKs in red. We note that the passive samples use only the ElaisN1 and XMM-LSS fields for the faintest two magnitude cuts. Components of the PLE functional form are shown as dashed lines in the corresponding colours.

SF-gzKs in Figure 4.20.

For the star-forming gzKs, we include all three available fields in the calculation of $\omega(\theta)$ at all magnitude cuts.

As with previous works (Hartley et al., 2008; McCracken et al., 2010; Ji et al., 2018), we show that the passively-evolving galaxies made with this type of selection exhibit significantly stronger clustering than the star-forming sample. We present this comparison for the faintest three magnitudes cuts only, as we point out that the uncertainties on the parameters for the PE-gzK fits are extremely large. In particular, we observe that the slope of the small scale clustering for the passive-galaxies is much steeper than that of the passive galaxies at the faintest magnitude cuts. For the passive galaxies, we measure slopes of $\delta = 1.29 \pm 0.08$, 1.35 ± 0.10 and 1.24 ± 0.09, compared with 1.19 ± 0.07, 1.12 ± 0.05 and 0.82 ± 0.03 for the star-forming galaxies, the latter of which is in fact consistent with the fiducial $\delta = 0.8$ slope.

We note that the differential number counts of passive galaxies have stopped increasing by $K \sim 22$, whereas the star-forming counts continue to increase very steeply. However, the decline is not so significant that we include no new galaxies with increasing depth at $K \sim 22$. Hartley et al. (2008)'s measurement of the 2PCF of the star-forming galaxies still shows a break from the power law.

As mentioned in the introduction, this increased strength in the clustering is to be expected given the prevailing picture of galaxy formation. It is expected that mergers play a role in the quenching of star-forming in galaxies, which are more likely to happen in galaxy-rich environments. The least star-forming galaxies are most likely to live in dense environments, which we measure as much stronger clustering. In other words, it is not the lack of star formation which causes passive galaxies to be clustered, but the reverse: the strong clustering of galaxies causes them to be quenched (cease forming stars), and become passive. Again we interpret this significantly stronger clustering as a result of the environmental quenching mechanism, a similar result of which is show in Ji et al. (2018). However, the advantage of the separation of star-forming and passive populations of BzKs allows us to explicitly demonstrate that this is indeed the case.

We do note a relatively strong break in the clustering for the brightest sample of SF-gzKs. This can be explained by considering that this is will be a narrow redshift range (the brightest cut will select only the nearest galaxies), and that we do expect there to be *some* level of physical processes in the haloes of these galaxies. It is more telling that this feature does not persist star-forming galaxies for the fainter cuts (which will be broader redshift ranges), but

does for the passive galaxies.

4.4 Correlation length

Although high-precision galaxy redshift surveys are the ultimate tool for studying galaxy clustering by measuring the full 3D correlation function $\xi(r)$ (Norberg et al., 2001; Percival et al., 2007; Dawson et al., 2013; Blanton et al., 2017), $\omega(\theta)$ can still provide meaningful insight into the 3D clustering properties of galaxies, given the comparatively-larger areas of sky and cosmological volumes that photometric imaging surveys are able to cover.

The 3D correlation function is mostly assumed to follow a power law,

$$\xi(r) = \left(\frac{r}{r_0}\right)^{-\gamma}, \tag{4.4.1}$$

where $\gamma = 1 + \delta$, and δ is the power law index in Equation 4.1.5. Knowing that the angular correlation function is in fact a projection of the 3D correlation function, the correlation length r_0 can be calculated using Limber's approximation (Limber, 1953; Peebles, 1993), which relates the amplitude of the 2PCF A_ω (measured at 1^{rad}) to the correlation length and the redshift distribution of the galaxy population being studied.

We follow the prescription outlined followed by Kim et al. (2011), further described in Blanc et al. (2008),

$$A_\omega = r_0^\gamma C_\gamma \frac{\int_0^\infty F(z)\, D_A^{1-\gamma}(z)\, \frac{dN}{dz}(z)\, g(z)\, dz}{\left[\int_0^\infty \frac{dN}{dz}(z)\, dz\right]^2}, \tag{4.4.2}$$

where where $C_\gamma = \sqrt{\pi}\Gamma\left(\frac{\gamma-1}{2}\right)/\Gamma\left(\frac{\gamma}{2}\right)$, Γ is the mathematical gamma function, $\frac{dN}{dz}(z)$ is the distribution of redshifts of galaxies in the sample, $D_A(z)$ is the angular diameter distance. The function $g(z)$ is

$$g(z) = \frac{H_0}{c}\left[(1+z)^2\sqrt{1 + \Omega_M z + \Omega_\Lambda\left[(1+z)^{-2} - 1\right]}\right]. \tag{4.4.3}$$

$F(z) = (1+z)^{-(3+\epsilon)}$ is a redshift evolution term, and Blanc et al. (2008) show that $\epsilon = -1.2$ corresponds to fixed clustering in comoving coordinates, and $\epsilon = 0.0$ describes fixed clustering in fixed clustering in proper coordinates. As with Kim, we use the fixed clustering in comoving coordinates.

Kim et al. (2011) use the inverted version of this Limber equation to measure the correlation lengths of their small and large scale power laws for their EROs.

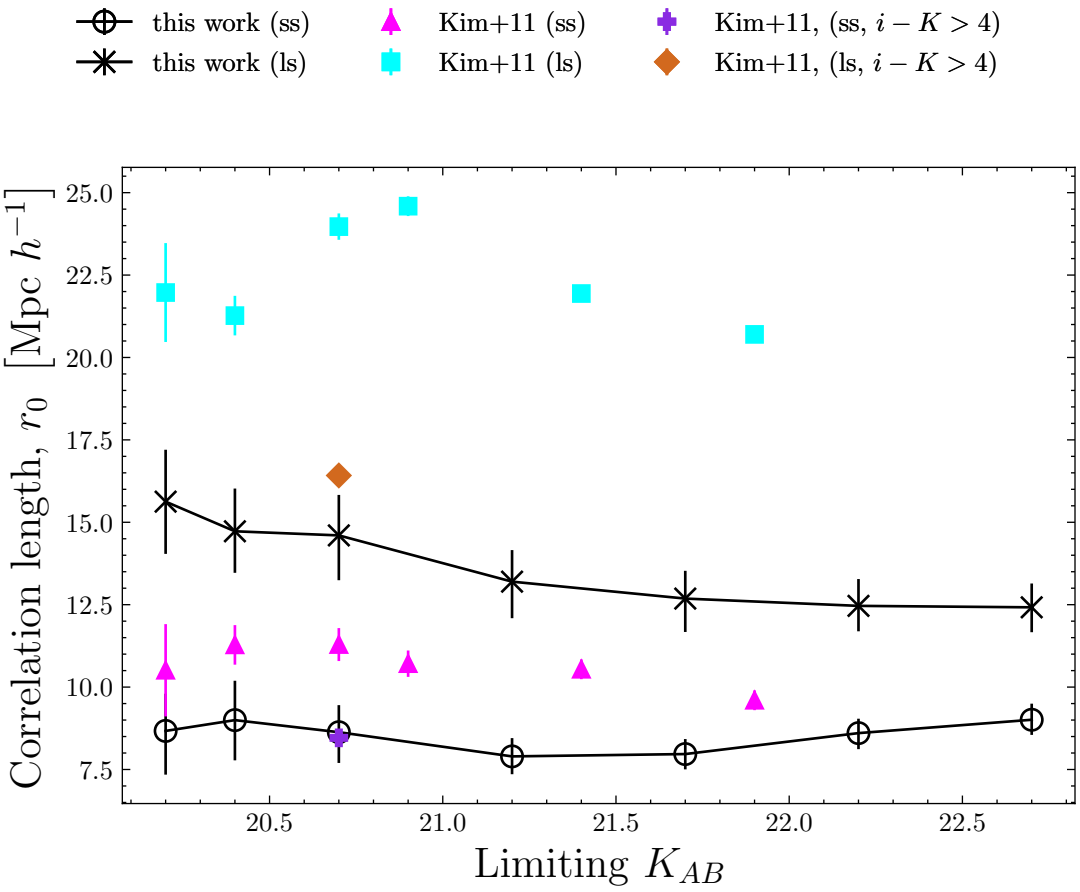

Figure 4.21: Small and large scale correlation lengths r_0 for HSC-selected EROs. Also shown are those of Kim et al. (2011), who use a redder criteria of $(I-K)_{\rm Vega} > 4.5$, which corresponds to $(i-K)_{\rm AB} > 3.05$, and one measurement at $I-K > 3.96$ (captioned as $I-K > 4$).

We use the redshift distributions presented in Chapter 3 as step functions for the functional forms of $\frac{dN}{dz}$ when computing r_0.

For comparison, we present the same analysis in Figure 4.21, with the measurements from Kim also shown.

Given that Kim et al. (2011) use a redder ERO criteria $I-K > 4.5$, their measurements of the correlation length are larger than ours: the reddest selections of galaxies are known to give stronger clustering. They also provide these values using $I-K > 3.96$ for $K_{\rm Vega} < 18.8$, which is an ERO criteria comparable with ours. For this colour cut, their measurements are much more similar to our own at the corresponding $K_{\rm AB} < 20.7$. Their large scale correlation length is still larger than our own, because as noted earlier, they report larger $\omega(\theta)$ on the largest scales (reflected in their significantly shallower large scale slopes of $\delta = 0.4$.

We recall the crude estimates of ERO host halo size we estimated from the simple conversion of break scale to comoving physical separation of $\sim 4\,{\rm Mpc}\,h^{-1}$. This value is most comparable

to the correlation length of the small scale power law, which is roughly 8 Mpc h^{-1} at all the magnitude cuts we provide. These values are similar to the same order of magnitude, but do not agree within formal uncertainties. This correlation length computed for the small scale clustering, however, is likely to be a more robust indicator of the typical scale of these haloes, given that it integrates over the redshift distribution. We, however, do not pretend that this is the exact *size* of these haloes, only indicative of their scale. As the correlation function on small scales is dominated by intra-halo clustering (ie, galaxies in the same halo), the mass (and hence size) of the halo will be determined by the most massive galaxy at all redshifts. We interpret this roughly constant small scale correlation length at all magnitude limits, and hence redshift, as meaning that the most mass of ERO halos is roughly constant over the redshift range we consider. Kim et al. (2014) measure this more explicitly by measuring the effective halo mass with a Halo Occupation Distribution investigation, and measure $\log_{10}(M_{\rm eff}/{\rm M}_\odot) = 13.223^{+0.018}_{-0.029}$ at $z = 1.1$, and $\log_{10}(M_{\rm eff}/{\rm M}_\odot) = 13.157^{+0.026}_{-0.053}$ at $z = 1.5$. This is not a strong change over a redshift change of 0.4.

We also compute the correlation lengths of the gzK selections of galaxies. Many other studies which are available for comparison compute the correlation length using the single power law form with $\delta = 0.8$ ($\gamma = 1.8$), so for better comparison, we do the same. For the faintest magnitude cut for the PE-gzKs we measure a correlation length of $r_0 = 18.3 \pm 0.5\ h^{-1}$ Mpc.

This is not extremely different to the value obtained by Hartley et al. (2008), who measure $r_0 = 15.8 \pm^{2.0}_{2.2}$ for PE-gzKs with $K_{\rm AB} < 23$. We note that our uncertainties are significantly smaller than those of Hartley, because they use a much more thorough treatment of the uncertainties on their photometric redshifts, which we have not considered in our analysis. We observe a small trend in this correlation length with fainter magnitudes, with $r_0 = 22.0$ and $19.9 \pm 0.5\ h^{-1}$ Mpc at $K < 20.5$ and $K < 21.5$.

The agreement with Hartley contrasts strongly with the values found by McCracken et al. (2010), who report $r_0 = 4.55 \pm 0.97\ h^{-1}$ Mpc for $K < 22$ pBzKs, using their significantly steeper values of γ. Even with our small scale power law slopes and A_ω, we measure $r_0 = 11 \pm 2\ h^{-1}$ Mpc at $K < 22$, which is clearly discordant with the measurement of McCracken. This is not unexpected, however: our number counts of PE-gzKs are in closer agreement with Hartley, whereas McCracken (and most other literature values) have much higher counts of sBzKs. When they compare their own number counts to Hartley's, McCracken state that the difference is likely due to (incorrect) compensation for the different photometric systems. However, as we observe that the counts we measure from the UDS-HSC catalogues (ie, the

same photometric system as DXS-HSC) are in closer agreement with other literature values, we attribute the difference to incompleteness of the sample.

Cheema et al. (2020) report an sBzK correlation length is $r_0 = 5.59 \pm 1.03\ h^{-1}$ Mpc, which is concordant with McCracken. This appears curious, given they use a much shallower slope of $\gamma = 1.92$ (ie, that of Sato et al., 2014), but can be explained when considering that instead calculate $\omega(\theta)$ in ranges of magnitude, $22 < K_{s,\mathrm{AB}} < 23$, meaning that their measurement excludes the brightest galaxies (which are known to the the most strongly clustered). Indeed, Cheema's work shows that the amplitude of the correlation function decreases from $A_\omega^{1-\gamma} = 39.32 \pm 6.78$ for $19.25 < K_{s,\mathrm{AB}} < 19.75$ to 1.79 ± 0.40 at $22 < K_{s,\mathrm{AB}} < 23$, which is far larger change in amplitude than we (and Sato) observe for fixed slopes.

Hartley further point out that the BzK (and so gzK) selection is designed to select galaxies at $1.4 < z < 2.5$. Truncating their redshift distributions to this range, they observe smaller values of the correlation length, measuring $r_0 = 11.1 \pm^{1.7}_{1.8}\ h^{-1}$ Mpc. With the same analysis, we measure $r_0 = 11.9 \pm 0.6$ for $K < 22.5$.

4.5 Future work

4.5.1 Halo modelling

The bulk of the investigation of the clustering properties of galaxy selections in this Chapter is by computing the 2PCF, $\omega(\theta)$, and fitting various functional forms to this measurement. However, a significant drawback of this type of investigation is that the parameters that we measure are not directly comparable to the properties of the galaxies we are investigating. Further, as we see when fitting individual power laws, the amplitude of such fits is not the most reliable metric for comparing the strength of clustering, as it is degenerate with the fitting of the slopes.

An alternative treatment is the halo model (eg. Cooray & Sheth, 2002), which estimates the mass of the dark matter haloes which host the galaxies in the sample. This approach uses the halo occupation distribution (HOD) to describe the mean number of galaxies $N(M) = N_c(M) + N_s(M)$, which separately considers the number of central galaxies N_c, and satellite galaxies N_s. N_c is described as $N_c = \frac{1}{2}\left[1 + \mathrm{erf}\left(\frac{\log_{10}(M/M_{\mathrm{cut}})}{\sigma_{\mathrm{cut}}}\right)\right]$. That is, the mean number of central galaxies in a halo does not exceed one. The mean number of satellites, $N_s = N_c\left(\frac{M-M_1}{M_0}\right)^\alpha$, if $M > M_1$, else 0.

Considering these free parameters, more physical statistics about the galaxies can be derived: M_h, the mean halo mass, $b_{\rm g}^{\rm eff}$, the effective galaxy bias, and $f_{\rm sat}$, the fraction of satellites.

Kim et al. (2014) present a halo modelling analysis for EROs, and demonstrate that EROs occupy dark matter halos with masses of over $10^{13}\ h^{-1}\ \mathrm{M}_{\odot}$

4.6 Summary

Using the UKIDSS-DXS catalogues, we are able to measure the angular two point correlation $\omega(\theta)$ function of red galaxy selections over three orders of magnitude in angular scale, $0.001^{\circ} \lesssim \theta \lesssim 1^{\circ}$. At this depth, this is competitive with other NIR surveys in terms of the smallest scales probed, and scales larger than many other surveys.

We show that over this range of scales, functional forms more complex than a power law are better suited to describe $\omega(\theta)$, and we choose to use the sum of a power law and an exponential, which describe the small and large scales respectively. This supports the two-halo interpretation of the correlation function: the clustering on the small scales represents the intra-clustering halo, and the large scale clustering represents pairs of galaxies which live in different dark matter haloes.

Using the catalogues which have been cross-matched with the deep HyperSuprimeCam optical imaging, we show that the clustering of $i-K$ selected EROs shows a strong break at $\theta \sim 36''$. We show that the clustering measurements obtained from the three separate DXS-HSC catalogues are concordant, especially on scales $\theta < 0.1^{\circ}$. By considering individual power laws fit to small and large scales, we show that (when both the amplitude and power law slope are allowed to vary), that there is a strong trend from very steep slopes at the brightest K band magnitude cuts, to shallower slopes at the faintest magnitude cuts we can make, for the small scale. However, those at the faint end are still significantly steeper than the typical $\delta = 0.8$ (we measure $d_{\rm ss} = 1.32 \pm 0.06$ for the brightest cut, and $d_{\rm ls} = 1.02 \pm 0.02$ for the faintest).

Further, we show that the slopes obtained for the power law-plus-exponential model are steeper than those of the small scale slopes obtained with the individual power law. This means that careful consideration of intermediate scales (around the power law break) is needed to accurately determine the slope of the clustering at the smallest scales.

We also present the angular correlation functions of the passive selections of gzK galaxies, which are designed to select the most massive galaxies at $1.4 < z < 2.5$ (although we note

that our survey limits us to $z < 1.5$). Similarly to the EROs, we observe a very strong break in the angular correlation function. Finally, we make a comparison to the star-forming sample which is selected at the same redshifts, and show that the passively-evolving galaxies have significantly stronger clustering, at all scales that we are able to measure. In particular, the slopes of the small scale clustering are much steeper for the passive galaxies. This is consistent with the current theory of galaxy evolution where merging of galaxies in dense (strongly clustered) environments quenches star-formation, causing them to become passively evolving. This behaviour is known as environmental quenching.

Finally, we measure the correlation lengths of the ERO clustering, for small and large scales. By interpreting the correlation length of the small scale power law correlation function component as a scale representative of the typical size of a halo, we estimate that the size of the typical halo does not change over the magnitude range, and so redshift range, we are able to measure with DXS. Further, by assuming that the halo size is set by the most massive galaxy (as the small scales are dominated by intra-halo clustering), we infer that this means that the mass of the host dark matter halo is also constant over this range. Using a HOD modelling analysis, Kim et al. (2014) show that the ERO effective halo mass increases only by a very small factor (1.16) from $z = 1.5$ to $z = 1.1$.

Chapter 5

Galaxy luminosity and stellar mass functions with DXS

The previous Chapters in this Thesis details testing our catalogues by demonstrating the clustering properties of selections of red galaxies detected with UKIDSS-DXS. Much of this Chapter is spent discussing the luminosity function of galaxies and further, the contribution of red galaxies to the luminosity function in redshift intervals. We make detailed comparisons of the best-fitting Schechter functions we obtain from our K-band luminosity functions with other observational studies. Finally, we investigate the stellar mass function of passive galaxies, and contribution (as a function of redshift) of the most massive galaxies by considering the stellar mass density in order to look at the quenching efficiency of galaxies.

5.1 Luminosity functions

The luminosity function (LF) of galaxies describes the number of galaxies of a given luminosity, $\phi(L)$, or absolute magnitude, $\phi(M)$, that are expected to be found in a (comoving, cosmological) unit volume, so it is expressed with units of $\mathrm{Mpc}^{-3}\ \mathrm{L}_{\odot}{}^{-1}$ or $\mathrm{Mpc}^{-3}\ \mathrm{mag}^{-1}$.

In particular, the K-band luminosity function of galaxies is a very useful tool in studies of galaxy evolution, as it is less sensitive to galaxies which have active star-formation (Kochanek et al., 2001; Mortlock et al., 2017). Further, there are a number of studies which show the strong relation between galaxy stellar mass and K-band luminosity (Longhetti & Saracco, 2009; Arcila-Osejo et al., 2019), particularly for passive galaxies.

One way to estimate the LF of galaxies is the $V_{\rm max}$ method (Schmidt, 1968),

$$\phi\left(M_K\right)\Delta M = \sum_i^N \frac{1}{V_{{\rm max},i}}, \tag{5.1.1}$$

where N are the galaxies whose (absolute) magnitude fall into each magnitude bin of width ΔM. That is, $\phi\left(M_K\right)$ is essentially a histogram of absolute magnitude M_K, weighted by $1/V_{\rm max}$. The quantity $V_{\rm max}$ represents the largest volume that each galaxy could appear in and still be included in the sample.

The luminosity function is often parameterised with a Schechter function, which is the product of a power law and an exponential,

$$\phi\left(M\right) = 0.4\ln\left(10\right)\ \phi^* 10^{-0.4\Delta M(\alpha+1)} \exp\left(-10^{-0.4\Delta M}\right), \tag{5.1.2}$$

with $\Delta M = M_K - M_K^*$, where ϕ^* is a normalisation, M_K^* is a characteristic magnitude, and α represents the slope of the faint end of the luminosity function. The constants are the result of converting the luminosity function $\phi\left(L\right) = \left(\phi^*/L^*\right)\left(L/L^*\right)^\alpha \exp\left(-L/L^*\right)$ into magnitudes, where L^* is the characteristic luminosity.

Other methods of calculating the luminosity function are also available. For instance, the maximum likelihood (ML) method of Sandage et al. (1979) assumes a functional form (ie., the Schechter), and considers instead the minimum luminosity a galaxy could be at and still included in a (magnitude-limited) survey. (This contrasts with view point of $V_{\rm max}$ where the distance, and hence volume, is the "varying" galaxy property.) The likelihood of $\phi\left(M\right)$ is then written as $\mathcal{L} = \prod_i p_i$, where

$$p_i\left(M_i|z_i\right) = \phi\left(M_i\right) \Big/ \int_{M_{\min(z_i)}}^{M_{\max(z_i)}} \phi\left(M_i\right) dM.$$

The integration limits $M_{\min(z_i)}$ and $M_{\max(z_i)}$ are the minimum and maximum intrinsic luminosity a galaxy could have at given that it is at redshift z_i, with minimum and maximum apparent survey magnitudes $m_{\rm min}$ and $m_{\rm max}$. This likelihood is then maximised by varying the free parameters of the Schechter function.

This ML method is considered less biased than the $V_{\rm max}$ method: the assumption of the LF shape means that the measurements of $\phi\left(M - \frac{\Delta M}{2} < M < M + \frac{\Delta M}{2}\right)$ are less likely to be influenced by large structures in the survey, although this is less and less of a problem for the increasingly large area (spectroscopic) surveys. One disadvantage of the ML method is that the normalisation ϕ^* is not constrained, and must be independently determined by considering eg. number counts. A downside of the $V_{\rm max}$ method is that it does not account

for the colour evolution of galaxies with redshift when considering colour-selected populations of galaxies. That is, a galaxy which is selected with a certain colour cut may not still fall into this selection if it were placed at the maximum distance. This can be mitigated to some extent by measuring the LF in redshift intervals which are not so wide that that there is expected to be an extreme evolution in colour - or at least a reversal in trend.

Ultimately, we choose the $V_{\rm max}$ method to estimate luminosity functions because the survey area we available with the DXS-HSC-SWIRE catalogues is $8.77\,\mathrm{deg}^2$, which corresponds to a (comoving) volume of $\sim 3 \times 10^8$ Mpc^3 in the interval $0.5 < z < 1.5$ and $\sim 2 \times 10^8$ Mpc^3 for $1 < z < 1.5$ (where a large fraction of our red galaxy selections are). This is likely large enough such that the volume is not dominated by a single large structure. Further, it is more convenient to use $V_{\rm max}$ and not have to compute the normalisation separately.

We note that Beare et al. (2019) use the ML method, Cirasuolo et al. (2007) use both $V_{\rm max}$ and ML, and Mortlock et al. (2017) use the $V_{\rm max}$ method, and all of these values are roughly consistent with each other. A similar variety of methods is used in literature which computes the mass function. In particular, Davidzon et al. (2017) use $V_{\rm max}$, the Sandage ML method, the step-wise ML method of Efstathiou et al. (1988, another non-parametric method), and a further method which considers the incompleteness of a sample as a function of stellar mass $\mathcal{M}$ and z at high redshifts, and find that all give concordant results.

5.1.1 Galaxy luminosity function

To measure the galaxy LF, we choose to use a faint apparent magnitude limit of $K < 22.5$. To decide what absolute magnitude limit this corresponds to for a given redshift (interval), Figure 5.1 shows the photometric redshift estimate (from EAZY) versus absolute K-band magnitude, for $0 < z < 1.6$, as measured from the DXS-HSC-SWIRE catalogues. We also indicate the redshift ranges (and absolute magnitude limits) of our analyses. Recall from Section 2.6 that the photometric redshifts we obtain are not reliable below redshift of $z < 0.4$. For this reason, we choose to study the LF only for galaxies $z > 0.5$, a reasonable "buffer" away from the less reliable measurements. The artificial curve bounding the lower is due to the $K < 22.5$ limit, and we use constant faint M_K limits for each redshift interval ensure a complete sample. The bright limits are chosen such that they are an integer number of bin widths away from the faint limit at $M_K \sim -26$, although the exact bright limit is less important. In truth, this is unimportant, as variable bin widths would be accounted for with the ΔM in Equation 5.1.1, but we use the constant bin width for consistency, choosing $\Delta M_K = 0.4$ We choose

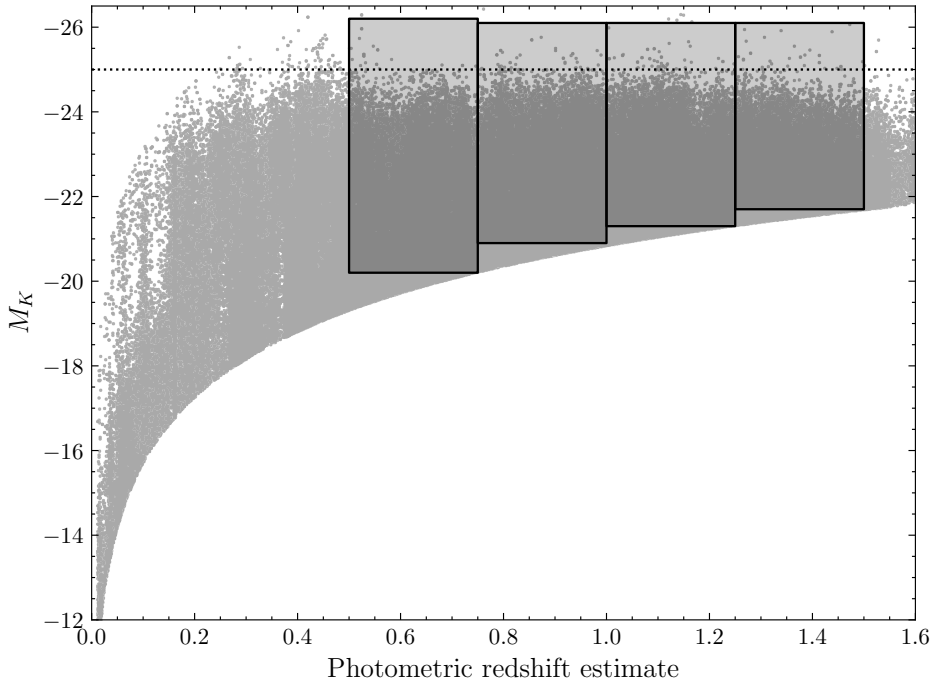

Figure 5.1: Photometric redshift estimate ("photo-z") vs. absolute K-band magnitude. The data for the two DXS-HSC-SWIRE fields (Elais-N1 and XMM-LSS) are shown. The shaded boxes indicate the redshift and absolute magnitude intervals that we estimate the galaxy luminosity function for (in Figure 5.2). We do not use the photometric redshifts $z < 0.5$, as they are unreliable. The dotted horizontal line is at $M_K = -25.0$

these redshift ranges and K limits because literature data with similarly-selected samples are available for comparison, and these Δz redshift intervals such that we reduce the number of galaxies we "waste" (due to their exclusion as fainter than the grey box of the complete sample), but not so narrow there are too few galaxies. The dotted horizontal line in this Figure is at $M_K = -25.0$, and serves to guide the eye for comparison with the similar Figure using the DXS-PS1-SWIRE catalogues (in Figure 5.4, discussed in detail later in this section). Further, Mortlock et al. (2017) also show this plot for their data (their Figure 3), which shows that their galaxy sample becomes sparse at a similar absolute magnitude, and is roughly constant with redshift (although this is difficult to judge by eye).

In Figure 5.2 we show our measured K-band luminosity function for all galaxies $K < 22.5$ in the four redshift ranges show in Figure 5.2. We present these data for the two fields with both HSC and SWIRE coverage (XMM-LSS and ElaisN1), and the combined measurement.

At absolute magnitudes brighter than $M_K < -26.25$, we judge there to be too few objects to obtain reasonable estimates of $\phi(M)$ (see Figure 5.1). Even so, in the two brightest absolute magnitude bins (particularly for the highest redshift interval), the residuals show that we deviate significantly from the Schechter fit. Given the very large error bars on these points,

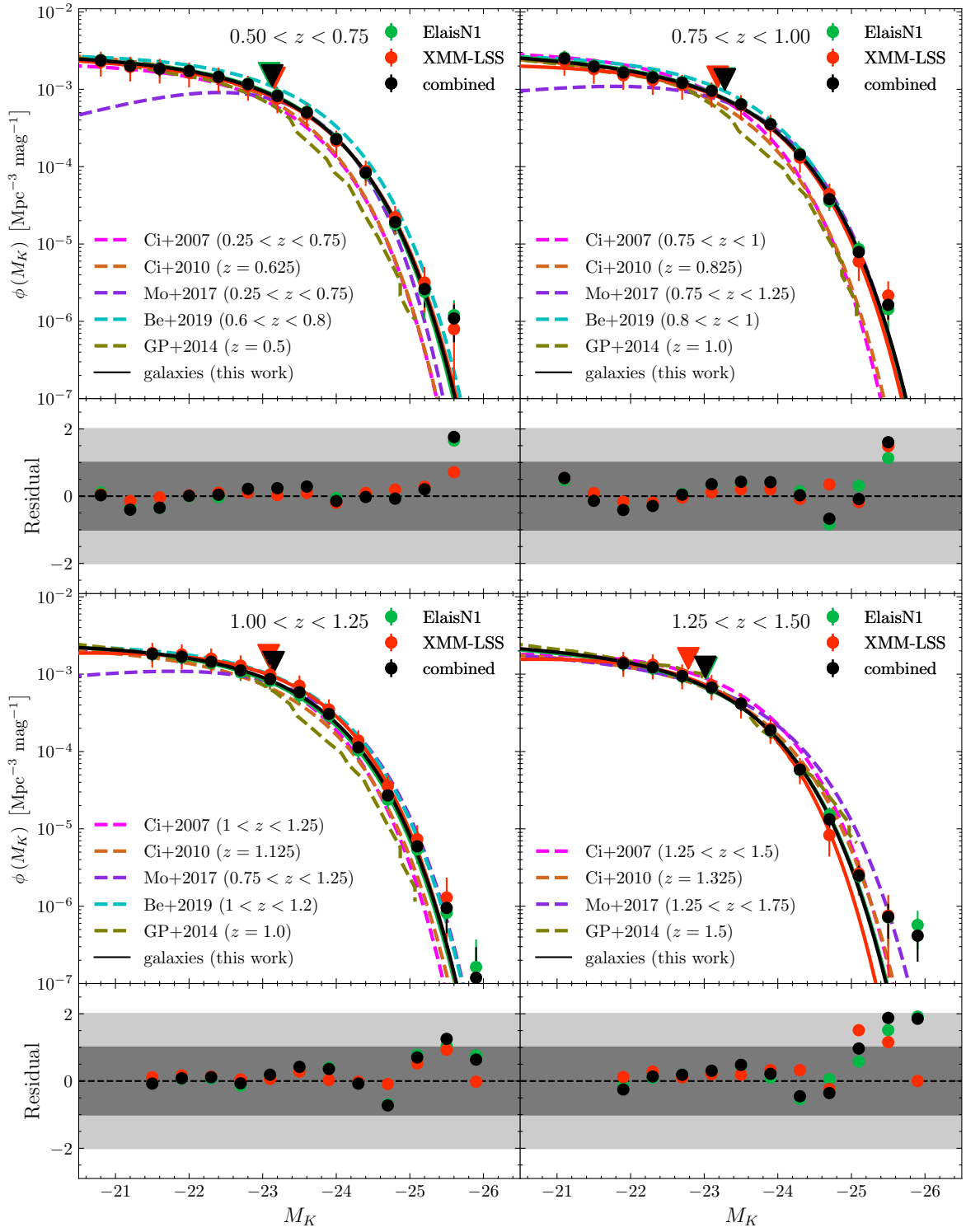

Figure 5.2: K-band luminosity function of galaxies with $K < 22.5$ (apparent magnitude), for DXS-HSC-SWIRE catalogues in XMM-LSS and ElaisN1, and the combined measurement. We also plot the best Schechter fits several other observational luminosity function studies: Cirasuolo et al. (2007, Ci+2017), Cirasuolo et al. (2010, Ci+2010), Mortlock et al. (2017, Mo+2017), Beare et al. (2019, Be+2019). We also show the predictions of semi-analytic model GALFORM Gonzalez-Perez et al. (2014, GP+2014) The auxiliary panels below each luminosity function show the residuals from our Schechter fits, whose parameters are listed in Table 5.1. Triangle markers indicate the location of the characteristic magnitude M_K^*.

it could be argued that even these bins contain too few objects.

The first contribution to the uncertainties on $\phi(M)$ measurements is computed using the jackknife method, $\sigma_{\rm jk}$, similarly to the correlation function uncertainties (see Section 4.1.2), using a target region size of $0.33\,\mathrm{deg}^2$.

The contribution to the LF uncertainty from the uncertainty on the photo-zs, σ_z is computed using a Monte Carlo method. We resample each galaxy photometric redshift from it's posterior from EASY, and recompute $\phi(M)$. This procedure is repeated a large number of times, and σ_z is the standard deviation of these perturbed estimates of $\phi(M)$.

These two contributions are then added in quadrature: $\sigma_\phi = \sqrt{\sigma_{\rm jk}^2 + \sigma_z^2}$. We note that at the faint end of the galaxy luminosity function, σ_z is a few percent of $\sigma_{\rm jk}^2$, rising to around 50% at the brightest magnitude bin of the highest redshift interval. This indicates that the errors on photometric redshift will not contribute significantly to the Schechter fit parameters we obtain.

The residuals (which are normalised by the ϕ uncertainties) in the auxiliary panels show structure in all redshift intervals, indicating that the Schechter fit is not the optimal description of the LF. Mortlock et al. (2017) use a combination of exceptionally deep datasets (UltraVISTA, CANDELS and HUDF) to probe the K-band galaxy luminosity function to much fainter absolute magnitudes intervals, reaching $M_K \sim -17.5$ at the redshifts studied here. Their work, along with prior studies, shows that the galaxy luminosity function is in fact better described by a double Schechter function,

$$\phi(M) = 0.4\ln(10)\,\exp\left(-10^{-0.4\Delta M}\right) \times \left[\phi_1^* 10^{-0.4\Delta M(\alpha_1+1)} + \phi_2^* 10^{-0.4\Delta M(\alpha_2+1)}\right],$$

which now has two slope parameters and two normalisation parameters, but is still modulated by a single characteristic magnitude parameter M_K^*. They show that this is especially true at the redshift ranges that we are studying, but that there is no (statistical) preference for the double Schechter over the single at $z > 2.5$. This would help to explain the structure in the residuals in our measurements. However, we do not have sufficient faint absolute magnitude data points to adequately constrain the five free parameters of the double Schechter fit, so we do not attempt this.

The majority of the residuals are within one standard deviation of the fit. From a Poisson point of view, this would mean that we are over-estimating the uncertainties on our measurements of the luminosity function (Poisson errors expect that $\sim 68\%$ should lie within the "1σ band"), but as with our measurements of the correlation function $\omega(\theta)$, we argue that these

Table 5.1: Best fitting Schechter parameters for the luminosity functions of galaxies in four redshift ranges, using the DXS-HSC-SWIRE catalogues (presented in Figure 5.2).

Redshift	$\phi^* \times 10^{-3}$	M_K^*	α
0.50 - 0.75	2.5 ± 0.4	-23.13 ± 0.09	-1.07 ± 0.10
0.75 - 1.00	2.2 ± 0.4	-23.28 ± 0.10	-1.11 ± 0.13
1.00 - 1.25	2.3 ± 0.5	-23.15 ± 0.12	-1.04 ± 0.17
1.25 - 1.50	2.0 ± 0.4	-23.01 ± 0.15	-1.1 ± 0.2

underestimate the true uncertainties on these measurements. Schechter parameters for each redshift interval (for the combined measurement) are given in Table 5.1. The uncertainties we quote in Table 5.1 are obtained by estimating the PDF using EMCEE, similarly to the parameter uncertainties for the functional forms for the correlation function (more discussion below).

At the very bright end, we observe (from the residuals) that the galaxy LF deviates from the prediction of the Schechter function: there are more bright galaxies per volume than the Schechter fit predicts. As a systematic effect, this could be interpreted simply as a limitation of the survey volume. On the other hand, a physical interpretation would imply that there is an excess of the most luminous (and hence) massive galaxies. As most studies (and Figures 5.9 and 5.8) show that a very large fraction of the galaxies at this redshift are passive, this would mean that there is excess growth of the most luminous passive galaxies. This could be due to gas poor mergers, which would take place in very dense environments: galaxy clusters.

We err on the side of caution, and interpret this deviation as a systematic, requiring larger volumes from eg. SHARKS which will also measure the K-band LF.

5.1.2 Comparison with literature

For each panel in Figure 5.2 we also plot the Schechter fit from Cirasuolo et al. (2007, hereafter C07), Cirasuolo et al. (2010, hereafter C10), Mortlock et al. (2017) and Beare et al. (2019)in similar redshift ranges. Note that the same much broader redshift interval is used from Mortlock's work in both the $0.75 < z < 1.0$ and $1.0 < z < 1.25$ intervals. Further, for the comparison to their work, we use the parameters for the bright end of their double Schechter function, which they "[expect] to mimic those that would be obtained by using single Schechter-function fits to only the bright end of the K-band luminosity function ($M_K \leq -21$)". Interestingly, the faint end slope of Mortlock is significantly different to our

own, indicating as with the residuals, that the secondary Schechter component plays a strong role even at the bright end. These literature values are presented for comparison in Table 5.2 in the interval $1 < z < 1.25$. We choose this redshift interval for detailed comparison, as in a later subsection we will estimate the LF of EROs, which are predominantly in the highest redshift intervals in Table 5.1. C10 provide formulae for calculating the parameters ϕ^* and M_K^* at any given redshift (their Equations (2) and (3), and Table 1), for the centre of each of our redshift ranges. For the lowest three redshift interval, our measurement of ϕ matches most well with those of Beare and Mortlock at the bright end, and are slightly higher than C07 and C10. However, in the highest redshift interval, our measurement is lower than all three presented observational literature studies, indicating that even these photometric redshift estimates are not entirely reliable. It would seem unreasonable to conclude that we are not selecting the brightest galaxies $M_K \sim -25$ in a given redshift interval but adequately selecting the faint galaxies $M_K \sim -23$ (where our measurements agree more).

We observe little to no evolution in the faint end slope and characteristic magnitude α and M_K^* in the interval $0.5 < z < 1.5$, and only a very modest increase in the normalisation parameter ϕ^* towards later times (that is, lower redshifts). We caveat this latter remark by noting that uncertainties on this parameter are large: ϕ^* in the highest redshift bin is even consistent with that in the lowest redshift bin within the uncertainty bounds. The observation that M_K^* is roughly constant across the redshift bins we use indicates that the most massive galaxies across this redshift range $0.5 < z < 1.5$ are no longer growing, and are already evolved by these cosmic times. This is evidence of galaxy downsizing: these objects have already formed the vast majority of their stellar mass at early times and their star formation has been quenched. Those galaxies which are still growing (ie, star-forming) must be at fainter magnitudes. The increase in ϕ^* towards earlier times is another observation which can be explained by this galaxy downsizing: galaxies which are lower luminosity (and hence mass) at early times have continued to grow, and increase in luminosity towards M_K^*.

All four α measurements are consistent with $\alpha = -1.0$, a value commonly assumed studies which do not allow the faint end slope to vary (including Beare). All four other studies we show in Figure 5.2 show the same trend of increasing normalisation for later times, and have smaller confidence intervals than ours, so can make this conclusion with more conviction. Beare use redshift intervals of 0.2, and show a small trend in their M_K^* from $z \sim 0.5$ to 1.1, reporting values of -23.08 ± 0.08 to -23.20 ± 0.06, which are distinct, but still have overlapping confidence intervals. In contrast, the values obtained from the C10 formula range from -22.81 at $z = 0.5$ to -23.18 at $z = 1.5$, an increase in brightness of 0.37 mag.

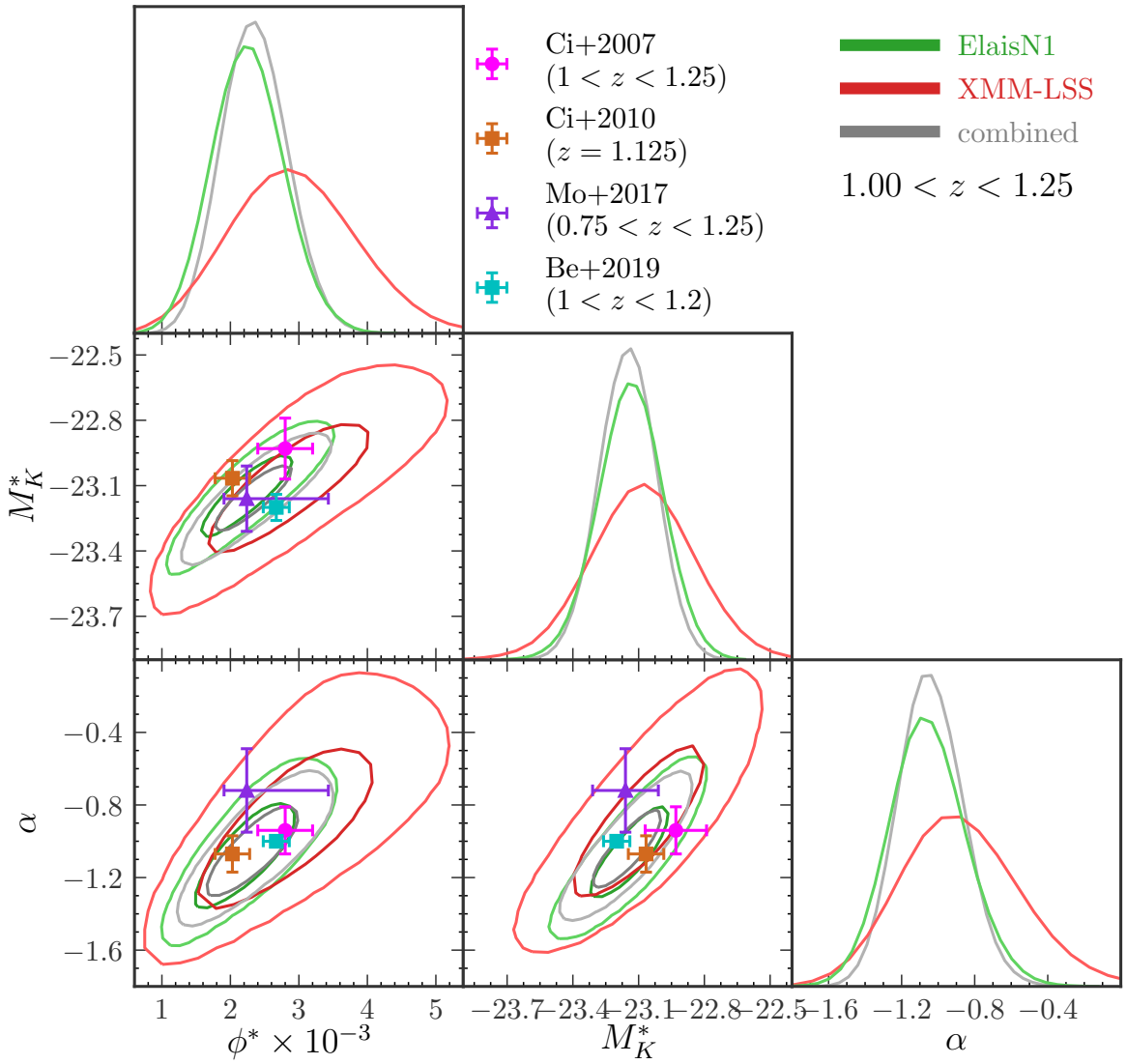

Figure 5.3: PDFs for Schechter fit parameters, for DXS-HSC-SWIRE selected galaxies $1 < z < 1.25$. Parameters for the ElaisN1 and XMM-LSS fields and the combined measurement are reported, along with those for comparable redshift intervals from literature (listed in Table 5.2).

Table 5.2: Best fitting Schechter parameters for the luminosity functions of galaxies for the two individual fields and the combined measurement, and the combined measurement for $1 < z < 1.25$, using the DXS-HSC-SWIRE catalogues (presented in Figure 5.2). Also listed are literature values presented in Figure 5.3. [a]Values calculated at this redshift using the formulae presented in C10, their Equations (2) and (3), and their Table 1, with Monte Carlo errors. [b]Bright-end parameters from double Schechter fit. [c]Asymmetric uncertainties calculated from log values quoted.

Field/work	$\phi^* \times 10^{-3}$	M_K^*	α	z
combined (this work)	2.3 ± 0.5	-23.15 ± 0.12	-1.04 ± 0.17	1<z<1.25
ElaisN1 (this work)	2.2 ± 0.5	-23.14 ± 0.14	-1.07 ± 0.19	1<z<1.25
XMM-LSS (this work)	2.9 ± 0.9	-23.1 ± 0.2	-0.9 ± 0.3	1<z<1.25
Cirasuolo et al. (2007, C07)	2.8 ± 0.4	-22.93 ± 0.14	-0.92 ± 0.13	$1 < z < 1.25$
Cirasuolo et al. (2010, C10)	2.0 ± 0.3	-23.07 ± 0.08	-1.07 ± 0.10	$z = 1.125$[a]
Mortlock et al. (2017)[b]	2.24[c]$\pm^{0.33}_{0.29}$	-23.16 ± 0.15	-0.72 ± 0.23	$0.75 < z < 1.25$
Beare et al. (2019)	2.67 ± 0.19	-23.20 ± 0.06	-1.0 (fixed)	$1 < z < 1.2$

The PDFs for the Schechter parameters for the $1 < z < 1.25$ redshift interval are presented in Figure 5.3. We quote the uncertainties of the parameters in Tables 5.1 and 5.2 as the width of the 1D distribution, which we judge by eye here to be symmetric. As with the PDFs we show in Chapter 4, the PDFs for the XMM-LSS parameters are much broader than the ElaisN1 due to the smaller area. However, the XMM-LSS data still has some impact on the PDF of the combined measurement, which is not completely aligned with the ElaisN1 data. We report the parameters for the Schechter fits along with the literature parameters in Table 5.2, as well as presenting them in the figure. We observe (as expected) that there are strong correlations between the parameters, indicated by the ellipticity of the 2D PDF projections. Brighter values of the characteristic magnitude M_K^* allow for smaller normalisation and more negative faint end slope values.

Taking the combined measurements as the best, our value of normalisation ϕ^* from the HSC-selection, agrees with all of the literature we compare with, although we quote larger uncertainties on this parameter than all of these analyses.

Our value of α also agrees with those of C07 and C10, and with the fixed $\alpha = -1.0$ assumed by Beare. Our M_K^* is around 0.2 mag brighter than that of C07 however, but is in agreement with the other three.

We also include the measurements of the galaxy LF from the semi-analytic model GALFORM, presented in Gonzalez-Perez et al. (2014). In our highest redshift bin, the GALFORM LF

agrees well with the other observational studies (although as we point out, our measurement is lower than these others). However, in the lower redshift intervals, GALFORM appears to under-predict the number of the most luminous galaxies, although matches well at fainter magnitudes. One of the questions the work of Gonzalez-Perez investigates is the effect of the stellar population synthesis (SPS) models on the luminosity function. They conclude that the effect is least strong for the shortest wavelength measurements (eg. UV galaxy LF), but is quite significant in the NIR, and the major contributing factor is the treatment of thermally-pulsing AGB (asymptotic giant branch stars). They conclude that the K-band luminosity function could be an important tool for constraining this stellar evolution phase, which is currently less-well understood than early phases of stellar evolution. We plot Gonzalez-Perez's LF measurements of the CW09 SPS model (Conroy et al., 2009), as these LF measurements are available at three comparable redshifts, although we note that they are quite similar to the commonly-used SPS model of Bruzual & Charlot (2003, BC99). One of the SPS models considered by Gonzalez-Perez is that of Maraston (2005, MN05), which carefully considers the amount of hydrogen and/or helium consumed by post-main sequence stars. LFs considered using this model give larger numbers of the most luminous galaxies, hinting that this may be a more suitable way to treat these objects, instead of relying on stellar isochrones.

Mortlock observe similar discrepancies with GALFORM in their measurements of the K-band LF at higher redshifts, plotting the BC99 SPS LF measurements. Mortlock further note that the hydrodynamical simulation MUFASA (Davé et al., 2016) excellently agrees with their measured LF, which specifically employs an empirical model of quenching based on galaxy dark matter halo mass, designed to reproduce the effects of mass quenching. Without this mechanism (which they note is most likely to be AGN feedback), Davé et al. (2016) report that they observe a significant excess of star formation in the most massive galaxies.

5.1.3 Galaxy luminosity function with DXS-PS1-SWIRE

We perform a similar analysis with the DXS-PS1-SWIRE catalogues. Although the optical photometry is not as deep, the advantage is that we have one additional field which has both optical and MIR photometry: Lockman Hole.

First, we again show redshift vs. M_K for these catalogues, in Figure 5.4. In contrast to the Figure 5.1 (the same plot but for HSC data), appears to be a more significant gradient at the bright edge with increasing redshift (using the dotted line at $M_K = -25$ to guide the eye). Neither our DXS-HSC-SWIRE catalogues nor the plot in Mortlock's work show

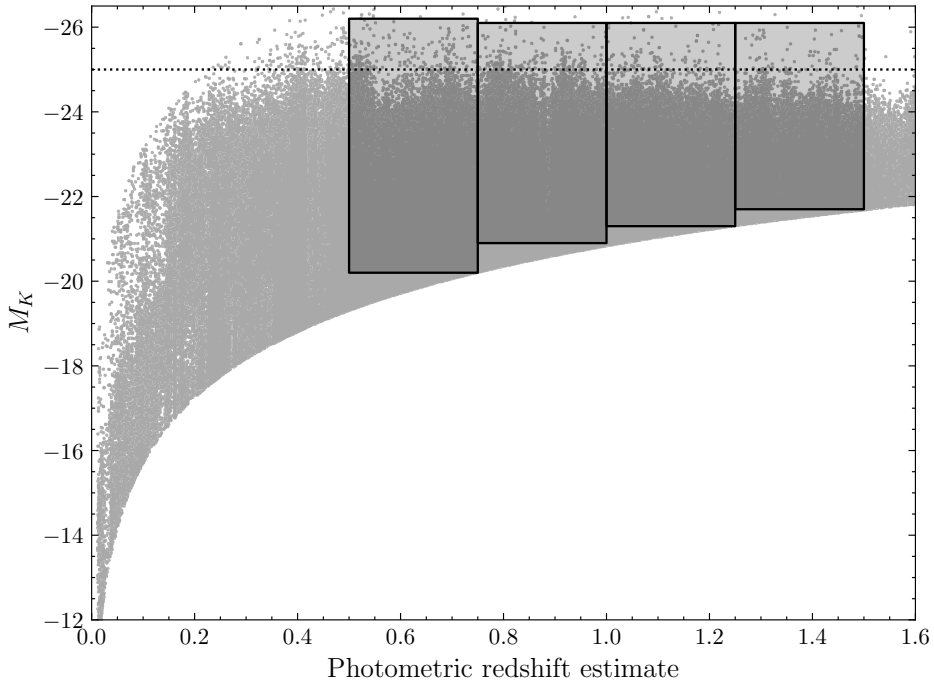

Figure 5.4: Photometric redshift estimate versus absolute K-band magnitude. The data for the three DXS-PS1-SWIRE fields (Elais-N1, Lockman and XMM-LSS) are shown. The shaded boxes indicate the redshift and absolute magnitude intervals that we estimate the galaxy luminosity for (in Figure 5.5). We do not use the photometric redshifts $z < 0.5$, as they are unreliable. The dotted horizontal line is at $M_K = -25.0$.

this, indicating that the photo-zs we obtain from the PS1 catalogues are not even reliable as those from the HSC-based catalogues. More specifically, it suggests that these photometric redshifts are underestimates. Modelling a galaxy at too *low* z implies that it is intrinsically less luminous than in reality.

We present measurements of the galaxy LF from the DXS-PS1-SWIRE catalogues in Figure 5.5.

We observe that the measurements of $\phi\,(M_K)$ using these catalogues are larger than for the brightest M_K values, that we are underestimating the redshift in these catalogues. However, we see in the $0.75 < z < 1.00$ bin that ϕ is consistently larger than the literature values at all M_K (unlike the DXS-HSC-SWIRE), suggesting that perhaps this is not systematic. The comparison with literature is especially poor in the highest redshift interval, where the $V_{\rm max}$ estimates are consistently lower than all of the literature Schechter functions, and our own Schecter function is severely distorted as a result: over-predicting at low luminosities (by extrapolation), and under-predicting at intermediate to bright luminosities.

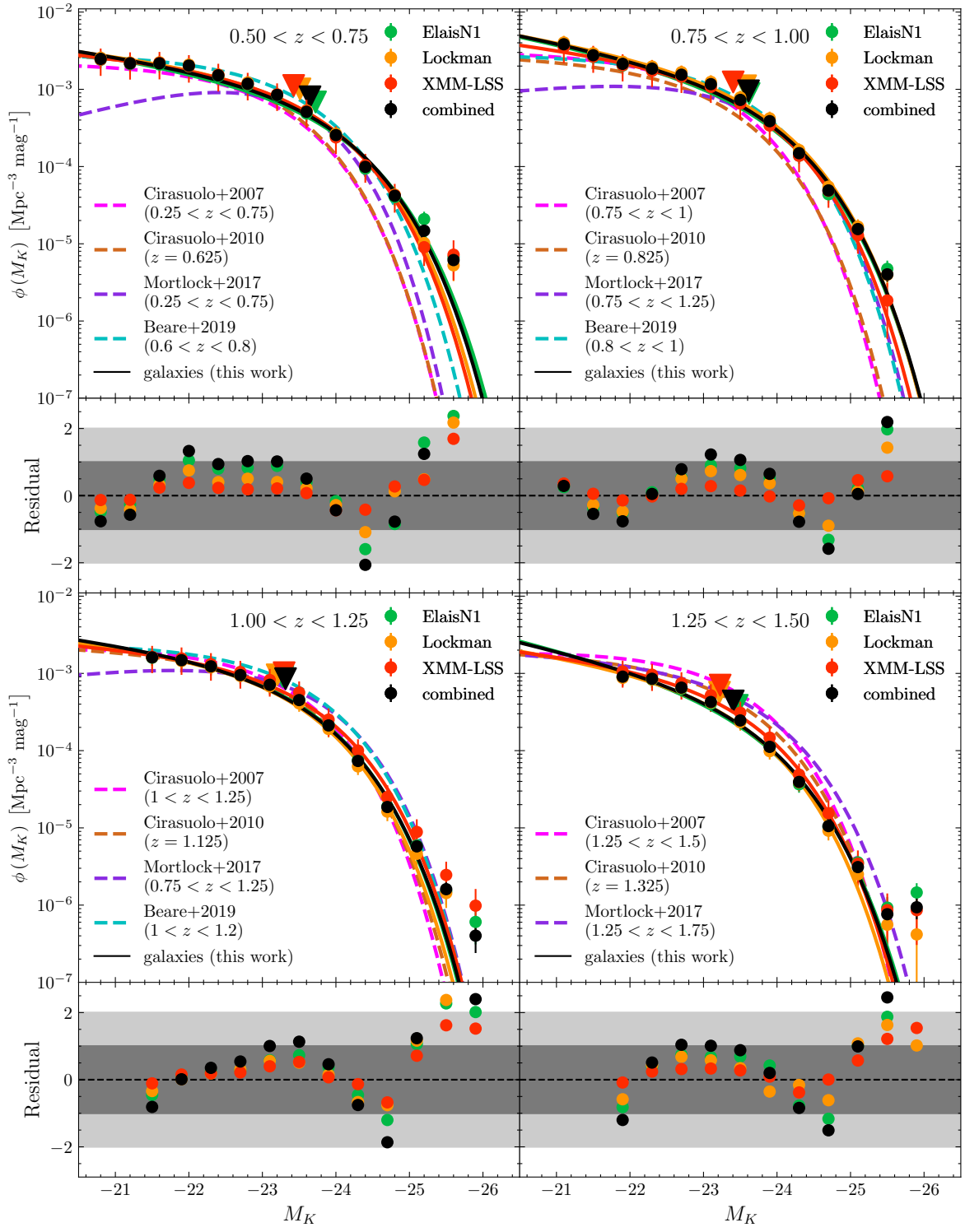

Figure 5.5: K-band luminosity function of galaxies with $K < 22.5$ (apparent magnitude), for DXS-PS1-SWIRE catalogues in XMM-LSS, Lockman, ElaisN1, and the combined measurement. We also plot the best Schechter fits several other luminosity function studies. The auxiliary panels below each luminosity function show the residuals from our Schechter fits, whose parameters are listed in Table 5.1. Triangle markers indicate the location of the characteristic magnitude M_K^*.

5.1.4 Luminosity function of red galaxies

We expect that the EROs we select in Chapter 3 are amongst the most massive, luminous galaxies we are able to select at the redshifts probed by DXS. Here, we calculate the luminosity function of EROs as a means of comparing their intrinsic luminosities with the population of galaxies as a whole.

5.1.4.1 Red restframe $U-B$ selected galaxies

The analyses of C07 and Beare also look at the luminosity function of red galaxies. However, rather than using a selection in $i-K$ (or similar) observed colours, they use the separation of red and blue galaxies in restframe $U-B$ colours (eg. Bower et al., 1992). The Johnson U and B bands are centred at 3571 Å and 4344 Å, the latter of which is marginally longer than the D_{4000} break, so we would expect that galaxies selected on a restframe red $(U-B)_{\text{restframe}}$ colour would have the same properties as the passively-evolving EROs.

We select red $U-B$ galaxies using the redshift-dependent criteria from Beare (first discussed in their earlier work Beare et al., 2015, their Equation 3),

$$U-B > 1.074 - 0.18z - 0.03\,(M_B + 19.4)\,, \tag{5.1.3}$$

where U and B are the restframe magnitudes (M_B is absolute restframe), and z is the redshift. We use this criteria per galaxy, rather than using a single redshift z value for the whole interval. C07 use a slightly different criteria, which is not redshift dependent.

To demonstrate that we are in fact selecting similar populations of galaxies, we show the $U-B$ vs. B restframe colour-magnitude diagram in the main panel of Figure 5.6. Restframe fluxes are one of the outputs of EAZY, so we are able to straightforwardly calculate restframe magnitudes. We highlight the $i-K > 2.55$ EROs in red, and a large fraction of them are above the criteria in Equation 5.1.3 (shown by the blue dashed line).

We also present histograms of restframe $U-B$ colour for all galaxies, EROs, and the red $U-B$ galaxies selected with Equation 5.1.3 in the left panel of this figure. This shows the expected clear bimodality in this distribution of colour, with the local minimum at $U-B \sim 0.9$, which Beare's selection attempts to exploit. By design, in this colour histogram, the red $U-B$ galaxies show a strong peak, and drop off rapidly (although not as a step, as the criteria line is not a constant in $U-B$). There is a tail of EROs in this histogram which extends into the blue $U-B$ population.

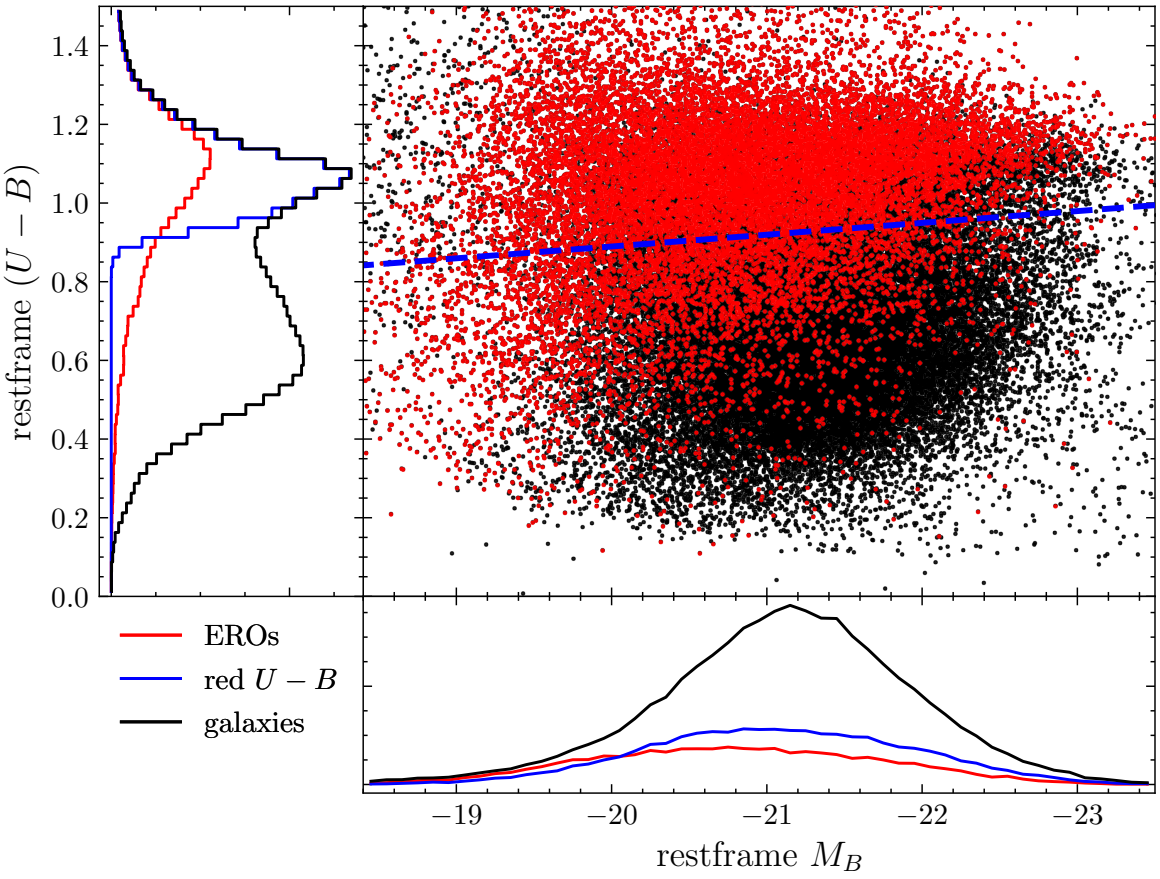

Figure 5.6: Restframe $U-B$ vs. M_B colour-magnitude diagram. Galaxies which are selected as $i-K>2.55$ EROs are highlighted in red. The red $U-B$ selection from Beare et al. (2015) (in Equation 5.1.3) is shown as the blue dashed line, using $z=1.125$. All galaxies $1<z<1.25$ from the XMM-LSS and ElaisN1 catalogues are shown in the main panel. Histograms of $U-B$ colour of all galaxies, EROs, and red $U-B$ galaxies are shown in the right panel in black, red, and blue respectively. Similarly, histograms of absolute (restframe) B are in the lower panel, with the same colour scheme.

Of the 17323 EROs we select in $1<z<1.25$ from our DXS-HSC-SWIRE catalogues, 76% of them are also selected as red $U-B$s, which is a considerable fraction. Considering the opposite, the Beare criteria selects 25221 red $U-B$ galaxies, meaning that the ERO colour cut of $i-K>2.55$ selects slightly more than half of them (55%) at $i<26$. At higher redshifts ($1.25<z<1.5$), the recovery increases to 68% (15478 of the 22674 EROs are red $U-B$ galaxies), with a corresponding 87% of all 17672 red $U-B$s being selected by the ERO criteria.

To make this comparison more fair, we also apply the $i<26$ cut to the $U-B$ sample. It is likely that there are galaxies with no i-band data (or at least $i>26$) which have zy and/or IRAC data which is sufficient to fit an SED to measure the restframe fluxes, whereas the simpler, two-band ERO selection would miss these. Although this makes it appear that the

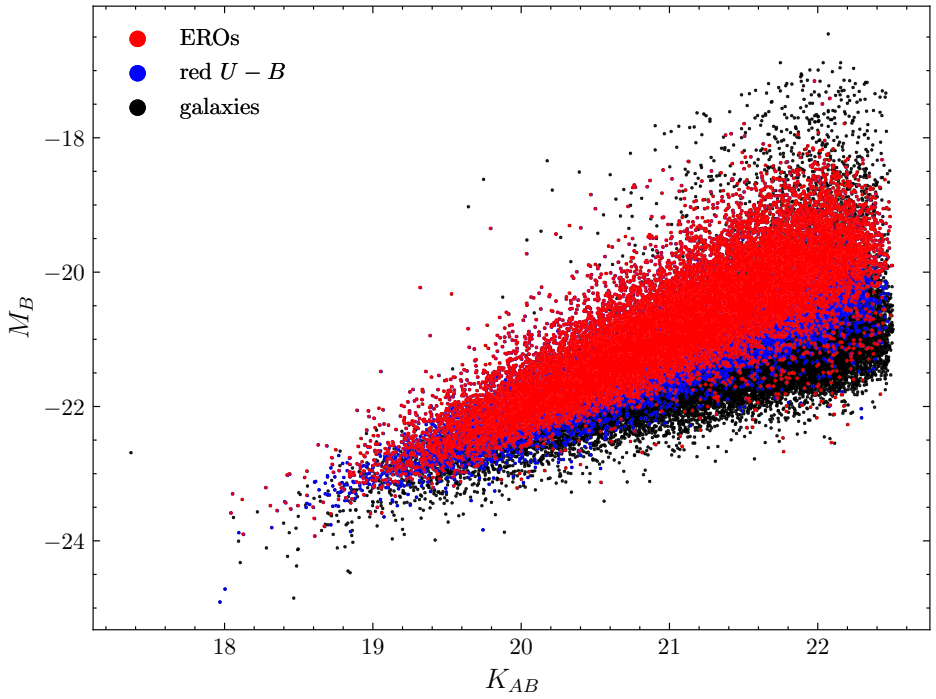

Figure 5.7: K-band absolute (observed frame) magnitude vs. B-band restframe absolute magnitude, for all galaxies in $1 < z < 1.25$. Galaxies selected as EROs are highlighted in red, on top of red $U - B$ galaxies in blue.

ERO selection is then a poorer criteria than the restframe $U - B$ criteria, we argue that the high recovery rate of these galaxies with a very cheap photometric selection (especially in the higher redshift range) is a success of the ERO technique.

The lower panel of Figure 5.6 shows the distribution of M_B, absolute restframe B-band magnitude. We note that this distribution of restframe B-band absolute magnitude is skewed slightly to fainter magnitudes for both selections of red galaxies. This is not unexpected for EROs, however, as by selection they are faint in the observed frame i band ($\lambda = 7727\,\text{Å}$) which corresponds to restframe 3680 Å at $z \sim 1.1$; very similar to the U-band wavelength.

To investigate this further, we plot the absolute K magnitude against the restframe absolute B-band magnitude in Figure 5.7. This demonstrates that the EROs do indeed have (on average) fainter restframe B-band magnitude than red $U-B$s for a given K-band luminosity.

5.1.4.2 Comparison of luminosity functions

We now show the luminosity function of our red $U - B$ galaxies in two redshift ranges $1 < z < 1.25$ and $1.25 < z < 1.5$ in Figure 5.8, and the LF of EROs (in the same redshift intervals) in Figure 5.9.

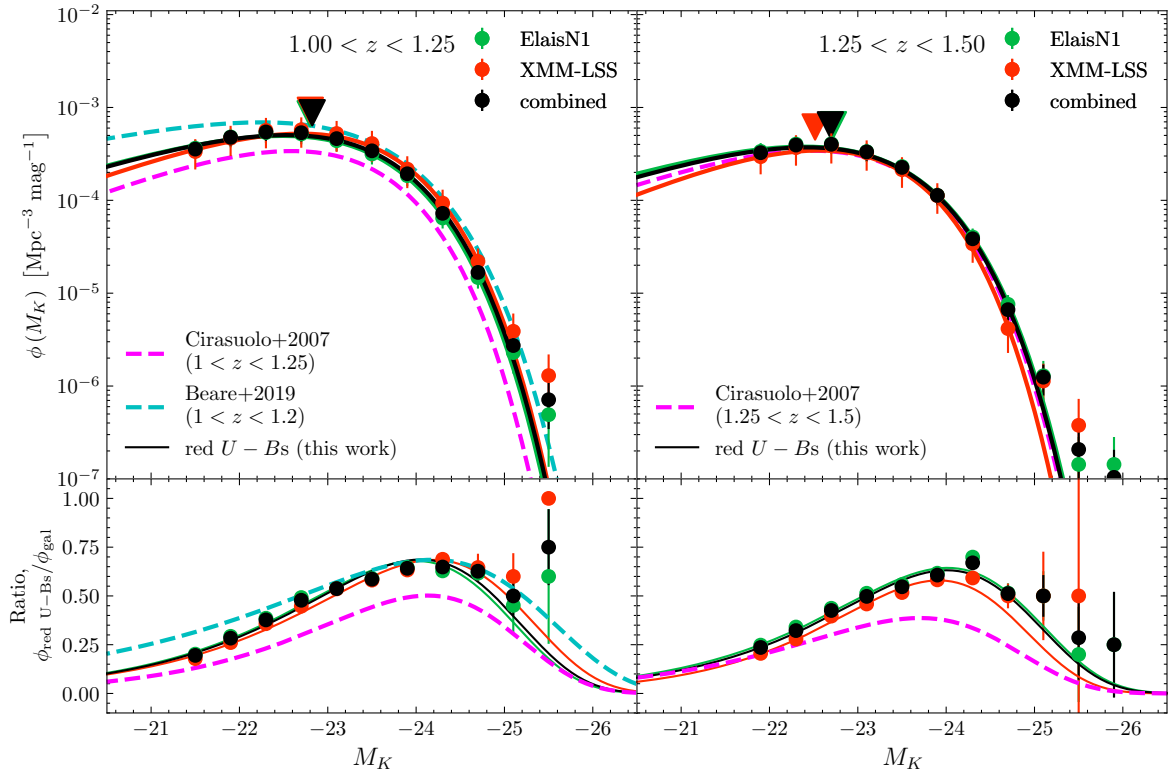

Figure 5.8: K-band luminosity function of red restframe $U-B$ selected galaxies. The lower panel shows the ratio of red $U-B$ LF to galaxy LF, $\phi_{\mathrm{red}\ U-B}/\phi_{\mathrm{gal}}$. Triangle markers show the location of the characteristic magnitude, M_K^*. Schechter fits for restframe red $U-B$ galaxy selections from literature are also shown, and similarly, their ratio to the galaxy luminosity function in the lower panels.

The lower panels of Figures 5.8 show the ratio of the selection LF to the LF of all galaxies in the same redshift interval (and ΔM bins). We stress that the lines in this figure are not fits to to the data, rather the ratio of the two Schechter functions evaluated on a fine grid. The data points are calculated as the ratio of the ϕ_{gal} and $\phi_{\mathrm{U-Bs}}$. The error bars on these data points are again estimated using the jackknife method, estimating the ratio of the LF points leaving out one of the N sub-regions of data each time.

Both the ERO and red $U-B$ samples show a slightly fainter M_K^* in the higher redshift interval, although again we do not state this definitively given the large size of the error bars. Further, we see that both selections have steep faint end slopes, meaning that they are selecting the most luminous galaxies.

We show also the Schechter functions of C07 and Beare for their red $U-B$ galaxy samples in similar redshift intervals for both samples. Beare use a fixed faint end slope of $\alpha = -0.5$ for each redshift interval, whereas we (and C07) again allow α to freely vary.

For the red $U-B$s, we see that our LFs agree most well with Beare in the lower redshift

Table 5.3: Schechter fit parameters for the ERO luminosity functions in Figure 5.9, red restframe $U - B$ selected galaxies in Figure 5.8 and literature Schechter fits for red $U - B$s.

Work/selection	$\phi^* \times 10^{-3}$	M_K^*	α	z
EROs (this work)	1.01 ± 0.12	-22.86 ± 0.11	-0.36 ± 0.18	$1 < z < 1.25$
	1.34 ± 0.16	-22.74 ± 0.12	-0.4 ± 0.2	$1.25 < z < 1.5$
red $U - B$ galaxies (this work)	1.44 ± 0.15	-22.82 ± 0.10	-0.24 ± 0.17	$1 < z < 1.25$
	1.07 ± 0.12	-22.69 ± 0.12	-0.2 ± 0.2	$1.25 < z < 1.5$
Cirasuolo et al. (2007, C07)	1.0 ± 0.3	-22.65 ± 0.17	-0.05 ± 0.4	$1 < z < 1.25$
	1.0 ± 0.4	-22.65 ± 0.24	-0.14 ± 0.5	$1 < z < 1.25$
Beare et al. (2019)	1.75 ± 0.13	-23.00 ± 0.05	-0.5 (fixed)	$1 < z < 1.2$

interval at the brightest magnitudes, but demonstrates a much steeper faint slope, which is barely concordant with C07's within our uncertainty range. In the higher interval, the normalisation no longer agrees with that of C07, but the slope and characteristic magnitude are in much closer agreement.

Parameters of the Schechter fits for the LF of red $U - B$s, along with EROs, are listed in Table 5.3.

The ERO luminosity functions agree well with C07's red $U-B$s in both redshift intervals, and we observe a slope which is steeper than the fixed $\alpha = -0.5$. Our values of $\alpha = -0.36 \pm 0.18$ and -0.4 ± 0.2 are shallower than those observed by C07, although their large uncertainties do overlap with our measurements in both cases. This is not entirely unexpected: while we show in Figure 5.6 that the ERO selection does select a large fraction of the red $U-B$s, there is still "contamination" of the restframe blue galaxies, which are particularly skewed to the fainted end of this diagram. Indeed, earlier Chapters did show that the ERO selection does select a population of dusty galaxies. It would be interesting in future work to compute the luminosity function only of the OG-EROs. However, we do not have sufficient depth in J to make this separation to a depth comparable to the ERO luminosity functions we compute here.

Further, our values of M_K^* are marginally brighter that of our own red $U - B$s, and C07's, although the overall normalisation ϕ^* is concordant in both redshift intervals.

The ratios we obtain for the EROs are comparable with those of C07's red $U-B$s in the lower redshift interval, particularly at faint magnitudes, where we observe that EROs contribute little to the overall luminosity function of galaxies. This contrasts with the bright end,

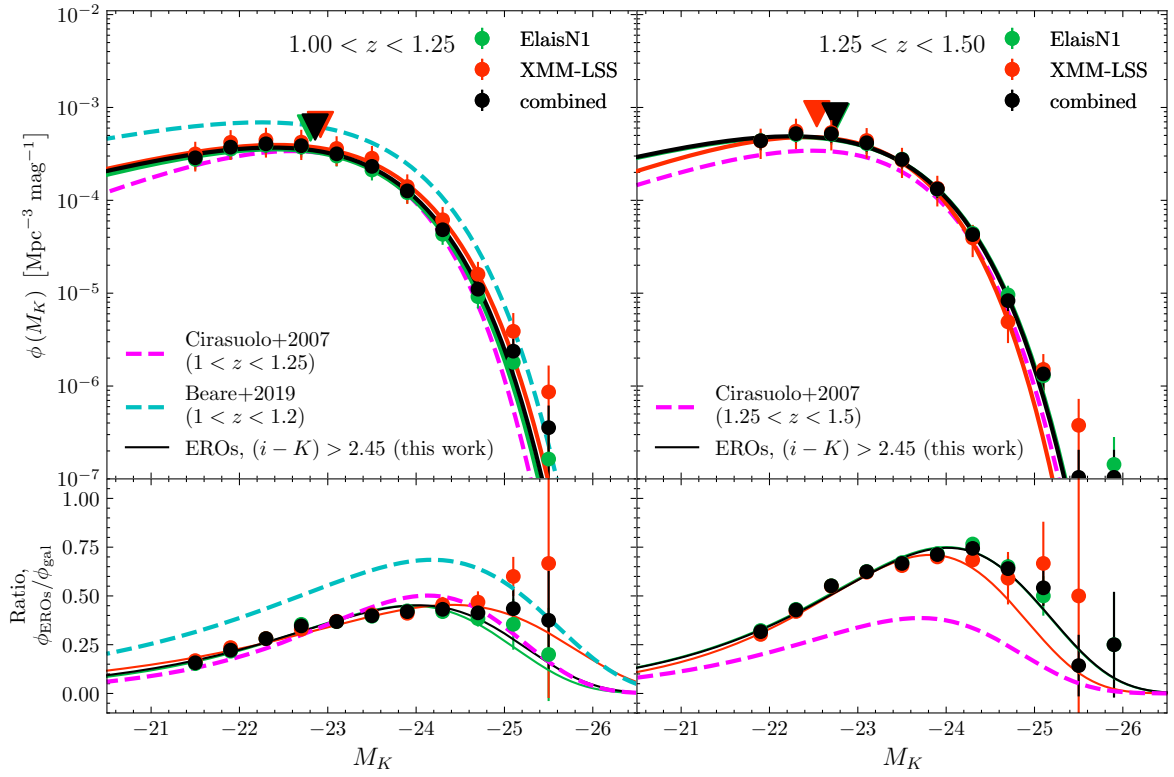

Figure 5.9: K-band luminosity function of $i - K > 2.55$ HSC-selected EROs. The lower panel shows the ratio of ERO luminosity function to galaxy luminosity function, $\phi_{\rm EROs}/\phi_{\rm gal}$. Triangle markers show the location of the characteristic magnitude, M_K^*. Schechter fits for restframe red $U - B$ galaxy selections from literature are also shown, and similarly, their ratio to the galaxy luminosity function in the lower panels.

where we see that at $M_K \sim -24.0$ (ie, brighter than the characteristic magnitude), EROs contribute up to half of the galaxy luminosity function, indicating as expected that EROs are selecting predominantly the most luminous galaxies at redshifts $z > 1$. At the extreme of the bright end (approaching $M_K \sim -25.5$), the ratio is not well constrained. The data indicate (albeit with very large uncertainty) that EROs continue to contribute a similar fraction of the LF, $\sim 50\%$, whereas the ratio of Schechter functions do not neither for our fits nor the literature presented. This disparity is likely due to the large uncertainties on the individual LF measurements at these magnitudes. That is, given the large uncertainties on ϕ data points at the extreme bright end, these points will have less influence over the fit parameters, so will extrapolate less well to $M_K < -25$.

At $1.25 < z < 1.5$, our ratio does not agree well with C07, where we predict a much larger ratio. Considering the discussion about the galaxy luminosity function in this redshift interval, where our LF is lower than all of literature works we show, but our red galaxy luminosity function does, this could explain the difference.

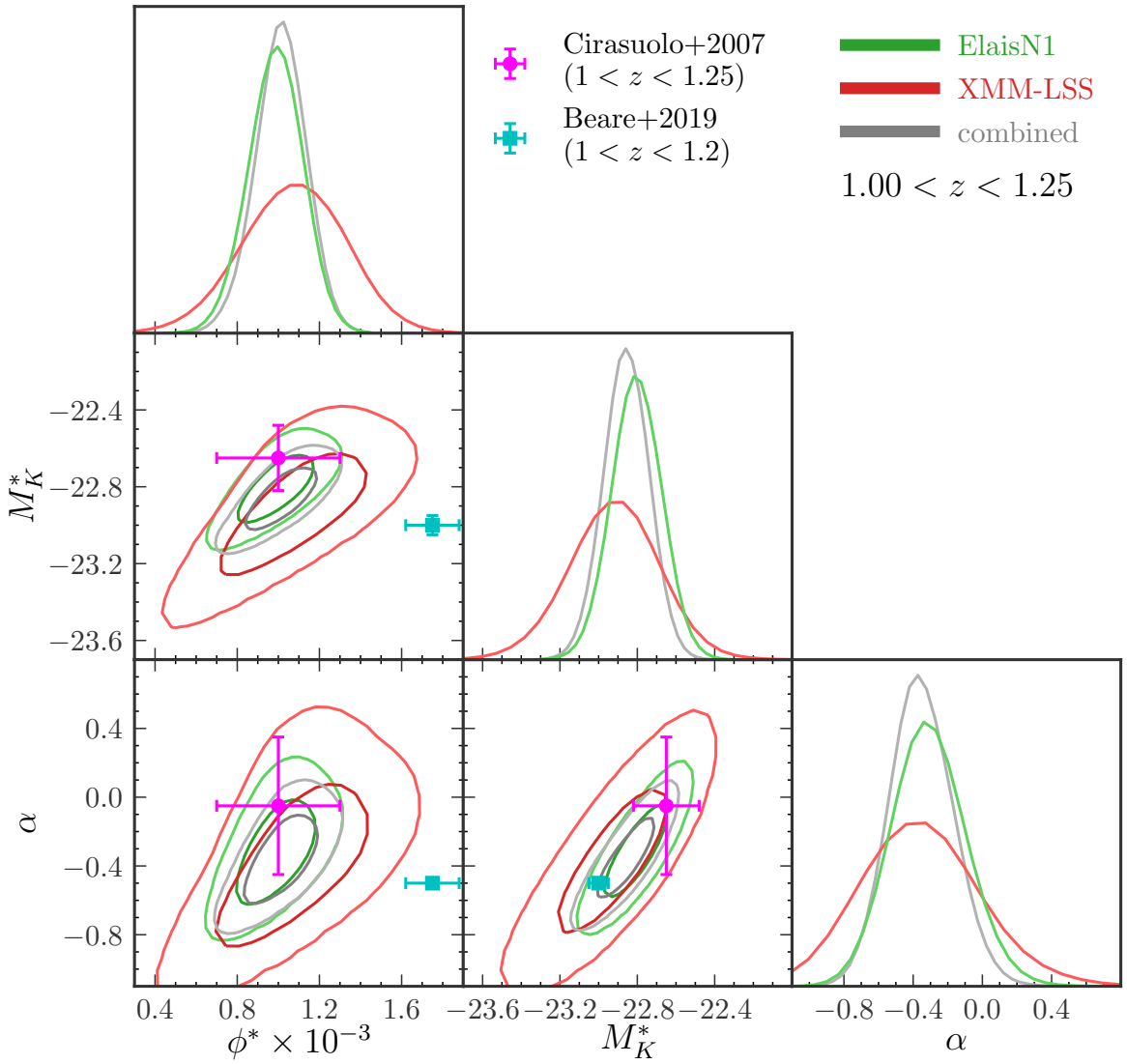

Figure 5.10: PDF of parameters for HSC-selected EROs, $1 < z < 1.25$. Also shown are literature Schechter parameters in similar redshift intervals.

The fact that these evolved stellar populations account for a significant fraction of the total luminosity of the brightest galaxies at redshift $1 \lesssim z \lesssim 1.5$ reveals that a significant amount of the star-formation in the universe happened at even higher redshift. While this is *certainly* not a new revelation from our work, it is still quite a fundamental result that we are able to demonstrate with our datasets.

As another visual comparison of the parameters, we again show the PDFs for these EROs. The PDF of the combined dataset shows that overall, our parameters are in reasonable agreement with those of C07.

Finally, we recall the discussion in Section 3.4 where we make a crude estimate of the characteristic magnitude of the ERO LF by considering the turnover in the number counts, and

the median redshift of the sample. Based on this, we estimate that the $M_K^* \sim -22.8$. This is not dissimilar to the values that we obtain for this parameter by correctly computing the LF - confirming that the turnover we observe in the number counts is indeed a physical effect, and not simply a systematic.

5.2 Galaxy stellar mass functions

In a similar manner to the LF, the galaxy stellar mass function (GSMF) describes the number of galaxies of a given stellar mass[1] $\mathcal{M}$ in a unit volume, $\phi(\mathcal{M})$. The units of the GSMF are typically expressed as Mpc^{-3} dex^{-1}, or Mpc^{-3} $\log_{10}(\mathcal{M}/\mathrm{M}_\odot)^{-1}$, as ϕ is (almost always) computed in logarithmic bins.

As with the LF, we compute the GSMF using the $V_{\max}$ method:

$$\phi(\mathcal{M})\, d\mathcal{M} = \sum_i^N \frac{1}{V_{\max,i}}.$$

The GSMF is also often described with a single or double Schechter function,

$$\phi(\mathcal{M}) = \ln(10)\phi^* 10^{\Delta\mathcal{M}(1+\alpha)} \exp\left(-10^{\Delta\mathcal{M}}\right) \tag{5.2.1}$$

or

$$\phi(\mathcal{M}) = \ln(10)\left[\phi_1^* 10^{\Delta\mathcal{M}(1+\alpha_1)} + \phi_2^* 10^{\Delta\mathcal{M}(1+\alpha_2)}\right] \exp\left(-10^{\Delta\mathcal{M}}\right), \tag{5.2.2}$$

where $\Delta\mathcal{M} = \log_{10}\left(\frac{\mathcal{M}}{\mathcal{M}^*}\right)$. The free parameters ϕ^* are normalisation parameters, α are the power law slope parameters, and $\mathcal{M}^*$ is the characteristic mass that the power laws are modulated by, in units of solar masses $\mathrm{M}_\odot$.

One further complication to be accounted for when computing the GSMF function is Eddington bias, which arises due to uncertainties on the stellar mass estimate. As the GSMF decreases exponentially at the high mass end, those galaxies which are overestimated in mass will have an significant impact on the number of galaxies on that bin, compared with galaxies whose mass is underestimated falling in to a bin which contain fewer galaxies.

To account for this, instead of fitting directly to the Schechter functions, a common approach is to estimate the parameters for the fitting function of choice which has been convolved with

[1] We use calligraphic typeface $\mathcal{M}$ for the log of the stellar mass to distinguish from absolute magnitude M used in Section 5.1

a function representing the uncertainty in the stellar mass function, often a Gaussian G,

$$\phi_{\rm meas}\left(\mathcal{M}\right) = \left(\phi_{\rm true} * G\right)\left(\mathcal{M}\right) = \int_{-\infty}^{\infty} \phi_{\rm true}\left(\mathcal{M}'\right)\ G\left(\mathcal{M} - \mathcal{M}', \sigma\right) d\mathcal{M}'. \tag{5.2.3}$$

The Gaussian G is defined as usual, $G\left(\mathcal{M} - \mathcal{M}', \sigma\right) = \frac{1}{\sigma\sqrt{2\pi}} \exp\left[-\frac{\mathcal{M}-\mathcal{M}'}{2\sigma^2}\right]$.

We calculate the GSMF using the mass estimates provided by the EAZY templates that we obtain with our photo-z fitting.

The quantiles for the posterior of the stellar mass estimate provided by EAZY suggest that the error on $\log_{10}\left(\mathcal{M}\right)$ are $\sigma \sim 0.15$. To test this, we fit Equation 5.2.3 with a least squares method, and allowed σ to be a free parameter. The obtained estimates of σ are similar to the average value from the EAZY posteriors, from 0.12 in the lowest redshift bin to 0.2 in the highest, with Schechter parameters which are similar to those which we obtain from the Monte Carlo fitting below.

When using these Monte Carlo methods, we fix σ to the estimate from the initial method.

In Figure 5.11, we show our estimate of the GSMF in the same four redshift bins as we calculate the LF. In lieu of showing the uncertainty contours of the best fitting parameters as we did with the galaxy LF parameters, we instead show shaded 68% confidence regions around our fits.

For all redshift bins, we fix $\alpha_1 = -1.3$ (the slope of the component which dominates at the lowest masses), which is around the value that are obtained by Davidzon et al. (2017) in similar redshift bins. As the minimum mass we measure is around $\log_{10}\mathcal{M} \sim 10$ in all redshift bins, this parameter is otherwise extremely poorly constrained if we allow it to vary.

For the lowest three redshift bins, our estimates of the GSMF are in reasonable agreement with those of Davidzon. In the highest redshift bin, however, our measurement of the GSMF is lower than that of Davidzon by a factor of two at $\log_{10}\left(\mathcal{M}/\mathrm{M}_{\odot}\right) \sim 11$. This is shown doubly so when considering the best fitting parameters in Table 5.4: the amplitude of the second component, ϕ_2^*, is consistent with zero within the uncertainties, implying that a single Schechter fit would suffice. Previous studies (eg. Ilbert et al., 2013; Davidzon et al., 2017) demonstrate that this is *not* the case until at least $z \sim 3$, meaning that our mass estimates of the most massive galaxies at the highest redshift bin the could be improved.

We plot the Tinker et al. (2008) halo mass function (HMF) computed at the centre of each redshift bin, computed with the Python package HMF[2] (Murray et al., 2013). The HMF

[2] `https://github.com/halomod/hmf`

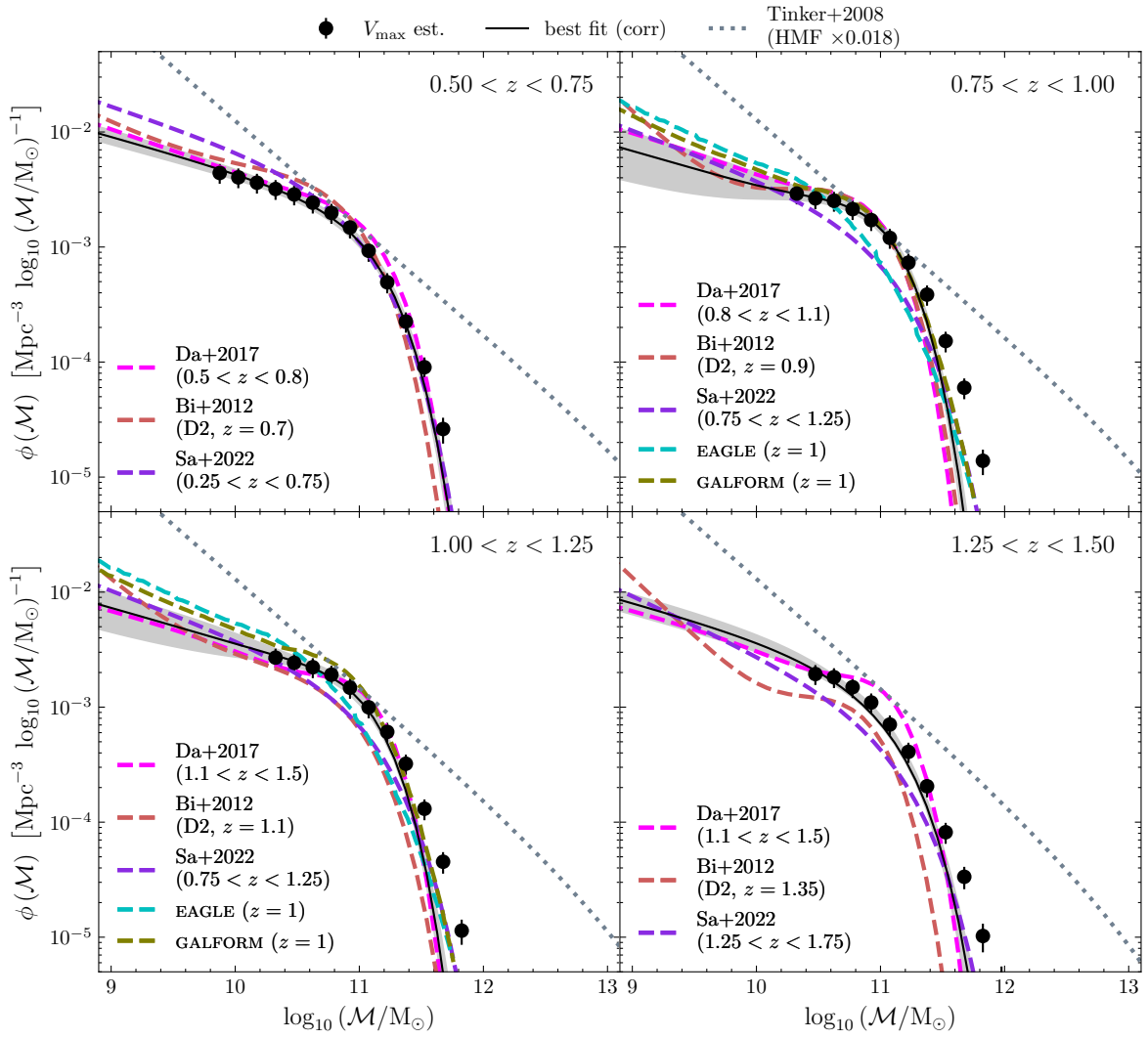

Figure 5.11: Galaxy stellar mass function of all galaxies, computed using the $V_{\rm max}$ method. The best fitting Eddington bias-corrected double Schechter functions are also plotted. The slope of the low-mass component is fixed to $\alpha_1 = -1.3$. The results from observational studies are also shown in each redshift bin: Davidzon et al. (2017, Da+2017), Bielby et al. (2012, Bi+2012) and Santini et al. (2022, Sa+2022), although we note that Santini use only a single Schechter to model their GSMF. The $z = 1$ GSMF from the EAGLE and GALFORM simulations (as computed by Guo et al., 2016) are shown (repeated in all panels). Finally, the halo mass function (scaled down) from Tinker et al. (2008) are plotted, computed at the centre of each redshift bin.

Table 5.4: Best-fitting parameters for the galaxy stellar mass function of the full galaxy population, modelled as a double Schechter function, in four redshift intervals. We note that the slope of the low mass component is fixed to a constant $\alpha_1 = -1.3$, marked with an asterisk.

Redshift	$\phi_1 \times 10^3$	α_1	$\phi_2 \times 10^3$	α_2	$\log_{10}(\mathcal{M}_*/\mathrm{M}_\odot)$
0.50 - 0.75	1.12 ± 0.17	-1.3^*	0.8 ± 0.4	-0.2 ± 0.3	10.84 ± 0.06
0.75 - 1.00	1.0 ± 0.4	-1.3^*	1.7 ± 0.5	0.1 ± 0.4	10.71 ± 0.06
1.00 - 1.25	0.9 ± 0.4	-1.3^*	1.3 ± 0.5	-0.1 ± 0.4	10.75 ± 0.07
1.25 - 1.50	1.0 ± 0.2	-1.3^*	0.2 ± 0.3	0.1 ± 0.4	10.86 ± 0.08

is multiplied by a constant 0.018 (as is presented in Davidzon et al., 2017, their Figure 18), which represents the stellar-to-halo mass relation (SHMR) at $z = 0$, at the SHMR peak. This allows a crude insight into the SHMR behaviour, and clearly HMF behaves differently than the GSMF. As described succinctly by Davidzon: "Reconciling the observed SMF with the [HMF] requires the introduction of quenching mechanisms". These mechanisms are required at both the low and high mass ends of the GSMF. At the low-mass end, this is expected to be supernovae feedback, and as mentioned earlier, the most likely candidate at large masses is AGN feedback.

In the central two redshift bins, where our comparison with the $z = 1$ GSMF estimates from EAGLE and GALFORM are most appropriate, we see that the measurement from GALFORM generally is the better match, although both predict more galaxies at the lower masses than our GSMF estimate and that of Davidzon. Further, the EAGLE GSMF predicts fewer galaxies at $\mathcal{M} \gtrsim \mathcal{M}^*$ than the all of the other work plotted.

Looking directly at the double Schechter parameters (which we present in Table 5.4), we observe that the characteristic mass is roughly constant. As with the characteristic luminosity M_K^* from the LF, this is in line with the prediction of galaxy downsizing in which the most massive galaxies are already assembled by DXS redshifts. To compare with literature, their whole redshift range ($0.2 < z < 4$) Davidzon et al. (2017) observe very little change in their values of $\mathcal{M}_*$ for the full galaxy population (at least when considering the large uncertainties on these parameters at $z > 2$) using the COSMOS2015 dataset. Bielby et al. (2012) observe similar behaviour in $0.5 < z < 2$ with the WIRDS dataset. We note that Santini et al. (2022) use a single Schechter function to model the full galaxy sample.

We further plot the GSMF of passive galaxies, selected as the red $U - B$ galaxies, in Figure 5.12, and report the best-fitting (single) Schechter parameters in Table 5.5.

We observe that there is a minor trend in increasing $\mathcal{M}_*$, unlike for the full galaxy sample,

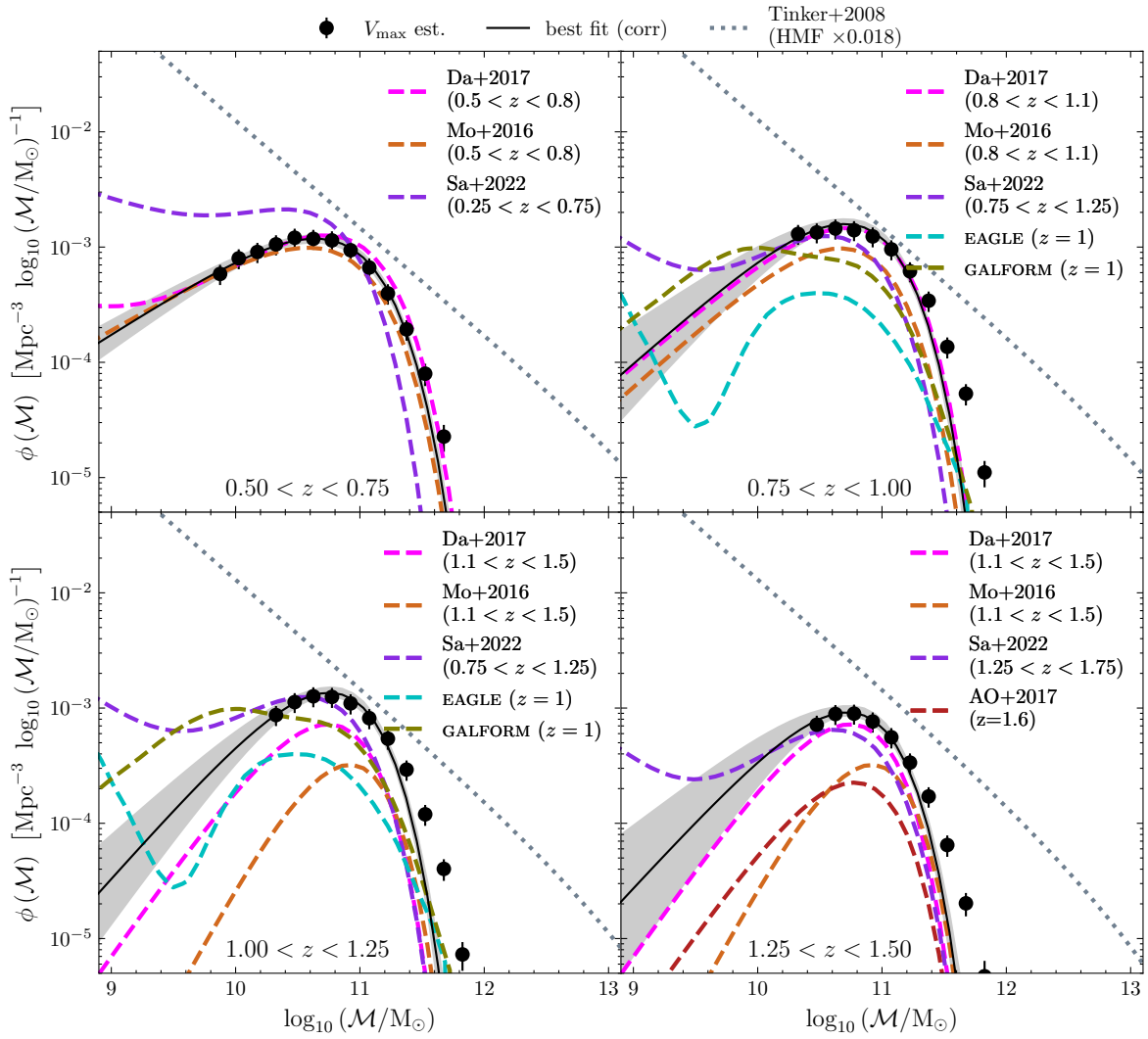

Figure 5.12: The GSMF of passive galaxies, selected as red $U-B$ galaxies, computed with with the V_{max} method, with the best fitting Eddington bias-corrected single Schechter function. Schechter fits from Davidzon et al. (2017, Da+2017), Moutard et al. (2016, Mo+2016), Santini et al. (2022, Sa+2022) and Arcila-Osejo et al. (2019, AO+2019). We again plot the $z = 1$ GSMF from the EAGLE and GALFORM simulations from Guo et al. (2016).

Table 5.5: Best-fitting parameters of the galaxy stellar mass of the red $U-B$ selected galaxies, modelled as a Schechter function, in four redshift intervals.

Redshift	$\phi \times 10^3$	α	$\log_{10}(\mathcal{M}_*/M_\odot)$
0.50 - 0.75	1.33 ± 0.13	-0.31 ± 0.10	10.80 ± 0.03
0.75 - 1.00	1.86 ± 0.17	-0.1 ± 0.2	10.72 ± 0.05
1.00 - 1.25	1.57 ± 0.14	0.2 ± 0.3	10.67 ± 0.05
1.25 - 1.50	1.07 ± 0.13	0.2 ± 0.4	10.65 ± 0.07

which, interpreted physically (and considering this parameter alone), would be in contradiction with the downsizing result supported by the full sample, and the LF of the full sample.

However, as with the LF parameters, there is a strong correlation between the slope α and the characteristic $\mathcal{M}_*$, and the same argument applies for the GSMF parameters. Figure 5.10 shows that more luminous M_K^* requires a more negative faint end slope, and we observe this behaviour in the red $U-B$ galaxy GSMF parameters. We note that the uncertainties on α are very large, especially at high redshifts. Similarly, Davidzon et al. (2017) quote a similar trade-off in their passive GSMF $\mathcal{M}_*$ and slopes (their Table 1).

The GSMF of passive central galaxies at $z = 1$ from hydrodynamical simulation EAGLE (eg. Schaye et al., 2015) and semi-analytic model GALFORM as measured by Guo et al. (2016) are also shown in Figure 5.12. On the whole, the GALFORM passive centrals GSMF does a better job of matching the observational data than EAGLE, in the central two redshift bins (where comparisons are most apt). Although, is to be expected, as the number counts of the brightest (hence most massive) passive galaxies are also under predicted by GALFORM.

EAGLE demonstrates an upturn in the central galaxies at (we highlight that this trace does *not* include satellite galaxies), which Guo state is likely due to sampling effects as this value of $\mathcal{M} \sim 10^{9.5}$ is near the resolution limit of galaxies in EAGLE. The observational passive GSMF measurement of Santini et al. (2022) shows a similar upturn, but their measurement includes all passive galaxies (both satellites and centrals), and hence requires a double Schechter function, due to the low mass limits they are able to probe.

We note that the Santini et al. (2022) passive GSMF is lower than our own at the largest masses in all redshift bins. This is likely due to the significantly smaller field sizes that Santini use: their fields are hundreds of square arcminutes, but reach depths of F160 $\sim H = 27$. These volumes are not sufficient to select the most massive galaxies, but the extreme depth allows the GSMF to be measured to very low masses, and demonstrate that a double Schechter fit is required for passive galaxies until $z \sim 3$. Davidzon's work, comparatively, only requires a double Schechter fit out to $0.5 < z < 0.8$ due to their higher mass limits.

Studies such as Arcila-Osejo et al. (2019) argue that the fact that the passive GSMF is well-described by a single Schechter function at $z \sim 1.6$, a single "mass-quenching" mechanism must be well-established by this time.

5.2.1 Stellar mass density

We compute the integrated stellar mass density (SMD), ρ_* based on our results above, in the range $8 < \log_{10}(\mathcal{M}/\mathrm{M}_\odot) < 13$. These are plotted in Figure 5.13.

Uncertainties on the SMD are computed by integrating each of the samples from the GSMF MCMC fitting (after removing the first thousand samples – which is several times the length of the chain correlation length – for a burn-in phase), and finding the 16% and 84% quantiles of the distribution.

On the whole, our stellar mass density estimates of the full galaxy sample are consistent with previous studies (although our estimate is lower for the lowest redshift bin): galaxy stellar mass density increases with cosmic time.

Although we pointed out earlier that we measure fewer of the most massive galaxies in our highest redshift bin than eg. Davidzon et al. (2017), our estimate of the SMD here is still concordant with other estimates.

We note that our estimates of stellar mass density for the passive galaxies are slightly higher than those of Davidzon and Ilbert at the highest redshifts. However, all of the literature values show more variation for the passive sample than the full galaxy sample. Given the agreement of our SMD estimates for the full galaxy sample, we attribute this to differences in the passive selection. Further, our SMD estimates for the lowest redshift ($0.5 < z < 0.75$) bin do actually follow the opposite trend, and are lower than in ($0.75 < z < 1.0$), although this is not unexpected, as we point out a similar behaviour in the normalisations ϕ we obtain from the GSMF we measure. The SMD measurements of galaxies from EAGLE and GALFORM as a function of redshift are plotted from Guo et al. (2016, their Figure 3). We do not attribute significance to the agreement of our SMD with EAGLE: it is the relative over prediction of the GSMF at lower masses and the under prediction at higher masses 'cancelling out'.

In order to investigate the most massive galaxies, we also compute the stellar mass density in $11.5 < \log_{10}(\mathcal{M}/\mathrm{M}_\odot) < 13$, labelled ultra-massive passive galaxies ("UMPEGs") in Arcila-Osejo et al. (2019) and in Figure 5.13.

Further, to ensure that our estimates of stellar mass density for passive galaxies are not dominated by by the low mass galaxies where our GSMF measurements are extrapolated, we compute ρ_* for $10.5 < \log_{10}(\mathcal{M}/\mathrm{M}_\odot) < 11.5$, which we label in Figure 5.13 as "MPEGS", "massive passively evolving galaxies" (for continuity with Arcila-Osejo's naming). Given that these estimates are only fractions of dex lower than the SMD of extrapolated full GSMF, we expect that we are not severely underestimating the stellar mass in passive galaxies.

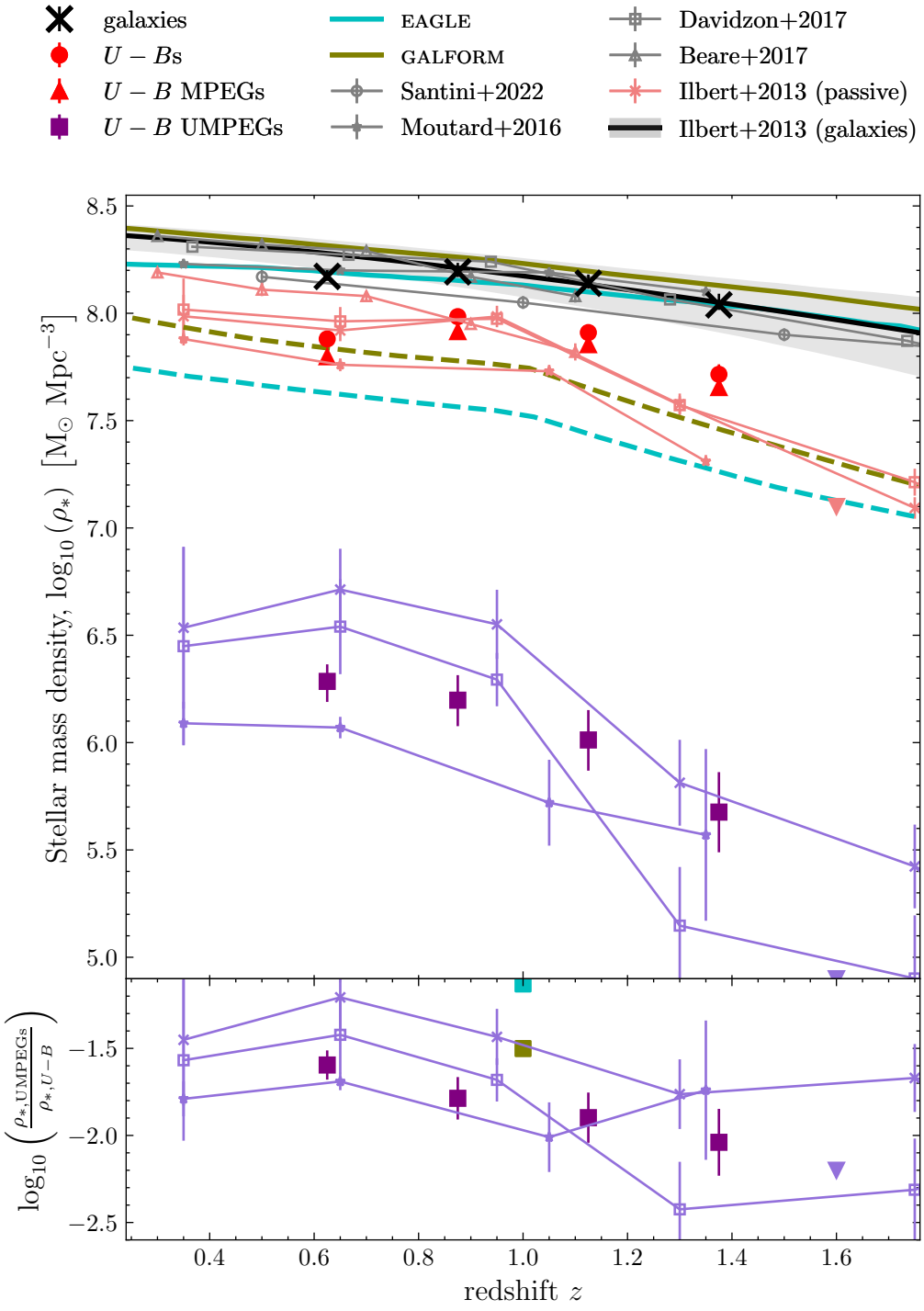

Figure 5.13: Stellar mass density as a function of redshift, for the full galaxy sample (black crosses), red $U-B$-selected passive galaxies, and the most massive passive galaxies ("UMPEGS") with $\log_{10}(\mathcal{M}/\mathrm{M}_\odot) > 11.5$. Results from various other observational studies are also plotted as smaller (joined) symbols. The symbols are consistent, and are black form the full galaxy samples, and red for passive galaxies. The exception is the SMD estimates of Ilbert et al. (2013), who provide a parametric fit to their data for galaxies, which is shown as the grey line.

In the lower panel of Figure 5.13 we plot the ratio of the SMD of the full sample of passive galaxies to the SMD of UMPEGs. Our results show that the SMD of UMPEGs increases relative to that of the full passive sample towards later times. We compute this same ratio for the GSMF parameters provided by other studies (Moutard et al., 2016; Davidzon et al., 2017; Santini et al., 2022), by integrating the GSMF fit parameters they provide. Although the normalisation is not the same for the ratios we compute for other studies, on the whole this trend is the same - we again attribute this difference to differences in passive selection. This indicates that the most massive of the passive galaxies are growing at a faster rate than passive galaxies on the whole. We estimate a relative increase of around 0.4 dex over the redshift range we are able to measure.

We also include the SMD ratio of these massive galaxies from the GALFORM and EAGLE simulations, integrating the traces in Figure 5.12. The GALFORM ratio is in best agreement with the observational data (but still slightly higher than our own measurements), whereas the EAGLE measurement is somewhat higher. This can be expected given their respective GSMF measurements, however. The EAGLE passive GSMF has a shallower cutoff, producing more high mass passive galaxies relative to the low mass ones. We further caveat the measurements of these ratios noting that the GSMF in Guo is only presented for $\log_{10}(\phi) \gtrsim -6.8$, at which $\log_{10}(\mathcal{M}/\mathrm{M}_{\odot}) \sim 11.7$ which is not much larger than the lower integral bound.

In their work which considers semi-analytic models, Contini et al. (2020) compute the mass quenching efficiency of central and satellite passive galaxies as a function of both stellar mass and redshift. Both samples show strong dependence on stellar mass at all redshifts, as is expected from the physical interpretation of the Schechter functional form of the GSMF. The global trend is that at all redshifts (for both passive and satellite galaxies) the quenching efficiency increases with mass for both central and satellite galaxies. This is in line with the expectation from the exponential cutoff of the mass function. More subtly, however, their trends show that the most massive centrals are less efficiently quenched at low redshifts, with little change in the quenching efficiency of the low mass galaxies (as a function of redshift).

We argue that our result supports this: excess growth of the most massive, passive galaxies towards later times indicates that the quenching of these galaxies is less efficient at lower redshifts.

An alternate explanation would be that this excess growth is driven by "dry" (gas poor) mergers. In their observational study using the NEWFIRM Medium-Band Survey, Brammer et al. (2011) infer that dry mergers can account for $\sim 50\%$ of the growth of stellar mass density

$\mathcal{M} > 10^{11}\mathrm{M}_{\odot}$ passive galaxies, but require transformation of star-forming to passive galaxies (ie, quenching) to explain the SMD growth of lower mass passive galaxies. This result is in contradiction with Arcila-Osejo, who conclude that such mergers are unlikely to be a strong contribution to the most massive passive galaxies, as they say that the mass function's strong adherence to the Schechter function implies only a single quenching mechanism: mergers would distort the GSMF shape.

Of course - the conclusions we draw are based on the integral of the massive end of the passive galaxy GSMF, where uncertainties are large (reflected in the large error bars on the SMD values plotted in Figure 5.13). We further caveat our conclusions by noting the discrepancy between our GSMF double Schechter fits in the furthest redshift bin, and the decrease in SMD for both the passive and full galaxy samples in the nearest redshift bin.

We point out that DXS is one of the best-placed existing surveys to perform measurements such as this at these redshifts. Given their rarity (as evidenced by the exponential tail $\phi(\mathcal{M})$), large cosmological volumes are needed to select them. In this work, we only include two of the four DXS fields due to our currently-limited photometric redshift estimates. Future improvements will allow all four fields to be utilised.

Although one of the advantages of the DXS survey is its large area for a survey which reaches $z \sim 1.5$, datasets from the *Euclid* and *Rubin* LSST surveys will provide estimates of the massive end of the passive GSMF with much higher precision.

5.3 Summary

This Chapter demonstrates that our catalogues are adequate to calculate the luminosity function of galaxies to a degree of precision comparable with previous studies over the range of redshifts that DXS was designed to probe, $0.5 < z < 1.5$. Further, we demonstrate similar trends in the parameters of these luminosity functions.

As the aim of this Thesis is to investigate the red populations galaxies which are able to be selected with a NIR survey, we also calculate the luminosity function of our largest sample of red galaxies, EROs.

We show that the LF of this selection of objects has properties similar to the selection of galaxies made with previous, similar selections of red galaxies (based on their restframe colours), although they are not identical due to the presence of the dusty star-forming galaxies also selected with the ERO criteria.

Our luminosity functions of these red selections of galaxies show that the majority of their contribution to the luminosity function is at the brightest K magnitudes (brighter than the characteristic magnitude), as is to be expected from the most massive galaxies which the EROs select. By considering the ratio between the LF of the passive galaxy selections and the full galaxy sample, we estimate that these contribute around $50-70\%$ of the luminosity of the galaxy LF at luminosities brighter than M_K^* (although the exact fraction depends on the exact selection method), which drops off quite rapidly (ie, within 1 mag of M_K^*).

We consider the galaxy stellar mass functions of the full galaxy sample, and of red $U-B$ selections in the redshift range $0.5 < z < 1.5$, and find strong agreement with previous studies. For the full sample, we measure very little change in the characteristic mass $\mathcal{M}_*$, which can be interpreted as evidence for downsizing: the growth of the most massive galaxies stalls at a constant mass over this redshift range. We similarly observe the characteristic luminosity M_K^* from the LF as roughly constant. On the contrary, and consistent with literature studies, we see a minor increase in this parameter for the passive sample over the redshift range. However, we note that this can also be explained by the degeneracy between the characteristic mass $\mathcal{M}_*$ and the low mass slope α.

Finally, by studying the integrated stellar mass density of passive galaxies, and the extreme of the massive tail of these galaxies, we observe that the most massive, passive galaxies ($\mathcal{M} > 10^{11.5}\mathrm{M}_\odot$) grow by an excess 0.4 dex compared to the whole passive sample. As many literature studies find excellent agreement of the stellar mass function to a Schechter function (implying a single quenching mechanism, and not a large contribution from mergers), one explanation of this could be that the mass quenching of galaxies is less efficient for the most massive galaxies at lower redshifts than at higher redshifts.

Chapter 6

Conclusions

In this Chapter we conclude by first providing a very brief summary the key results from this work, then give a slightly longer synopsis of the whole Thesis, and finally discuss some future investigations we would make based on this work.

6.1 Key result summary

In this Thesis, we:

- produce deep, uniform NIR catalogues to $K_{\rm AB} \sim 22.7$ (5σ for point sources) over $\sim 28\,{\rm deg}^2$ which will be made public in the near future;
- measure the number counts of galaxies $14 < K < 22$ which agree very well with previous measurements and the semi-analytic model GALFORM;
- show that there is a significant overlap between various photometric passive galaxy selections, and demonstrate that EROs (one of these selections) can be recovered with $(i - H)_{\rm AB} > 1.90$, a result that will be useful for (photometrically) cheap studies with *Euclid*-*Rubin* LSST catalogues and comparing with existing literature;
- illustrate the strong break in the passive galaxy correlation function, and show that passive galaxies are much more strongly clustered than star-forming galaxies, supporting environmental quenching;
- measure that the correlation length of the small scale (intra-halo) clustering of the ERO (passive) population is roughly constant $r_0 \sim 8\,{\rm Mpc}\ h^{-1}$, qualitatively suggesting that the halo mass of the most massive ERO is also roughly constant over the range $1 < z < 1.5$;

- the K-band galaxy luminosity function and galaxy stellar mass function over the range $0.5 < z < 1.5$, which agree well with previous measurements of these statistics, and support the galaxy downsizing picture (by means of roughly constant characteristic luminosities and stellar masses M_K^* and $\mathcal{M}_*$);
- compute the integrated galaxy stellar mass density as a function of redshift, and uncover evidence that suggests that the most massive passive galaxies are less efficiently quenched at lower redshift than they were at high redshift.

6.2 Thesis synopsis

In Chapter 2, we first introduce the UKIDSS-DXS survey by describing its place amongst a large range of other NIR surveys. Using the 5458 WFCAM pawprints taken as part of the DXS survey we produce 28.2 deg^2 of J and K band mosaics in the four DXS fields. We use a two-step background subtraction technique to ensure that the sky background is very flat, and further demonstrate that this method does not have a significant impact on the photometry. We describe the processes we use to significantly reduce the risk of including spurious sources from read-out electronics, and diffraction spikes from bright stars.

Tests in this Chapter show that our mosaics meet the target depths of $K_{AB} \sim 22.7$ and $J_{AB} \sim 23.2$ (5σ, point sources) set out by Lawrence et al. (2007) at $> 90\%$ completeness for a majority of the DXS area. Significant fractions of the four DXS fields are also covered by optical and MIR data, and we describe those which we use in later analysis. Finally, we present the photometric redshift estimates we obtain using EAZY. Our photometric redshifts are poor at $z < 0.4$ in comparison to those of other works, but we argue that is our application of the photometric redshift procedure that is poor and not the DXS photometry, by comparison to the UDS-HSC catalogues (which have extremely reliable photometry).

Chapter 3 discusses selections of red populations of galaxies that we are able to make. First, however, we discuss various star-galaxy separation criteria, and choose a star-galaxy separation which uses the $r - i$ and $J - K$ colours. To ensure that the number of stars that we remove is roughly correct, we compare the number counts of galactic stars to those of *Gaia*, for each of the four fields. We then move on to the K-selections of galaxies, of which we select Distant Red Galaxies, ($(J - K)_{AB} > 1.3$), Extremely Red Objects ($i - K > 2.45$ or $i - K > 2.55$), and gzKs (an adaptation of the BzK selection of Daddi et al., 2004).

Our number counts of these selections of agree well with previous literature values, and for the star-forming sample, agree well with the predictions of semi-analytic model GALFORM. GALFORM under predicts the number of passive galaxies at bright magnitudes, compared with our counts, and those of literature. We provide a detailed comparison of the selections (for objects selected $K < 21.5$), and demonstrate that there is significant overlap between objects with similar properties. In particular, we note that the majority of passively-evolving gzK galaxies are also selected as EROs at this magnitude cut. Finally, we investigate the $i - H$ criteria which most closely matches our (HSC) $i - K > 2.55$ criteria. We find that $i - H > 1.90$ recovers $\sim 95\%$ of the $i - K$ EROs, with only a contamination of 5%, a result which could be useful for the extremely large surveys the future (eg. *Euclid-Rubin* LSST) to provide cheap methods to select samples of galaxies from the vast photometric catalogues which will be available. This cut is not a newly proposed selection technique, but rather proof that these selections are roughly equivalent.

The angular two-point correlation functions of these selections of red galaxies are presented in Chapter 4. Firstly, we measure the correlation function of EROs. We demonstrate that over the range of scales that DXS is able to probe, a single power law is insufficient to describe the angular correlation function - there is a significant break which has been and further show that the slope of the angular correlation function on the smallest scales is significantly steeper on the smallest scales that the slope of $\delta = 0.8$ which is often assumed. Although they are only empirical descriptions of the correlation function of the galaxy selections, the concordance of our estimates (and best fitting parameters) of the correlation function between fields, and with previous measurements is an extremely useful verification test of our catalogues: they are uniform, and not incorrectly reduced. By comparing the small scale slope using the separate power laws to that of the power law which is obtained with the function which describes all scales, we obtain yet a steeper slope. We argue that this shows that careful consideration of the clustering on intermediate scales is necessary to accurately describe the very smallest scales. We do not observe the extremely shallow slopes on the largest scales which have been measured by previous studies, however, and measure that these are similar to (or marginally shallower than) $\delta = 0.8$ for the faintest magnitude cuts. When considering the strength of the angular clustering for increasingly faint magnitude cuts, we show, as with previous works, that the brightest selections of galaxies do indeed show the strongest clustering. Our measurement the correlation length r_0 of the small scale clustering of EROs across the range of magnitudes where we detect an appreciable number of EROs to

be roughly constant. Interpreting the correlation length as an indicator of the typical scale of the host dark matter halo, and assuming that the halo mass is determined by the most massive galaxy, we quantitatively expect that the mass of the host haloes of most massive EROs is roughly constant over the redshift range of DXS, a result which is not dissimilar to the trend demonstrated in Kim et al. (2014) who use a more robust HOD approach.

We move on to discussing the angular clustering properties of passive gzKs. Similarly to the EROs, we observe a very strong break at $\sim 1'$ in the angular correlation function. Again we see that the brightest selections of galaxies exhibit significantly stronger clustering, and that the small scale clustering shows much steeper slopes than $\delta = 0.8$. Finally, we compare the angular correlation functions of the passive gzKs with the star-forming galaxies. We show that at all scales, the passive galaxies have a much stronger clustering signal than the star forming ones.

Chapter 5 investigates the K-band luminosity function of our galaxy catalogues. We compute the LF of all galaxies $0.5 < z < 1.5$, and compare with previous measurements in similar redshift ranges. The fact that our measured LFs agree well with the literature values give us confidence that our photometric redshifts are at least sufficient to use in redshift ranges (at least for $0.5 < z < 1.5$). We measure the LF of two selection of red galaxies. Firstly, we use the restframe red $U - B$ selection which has been demonstrated in previous works, and show that our catalogues produce a restframe colour-magnitude diagram with a similar bimodality between the red and blue populations. We then demonstrate that the EROs we select are a very similar population to that of the red $U - B$s. We show that the LF of our EROs are not dissimilar to that of the red $U - B$s, although we observe a slightly shallower faint end slope, which we attribute to the ERO criteria also selecting dusty star-forming galaxies. By comparing the ERO LF to the LF of the full galaxy population, we show that the ERO criteria is in fact selecting the most luminous (and hence most massive) galaxies in this redshift range. At absolute magnitudes fainter than the characteristic magnitude, we observe that the EROs and $U - B$s contribute very little to the galaxy LF, whereas they account for $\sim 50\%$ of the luminosity function at the bright end. Given that this luminosity (and hence mass) is produced by very old stellar populations, this is evidence that a significant fraction of star-formation in the universe occurred at redshifts even higher than the those we measure with DXS. By considering the characteristic luminosity, M_K^*, we conclude that the K-band luminosity functions are evidence in support of galaxy downsizing: the fact that this parameter stays roughly constant from $1.5 < z < 0.5$ ($\sim 4\,\mathrm{Gyr}$) demonstrates that the mass at which galaxies begin to be quenched is constant.

6.3 Future work and outlook

6.3.1 Red galaxy selections

There are several immediate follow up investigations that lead on from the work we present in this Thesis.

The most obvious is to compute the correlation functions of the other selections of red galaxies. Although the DRGs we select in Chapter 2 are have smaller number counts (and a brighter limiting magnitude) than the other selections we make, they are expected to be extremely strongly clustered. Further, luminosity functions of the red restframe $U - B$ galaxies that we select in Chapter 5 demonstrate that this selection is effective at selecting the most luminous red galaxies in a similar manner to the ERO selection we make, but in a manner that makes use of much more of the available photometry. It would be interesting to contrast the correlation functions of this selection with the ERO selection, knowing that the ERO selection also includes the dusty star-forming population.

The angular correlation functions of the most massive, evolved galaxy populations are very good tests of models of galaxy formation. The physical characteristics of the dark matter haloes that can be derived from the halo modelling approach mentioned in Section 4.5.1 can be directly compared with the haloes that host the EROs in semi-analytic simulations such as GALFORM (Cole et al., 2000), as in Gonzalez-Perez et al. (2011) and Kim et al. (2014).

Further: including any U- or u-band legacy data would allow for improved photometric redshifts at $z < 0.5$, meaning that we would be able to include our analysis. Many of the deepest surveys (eg. COSMOS, UDS) surveys have very broad wavelength coverage, which allows them to primarily make galaxy based on template-fitting, including based on very accurate stellar mass estimates that this broad coverage provides. Including legacy datasets as described (and further investigation into improving the photo-z estimates with the current data) would be useful for studying the clustering of samples selected on these more physical properties with higher accuracy, while still retaining the significant area advantage that DXS has over deep and narrow surveys. Simulations typically also study galaxy evolution in this manner, so would provide a more direct means of comparison with simulations.

Moving beyond DXS, however, the vast datasets that the next generation of instruments and surveys will provide will allow for the study of the populations of galaxies that we select to much higher precision.

Ongoing surveys like SHARKS will observe to the same depth as DXS in K_s, but increase the area covered by a factor of 10, $\sim 300\,\mathrm{deg}^2$. An immediate investigation of EROs selected with SHARKS using DES, with i band depth of $\sim 24\,\mathrm{mag}$ as the optical counterparts would limit the faintest selection of $i - K > 2.5$ EROs to $K_s < 21.5$. However, this would be a complementary study to our work: the (relatively) limited area of the four DXS fields means that SHARKS would have a significantly larger (absolute) number of the brightest EROs which our work does not detect.

Further, as SHARKS is in the *Rubin*-LSST and *Euclid* footprints, as well as the spectroscopic WAVES wide survey, it will provide one of the richest datasets for K-band selection of galaxies when these surveys are in full operation. The SHARKS survey is also designed to be in the *Herschel*-ATLAS survey footprint giving FIR data for a large fraction of the brightest galaxies, meaning that extremely high quality photometric redshifts will be available for many of the objects.

As described in in Chapter 2, *Euclid* will observe an area ~ 500 times larger than DXS, and to significantly fainter magnitudes. Combined with *Rubin*-LSST, the numbers of objects will give orders of magnitude increase in the number of objects selected (including EROs). *Roman* will similarly observe up to thousands of square degrees in the NIR. The techniques described in this Thesis will be useful for cheap selection of extremely large samples of galaxies, compared to the computationally intensive template fitting (which will not be a trivial task for surveys of this magnitude).

Very large multiplexed spectroscopic surveys such as VLT-MOONS will further allow spectroscopic follow up of much larger samples of the NIR-selected galaxies than is currently possible.

6.3.2 Other DXS goals

Of course, the investigations which DXS will enable are not limited to the study of the red populations of galaxies selected in this Thesis.

Using DXS data from the Early Data Release (EDR), Swinbank et al. (2007) identify a massive supercluster in the ElaisN1 field at $z \sim 0.9$ using by measuring the surface density of objects in slices in $J - K$ and $I - K$ colour to identify candidate clusters. The galaxies in the five candidate clusters which they identify are then spectroscopically confirmed to exist within a range of $3000\,\mathrm{km\,s^{-1}}$, despite being selected across the whole $0.8\,\mathrm{deg}^2$ EDR field. They then interpret these as all belonging to the same massive supercluster, with the total

mass of the five candidates estimated at $> 10^{14.7}\,M_{\odot}$ by comparing to N-body simulations. Further, Chapter 6 of Jae-Woo Kim's PhD Thesis (Kim, 2011) uses a similar red sequence technique to identify similar surface density of clusters (with > 10 identified members) in a larger area of the ElaisN1 field and SA22 using their DXS-PS1 and DXS-CFHTLS catalogues, and show that galaxy clusters exhibit clustering which is significantly stronger than any of the selections based on individual galaxies. Given the final area of DXS is more than double the area of Jae-Woo Kim's Thesis work, with a significant fraction of the area still covered by PS1, these other DXS fields represent the opportunity to discover yet more extremely large structures.

6.4 Scientific acknowledgements

We are grateful to Nigel Metcalfe and Peter Draper for providing the PanSTARRS-MDS catalogues, and for their subsequent advice on using these data.

This work used the DiRAC@Durham facility managed by the Institute for Computational Cosmology on behalf of the STFC DiRAC HPC Facility (www.dirac.ac.uk). The equipment was funded by BEIS capital funding via STFC capital grants ST/K00042X/1, ST/P002293/1, ST/R002371/1 and ST/S002502/1, Durham University and STFC operations grant ST/R000832/1. DiRAC is part of the National e-Infrastructure.

This Thesis is based [in part] on data collected at the Subaru Telescope and retrieved from the HSC data archive system, which is operated by the Subaru Telescope and Astronomy Data Center (ADC) at National Astronomical Observatory of Japan. Data analysis was in part carried out with the cooperation of Center for Computational Astrophysics (CfCA), National Astronomical Observatory of Japan. The Subaru Telescope is honored and grateful for the opportunity of observing the Universe from Maunakea, which has the cultural, historical and natural significance in Hawaii.

Appendix A

List of abbreviations

2PCF	Two-point correlation function
BzK	Object selected with Daddi et al. (2004) BzK criteria
DRG	Distant red galaxy
DXS	Deep eXtragalactic Survey (component of UKIDSS)
DG-ERO	Dusty galaxy - extremely red object
ERO	Extremely red object
FWHM	Full Width at Half Maximum (measure of distribution spread, FWHM = 2.355σ)
gzK	Modified version of BzK criteria
HSC	HyperSuprimeCam (optical camera on Subaru telescope)
IRAC	InfraRed Array Camera (*Spitzer* MIR imaging instrument)
LF	Luminostity Function
MIR	Mid Infrared (wavelength range, $3\,\mu\text{m} \lesssim \lambda \lesssim 8\,\mu\text{m}$)
NIR	Near Infrared (wavelength range, $0.8\,\mu\text{m} \lesssim \lambda \lesssim 2.5\,\mu\text{m}$)
OG-ERO	Old galaxy - extremely red object
PE-BzK	Passively evolving BzK-selected object
PE-gzK	Passively evolving gzK-selected object
PLE	Power law plus exponential cutoff (model)
PSF	Point spread function
SED	Spectral energy distribution
SF-BzK	Star-forming BzK-selected object
SF-gzK	Star-forming gzK-selected object
SpUDS	*Spitzer* Ultra Deep Survey (MIR survey)
SWIRE	*Spitzer* Wide-area Infrared Extragalactic (MIR survey)
UDS	Ultra Deep Survey (component of UKIDSS)
UKIDSS	UKIRT Infra-red Deep Sky Survey (multi-component NIR survey)
UKIRT	UK Infra-red Telescope
UV	Ultraviolet (wavelength range, $100\,\text{nm} \lesssim \lambda \lesssim 400\,\text{nm}$)
WFCAM	Wide-field camera (NIR camera on UKIRT)

Appendix B

Survey characteristics

Table B.1 lists representative coordinates for each of the 43 tiles DXS and the UDS field. Finally, Table B.2 reports the data presented in the NIR survey comparison, in Figure 2.3.

Table B.1: Representitive coordinates for all tiles in each DXS field. UDS is included for completeness.

Field	Tile	R.A.	Dec	Field	Tile	R.A.	Dec
ElaisN1	1	16 11 09.5	+54 36 45	SA22	1	22 17 30.9	+00 16 48
	2	16 05 24.7	+54 37 39		2	22 21 00.7	+00 17 28
	3	16 05 21.0	+55 25 32		3	22 21 01.2	+01 09 53
	4	16 11 15.3	+55 25 33		4	22 17 30.6	+01 09 21
	5	16 16 48.9	+55 25 42		5	22 14 01.5	+01 09 47
	6	16 16 45.2	+54 36 48		6	22 14 01.3	+00 18 51
	7	16 13 40.7	+53 46 02		7	22 14 01.5	-00 35 01
	8	16 08 05.1	+53 46 03		8	22 17 30.7	-00 35 00
	9	16 13 58.3	+56 15 58		9	22 21 02.7	-00 34 56
	10	16 07 47.7	+56 15 56		10	22 10 31.4	+01 10 02
	11	16 22 31.5	+54 57 28		11	22 10 31.2	+00 17 36
	12	15 59 28.0	+54 57 28		12	22 10 31.5	-00 35 06
Lockman	1	10 54 12.2	+57 34 53	XMM-LSS	1	02 26 45.1	-04 38 30
	2	10 54 14.2	+58 23 59		2	02 23 17.1	-04 38 27
	3	10 47 47.3	+58 23 49		3	02 23 16.8	-03 45 37
	4	10 47 45.1	+57 32 57		4	02 26 50.2	-03 45 36
	5	10 54 18.0	+59 15 18		5	02 19 46.0	-03 45 26
	6	10 47 33.4	+59 14 10		6	02 19 54.6	-02 51 24
	7	10 41 27.6	+59 16 32		7	02 23 19.7	-02 51 48
	8	10 41 33.3	+58 25 58		8	02 26 47.7	-02 52 37
	9	10 41 30.3	+57 31 09				
	10	10 45 04.6	+56 41 08		UDS	02 17 48.0	-02 06 14
	11	10 51 24.3	+56 41 58				

Table B.2: The data presented in Figure 2.3, in tabular form. Unless otherwise stated, the depth values are point source 5σ depths, in the K-band. [a]Variable depth, included as a component of UKIDSS, of which this work is also a component. [b]URL `https://roman.gsfc.nasa.gov/science/WFI_technical.html`

Survey/Instrument	Component	Area	Depth (AB)	Reference
UKIDSS/WFCAM	DXS	28	22.7	this work, Lawrence et al. (2007)
	UDS	0.8	25.3	Almaini et al. (in prep.)
	LAS	4028	20.3	Lawrence et al. (2007, 2012)
	GCS	1067	20.5	Lawrence et al. (2007, 2012)
	GPS	1868	-[a]	Lawrence et al. (2012)
UHS/WFCAM	UHS	12700	20.3	Dye et al. (2018)
VISTA/VIRCAM	VIDEO	12.0	23.5	Jarvis et al. (2013a,b)
	VEILS	9.0	24.5	Hönig et al. (2017)
	VIKING	1350	21.2	Edge et al. (2013); Arnaboldi et al. (2019); Wright et al. (2019)
	VHS	16684	20.0	Pons et al. (2020, DR5)
	UltraVISTA	0.73	25.6	McCracken et al. (2012); Moneti et al. (2019, DR4)
	SHARKS	300	22.7	Arnaboldi et al. (2019)
	G-CAV	30.0	23.0	“” “”
WIRCAM	WUDS	0.111	26.0 (3.0σ)	Pelló et al. (2018)
	WIRDS	2.1	24.5	Bielby et al. (2012)
NEWFIRM	NMBS	0.42	24.2	Whitaker et al. (2011)
ALHAMBRA	ALHAMBRA-K_s	2.47	23.4	Moles et al. (2008); Nieves-Seoane et al. (2017)
Euclid	*Euclid* Wide	14500	24.5 (H band)	Laureijs et al. (2011)
	Euclid Deep	40	26.5 (H band)	“” “”
Roman	1hr-pointing	0.32	26.2 ($F213$ band)	Roman WFI Webpages[b]
	55s-pointing	0.32	23.7 ($F213$ band)	“” “”
	EWAS	2000.0	27 ($F213$ band)	Benford & McEnry (2021)
	ETDS-coadd	20	28.0 ($F213$ band)	“” “”
	ETDS-epoch	20	26.0 ($F213$ band)	“” “”
WISE	allWISE	41252	20.0 ($W1$ band)	Wright et al. (2010)
	unWISE	41252	20.7 ($W1$ band)	Lang (2014); Meisner et al. (2017)
Spitzer	SERVS	18.0	23.1 ([3.6] band)	Mauduit et al. (2012)
	SWIRE	55	21.7 ([3.6] band)	Lonsdale et al. (2003)
	SpUDS	1.0	24.7 ([3.6] band)	Dunlop et al. (2007); Caputi et al. (2011)
	DeepDrill	29	23.1 ([3.6] band)	Lacy et al. (2021)
2MASS	2MASS	41252	16.2 (10.0σ)	Skrutskie et al. (2006)
DENIS	DENIS	22678	15.9	Harmon & Mamon (1993); Epchtein et al. (1994)

Bibliography

Abbott, T.M.C., Abdalla, F.B., Allam, S., et al. ApJS, **239**(2) (2018), 18.

Abell, G.O., Corwin, Harold G., J., Olowin, R.P. ApJS, **70** (1989), 1.

Aihara, H., AlSayyad, Y., Ando, M., et al. PASJ, **71**(6) (2019), 114.

Alam, S., Aubert, M., Avila, S., et al. Phys. Rev. D, **103**(8) (2021), 083533.

Alcalde Pampliega, B., Pérez-González, P.G., Barro, G., et al. ApJ, **876**(2) (2019), 135.

Alexander, D.M., Hickox, R.C. New A Rev., **56**(4) (2012), 93.

Almaini et al., O. (in prep.).

Arcila-Osejo, L., Sawicki, M. MNRAS, **435**(1) (2013), 845.

Arcila-Osejo, L., Sawicki, M., Arnouts, S., et al. MNRAS, **486**(4) (2019), 4880.

Arnaboldi, M., Delmotte, N., Gadotti, D., et al. The Messenger, **178** (2019), 10.

Banerji, M., McMahon, R.G., Hewett, P.C., et al. MNRAS, **427**(3) (2012), 2275.

Battisti, A.J., da Cunha, E., Grasha, K., et al. ApJ, **882**(1) (2019), 61.

Baugh, C.M. Private communication (2021).

Beare, R., Brown, M.J.I., Pimbblet, K., et al. ApJ, **815**(2) (2015), 94.

Beare, R., Brown, M.J.I., Pimbblet, K., et al. ApJ, **873**(1) (2019), 78.

Benford, D., McEnry, J. *Roman Space Telescope Project Status* (2021). URL `https://www.nsf.gov/attachments/300822/public/11_Roman_Space_Telescope_Update_Dominic_Benford_Julie_McEnry.pdf`.

Bertin, E., Arnouts, S. A&AS, **117** (1996), 393.

Bertin, E., Mellier, Y., Radovich, M., et al. *The TERAPIX Pipeline*. In D.A. Bohlender, D. Durand, T.H. Handley, eds., *Astronomical Data Analysis Software and Systems XI*, vol 281 of ASP Conf. Ser. (2002), page 228.

Bielby, R., Hudelot, P., McCracken, H.J., et al. A&A, **545** (2012), A23.

Blanc, G.A., Lira, P., Barrientos, L.F., et al. ApJ, **681**(2) (2008), 1099.

Blanton, M.R., Bershady, M.A., Abolfathi, B., et al. AJ, **154**(1) (2017), 28.

Bower, R.G., Benson, A.J., Malbon, R., et al. MNRAS, **370**(2) (2006), 645.

Bower, R.G., Lucey, J.R., Ellis, R.S. MNRAS, **254** (1992), 589.

Bradley, L., Deil, C., Patra, S., et al. *astropy/regions: v0.5* (2022). URL `https://doi.org/10.5281/zenodo.5826359`.

Bradley, L., Sipőcz, B., Robitaille, T., et al. *astropy/photutils: 1.1.0* (2021). URL `https://doi.org/10.5281/zenodo.4624996`.

Brammer, G.B., van Dokkum, P.G., Coppi, P. ApJ, **686**(2) (2008), 1503.

Brammer, G.B., Whitaker, K.E., van Dokkum, P.G., et al. ApJ, **739**(1) (2011), 24.

Brown, M.J.I., Jannuzi, B.T., Dey, A., et al. ApJ, **621**(1) (2005), 41.

Bruzual, G., Charlot, S. MNRAS, **344**(4) (2003), 1000.

Bruzual A., G. ApJ, **273** (1983), 105.

Caputi, K.I., Cirasuolo, M., Dunlop, J.S., et al. MNRAS, **413**(1) (2011), 162.

Casali, M., Adamson, A., Alves de Oliveira, C., et al. A&A, **467**(2) (2007), 777.

Chambers, K.C., Magnier, E.A., Metcalfe, N., et al. arXiv e-prints (2016), arXiv:1612.05560.

Cheema, G.K., Sawicki, M., Arcila-Osejo, L., et al. MNRAS, **494**(1) (2020), 804.

Cimatti, A., Daddi, E., Mignoli, M., et al. A&A, **381** (2002), L68.

Cirasuolo, M., Fairley, A., Rees, P., et al. The Messenger, **180** (2020), 10.

Cirasuolo, M., McLure, R.J., Dunlop, J.S., et al. MNRAS, **380**(2) (2007), 585.

Cirasuolo, M., McLure, R.J., Dunlop, J.S., et al. MNRAS, **401**(2) (2010), 1166.

Cole, S., Lacey, C.G., Baugh, C.M., et al. MNRAS, **319**(1) (2000), 168.

Conroy, C., Gunn, J.E., White, M. ApJ, **699**(1) (2009), 486.

Conselice, C.J., Newman, J.A., Georgakakis, A., et al. ApJ, **660**(1) (2007), L55.

Contini, E., Gu, Q., Ge, X., et al. ApJ, **889**(2) (2020), 156.

Cooray, A., Sheth, R. Phys. Rep., **372**(1) (2002), 1.

Coupon, J., Czakon, N., Bosch, J., et al. PASJ, **70** (2018), S7.

Cowie, L.L., Songaila, A., Hu, E.M., et al. AJ, **112** (1996), 839.

Daddi, E., Cimatti, A., Renzini, A., et al. ApJ, **617**(2) (2004), 746.

Dalton, G.B., Caldwell, M., Ward, A.K., et al. *The VISTA infrared camera.* In I.S. McLean, M. Iye, eds., *Society of Photo-Optical Instrumentation Engineers (SPIE) Conference Series*, vol 6269 of *Society of Photo-Optical Instrumentation Engineers (SPIE) Conference Series* (2006), page 62690X.

Davé, R., Thompson, R., Hopkins, P.F. MNRAS, **462**(3) (2016), 3265.

Davidzon, I., Ilbert, O., Laigle, C., et al. A&A, **605** (2017), A70.

Davies, L.J.M., Thorne, J.E., Robotham, A.S.G., et al. MNRAS, **506**(1) (2021), 256.

Dawson, K.S., Schlegel, D.J., Ahn, C.P., et al. AJ, **145**(1) (2013), 10.

Dressler, A. ApJ, **236** (1980), 351.

Dudzevičiūtė, U., Smail, I., Swinbank, A.M., et al. MNRAS, **494**(3) (2020), 3828.

Dunlop, J., Farrah, D., Ouchi, M., et al. *A Spitzer Public Legacy survey of the UKIDSS Ultra Deep Survey.* Spitzer Proposal (2007).

Dye, S., Lawrence, A., Read, M.A., et al. MNRAS, **473**(4) (2018), 5113.

Dye, S., et al. MNRAS, **372**(3) (2006), 1227.

Edge, A., Sutherland, W., Kuijken, K., et al. The Messenger, **154** (2013), 32.

Efstathiou, G., Ellis, R.S., Peterson, B.A. MNRAS, **232** (1988), 431.

Eisenstein, D.J., Zehavi, I., Hogg, D.W., et al. ApJ, **633**(2) (2005), 560.

Elbaz, D., Daddi, E., Le Borgne, D., et al. A&A, **468**(1) (2007), 33.

Elston, R., Rieke, G.H., Rieke, M.J. ApJ, **331** (1988), L77.

Epchtein, N., de Batz, B., Copet, E., et al. Ap&SS, **217**(1-2) (1994), 3.

Fabian, A.C. ARA&A, **50** (2012), 455.

Fang, G.W., Kong, X., Wang, M. Research in Astronomy and Astrophysics, **9**(1) (2009), 59.

Fontana, A., Santini, P., Grazian, A., et al. A&A, **501**(1) (2009), 15.

Fontanot, F., De Lucia, G., Monaco, P., et al. MNRAS, **397**(4) (2009), 1776.

Foreman-Mackey, D., Hogg, D.W., Lang, D., et al. PASP, **125**(925) (2013), 306.

Franx, M., Labbé, I., Rudnick, G., et al. ApJ, **587**(2) (2003), L79.

Frith, W.J., Busswell, G.S., Fong, R., et al. MNRAS, **345**(3) (2003), 1049.

Gaia Collaboration, Prusti, T., de Bruijne, J.H.J., et al. A&A, **595** (2016), A1.

Giavalisco, M. ARA&A, **40** (2002), 579.

Girelli, G., Bolzonella, M., Cimatti, A. A&A, **632** (2019), A80.

Gonzalez-Perez, V., Baugh, C.M., Lacey, C.G., et al. MNRAS, **417**(1) (2011), 517.

Gonzalez-Perez, V., Lacey, C.G., Baugh, C.M., et al. MNRAS, **439**(1) (2014), 264.

Goto, T., Yamauchi, C., Fujita, Y., et al. MNRAS, **346**(2) (2003), 601.

Grazian, A., Fontana, A., Moscardini, L., et al. A&A, **453**(2) (2006), 507.

Grazian, A., Salimbeni, S., Pentericci, L., et al. A&A, **465**(2) (2007), 393.

Green, G. The Journal of Open Source Software, **3**(26) (2018), 695.

Greve, T.R., Weiβ, A., Walter, F., et al. ApJ, **719**(1) (2010), 483.

Groth, E.J., Peebles, P.J.E. ApJ, **217** (1977), 385.

Guo, Q., Gonzalez-Perez, V., Guo, Q., et al. MNRAS, **461**(4) (2016), 3457.

Harmon, R., Mamon, G. *The Detection of Galaxies in Infrared Surveys.* In B.T. Soifer, ed., *Sky Surveys. Protostars to Protogalaxies*, vol 43 of ASP Conf. Ser. (1993), page 15.

Hartley, W.G., Almaini, O., Cirasuolo, M., et al. MNRAS, **407**(2) (2010), 1212.

Hartley, W.G., Lane, K.P., Almaini, O., et al. MNRAS, **391**(3) (2008), 1301.

Hodgkin, S.T., Irwin, M.J., Hewett, P.C., et al. MNRAS, **394**(2) (2009), 675.

Hönig, S.F., Watson, D., Kishimoto, M., et al. MNRAS, **464**(2) (2017), 1693.

Hubble, E. Proceedings of the National Academy of Science, **15**(3) (1929), 168.

Hubble, E.P. The Observatory, **48** (1925), 139.

Huchra, J.P. *Hubble's On Infall into the Virgo Cluster*. In S. van den Bergh, C.J. Pritchet, eds., *The Extragalactic Distance Scale*, vol 4 of *Astronomical Society of the Pacific Conference Series* (1988), page 257.

Hughes, I., Hase, T. *Measurements and their Uncertainties: A practical guide to modern error analysis*. OUP Oxford (2010). ISBN 9780199566334.

Ilbert, O., McCracken, H.J., Le Fèvre, O., et al. A&A, **556** (2013), A55.

Ishikawa, S., Kashikawa, N., Toshikawa, J., et al. MNRAS, **454**(1) (2015), 205.

Jarvis, M., Bernstein, G., Jain, B. MNRAS, **352**(1) (2004), 338.

Jarvis, M.J., Bonfield, D.G., Bruce, V.A., et al. MNRAS, **428**(2) (2013a), 1281.

Jarvis, M.J., Häußler, B., McAlpine, K. The Messenger, **154** (2013b), 26.

Jauzac, M., Jullo, E., Eckert, D., et al. MNRAS, **446**(4) (2015), 4132.

Ji, Z., Giavalisco, M., Williams, C.C., et al. ApJ, **862**(2) (2018), 135.

Johnson, B.D., Leja, J., Conroy, C., et al. ApJS, **254**(2) (2021), 22.

Kaiser, N. ApJ, **284** (1984), L9.

Kajisawa, M., Kodama, T., Tanaka, I., et al. MNRAS, **371**(2) (2006), 577.

Kim, J.W. *Galaxy clustering and galaxy clusters from the UKIDSS DXS* (2011). URL `http://etheses.dur.ac.uk/3270/`.

Kim, J.W., Edge, A.C., Wake, D.A., et al. MNRAS, **410** (2011), 241.

Kim, J.W., Edge, A.C., Wake, D.A., et al. MNRAS, **438**(1) (2014), 825.

Kochanek, C.S., Pahre, M.A., Falco, E.E., et al. ApJ, **560**(2) (2001), 566.

Lacey, C., Cole, S. MNRAS, **262**(3) (1993), 627.

Lacy, M., Surace, J.A., Farrah, D., et al. MNRAS, **501**(1) (2021), 892.

Landy, S.D., Szalay, A.S. ApJ, **412** (1993), 64.

Lane, K.P., Almaini, O., Foucaud, S., et al. MNRAS, **379**(1) (2007), L25.

Lang, D. AJ, **147**(5) (2014), 108.

Laureijs, R., Amiaux, J., Arduini, S., et al. arXiv e-prints (2011), arXiv:1110.3193.

Lawrence, A., Warren, S.J., Almaini, O., et al. MNRAS, **379**(4) (2007), 1599.

Lawrence, A., Warren, S.J., Almaini, O., et al. VizieR Online Data Catalog (2012), II/314.

Licquia, T.C., Newman, J.A. ApJ, **806**(1) (2015), 96.

Limber, D.N. ApJ, **117** (1953), 134.

Longhetti, M., Saracco, P. MNRAS, **394**(2) (2009), 774.

Lonsdale, C.J., Smith, H.E., Rowan-Robinson, M., et al. PASP, **115**(810) (2003), 897.

Madau, P., Dickinson, M. ARA&A, **52** (2014), 415.

Maddox, N., Hewett, P.C., Warren, S.J., et al. MNRAS, **386**(3) (2008), 1605.

Mainzer, A., Bauer, J., Grav, T., et al. ApJ, **731**(1) (2011), 53.

Mamon, G.A. *The Wide-Field DENIS Near-IR Imaging Survey and 6dF Redshift and Peculiar Velocity Surveys*. In S. Colombi, Y. Mellier, B. Raban, eds., *Wide Field Surveys in Cosmology*, vol 14 (1998), page 323. `astro-ph/9809376`.

Maraston, C. MNRAS, **362**(3) (2005), 799.

Martin, D.C., Fanson, J., Schiminovich, D., et al. ApJ, **619**(1) (2005), L1.

Mauduit, J.C., Lacy, M., Farrah, D., et al. PASP, **124**(917) (2012), 714.

Mawatari, K., Inoue, A.K., Hashimoto, T., et al. ApJ, **889**(2) (2020), 137.

Mawatari, K., Yamada, T., Fazio, G.G., et al. PASJ, **68**(3) (2016), 46.

McCarthy, P.J. ARA&A, **42**(1) (2004), 477.

McCracken, H.J., Capak, P., Salvato, M., et al. ApJ, **708**(1) (2010), 202.

McCracken, H.J., Metcalfe, N., Shanks, T., et al. MNRAS, **311**(4) (2000), 707.

McCracken, H.J., Milvang-Jensen, B., Dunlop, J., et al. A&A, **544** (2012), A156.

Meisner, A.M., Lang, D., Schlegel, D.J. AJ, **154**(4) (2017), 161.

Merson, A.I., Baugh, C.M., Helly, J.C., et al. MNRAS, **429**(1) (2013), 556.

Metcalfe, N., Draper, P.W. Private communication (2021).

Metcalfe, N., Shanks, T., Weilbacher, P.M., et al. MNRAS, **370**(3) (2006), 1257.

Moles, M., Benítez, N., Aguerri, J.A.L., et al. AJ, **136**(3) (2008), 1325.

Moneti, A., McCracken, H.J., Hudelot, P., et al. ESO Science Archive Facility (2019, DR4). URL `http://ultravista.org/release4/dr4_release.pdf`.

Mortlock, A., Conselice, C.J., Bluck, A.F.L., et al. MNRAS, **413**(4) (2011), 2845.

Mortlock, A., McLure, R.J., Bowler, R.A.A., et al. MNRAS, **465**(1) (2017), 672.

Moutard, T., Arnouts, S., Ilbert, O., et al. A&A, **590** (2016), A103.

Murray, S.G., Power, C., Robotham, A.S.G. Astronomy and Computing, **3** (2013), 23.

Natarajan, P., Chadayammuri, U., Jauzac, M., et al. MNRAS, **468**(2) (2017), 1962.

Navarro, J.F., Frenk, C.S., White, S.D.M. ApJ, **490**(2) (1997), 493.

Neistein, E., van den Bosch, F.C., Dekel, A. MNRAS, **372**(2) (2006), 933.

Nieves-Seoane, L., Fernandez-Soto, A., Arnalte-Mur, P., et al. MNRAS, **464**(4) (2017), 4331.

Nilson, P. *Uppsala general catalogue of galaxies* (1973).

Norberg, P., Baugh, C.M., Gaztañaga, E., et al. MNRAS, **396**(1) (2009), 19.

Norberg, P., Baugh, C.M., Hawkins, E., et al. MNRAS, **328**(1) (2001), 64.

Oke, J.B., Gunn, J.E. ApJ, **266** (1983), 713.

Palamara, D.P., Brown, M.J.I., Jannuzi, B.T., et al. ApJ, **764**(1) (2013), 31.

Pecaut, M.J., Mamajek, E.E. ApJS, **208**(1) (2013), 9.

Peebles, P.J.E. A&A, **32** (1974), 197.

Peebles, P.J.E. *Principles of Physical Cosmology*. Princeton University Press (1993).

Peebles, P.J.E., Groth, E.J. ApJ, **196** (1975), 1.

Peebles, P.J.E., Yu, J.T. ApJ, **162** (1970), 815.

Pelló, R., Hudelot, P., Laporte, N., et al. A&A, **620** (2018), A51.

Peng, Y.j., Lilly, S.J., Kovač, K., et al. ApJ, **721**(1) (2010), 193.

Percival, W.J., Cole, S., Eisenstein, D.J., et al. MNRAS, **381**(3) (2007), 1053.

Perlmutter, S., Aldering, G., Deustua, S., et al. *Cosmology From Type IA Supernovae: Measurements, Calibration Techniques, and Implications*. In *American Astronomical Society Meeting Abstracts*, vol 191 of *American Astronomical Society Meeting Abstracts* (1997), page 85.04. `astro-ph/9812473`.

Phillips, M.M. ApJ, **413** (1993), L105.

Planck Collaboration. A&A, **641** (2020), A6.

Poggianti, B.M., Barbaro, G. A&A, **325** (1997), 1025.

Pons, E., McMahon, R., Banerji, M., et al. *VISTA Hemisphere Survey Data Release (DR5)* (2020). URL `https://www.eso.org/rm/api/v1/public/releaseDescriptions/144`.

Pozzetti, L., Mannucci, F. MNRAS, **317**(1) (2000), L17.

Riess, A.G., Press, W.H., Kirshner, R.P. ApJ, **473** (1996), 88.

Robitaille, T. *reproject: astronomical image reprojection in Python* (2018). URL `https://doi.org/10.5281/zenodo.1162674`.

Roche, N., Eales, S.A., Hippelein, H., et al. MNRAS, **306**(3) (1999), 538.

Rodighiero, G., Daddi, E., Baronchelli, I., et al. ApJ, **739**(2) (2011), L40.

Ross, N.P., Shanks, T., Cannon, R.D., et al. MNRAS, **387**(3) (2008), 1323.

Rubin, V.C., Burstein, D., Ford, W. K., J., et al. ApJ, **289** (1985), 81.

Rubin, V.C., Ford, W. K., J., Thonnard, N. ApJ, **238** (1980), 471.

Rubin, V.C., Ford, W. Kent, J. ApJ, **159** (1970), 379.

Salmon, B., Papovich, C., Finkelstein, S.L., et al. ApJ, **799**(2) (2015), 183.

Sandage, A., Tammann, G.A., Yahil, A. ApJ, **232** (1979), 352.

Santini, P., Castellano, M., Fontana, A., et al. arXiv e-prints (2022), arXiv:2209.11250.

Santini, P., Castellano, M., Merlin, E., et al. A&A, **652** (2021), A30.

Saracco, P., Longhetti, M., Giallongo, E., et al. A&A, **420** (2004), 125.

Sato, T., Sawicki, M., Arcila-Osejo, L. MNRAS, **443**(3) (2014), 2661.

Sawangwit, U., Shanks, T., Abdalla, F.B., et al. MNRAS, **416**(4) (2011), 3033.

Schaye, J., Crain, R.A., Bower, R.G., et al. MNRAS, **446**(1) (2015), 521.

Schlegel, D.J., Finkbeiner, D.P., Davis, M. ApJ, **500**(2) (1998), 525.

Schmidt, M. ApJ, **151** (1968), 393.

Schreiber, C., Glazebrook, K., Nanayakkara, T., et al. A&A, **618** (2018), A85.

Seo, H., Jeong, W.S., Shim, H., et al. PASJ, **71**(5) (2019), 96.

Seo, H., Jeong, W.S., Shim, H., et al. MNRAS, **502**(2) (2021), 1933.

Shin, J., Shim, H., Hwang, H.S., et al. Journal of Korean Astronomical Society, **50**(3) (2017), 61.

Skrutskie, M.F., Cutri, R.M., Stiening, R., et al. AJ, **131**(2) (2006), 1163.

Slipher, V.M. The Observatory, **40** (1917), 304.

Smith, M.C., Sijacki, D., Shen, S. Monthly Notices of the Royal Astronomical Society, **478**(1) (2018), 302.

Sunyaev, R.A., Zeldovich, Y.B. Ap&SS, **7**(1) (1970), 20.

Swinbank, A.M. *The UKIDSS Deep eXtra-Galactic Survey.* In *Thirty Years of Astronomical Discovery with UKIRT*, vol 37 of *Astrophysics and Space Science Proceedings* (2013), page 299.

Swinbank, A.M., Edge, A.C., Smail, I., et al. MNRAS, **379**(4) (2007), 1343.

Szalay, A.S., Connolly, A.J., Szokoly, G.P. AJ, **117**(1) (1999), 68.

Taylor, M.B. *STILTS - A Package for Command-Line Processing of Tabular Data.* In *Astronomical Data Analysis Software and Systems XV*, vol 351 of ASP Conf. Ser. (2006), page 666.

Tilvi, V., Papovich, C., Tran, K.V.H., et al. ApJ, **768**(1) (2013), 56.

Tinker, J., Kravtsov, A.V., Klypin, A., et al. ApJ, **688**(2) (2008), 709.

Tonry, J.L., Stubbs, C.W., Lykke, K.R., et al. ApJ, **750**(2) (2012), 99.

van Albada, T.S., Bahcall, J.N., Begeman, K., et al. ApJ, **295** (1985), 305.

van Dokkum, P.G., Förster Schreiber, N.M., Franx, M., et al. ApJ, **587**(2) (2003), L83.

Vorontsov-Vel'Yaminov, B.A., Arkhipova, V.P. Morphological catalogue of galaxies, **C01** (1962), 0.

Wake, D.A., Whitaker, K.E., Labbé, I., et al. ApJ, **728**(1) (2011), 46.

Walsh, D., Carswell, R.F., Weymann, R.J. Nature, **279** (1979), 381.

Whitaker, K.E., Labbé, I., van Dokkum, P.G., et al. ApJ, **735**(2) (2011), 86.

White, S.D.M., Frenk, C.S. ApJ, **379** (1991), 52.

White, S.D.M., Navarro, J.F., Evrard, A.E., et al. Nature, **366**(6454) (1993), 429.

White, S.D.M., Rees, M.J. MNRAS, **183** (1978), 341.

Willett, K.W., Lintott, C.J., Bamford, S.P., et al. MNRAS, **435**(4) (2013), 2835.

Williams, R.J., Quadri, R.F., Franx, M., et al. ApJ, **691**(2) (2009), 1879.

Wright, A.H., Hildebrandt, H., Kuijken, K., et al. A&A, **632** (2019), A34.

Wright, E.L., Eisenhardt, P.R.M., Mainzer, A.K., et al. AJ, **140**(6) (2010), 1868.

Wuyts, S., Labbé, I., Franx, M., et al. ApJ, **655**(1) (2007), 51.

Xu, H., Dai, Y.S., Huang, J.S., et al. ApJ, **905**(2) (2020), 103.

York, D.G., Adelman, J., Anderson, John E., J., et al. AJ, **120**(3) (2000), 1579.

Zwicky, F. Helvetica Physica Acta, **6** (1933), 110.